Università degli Studi di Ferrara

DOTTORATO DI RICERCA IN
"SCIENZE DELLA TERRA"

CICLO XXVIII

COORDINATORE Prof. Massimo Coltorti

Metasomatism vs Refertilisation: New Insights from Northern Victoria Land mantle xenoliths (Antarctica)

Settore Scientifico Disciplinare GEO/07

Dottorando
Dott. Pelorosso Beatrice

_____
(firma)

Tutore
Prof. Bonadiman Costanza

_____
(firma)

Anni 2013/2016

Table of Contents

Introduction and aim of the thesis

This thesis is a part of a wider project focused on the study of Antarctica Sub Continental Lithospheric Mantle (SCLM), through the characterisation of the primary products of Cenozoic magmatism and the mantle xenoliths carried out on to the surface by the lavas.

As it is known, ultramafic xenoliths are an essential source of information on the nature and evolution of the lithospheric mantle. In this regard the main objective of this thesis is to provide a complete petrological characterisation of a wide area of the lithospheric mantle beneath Northern Victoria Land (NVL, Antarctica), focusing on the comprehension of the depletion and enrichment processes that have affected the peridotite matrix (i.e. melting, refertilisation, metasomatism), as well as on the constrains of the thermo-barometric conditions of the analysed suites.

Extensive petrological studies were carried out on mantle xenoliths from NVL, in order to define the petrological features of this portion of the lithospheric mantle.

Thermo-barometric conditions were investigated by Berg et al. (1989) on a suite of granulites entrained in Cenozoic alkaline volcanic rocks from the McMurdo Volcanic Group from Southern Victoria Land. The authors depicted a geotherm, later confirmed by P-T estimates obtained from mantle xenoliths in Mt. Melbourne lavas (Beccaluva et al.,1991a).

Recent studies on mantle xenoliths from Southern Victoria Land (Martin et al.; 2015) provide oxybarometer and geothermobarometer data in accord with those obtained in Northern Victoria Land (Perinelli et al., 2012; Bonadiman et al., 2014).

Zipfel and Worner (1992) proposed that the mantle xenoliths from Mt. Melbourne record three main stages: (1) adiabatic rise and dynamic high temperature recrystallization of mantle phases at lower pressure; (2) cooling and re-crystallization under low pressure; (3) local heating of lithospheric mantle linked to the magmatism of the Ross Sea Rift (West Antartic Rift system (WARS). Constraints on the nature and evolution of the mantle beneath this region were also suggested by Coltorti et al. (2004), who explained the amphibole in mantle xenoliths from Baker Rocks as a reaction product between under-saturated alkaline-silicate metasomatic fluids and pre-existing clinopyroxene and spinel. Cenozoic basalts from NVL were described in detail in terms of major and trace element compositions, as well as isotopic ratios by Nardini et al. (2009) with the aim to constrain the evolution of the WARS. On the basis of He isotopic ratio they excluded a mantle plume as the driving force responsible for the rifting processes, suggesting that the magmas originated in the lithospheric mantle were modified during a progressive replacement by asthenosphere-derived material. Small amounts

of melt were generated during the Cretaceous, which were unable to reach the surface, but strongly metasomatized the lithospheric domains. These enriched domains successively melted as a consequence of the transtensional tectonics that formed the WARS. Finally, magmas erupted to the surface following a NW– SE fault system to form plutons, dykes and lavas.

Most of the above mentioned studies concluded that the lithospheric mantle below the WARS is highly chemically and mineralogically heterogeneous. In order to contribute to this debate, in the following a detail petrological dataset (major, trace elements and isotopic data) of three Antarctic mantle xenolith suites is presented: Greene Point (GP, 73°46,186'S, 165°57,003E'), Handler Ridge (HR, 72° 31'S 167° 18'E) and Harrow Peaks (HP, 74° 04' 00" S 164° 45' 00" E), these latter never studied before, extending the knowledge of the Antarctica SCLM over a large area. This allowed to investigate the depletion and enrichment processes such as depletion, metasomatism and refertilisation, and to implement the geothermobatometer dataset of NVL, comparing also with recent mineralogical studies based on amphibole crystallochemistry (Bonadiman et al., 2014; Gentili et al., 2015).

The thesis is subdivided in six chapters, including the general introduction presented here and followed by the other chapters:

Chapters 1: gives a brief introduction to the Geological setting and the geological evolution of the Antarctica continent and the Northern Victoria Land.

Chapter 2: describes the analytical methods which include mineral major (EMP) and trace (LA-ICP-MS) analyses, as well as isotopic (TIMS) measurements of separate cpx.

Chapter 3 to chapter 5 follow the structure of a typical scientific paper, as they were written during my PhD period (*Pervasive, tholeiitic refertilisation and heterogeneous metasomatism in Northern Victoria Land lithospheric mantle (Antarctica),* by Pelorosso et al., Lithos 248–251 (2016) 493–505; *The role of percolating melts in Antarctic SCLM: new insights from Handler Ridge mantle xenoliths (Northern Victoria Land, Antarctica)*, by Pelorosso et al., submitted to GSA Special Paper entitled "The crust-mantle and lithosphere-asthenosphere boundaries: insights from xenoliths, orogenic deep sections and geophysical studies" (eds. Gianluca Bianchini, Jean-Louis Bodinier , Roberto Braga, Marjorie Wilson), in detail:

Chapter 3: consists of the petrological characterisation of GP xenoliths in term of major, trace elements and isotopic data.

Chapter 4: reports the petrological study of HR xenoliths in term of major, trace elements and isotopic data.

Chapter 5: provides the characterisation of the amphibole-bearing mantle xenolith suite of HP in term of major and trace elements composition and a comparison with the previously studied area of Baker Rocks (BR, Coltorti et al., 2004).

Chapters 6: reports the comparison between the three localities and an overview of the main outcomes of the present study.

Chapter 1. Geological Setting

1.1 Geology of Antarctica

Most Earth scientists consider the continents to have been organized on Earth in two distinct ways through time: dispersed, with several large continents and intervening oceans; and coalesced, with one or, perhaps, two 'supercontinents' present (Nance et al. 2013). Some authors suggest that there have been three principal periods of continental amalgamation, responsible for the Pangaea (0.3 Ga), Rodina (Fig 1.1a, b; 1.0 Ga) and Nuna (1.7 Ga) supercontinents, together with a time at the end of the Archaean when Earth's continents were assembled into either one dominant landmass (Kenorland: Williams et al. 1991) or into a small number of independent 'supercratons' (Superia, Scalvia and Vaalbara: Bleeker 2003). It is also commonplace to grant supercontinent status to Gondwana (Fig. 1.1b), the amalgam of present-day southern continents that formed at c. 0.5 Ga as a precursor to Pangaea. The influence of this continual reorganization of Earth's landmasses is not restricted to the continental crust, and it is also believed to have affected the surface environment and to have triggered profound changes in climatic and biological evolution (e.g. Valentine & Moores 1970; Campbell & Allen 2008). This history is also linked to Earth's deep interior, with evidence that the supercontinent cycle is coupled with mantle convection patterns (Gurnis 1988; Li & Zhong 2009). Relicts of these former continental amalgamations are now dispersed amongst the present-day continents, and correlations between these fragments can be used to reconstruct supercontinent palaeogeography. Despite being largely concealed beneath an extensive ice sheet, Antarctica contains rocks spanning some 3.5 billion years of history (Elliot 1975; Tingey 1991; Dalziel 1992; Fitzsimons 2000a; Harley 2003; Torsvik et al. 2008), and is likely to contain remnants of all Earth's recognized supercontinents.

The Antarctic continent is commonly divided into two distinct geological provinces, separated by the Transantarctic Mountains (Fig. 1.2).

East Antarctica lies to the Indian Ocean side of these mountains, and is dominated by cratonic igneous and metamorphic rocks of Archaean– Cambrian age, which are exposed sporadically along the coast and inland along the flanks of the Lambert Glacier – a topographical low in the ice sheet that overlies the late Palaeozoic–Mesozoic Lambert Graben (Fedorov et al. 1982; Lisker et al. 2003). The Transantarctic Mountains mark the site of the Ross Orogen, a Neoproterozoic passive margin on the edge of the East Antarctic Craton that had transformed into an active convergent margin by the Cambro- Ordovician (Stump 1995; Goodge 2002). West Antarctica lies to the Pacific Ocean side of the Transantarctic Mountains, and comprises

several Palaeozoic–Mesozoic terranes dominated by magmatic arc and turbidite systems with a complex history of subduction, accretion, magmatism and deformation throughout the Palaeozoic and Mesozoic (Dalziel & Elliot 1982; Vaughan et al. 2005).

As such, Antarctica has a remarkable story to tell about the evolution of our Earth, from the hottest crustal rocks yet found in an orogenic system and what they might mean for supercraton formation at 2.5 Ga, to the assembly and breakup of Gondwana in the Phanerozoic (Harley et al., 2013).

The actual geological asset is thus the result of an intense geological activity. Hereafter it is briefly summarised the main geological event that have characterised this continent.

During Archean and Proterozoic the continental mass of Antarctica was subjected to several episodes of aggregation into supercontinents through collisions and separation due to the formation of new oceanic basins. Major events that produced or modified the crustal and Sub-Continental Lithospheric Mantle occurred in the Archean between 2.9 and 3.6 Ga (Condie, 1998; Griffin et al., 2004). Subsequently two main suturing events occurred, one at 2.7 and one at 1.9 Ga (Condie, 1998). The supercontinent Rodinia (Fig 1.1a) was formed during the Grenville Orogeny, resulting from the collision of ancient continental masses and remnants of this belt outcrop in Australia, Antarctica, North America (the present day eastern coast of Laurentia), the Andean margin of Amazonia and East Africa (Kaz'min, 1988; Khain, 2000). As a result of rifting between 850 and 800 Ma ago, Rodinia (Fig 1.a, 1b) separated into three main groups of continental masses: the first comprised Antarctica, southwestern Africa (Congo and the Kalahari), India and Australia (Group 1); the second (Group 2) Laurentia, Amazonia, West Africa and Baltica, while the third was formed by North China, Tarim-Tien Shan continent and Siberia (Group 3). The spreading processes resulted in the formation of two new oceans: The Protopacific, separating Group 1 from Group 2, and the Paleoasian, which divided Siberia from North China and Tarim-Tien Shan (Kheraskova et al., 2009; Mossakovsky et al., 1996). According to Li et al. (2008) the separation of Antarctica from Australia and India was completed ~780 Ma ago and was related to the intense magmatic activity which occurred along the large Amadeus–Savory Rift System, on the western margin of the Protopacific in Australia (Preiss, 2000). Between 750 and 700 Ma Rodinia underwent further break-up as a result of the opening of three oceanic basins, i.e. the Celtic, Iapetus and Mauritanian (Cawood et al., 2001; Khain, 2000; Khudolei, 2003). The subsequent amalgamation of Laurentia, Antarctica and southwestern Africa (Congo–Kalahari) represented the beginning of the new supercontinent Gondwana (1.1b).

The actual East Antarctica is widely considered as an extension of the old supercontinent Gondwana, taking into account the strong similarities with the areas to which was connected.The subduction of oceanic lithosphere beneath the Paleo-Pacific margin of Gondwana (Borg et al., 1987; Kleinschmidt and Tessensohn, 1987) during the early Paleozoic produced the Ross Orogen and NW–SE- to NNW–SSE-striking tectonic discontinuities were generated within the Transantarctic Mountains (Gibson and Wright, 1985; Rocchi et al., 1998; Finn et al., 1999). One of these was the Tinker–Campbell Discontinuity (Rocchi et al., 1998), which separates two of the studied localities, Baker Rocks and Greene Point.After 100 Ma (from Devonian to Triassic) the Paleozoic Ross Orogen became the Kukri Peneplain and was affected by the Jurassic magmatism represented by the Ferrar Dolerites, a large igneous province emplaced along the backbone of the Ross Orogen (Elliot, 1999; Schmidt and Rowley, 1986; Storey and Alabaster, 1991). The Cretaceous was characterized by a phase of amagmatic rifting with the formation of four basins elongated in N–S direction in the Ross Sea and a widespread denudation in the Transantarctic Mountains (Balestrieri et al., 1994; Fitzgerald, 1994; Fitzgerald and Stump, 1997; Stump and Fitzgerald, 1992). According to Stump (1995, and references therein) they represent the uplifted roots of the early Paleozoic Ross Orogen, and constitute the western flank of the WARS, one of the largest and least known active rifts on Earth. It is over 3000 km long, from Queen Maud Mountains–Northern Victoria Land to the Ellsworth–Whitmore–Horlick Mountains, and 750 to 1000 km wide (Fig. 1.3) (Behrendt et al., 1991, 1992; LeMasurier and Thomson, 1990). Its eastern flank is located in Marie Byrd Land with an average elevation of 3000 m in the central part and is characterized by a basin and range topography (LeMasurier and Rex, 1989). During the Cenozoic, from 50 Ma onward (Rocchi et al., 2002; Tonarini et al., 1997), widespread magmatic activity affected the WARS, producing plutonic complexes, dike swarms and volcanoes. Volcanics of the McMurdo Volcanic Group (MVG) occur as stratovolcanoes, shield volcanoes, scoria cones, plugs, flows and volcanic piles up to 4000 m high along the Ross Sea margin of the Transantarctic Mountains and make up the Balleny Islands 300 km north of the Antarctic continental margin (Kyle, 1976).

The MVG is formed by four provinces: Balleny, Hallett, Melbourne and Erebus, this latter being still an active volcano.

The most part of samples studied in this thesis belong to Melbourne volcanic province, it covers the Transantarctic Mountains in Northern Victoria Land and ranges in age from 0 to 7 m.y. It includes The Pleiades, Mt. Overlord and Mt Melbourne, this latter being a strato-

volcano, the presence of fumarolic ice towers and ground heating could attest the presence of near-surface cooling magma (Kyle, 1990 and reference therein).

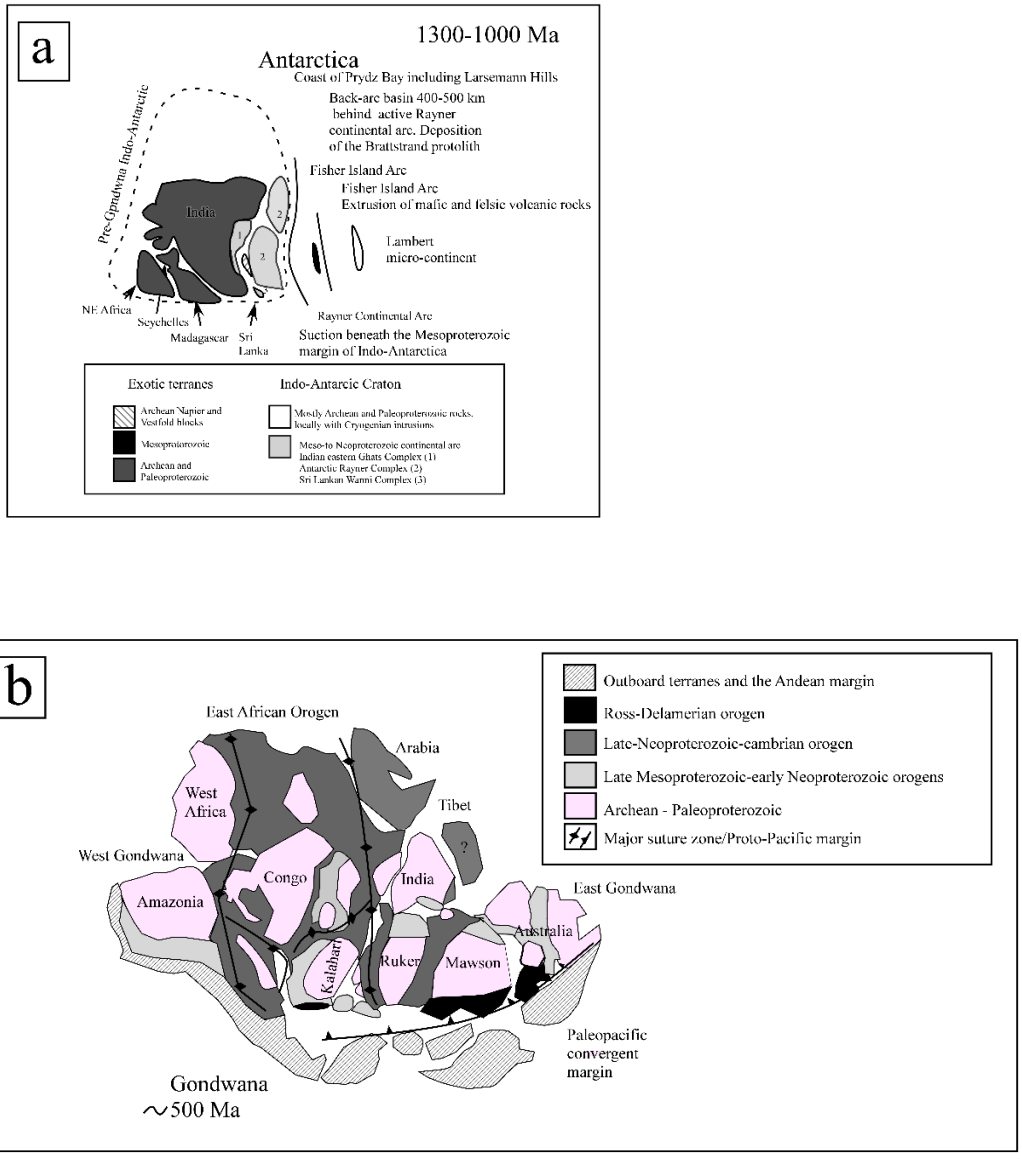

Fig.1.1 a) The Indo-Antarctic craton from 1300 Ma to 1000 Ma. Fit of the craton was taken from Reeves et al. (2002). Inclusion of North-Central Madagascar within pre-Gondwana India according to Tucker et al. (2011). Overall reconstruction is adapted from Boger (2011); b) Simplified map showing possible reconstruction model of Gondwana (modified after Ftzsimos 2000a; Zhao et a., 2003, Tohver et al., 2006).

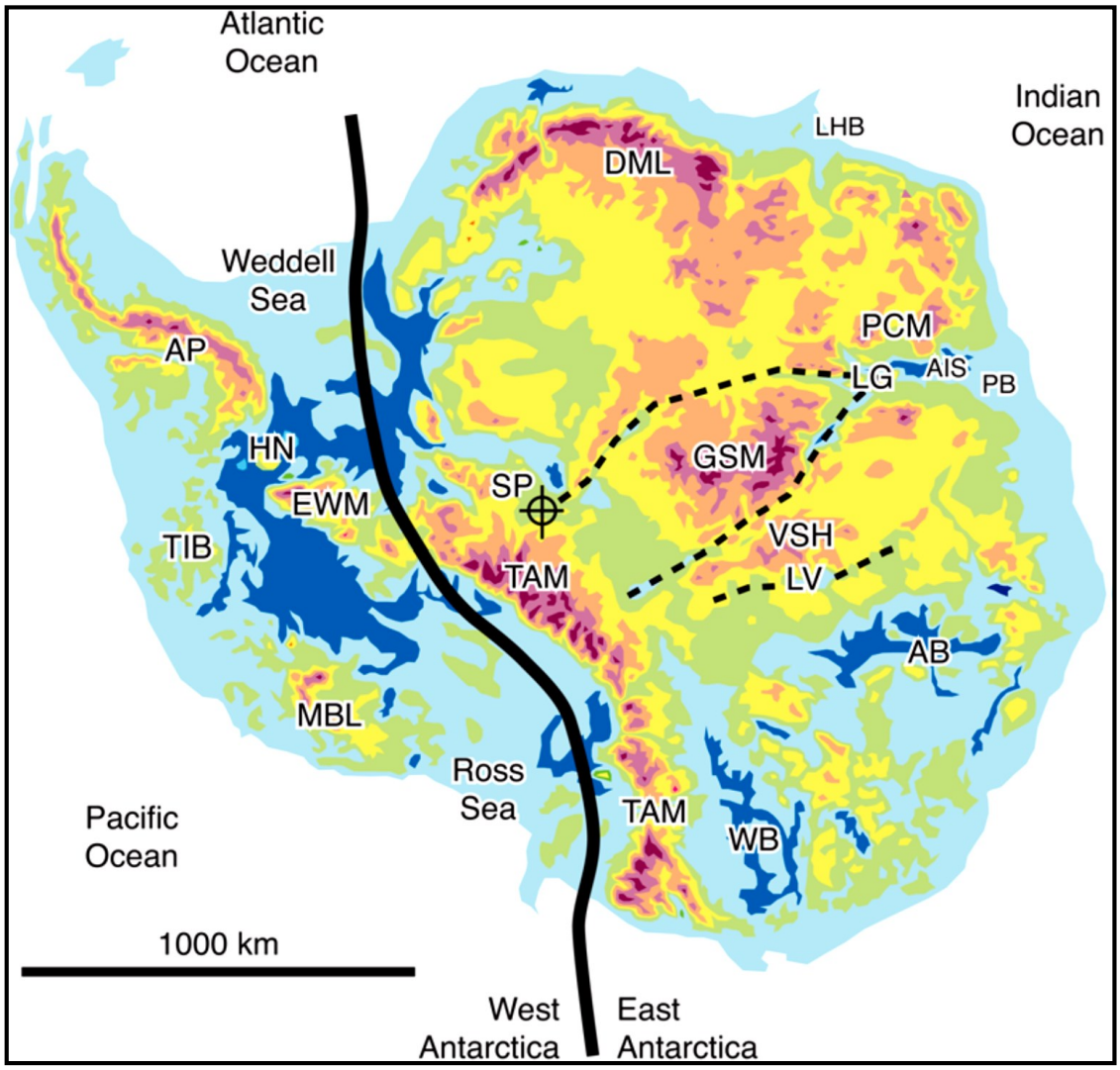

Fig. 1.2 Bedrock topography of Antarctica (blues below sea level; yellows and reds above sea level). The solid black line joining the Ross and Weddell seas divides East and West Antarctica. Prominent features of East Antarctica include: The Transantarctic Mountains (TAM); Gamburtsev Subglacial Mountains (GSM); Vostok Subglacial Highlands (VSH); Dronning Maud Land mountains (DML); Prince Charles Mountains (PCM); Lambert Graben (LG); Amery Ice Shelf (AIS); Prydz Bay (PB); Lutzow–Holm Bay (LHB); Lake Vostok (LV); Aurora Subglacial Basin (AB); Wilkes Subglacial Basin (WB). Black dashed lines denote the East Antarctic Rift System (Ferraccioli et al. 2011). Also shown is the South Pole (SP), and the five principal blocks of West Antarctica: the Antarctic Peninsula (AP); the Ellsworth–Whitmore Mountains Block (EWM); Haag Nunataks (HN); Marie Byrd Land (MBL); the Thurston Island Block (TIB). From Harley et al. (2013).

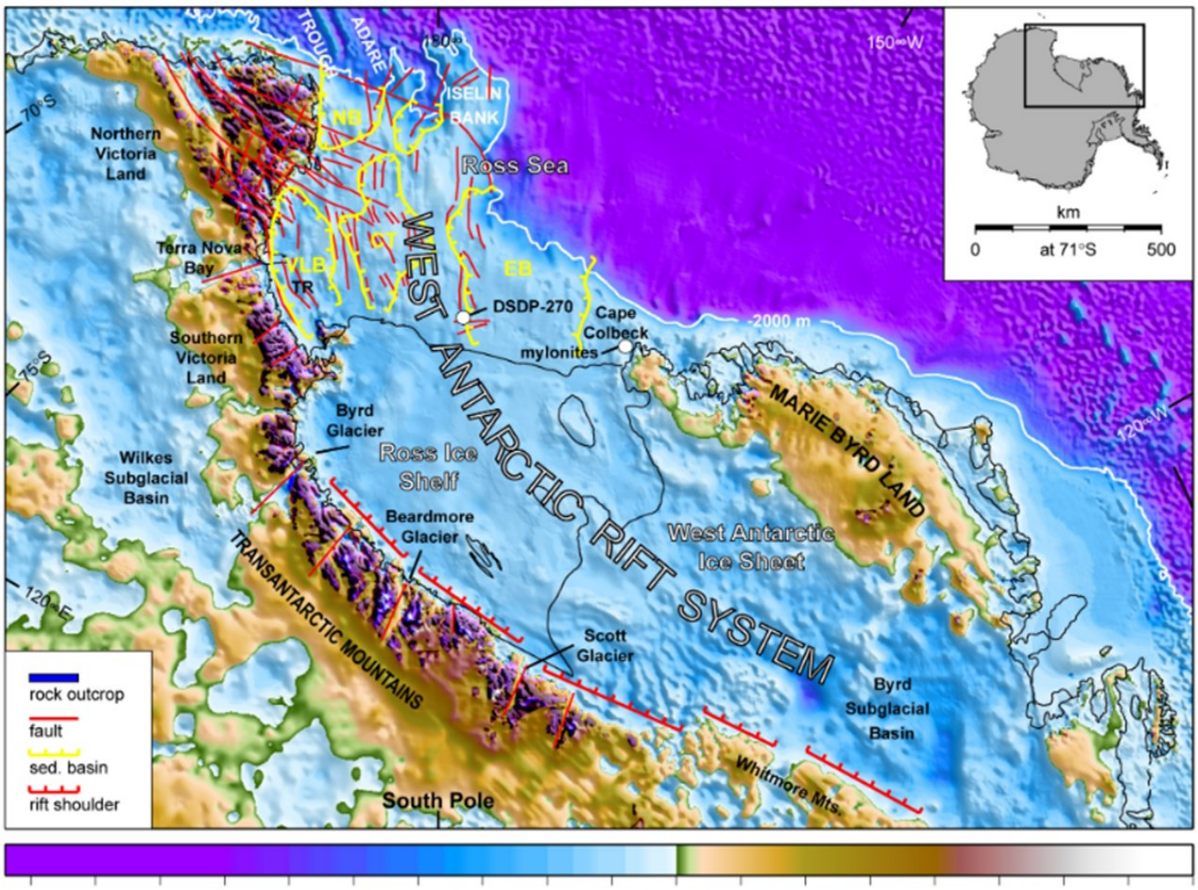

Fig. 1.3 Topographic and bathymetric map of Transantarctic Mountains and Ross Embayment. From Bialas et al. (2007).

1.2 Victoria Land

Victoria Land is a region of Antarctica bounded on the east by the Ross Ice Shelf and the Ross Sea and on the west by Oates Land and Wilkes Land. It is separated by the Greenwich meridian in two part Southern Victoria Land (SVL) and Northern Victoria Land (NVL).

1.2.1 Northern Victoria Land

NVL is located at the boundary between East and West Antarctica, at the Pacific termination of the Transantarctic Mountains (Fig. 1.4). The overall tectonic architecture of NVL has been commonly referred to the assembly and stabilisation of three different NNW-trending, Neoproterozoic to Early Palaeozoic, fault-bound lithotectonic units or "terranes" onto the East Antarctic Craton during the Early Palaeozoic Ross orogeny (i.e. Bradshaw et al., 1985; GANOVEX Team, 1987; Kleinschmidt & Tessensohn, 1987; Borg & Stump, 1987; Stump, 1995). From west to east These terranes are (Fig. 1.4): The Wilson, Bowers, and Robertson Bay Terranes. Weaver et al. (1984) introduced and Bradshaw et al. (1985) extended the concept of suspect terranes and Cambrian tectonics as a major contribution to the geological framework of NVL and hence increased the number of possible terranes. In addition to the Wilson, Bowers, and Robertson Bay terranes, they in fact outlined within the Wilson Terrane a so-called Daniels Terrane and a Lanterman Terrane and separated a Millen Terrane from the Robertson Bay Terrane.

These terranes are limited by faults system NW-SE: Lanterman Fault e la Leap Year Fault.

Wilson Terrane is made up of metamorphic rocks with different metamorphism degree.

The dominant lithology is constituted by the Granite Harbour Intrusive, this complex with calc-alkaline affinity is related to SW subduction of the Paleopacific plate below the craton. In the Wilson Terrane the following tectonic sequences Deep Freeze, Daniel Range and Morozuni Range and Desssent ridge Unit are also present.

Bowers Terrane is 400 km large from Marine Glacier (Ross Sea) to Rennick Bay (Pacific Ocean). It is constituted by sedimentary and volcanic rocks of Cambrian and Ordovician age (Stump, 1995). In the Bowers Supergroups there are three lithologic group Sledgers Group, Mariner Group, and Leap Year Group.

The Robertson Bay Terrane is 200 Km long, and it is made up a sequence of continental/marine sediments (Robertson Bay Group, Cambro-Ordovician). This sequence is

intruded by post-tectonic biotite granite and granodiorite of Devonian age (Admiralty Intrusive Complex).

As said above, during Cenozoic, Antarctica continent was interested by an intense volcanic activity, in Northern Victoria Land, this is testified by plutons and dike swarms (Meander Intrusive Group, Müller et al., 1991; Tonarini et al., 1997), emplaced over an area of about 400x80 km, and volcanic products, the McMurdo Volcanic Group (MVG, Kyle, 1990).

In the MVG, basic lavas carry abundant ultramafic xenoliths, providing a useful source of information on the nature of the lithospheric mantle beneath the rift.

Xenoliths studied in this thesis, were collected during two Italian expeditions, in three localities: Harrow Peaks (HP, Fig. 1.5a), Greene Point (GP, Fig. 1.5b) and from Handler Ridge (HR, Fig 1.5c). HP and HR have never been studied before.

This study allowed to extend the Antarctica SCLM petrological characterization under a wide area from Mt Melbourne (74 21′S, 164 42′E) to Handler Ridge (72°30′S, 167°0′E) for about 400 Km (Fig. 1.4, and Fig. 1.5c).

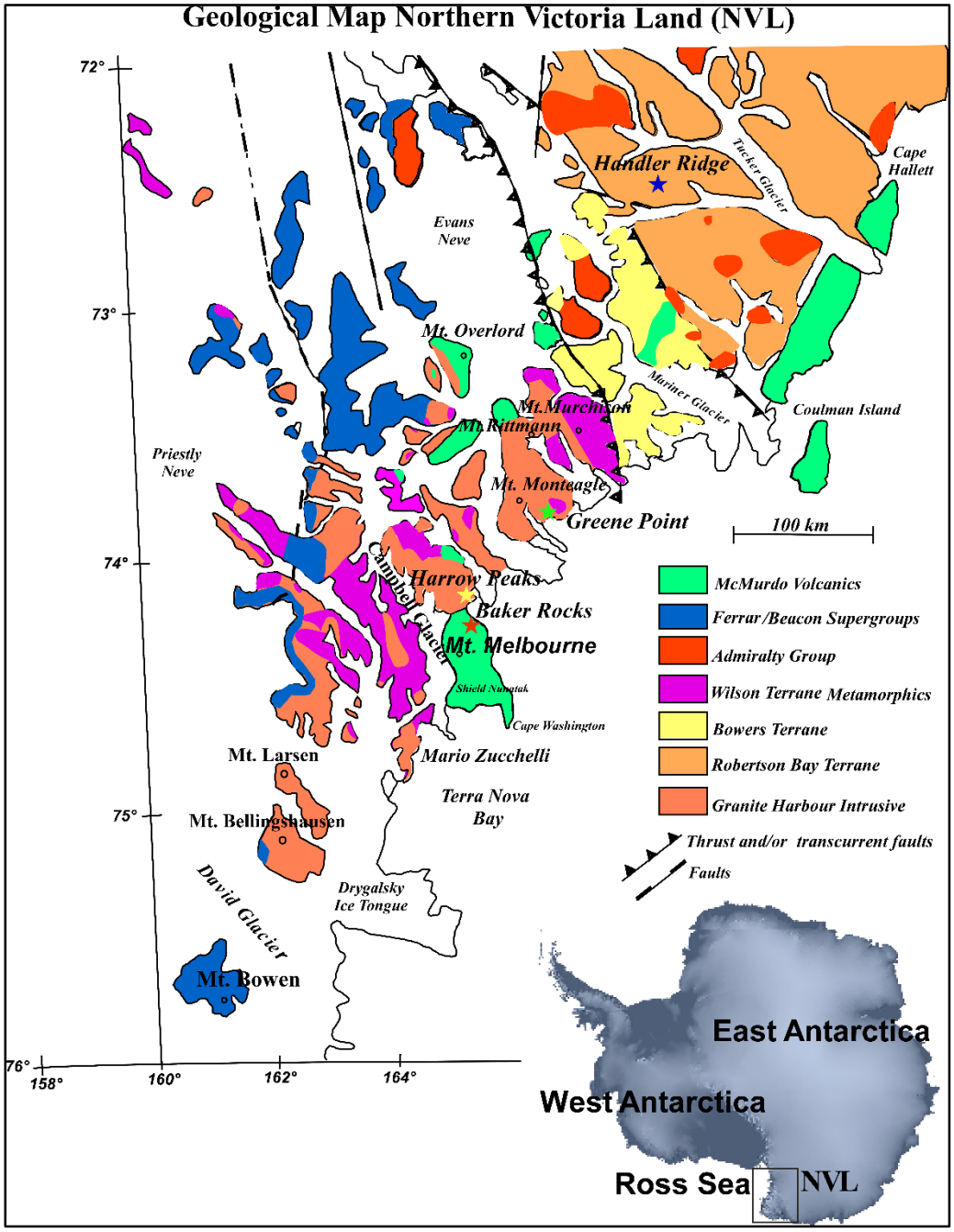

Fig. 1.4 Map of Northern Victoria Land modified from Carmagnani et al. (1989). In the map are reported the three studied localities of HP, GP, HR and the previously studied locality of BR (Coltorti et al., 2004; Perinelli et al. 2006, 2008, 2011; Melchiorre et al. 2011, Bonadiman et al., 2014).

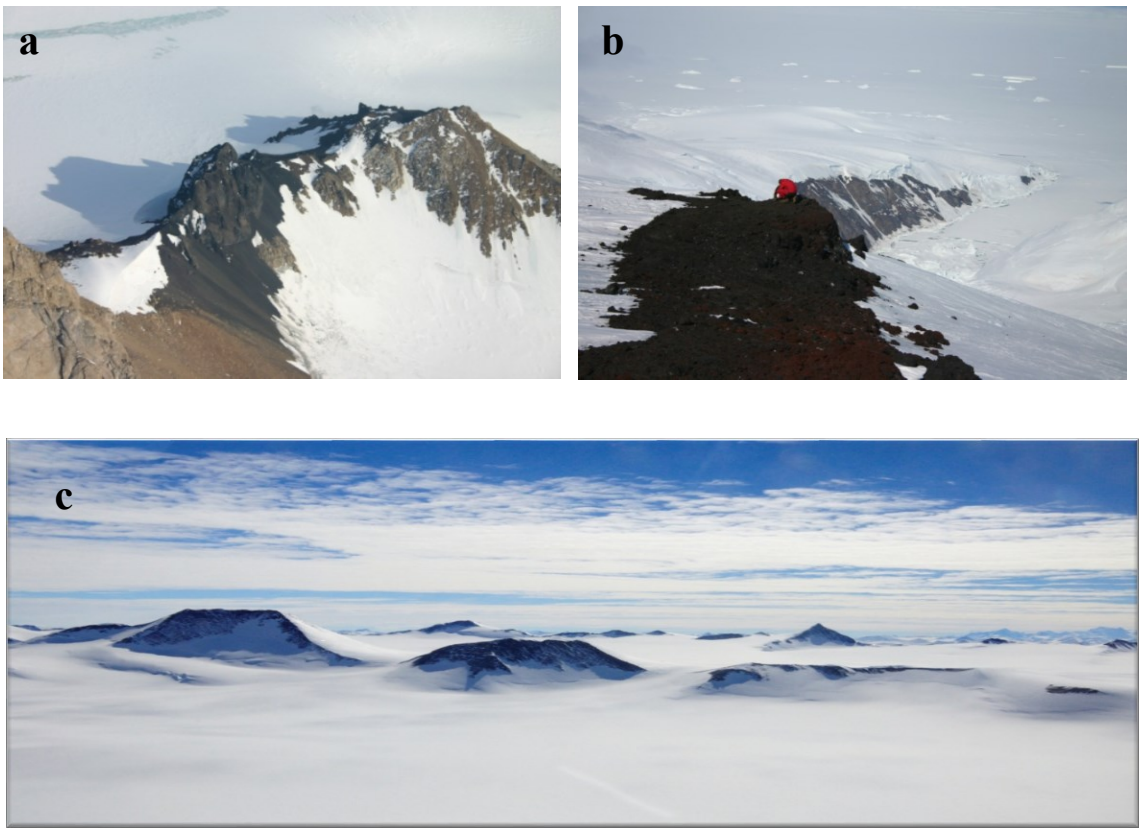

Fig. 1.5 a) Harrow Peaks, b) Greene Point, c) Handler Ridge outcrops.

Fig. 1.6 Antarctica mantle xenoliths from Greene Point

Chapter 2. Analytical Methods

2.1 Electron Microprobe (EMPA)

Major element compositions of minerals and glass were determined by combined microscopic and back-scattered electron (BSE) imagining, followed by analysis using a CAMECA SX100 electron microprobe equipped with four WD and one ED spectrometers at the Department of Lithospheric Research, University of Wien (Austria). The operating conditions were as follows: 15 kV accelerating voltage, 20 nA beam current, 20 s counting time on peak position. In order to minimise the loss of Na and K, a 5μm defocused beam and 10 s counting time on peak position were applied for glass analyses. Natural and synthetic standards were used for calibration and PAP corrections were applied to the intensity data (Pouchou and Pichoir, 1991).

2.2 Laser ablation microprobe-inductively coupled plasma mass spectrometry (LA-ICP-MS)

The concentration of trace elements in pyroxenes and glass was obtained by laser ablation microprobe-inductively coupled plasma mass spectrometry (LAM-ICP-MS) at Geosciences Montpellier Université de Montpellier and at the C.N.R. Istituto di Georisorse, Pavia (Italy).

Trace element analyses of minerals were performed in situ by laser ablation ICP-MS on an Element XR single collector ICP-MS coupled to a 193 nm Compex 102 Excimer laser.

Each analysis included a background acquisition of 120 s, followed by 60 s data acquisition of the sample. The analysis was corrected with internal standards using CaO for cpx and glass, and SiO_2 for opx. The detection limit is a function of the ablation volume and counting time, and is therefore calculated for each analysis; the ablation volume, in fact, greatly depends on the instrument configuration. As a consequence, the detection limit reduces if spot size, beam power and cell gas flow are decreased. Since analyses for clinopyroxene were performed using a smaller spot size and lower beam power, the detection limit for some elements was up to two times less than that of standard analyses. A beam diameter of 40-100 μm and a scanning rate of 20 μm s^1 were used. The theoretical limit of detection ranges between 10 and 20 ppb for REE, Ba, Th, U, and Zr and 2 ppm for Ti.

Data were processed using the Glitter software (Gemoc). Element concentrations were calibrated against the NIST612 certified reference material, using the values of Pearce et al. (1997)

2.3 Isotopic Analysis

Isotopic analyses for Sr and Nd were performed at Geosciences Environment Toulouse (GET), Observatoire Midi-Pyrenèes, University Toulouse III. Clinopyroxene separates were first cleaned with ethanol, then dried and crushed using an agate mortar in a dust-free room. Following this, 100mg of clinopyroxene powder was weighed and leached in a Teflon_ beaker using 1N HCl for 10min. After centrifugation, the leaching solution was discarded and the samples were dissolved in a 2:1 mixture of HF^HNO_3. Nd and Sr were extracted from the matrix using a combination of Sr-spec, Thru-spec and Ln-spec resins. An equivalent of 500 ng Sr and 150 ng Nd was run on a MAT261 Finnigan mass spectrometer (GET, University Toulouse III). NBS987 and La Jolla isotopic standards were regularly run during the measurements. Typical blanks are 50 pg for Nd and 150 pg for Sr. Taking into account the low concentration of Rb and Sm in the cpx age corrections for Cenozoic age, are negligible, therefore the data reported are not age-corrected.

Chapter 3. Greene Point Mantle xenoliths

3.1 Introduction

Anhydrous mantle xenoliths from Greene Point (GP), were already investigated by Perinelli et al. (2006). On the basis of the clinopyroxene trace element contents the authors concluded that some portions of the lithospheric mantle were originated in the garnet stability field and later equilibrated in the spinel stability field, while partial melting event/s were followed by cryptic and modal metasomatism characterised by Fe-Ti addition and variable LREE-enrichments in the clinopyroxene.

Isotopic studies on GP and amphibole-bearing xenolith from Baker Rocks (BR) also highlighted an eclogitic component in the mantle source of the magmatism, possibly related to the Ross subduction event (Melchiorre et al., 2011).

In this study a petrological characterisation of GP (NVL, 73°46,186'S, 165°57,003E') mantle xenolith is presented, based on new geochemical, isotopic and geothermobarometer dataset. This allows to shed light on the mantle processes occurring below NVL, and provide an additional explanation for the garnet signature evidenced in some GP clinopyroxene.

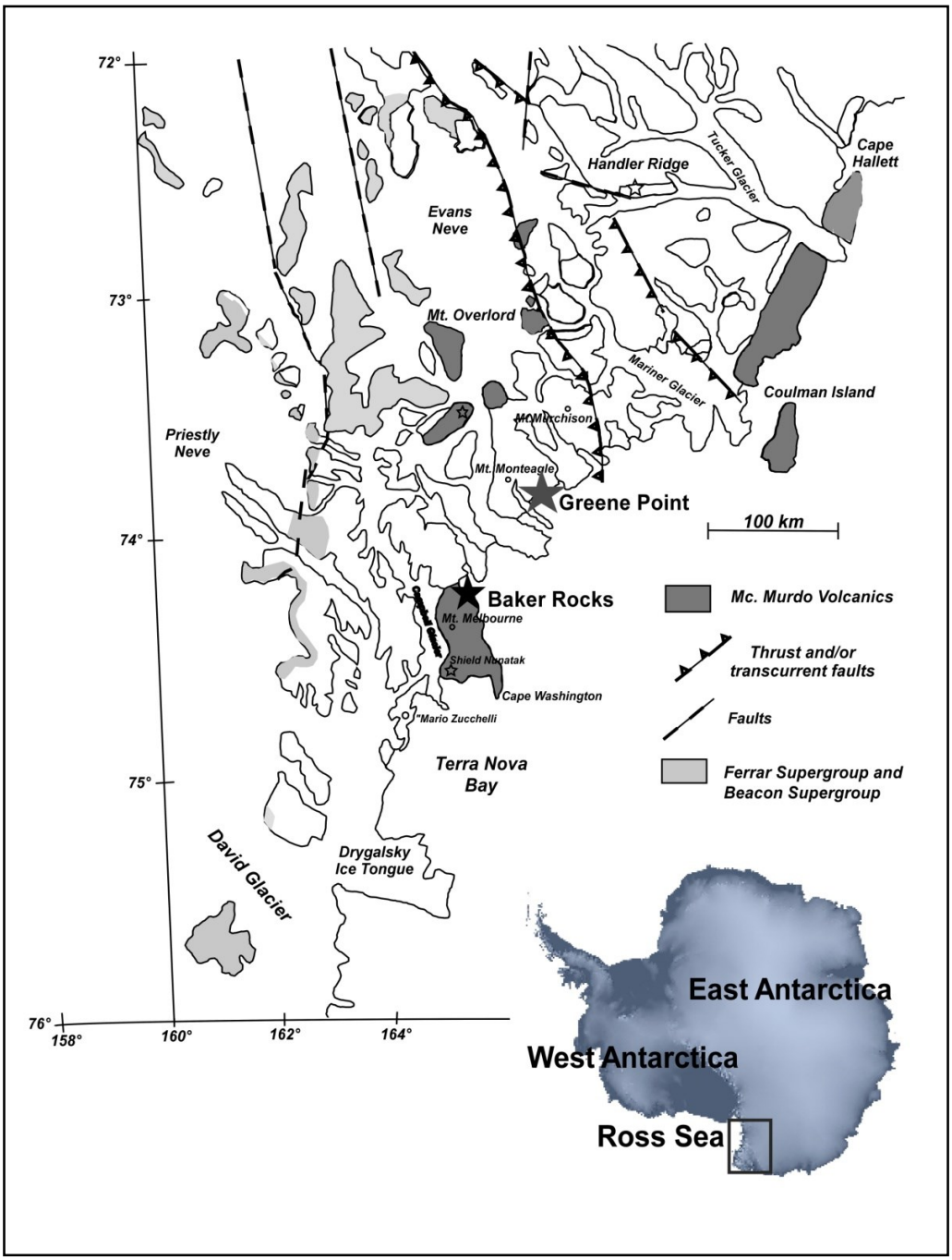

Fig.3.1 Map of Northern Victoria Land showing the location of Greene Point and Baker Rocks. Ferrar and McMurdo Volcanic products are also shown. Inset shows the location of Northern Victoria Land**.**

3.2 Petrography

Greene Point mantle xenoliths are anhydrous lherzolites and harzburgites and are almost equally represented. Whole-rock analysis was not performed due to the relatively small sizes; the modal proportion was estimated by point counting and averaging two runs with more than 2,000 points for each thin section (Table 3.1). Lherzolites contain olivine (60-76 vol.%), orthopyroxene (15-27 vol.%), clinopyroxene (7-13 vol.%) and spinel (1-3 vol.%), while harzburgites contain olivine (62-84 vol.%), orthopyroxene (15-35 vol.%), clinopyroxene (2-5 vol.%), and spinel (<1 vol.%). Even considering the modal estimating error, as well as limited lithotypes representativeness, two out of three samples (GP78, GP23) were classified as harzburgites as a result of containing less than 5% clinopyroxene; GP78, GP23 also had a high orthopyroxene content (Table 3.1) compared to the common residual peridotite modal proportion (Niu, 2004).

The dominant textural type in the Greene Point xenoliths is protogranular (Fig. 3.2) according to terminology by Mercier and Nicolas (1975), with large (up to 3 mm in size) orthopyroxene and olivine grains. Orthopyroxene can occasionally reach 5 mm in size and is accompanied by strong kink-banded olivine (GP23 and CD305; Fig. 3.2A). Olivine is present as large crystals (up to 5 mm in GP23 and CD305). Clinopyroxene is smaller (~ 0.5 mm) than olivine and orthopyroxene and is often associated with spinel, this latter vermicular and lobate shapes (Fig. 3.2 F and G).

The primary paragenesis shows no evidence of phase destabilisation in most of the samples, although some xenoliths preserve a sort of “pyrometamorphic” texture (Coltorti et al., 1999; Beccaluva et al., 2001). This includes orthopyroxene and clinopyroxene grains exhibiting partial (spongy rim) or complete destabilisation (Figs. 3.2E and F) with progressive replacement by secondary clinopyroxene and rare glassy patches and veinlets. The latter do not propagate from the host basalt and do not present textural signs of being linked to basaltic infiltration. The largest clinopyroxene grains sometimes show orthopyroxene exsolution lamellae (i.e. GP 9, Fig. 3.2H).

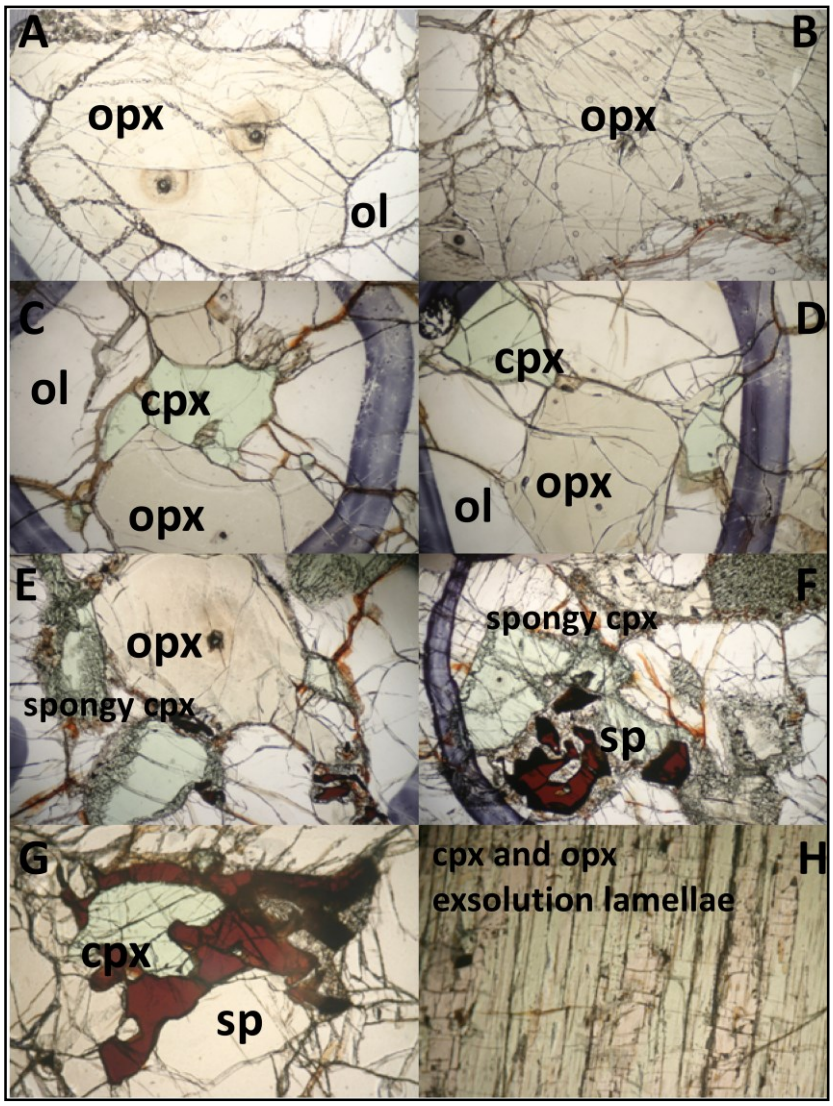

Fig. 3.2 Photomicrograph of representative microstructures in the Greene Point xenoliths. A) Protogranular lherzolites (CD305) comprising large orthopyroxene olivine; B) Harzburgites (GP81) with pervasive presence of orthopyroxene surrounded by olivine grains and small grains of clinopyroxene, (C) and (D) lherzolite GP30 characterised by large orthopyroxene and olivine grains, and smaller equilibrated clinopyroxene grains; (E) and F) Lherzolite GP25 with large orthopyroxene surrounded by spongy clinopyroxene and lobated spinel; (G) lherzolite GP13, characterised by the presence of large spinel grains surrounding clinopyroxene and larger orthopyroxene and olivine grains; (H) lherzolite GP9 with a detail of the large clinopyroxene grain characterised by orthopyroxene exsolution lamellae

Table 3.1 : Texturale features, modes, T, fO_2 estimates of GP mantle xenoliths

			OL	OPX	CPX	SP	Glas/react	opc/cpx	ol/opx	T (°C) *	σ	T (°C)~	σ	Δ log *f* O2
CD305	Lh	protogranular	76	15	7	trace	1	2	5	962	8			-1.00
GP23	Hz	protogranular	66	25	5	1	trace	5	3	963	51			-1.41
GP25	Lh	protogranular	62	26	11	1	trace	2	2	937	20			-1.11
GP28	Lh	protogranular	74	15	9	1	1	2	5	963	20			-1.70
GP30	Lh	protogranular	62	27	9	1	trace	3	2	981	0			-1.57
GP78	Hz	protogranular	62	35	2	trace	1	18	2					
GP81	Hz	protogranular	84	15	2	trace	trace	8	6	952	11			-0.39
GP84	Lh	protogranular	70	19	8	1	2	2	4	972	0			-1.22
GP9	Lh	protogranular	72	15	10	3	trace	2	5	888	43	905	54	-1.29
GP13	Lh	protogranular	60	24	13	3		2	3	1073	40			-0.60

T (°C) * = T from O'Neil &Wall (1987), modified by Ballhaus et al., 1991
T (°C T&K of Brey & Kohler (1990)
Δ log *f* is calculated using T from O'Neill & Wall (1987), modified by Ballhaus et al., 1991

3.3 Mineral chemistry

Three main groups can be identified in Greene Point mantle xenoliths based on both major and trace orthopyroxene and clinopyroxene element contents.

3.3.1 Lherzolite Group 1

This group is represented by samples GP 9 and GP 13. Within each sample, orthopyroxene is homogenous in composition, with mg# [=Mg/(Mg+Fe_{tot}) atomic %] varying from 91.0 and to 91.6 and Al_2O_3 contents from 2.6 to 4.3 wt.%; (Fig. 3.3A; Table A3.1). Chondrite-normalised trace element patterns of orthopyroxene are characterised by a systematic depletion of Light Rare Earth Elements (LREE) compared to Heavy REE (HREE) (Fig. 3.4A; Table A3.2).

Large unreacted clinopyroxenes and the core of spongy grains are Cr-rich augites (Morimoto et al., 1988). These have mg# values in the range of 91.6-93.2 and Al_2O_3 contents from 3.6 to 6.0 wt.% (Fig. 3.3B; Table A3.3); TiO_2 never exceeds 0.4 wt.% and Cr_2O_3 is relatively constant. These clinopyroxenes are depleted in Th, U, Nb, and Ta compared to LREE (Fig. 3.5A; Table A3.4) in the chondrite-normalised diagrams and show slight Ti, Zr and Hf negative anomalies with a relative depletion in LREE (Fig. 3.5D).

3.3.2 Lherzolite Group 2

Samples CD305, GP28, GP30, GP25 and GP84 belong to this group in terms of major element contents. However, GP84 has clinopyroxene trace element contents comparable to those of harzburgites (Fig. 3.5C and 3.5F). It was therefore removed from the *Lherzolite*

Group 2 and described in the harzburgites group (*see Harzburgite Group 3*). Three clinopyroxene separates (GP73, GP66, GP98) were also analysed, which can be attributed to this group in terms of major and trace elements, although GP73 shows a slight enrichment in LREE compared to the others.

Overall, this group shows orthopyroxene characterised by mg# values ranging from 91.4 to 92.6 and Al_2O_3 contents ranging from 4.0 to 4.9 wt.% (Fig. 3.3A). Orthopyroxenes are enriched in Al_2O_3 at comparable or higher MgO contents (Table A3.1). Similar to *Lherzolite Group 1*, chondrite-normalised trace element patterns are characterised by a systematic depletion of LREE compared to HREE (Fig. 3.4 B; Table A3.2).

Like orthopyroxene, clinopyroxene major element compositions show Al_2O_3 contents which are higher than *Lherzolite Group 1* (Table A3.3). In chondrite-normalised diagrams, clinopyroxenes are depleted in Th, U, Nb, and Ta compared to LREE and show slight to marked Zr, Hf and Ti negative anomalies (Fig. 3.5B). Distinct REE profiles are characterised by slightly convex patterns (Fig. 3.5E; Table A 3.4). GP30 clinopyroxene unusually shows a slightly positive Eu anomaly (Eu/Eu*=1.25) for Sub Continental Lithospheric Mantle (SCLM) peridotites. *Lherzolites Group 2* clinopyroxene HREE profiles suggest a relationship with a co-existing garnet.

3.3.3 Harzburgite Group 3

Harzburgites GP23 and GP78 belong to this group and, overall, follow the same major element residuum trend for *Lherzolite Group 1* (Fig. 3.3). Harzburgite GP81 can be included in *Harzburgite Group 3,* on the basis of its orthopyroxene composition.

Orthopyroxenes have mg# values of 92.0 to 92.6 and Al_2O_3 contents ranging from 2.3 to 3.4 wt.%, (Table A3.1). The chondrite-normalised trace elements are characterised by fractioned REE patterns which are systematically depleted in LREE. As expected, orthopyroxenes in this group show the most residual character (i.e., $Yb_N = 0.44$ in GP81; Fig. 4C).

Harzburgite Group 3 tends to have clinopyroxene with lower Al_2O_3 contents and higher mg# than both *Lherzolite Groups 1* and *2* (Fig. 3.3B; Table A3.3) except for GP81 which shows clinopyroxene with Al_2O_3 contents which are comparable to *Lherzolite Group 1*. Clinopyroxene have the lowest HREE contents (Table A3.4), with a strong positive fractionated L-MREE and flat HREE trace element patterns (Fig. 3.5F).

Harzburgite GP81 has clinopyroxene trace element profiles corresponding to clinopyroxene *Lherzolite group 1*; this sample also has small re-crystallized clinopyroxenes which can be

texturally ascribed to the secondary clinopyroxenes type (Fig. 3.2); of all the groups, they record the highest LREE values (Fig. 3.5D).

3.3.4Olivine, Spinel and Secondary phases (and glasses)

Although the above described groups can also be distinguished on the basis of olivine mg# values (Fig. 3.3C), three distinct trends are not clearly identifiable. NiO content is ~0.40 wt.%, on average, similar to typical values for mantle olivine and CaO is always close to the detection limit (Table A3.5).

In the entire xenolith suite, spinel follows the expected negative correlation between Cr# [=Cr/(Cr+Al) at. %] and mg#, with Cr# ranging from 17.5 to 50.5 and mg# from 67.3 to 82.7, with the harzburgites showing the most restitic composition (Table A3.6). Overall, these are similar to the composition of abyssal peridotites as defined by Dick and Bullen (1984) (Fig. 3.3D). Both olivine and spinel record an abrupt decrease in mg# in all lithotypes accompanied by an increase in TiO_2 contents approaching the host basalt, as indicated by displacement towards iron-rich compositions (not included in Fig. 3.3D) (Bonadiman et al., 2011).

Clinopyroxene spongy rims tend to have higher Cr_2O_3 and lower Al_2O_3 contents compared to the clean portion of the same crystal. Rare glass veins and patches are recognised in all lithotypes. These are silica-rich, rather homogeneous in composition and characterised by high SiO_2 and alkali contents (Table A3.7). In the silica *vs.* total alkali diagram (TAS), these glasses plot in the phonolite and trachyte fields (Fig. 3.7). It was possible to carry out trace element glass analyses for only two samples from *Lherzolite Group 2*. Glasses record high Large Ion Lithophile Element (LILE) abundance and are characterised by flat to positive fractioned-REE patterns (Table A3.8), with marked Rb and K positive anomalies (Fig. 3.7).

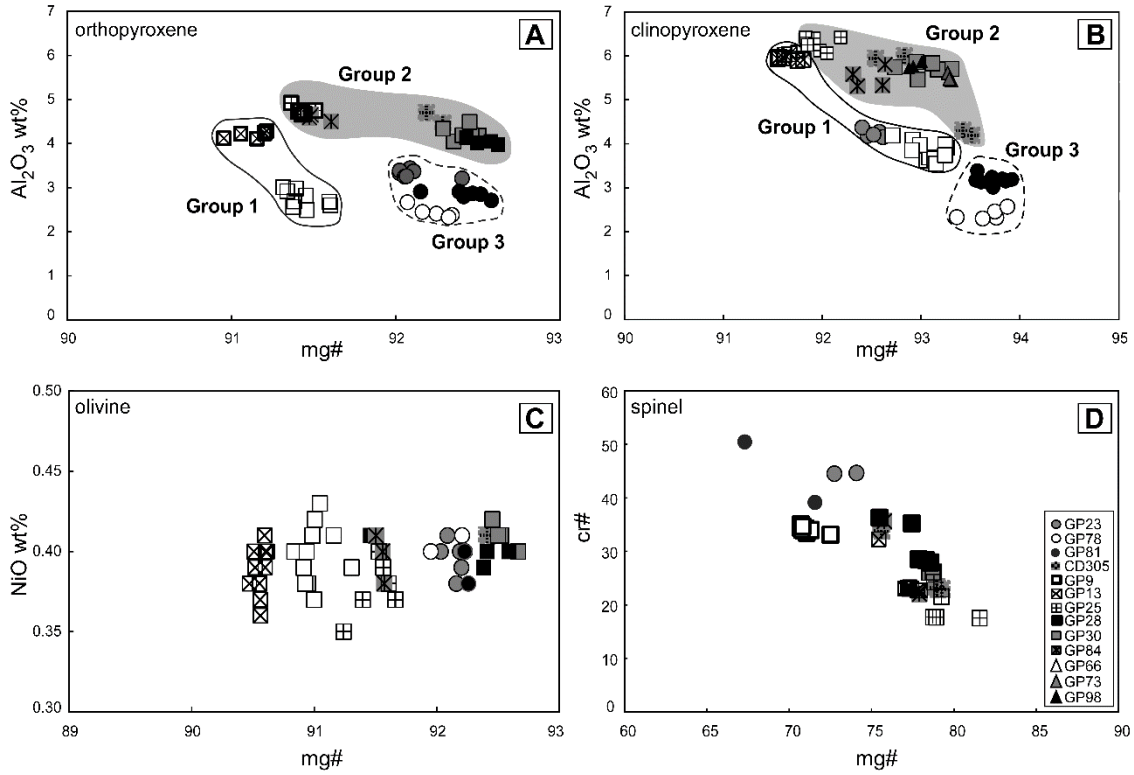

Fig. 3.3 (A) orthopyroxene compositional variation in terms of Al_2O_3 vs. mg# [(MgO/MgO+FeOtot) *100 mol]; (B) clinopyroxene compositional variation in terms of Al_2O_3 *vs* mg#. The three different groups (*Lherzolites Group 1*, *Lherzolites Group 2*, *Lherzolites Group 3*) are also reported. (C) olivine compositional variation in terms of NiO *vs* mg#, (D) spinel compositional variation in terms of cr# = [Cr_2O_3/(Cr_2O_3+Al_2O_3)*100 mol] vs. mg#. Squares are for lherzolites, circle for harzburgites and triangles for clinopyroxene separates.

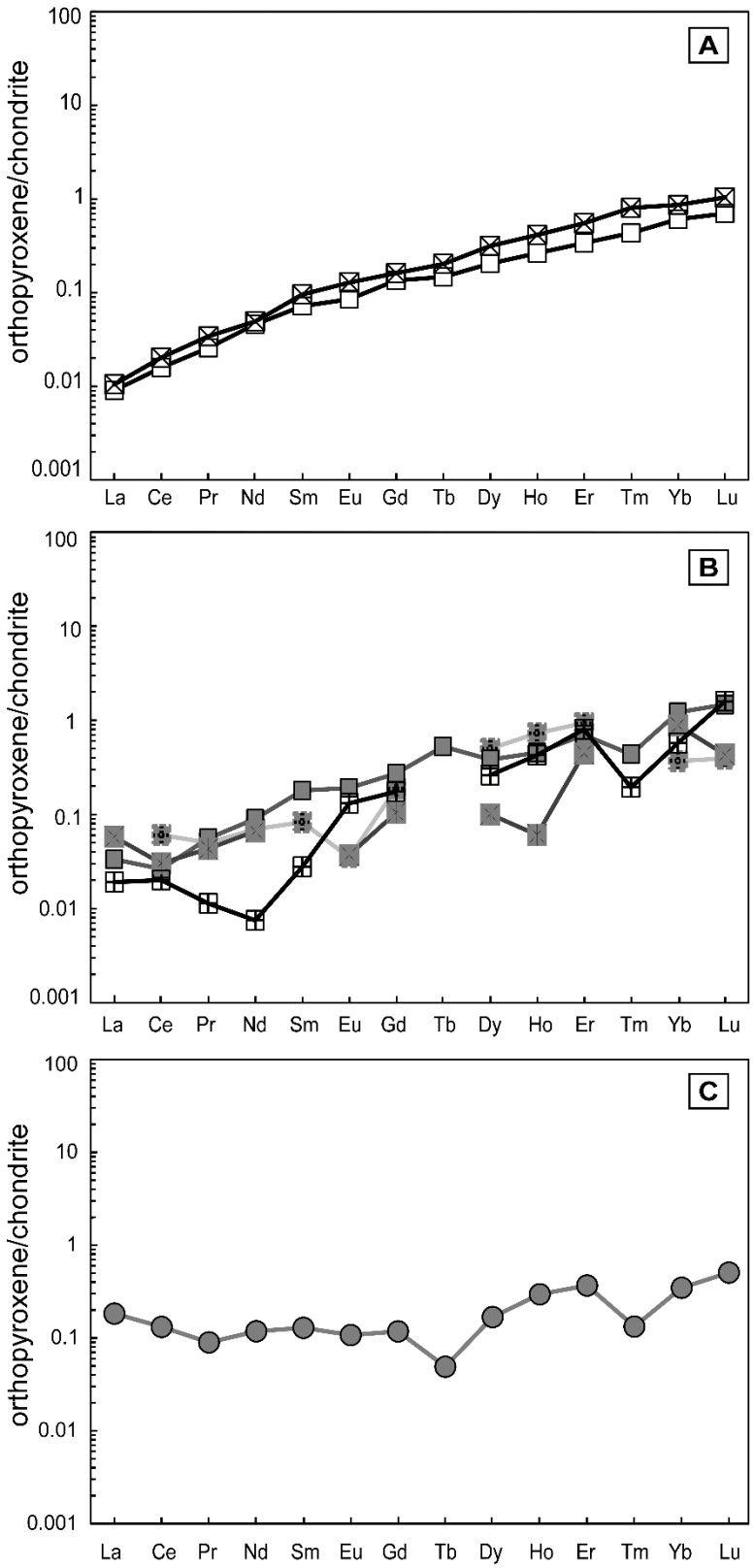

Fig. 3.4 Chondrite-normalised Rare Earth Element (REE) patterns of orthopyroxenes from Greene Point xenoliths. (A) *Lherzolite Group 1*, (B) *Lherzolite Group 2*, (3) *Harzburgite Group 3*. Symbols as in Fig. 3.

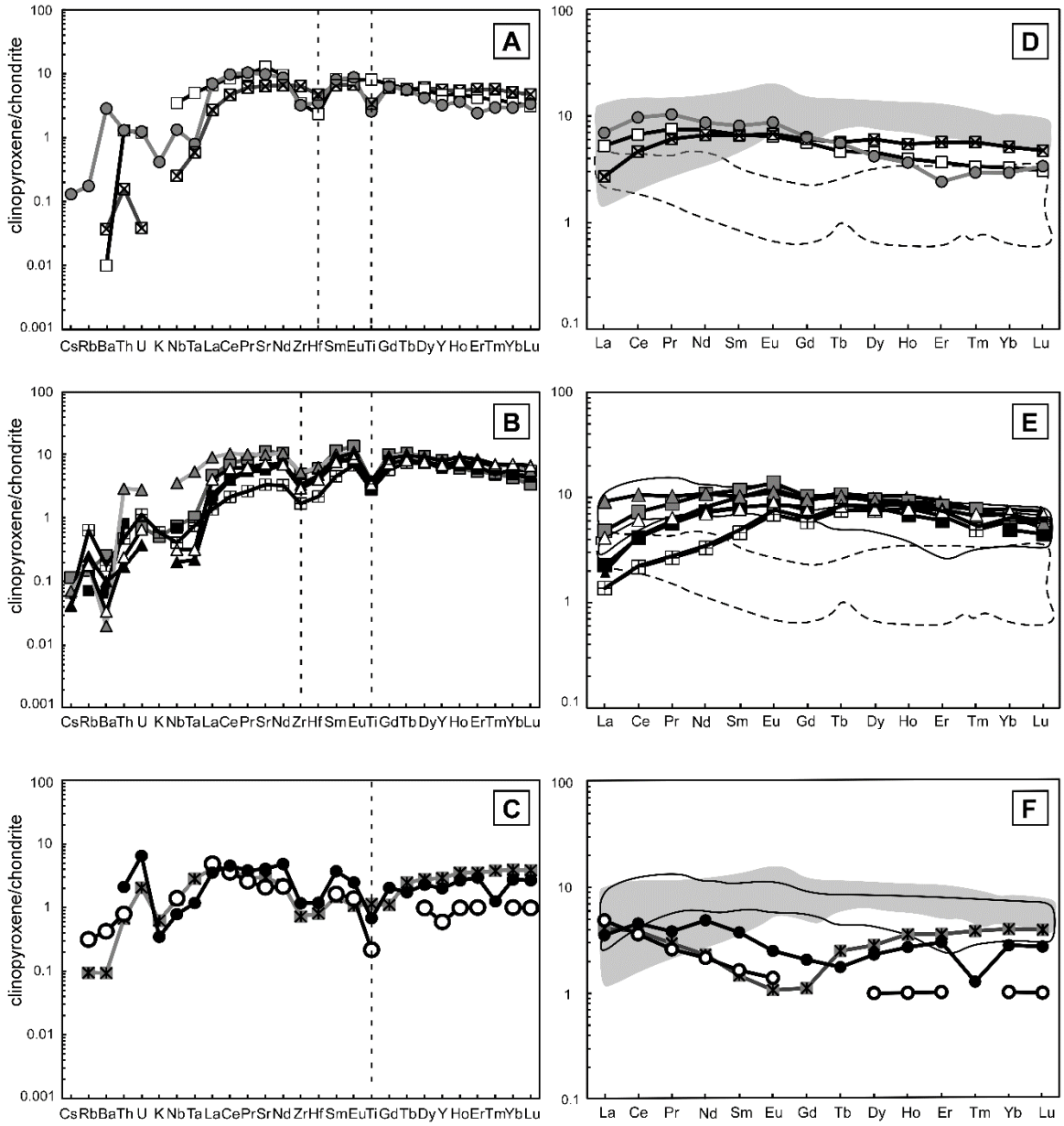

Fig. 3.5 Chondrite-normalised multi-element diagrams of clinopyroxenes from Greene Point xenoliths. (A) *Lherolites Group 1*, (B) *Lherzolites Group 2*, (3) *Harzburgites Group 3*. Chondrite-normalised REEpatterns of clinopyroxenes from Greene Point xenoliths. (D) *Lherzolites Group 1*, (E) *Lherzolites Group 2*, (F) *Harzburgites Group 3*.

The shadow areas represent: *Lherzolites Group 1* dark grey*, Lherzolites Group 2* in light grey, and *Harzburgites Group 3* in grey. Symbols as in Fig. 3.3.

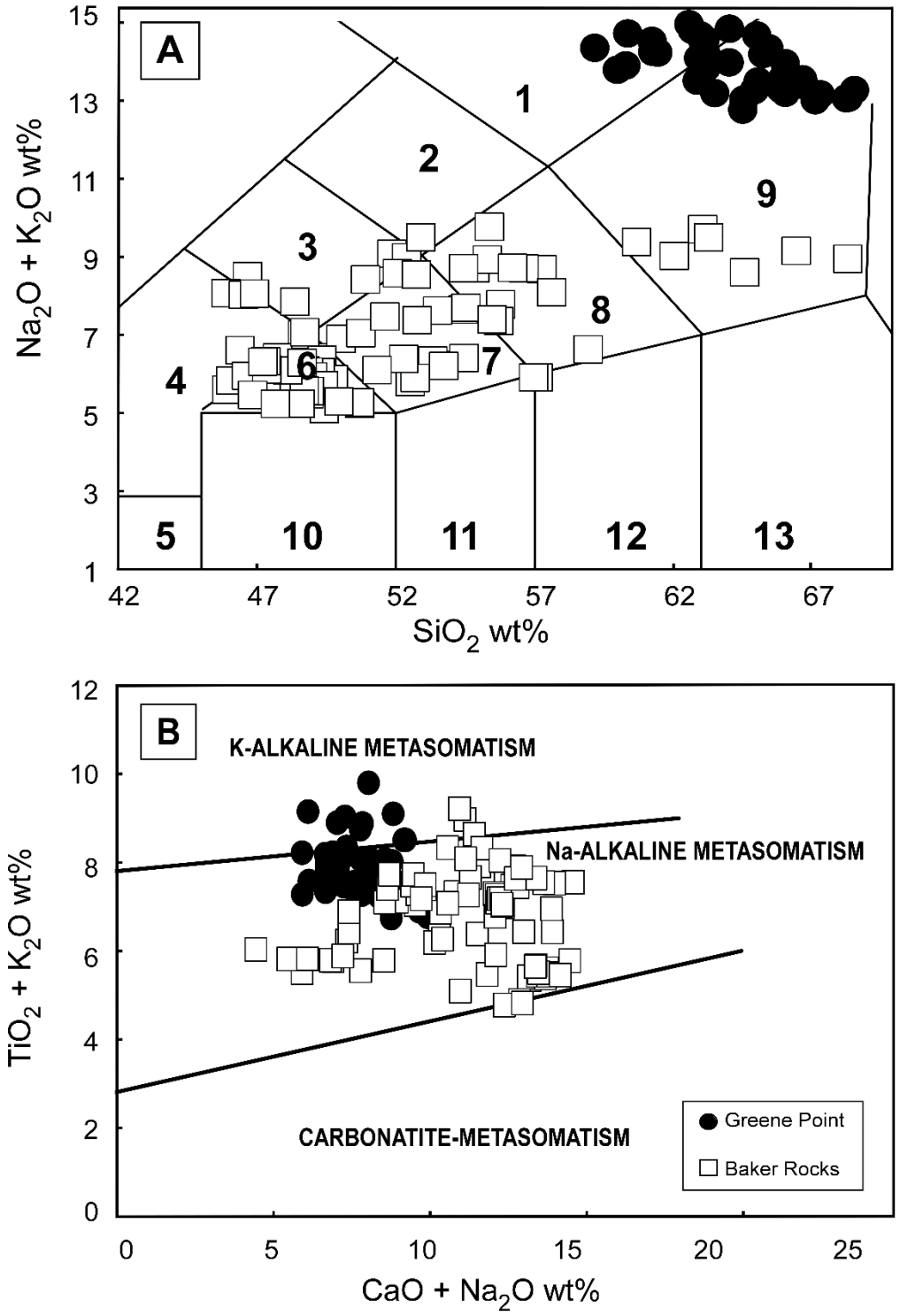

Fig. 3.6 A) Total alkali silica (TAS) (after Le Bas, et al., 1992) of Greene Point and Baker Rocks glasses. Samples from Greene Point fall on the Phonolite and Trachyte fields, while Baker Rocks, presenting a higher variability, span from the trachy-basalt to trachy-dacite compositions. B) Greene Point and Baker Rocks glasses plotted on major element discrimination diagrams (after Coltorti et al., 2000).

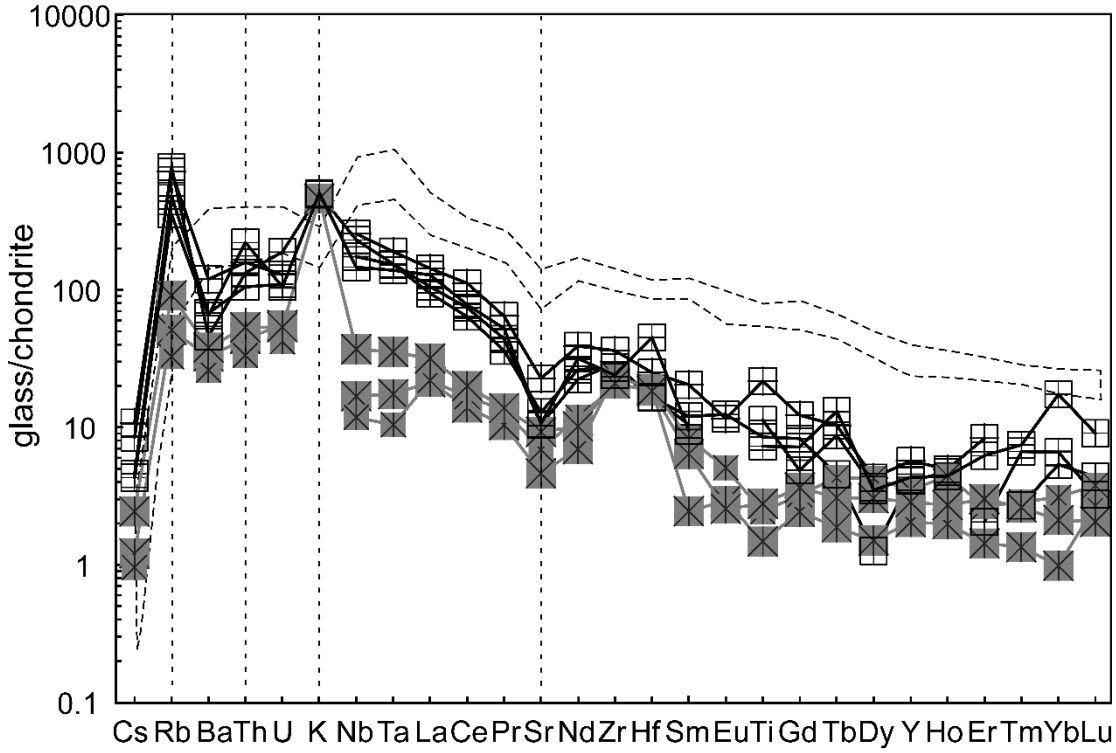

Fig. 3.7 Chondrite-normalised multi-element diagrams of glasses from Greene Point xenoliths. Baker Rocks glass are also reported for comparison (dotted line). Symbols as in Fig. 3.

3.4. Discussion

3.4.1. Geothermobarometric constrains and redox conditions

The inter-mineral chemical equilibrium between silicate phases and spinel was evaluated in order to assess the thermobarometric conditions for this mantle segment. Fe/Mg equilibrium (K_d) between olivine, orthopyroxene and clinopyroxene core pairs was calculated using the equations experimentally obtained by Brey and Kôhler (1990) applied at various temperatures. The Fe/Mg distribution between orthopyroxene and spinel (core pairs) was estimated following Liermann and Ganguly (2003). In the entire xenolith suite, orthopyroxene-olivine are equilibrated along two theoretical curves at 900 and 1100 °C (Fig. 3.8A). K_d $Fe/Mg^{sp/ol}$ *vs* cr# in spinel (Liermann and Ganguly, 2003) reveals that spinel is also in equilibrium with olivine (Fig. 3.8B).

Orthopyroxene and clinopyroxene Fe/Mg pairs (not shown) are randomly distributed; this implies that the temperatures estimated using the orthopyroxene-clinopyroxene equilibrium are unreliable. The olivine-spinel thermometer of O'Neill and Wall (1987) modified by Ballhaus et al. (1991), has therefore been selected as the most reliable geothermometer for evaluating Greene Point thermal conditions. As no reliable geobarometer exists for spinel-bearing peridotites (Green and Hibberson, 1970; O'Neill, 1981), pressure can only be constrained by spinel and for calculations it is assumed to be 15 kbar, as for previously studied xenolith suites in the nearby area (Coltorti et al., 2004; Perinelli et al., 2006; Bonadiman et al., 2014).

Irrespective of lithology, temperature varies from 888°C to 1073°C, although for the vast majority of samples it is close to 950°C (Table 3.1). The intrinsic error of the method is ~30°C (1σ). The highest temperature was observed on the texturally most-highly equilibrated GP13 lherzolite. By contrast, the lowest temperature was recorded on GP9 lherzolite. This sample was the only one to show clinopyroxene with evident exsolution lamellae (Fig. 2H), therefore the orthopyroxene-clinopyroxene geothermometer was only applied in these circumstances. The estimated temperature of the exsolved crystal was 905°C (σ~ 50 °C), in agreement with temperatures for co-existing olivine and spinel. On the whole, these data confirm the tendency of the anhydrous Greene Point xenolith population to have higher equilibration temperatures compared to nearby amphibole-bearing Baker Rocks peridotites (800-940 °C), (Coltorti et al., 2004; Perinelli et al., 2012; Bonadiman et al., 2014). These are comparable with data recently published on Southern Victoria Land (Martin et al., 2015, Fig. 3.9).

Redox conditions were estimated using the Ballhaus et al. (1991) oxygeobarometer equation on the basis of olivine-spinel temperatures. Greene Point samples yield fO_2 ranging from Δlog (QFM) -1.70 to -0.39, reflecting redox conditions comparable to amphibole-bearing Baker Rocks xenoliths (Fig. 3.9). These results, compared with those from Mt. Morning (Martin et al., 2015), suggest that most of the samples from Victoria Land fall into the range of abyssal peridotites (Δlog fO_2 (QFM) from -2.0 to +1.0), which is close to the mean value of the continental (non cratonic) lithosphere dataset (Δlog fO_2 =-0.68 Foley, 2010).

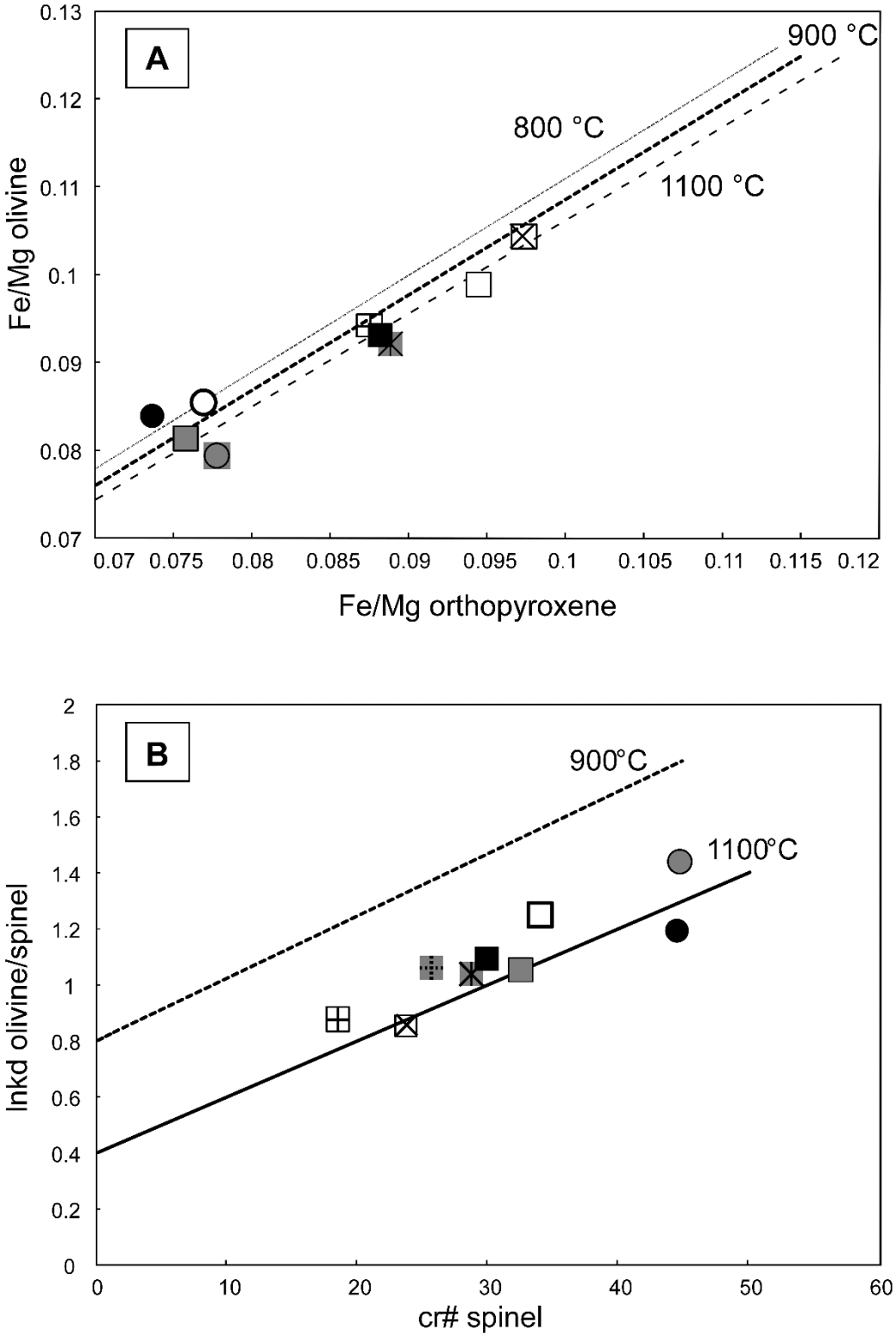

Fig. 3.8 Fe/Mg equilibrium diagrams for olivine *vs* orthopyroxene (A), olivine *vs* spinel (B). In (A) the equilibrium lines are from Brey & Köhler (1990) at 800, 900 and 1100 °C. In (B) Kd Spinel-Olivine is Fe-Mg partitioning between olivine and spinel determined on the basis

of the Liermann & Ganguly (2003) model. (Fe/Mg) indicates Fe^{2+}/Mg, as calculated by stoichiometry for each mineral. Symbols as in Fig. 3.3

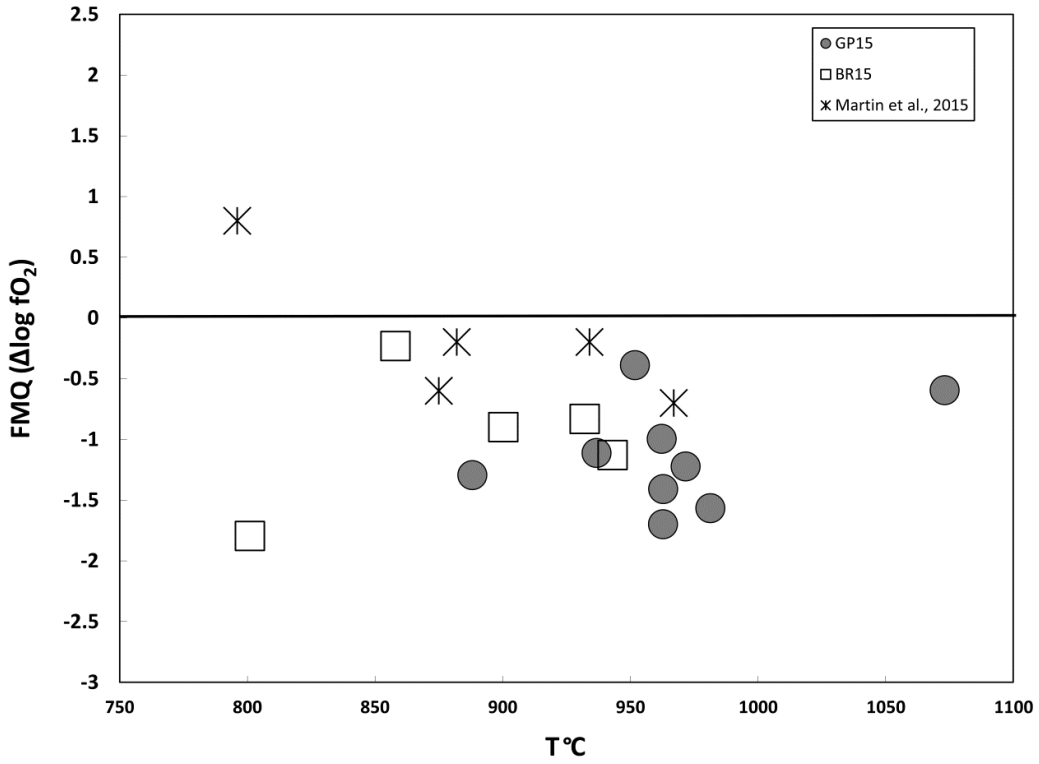

Fig. 3.9 Temperature and ($\Delta \log fO_2$) FQM = fO_2 relative to the buffer reaction FMQ calculated with the formula of Ballhaus et al. (1991). P is fixed at 15 Kbar. Grey circles Greene Point, white squares Baker Rocks, stars are data from Martin et al., 2015.

3.4.2 Melting modelling

In the framework of a hypothetical progressive residual trend, the abundance of the most fusible elements (i.e., Al, Ti) systematically decreases with increasing mg#. Melting degrees (F) are provided using major element mineral compositions according to the method of Upton et al. (2011); Primitive Mantle (PM) modal composition was obtained from the McDonough & Sun (1995) bulk geochemical model, using a mass-balance calculation between the four peridotite phases and progressive melting residua derived from the experimental results by Herzberg (2004) (see also Bonadiman and Coltorti 2011; Faccini et al., 2013).

Aluminium is a good parameter, as it is extremely fusible in a basaltic system and rapidly decreases in orthopyroxene, clinopyroxene and spinel with an increase in the degree of partial melting (Ionov and Hofmann, 2007; Faccini et al., 2013). The hypothetical melting curve shows Al_2O_3 distribution between the two phases (Fig. 3.10A) and provides reliable results

for estimating the degree of melting by taking into account potential Mg/Fe and Al equilibria between orthopyroxene and spinel (Fig. 3.8 A and B). Accordingly, Greene Point orthopyroxene-spinel pairs plot on the theoretical curve and indicate that the Greene Point suite have undergone 10-17 % melting (the absence of a primary spinel analysis in GP78 prevented this sample from being modelled). It is difficult to cluster melting degree values in GP9, due to the wide variation in Al_2O_3 contents, which most likely relate to significant amounts of exolved clinopyroxene (Fig. 3.2H) influencing the Al diffusion path.

If Al_2O_3 *vs* MgO intra-mineral distribution in orthopyroxene (Fig. .3.10B) is taken into account, it reflects not only a residual character but also the more complex process, including an enrichment effect (i.e., refertilisation). Indeed, with the exception of orthopyroxene in GP13 lherzolite (which coherently reflects the same partial melting degree value as was deduced by the orthopyroxene-spinel curve), the entire suite follows a melting trend which is shifted towards higher MgO contents compared to the theoretical curve (Fig. 3.10B). This effect was also observed in clinopyroxene, where the Al_2O_3 *vs* MgO theoretical melting curve (Fig. 3.10C) was not followed by any sample, with the exception of GP13. In this framework, it is difficult to assign a potential residual melting degree on the basis of only intra-mineral (pyroxene) major element compositions. GP13 lherzolite is only texturally well equilibrated (Fig. 3.2G) without any modal disproportion in the peridotitic phases (Table 3.1). All the coherently applied melting models indicate F at around ~10-12% (Table A3.9).

The Greene Point xenolith suite shows melting degree estimated by Al_2O_3 orthopyroxene-spinel distribution in agreement with what was calculated using HREE (Yb) and Y partitioning in clinopyroxene (F=8-23%; Fig. 3.10D; Johnson et al., 1990; Hellebrand et al., 2002; Bonadiman et al., 2005).

It is worth noting that, despite GP13 lherzolite representing the most equilibrated Greene Point peridotite and reflecting the same F values throughout the applied models, as harzburgites doing at coherent higher F values, a general discrepancy in F values was recorded (Table A3.9), between major and trace melting models.

Reliable F values can be calculated by considering the average between the values obtained from orthopyroxene-spinel and HREE methods (averaged F range: 11- 23 %; Table A3.9) by taking into account F results from the two methods and potential errors in these estimates.

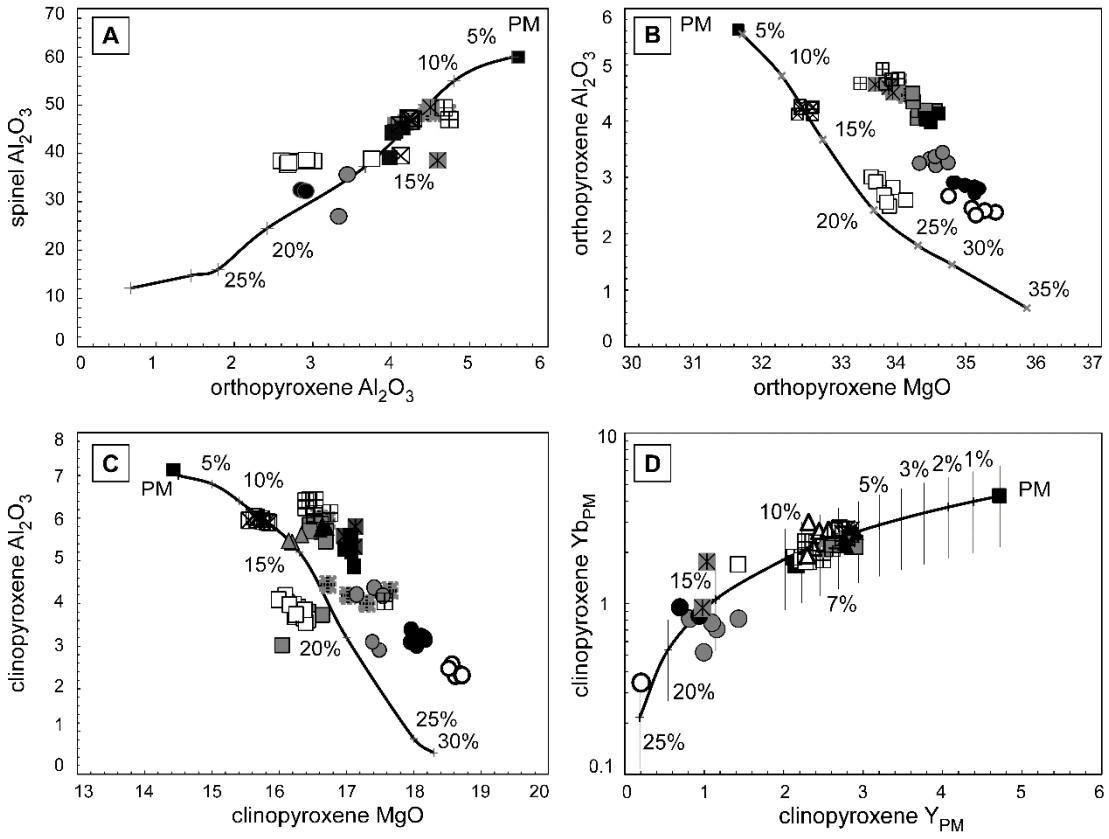

Fig. 3.10 Plot of Al_2O_3 in spinel vs Al_2O_3 in orthopyroxene (A), Al_2O_3 *vs* MgO melting trends as deducd from orthopyroxene (B) and clinopyroxene (C) compositions (Upton et al., 2011). In (D) melting degrees are estimated on the basis of HREE (Yb) and Y clinoproxene contents, following the fractional melting model within the spinel stability field of Zou (1998). In (A) (B) and (C) the Al_2O_3 and MgO contents of PM were calculated on the basis of the McDonough & Sun (1995) mantle model. Model parameters as in Bonadiman *et al*. (2005) and Faccini *et al*. (2013). Thick marks on curves indicate partial melting percentages (F), numbers in brackets are ideal clinopyroxene modal contents at F. Symbols as in Fig. 3.3.

3.4.3 Isotopic composition

Greene Point mantle xenolith Sr, Nd, Hf and Os isotope data has already been presented in a previous paper (Melchiorre et al., 2011), highlighting the complexity of mantle portion evolution beneath Greene Point. In this contribution, the Sr-Nd isotopic data (not fully discussed in the quoted paper) have been re-assessed, with the aim of better constraining the nature and role of percolating melts responsible for the refertilised character of Greene Point lithospheric mantle. In Fig. 11, Greene Point peridotites show a trend from DMM (Workman and Hart, 2005) towards EMI (Zindler and Hart, 1986). GP 25 is the least radiogenic sample, falling close to the DMM field, although it is characterised by a slightly higher $^{87}Sr/^{86}Sr$

isotopic ratio (0.70277) compared to the depleted reservoir. GP98 and GP73 plot near the HIMU field, while GP66 has an Sr-Nd isotopic composition similar to the typical sub continental lithospheric mantle (SCLM) from Victoria Land (Fig. 3.11) (Nardini et al., 2009; Melchiorre et al. 2011; Perinelli et al., 2011).

The progressive radiogenic enrichment trend of the Greene Point mantle xenoliths may be reproduced assuming that an old asthenospheric DMM-like component represented by GP 25, interacted with a radiogenic Sr reservoir (i.e., the EM-like component). This radiogenic end member is identified in the Ferrar dolerites, which represent the Gondwana low-Ti province (Cox et al., 1967; Cox 1988). These are generally characterised by higher $^{87}Sr/^{86}Sr$ (>0.707) and lower $^{143}Nd/^{144}Nd$ (<0.5124) compared to worldwide CFB provinces (Demarchi et al., 2001). According to several authors (Hergt et al., 1989b, 1991, 2000; Molzahn et al., 1996) it is difficult to reproduce the crustal signature of Ferrar dolerites using the radiogenic Sr AFC (fractionation crystallization) model (De Paolo, 1981), rather they it is derived from a depleted source variably enriched by $\leq$ 3 wt.% of subducted sediments. A simple Sr-Nd linear mixing (Faure, 1998) between the DMM component and Ferrar dolerites (Elliot et al., 1999) isotopic compositions can reproduce Greene Point isotopic variability, inferring a contribution of ~5% for the Ferrar component (model mixing 1, Fig. 3.11).

In a wider framework, isotopic data for the NVL Cenozoic lavas (Nardini et al., 2009) point towards the HIMU-like isotopic component, as do most of the Baker Rocks amphibole-bearing mantle xenoliths. This supports a hypothesis of intensive interaction for the Baker Rocks mantle fragment with the Cenozoic alkaline melt (Coltorti et al., 2004) leading to the hypothesis that the NVL mantle domain interacted with the Jurassic melt and was able to move the isotopic composition towards the EM end member. As evidenced by some Greene Point and the majority of the Baker Rocks samples, this interaction was subsequently obscured by the isotopic fingerprint of the younger metasomatism related to the Cenozoic magmatism (Fig. 3.11).

The model is based on a Ferrar isotopic composition by Elliot et al. (1999) (Table A3.10), which reflects the average values reported in literature (Elliot et al., 1999; Fleming et al, 1995; Kyle, 1980). For comparison, data from Fleming et al. (1995) are also used (model mixing 2; Fig. 3.11). It is worth noting that Greene Point samples are closely aligned to the Ferrar-DMM lines, although the best model appears to be model 1 (Fig. 3.11). We cannot exclude that the high radiogenic Sr signature transferred from Ferrar to NVL peridotite could have been inherited from an old subduction process (pre-Ross orogeny), as has already been

argued by several authors (Kyle 1980; Hergt et al. 1989a, b; 1991; Brewer et al. 1992; Molzahn et al. 1996).

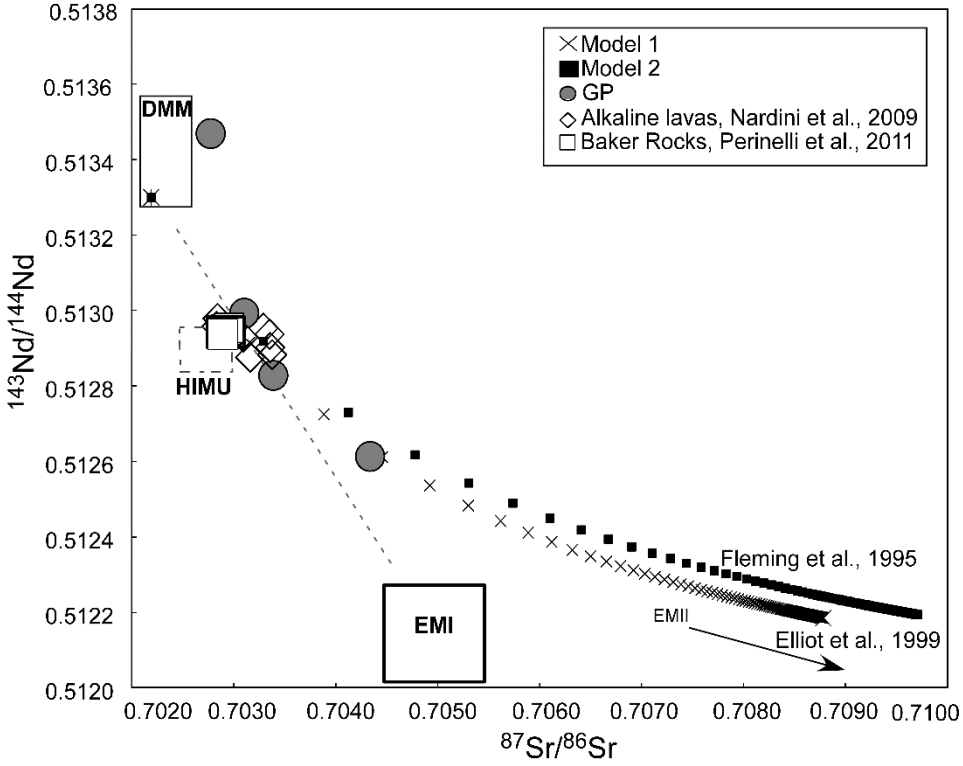

Fig. 3.11: $^{143}Nd/^{144}Nd$ *vs* $^{87}Sr/^{86}Sr$ plot of Greene Point clinopyroxene. Crossed line represents the mixing line (Model 1) between the DMM composition and the Ferrar Dolerites (Elliot et al., 1999); square line represents mixing line (Model 2) between DMM and Ferrar dolerites (Fleming et al, 1995). Amphibole-bearing Baker Rocks xenoliths and Cenozoic alkaline lavas also plot onto the mixing line.

3.4.4. The role of metasomatism

Evidence of modal and cryptic metasomatism has been widely reported in NVL (Coltorti et al., 2004; Perinelli et al., 2006; 2008; 2011). Greene Point peridotites present petrographic (sieved and spongy rim clinopyroxene, glassy patches and veinlets) and geochemical features (LREE-enriched clinopyroxene) which are clearly related to the interaction between the peridotite matrix and a Na-alkaline melt (Fig. 3.6B). Glass in pyrometamorphic textures implies the circulation of metasomatic melts that occurred at depth just before (or concomitant with) the rise of xenoliths to the surface.

Reconstructed geochemical features for the potential metasomatic agent in the amphibole-bearing mantle xenoliths in the nearby area are similar to the highly under saturated basic magma sampled in the area, thus linking the metasomatic process with the system which formed the Ross Sea Rift magmatism (Coltorti et al. 2004). Greene Point anhydrous xenoliths do not exhibit clinopyroxenes with typical TiO_2 enrichment and/or alkalis (i.e., Na_2O), which are commonly associated with NVL metasomatic melts which ultimately gave origin to the amphibole (i.e., Baker Rocks, Coltorti et al., 2004). Metasomatism in Greene Point mantle xenoliths is limited to the LREE-enriched clinopyroxene in a few lherzolites (i.e., GP9 and GP84) whereas it strongly modifies the geochemistry (and textures) of the great majority of harzburgites. Furthermore, the presence of glassy veinlets and patches formed mainly at the expense of orthopyroxene (and clinopyroxene) supports the hypothesis of interaction between the Greene Point peridotite matrix and an alkaline SiO_2-undersaturated melt.

These glasses are notably different from those found in the amphibole-bearing xenolith suite in the nearby Baker Rocks (Coltorti et al., 2004; Perinelli et al., 2006). Firstly, they are essentially "anhydrous", whereas the Baker Rocks glasses contain 3-4 wt.% volatiles. The latter also have lower TiO_2 and CaO contents and relatively higher alkali contents, (in particular K_2O; Fig. 3.6A) compared to Baker Rocks glasses. Greene Point glasses do not show negative correlation between SiO_2 and major oxides as CaO, FeO_{tot} and TiO_2 compared to Baker Rocks. Coltorti et al. (2004) proposed that amphibole was formed by a reaction between the metasomatic melt and anhydrous parageneses (mainly clinopyroxene and spinel). The absence of amphibole and the "volatile free" character of Greene Point glass suggest that the peridotite system and percolating melt were relatively poor in volatiles (OH, F, Cl). The comparison between anhydrous (Greene Point) and hydrous (Baker Rocks) mantle parageneses reveals that, the metasomatic melts which were responsible for the pyrometamorphic features have the same geochemical signature (lithophile elements); the effects, however, may be different as a function of the peridotite reactive matrix and, most importantly, volatile circulation (and thermal conditions) which may (or not) induce the amphibole formation.

3.4.5 The role of the Jurassic tholeiitic melt

Using the mineral percentages *vs.* the F model for abyssal peridotites (Niu, 2004), only GP13 records compositional (and textural) features representing a coherent melting residua (F ~10%; Fig.12A). In all the other samples, whether the clinopyroxene modal percentage of

lherzolites properly fits the theoretical trend (Fig. 12A) or not, orthopyroxene contents tend to be anomalously high. This disproportion, compared to the expected modal composition, combined with an apparent textural equilibrium and the absence of different generations of orthopyroxene (i.e., Patagonia; Melchiorre et al., 2015), suggests that the peridotite matrix suffered a long term interaction with a sub-alkaline (silica-saturated) melt. This melt was able to increase orthopyroxene volume and, contemporaneously, its Al_2O_3 content.

On the other hand, clinopyroxene in a fertile mantle, having more compatible behaviour for basic melt components, maintains its model percentage, but certainly not its geochemical features (i.e. Al_2O_3, REE). Indeed, a marked similarity in REE contents can be observed between clinopyroxene in both *Lherzolite Group 2* and those calculated in equilibrium with the Ferrar Dolerites (Kyle, 1980; Antonini et al., 1999), using $Kd^{cpx/th}$ from the GERM database (Fig. 3.12B). The magmatic expression of these mantle re-fertilising melts can be identified in the Jurassic tholeiites of the Ferrar Group (ca. 177 Ma).

Riley et al. (2005) reported dolerites with geochemical features that reflect a genesis in the presence of garnet in the mantle source in Western Dronning Maud Land (Karoo large igneous province). Victoria Land mantle segment records potential garnet signatures as observed in *Lherzolite Group2* samples and documented by Perinelli et al. (2006), Melchiorre et al. (2011), Martin et al. (2015) in patchy areas.

The MREE/HREE ratios and a slightly depleted LREE pattern *in Lherzolite Group 2* clinopyroxene (Fig.5E), as well as the characteristic Ti anomaly, associated with the high mg# and high Al_2O_3, rule out the likelihood that a melting episode occurred in the garnet-facies and successively re-equilibrated in the spinel stability field (see also Bonadiman et al., 2005; Fig.3.12C). On the contrary, the garnet signature observed in a few GP lherzolites may reflect the composition of the impregnating tholeiitic melts generated from garnet-bearing lherzolites (Riley et al. 2005).

Taking into account that the Ferrar province is generally considered as an extension of the Karoo large igneous province (Harris et al., 1991; Luttinen et al., 1998) and is related to the same event that emplaced the Ferrar dolerites in the NVL region, it is reasonable to think that the asthenospheric (garnet facies) Ferrar tholeiitic magmatism was also responsible for the garnet signature in the refertilised Greene Point mantle domain (mainly *Lherzolite Group 2*).

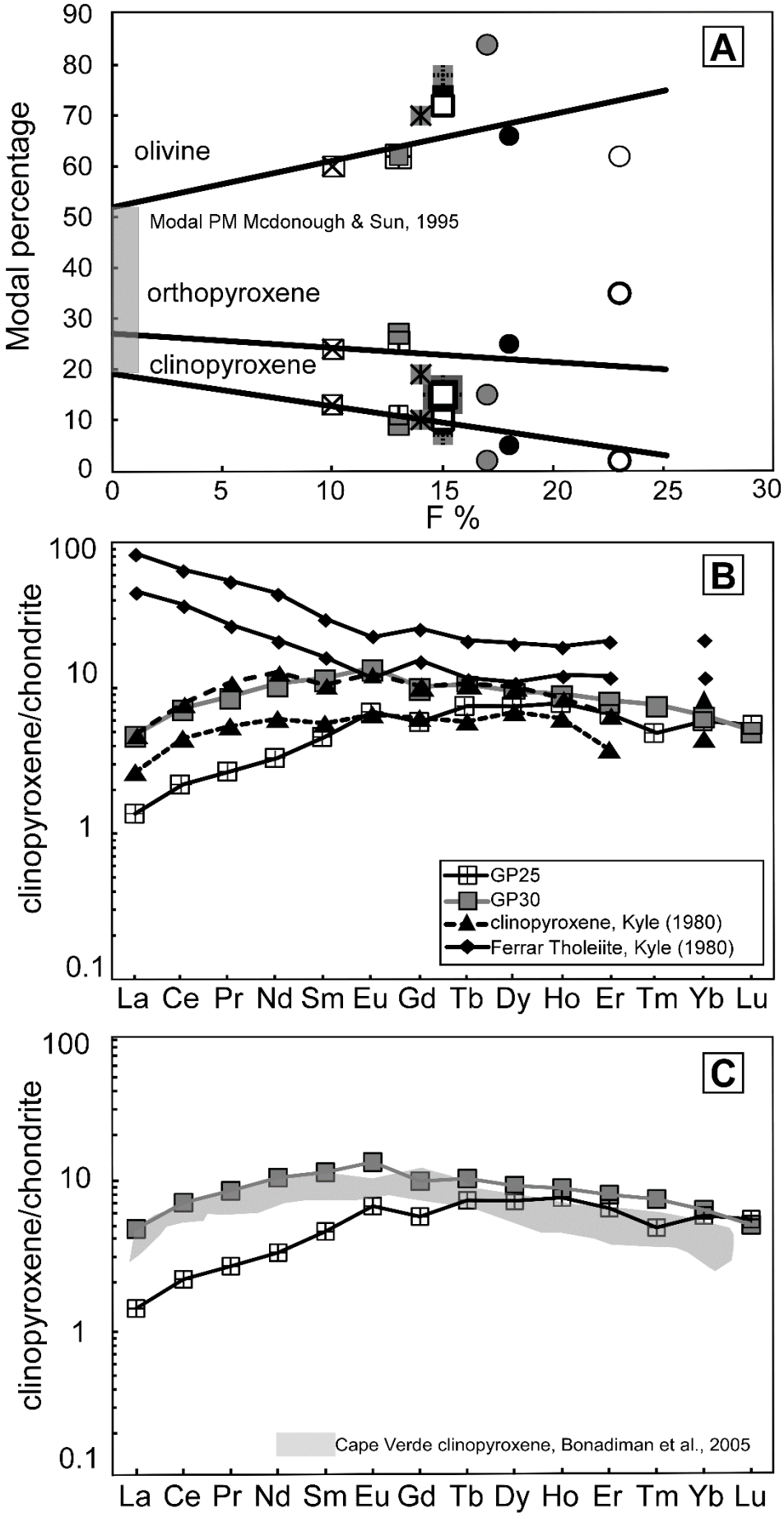
A
Modal percentage
F %
olivine
orthopyroxene
clinopyroxene
Modal PM Mcdonough & Sun, 1995
B
clinopyroxene/chondrite
GP25
GP30
clinopyroxene, Kyle (1980)
Ferrar Tholeiite, Kyle (1980)
La Ce Pr Nd Sm Eu Gd Tb Dy Ho Er Tm Yb Lu
C
clinopyroxene/chondrite
Cape Verde clinopyroxene, Bonadiman et al., 2005
La Ce Pr Nd Sm Eu Gd Tb Dy Ho Er Tm Yb Lu

Fig 3.12 A): Observed modes of olivine, orthopyroxene and clinopyroxene (%) in Greene Point xenoliths *vs* F (extend of melting). PM composition is from Mc Donough and Sun (1995); B) Comparison between REE patterns of *Lherzolites Group 2* clinopyroxene and those calculated in equilibrium with the Ferrar Dolerites (Kyle, 1980), using the $Kd^{cpx/th}$ from GERM database; C) Comparison between REE patterns of clinopyroxene *Lherzolites Group 2* with those of clinopyroxene suggesting melt in garnet-facies, successively re-equilibrated in the spinel stability field (Bonadiman et al., 2005). Symbols as in Fig. 3.3.

3.5 Conclusions

1. The entire GP mantle xenolith suite reflects an NVL mantle segment equilibrated in a thermal regime of ~950 °C, with redox conditions close to ~ -1.04 log units below QFM. Compared with amphibole-bearing mantle xenoliths from nearby localities, the Greene Point xenolith population presents higher T at comparable oxidised conditions.
2. Based on spinel and orthopyroxene major elements, and HREE in clinopyroxene, *Lherzolite Groups 1* and *2* may represent a residuum of partial melting after ~10 to 17% in the spinel stability field, which was afterward largely modified by interaction with tholeiitic and, to a lesser extent, alkaline melts, most probably affecting the mantle domain at different times.
3. The tholeiitic magmatism that preceded (Jurassic) Gondwana break-up, was able to reset the peridotitic system, modifying its mineralogical and geochemical features (i.e., peridotite mineral disproportion and high orthopyroxene-clinopyroxene Al_2O_3 contents; slightly convex to flat REE clinopyroxene patterns), transferring a garnet signature to the NVL mantle region.
4. During the Cenozoic, alkaline metasomatism widely observed in Northern Victoria Land, related to the WARS opening locally interacted with the previously re-fertilised peridotitic system, and in some case (Baker Rocks area), almost completely obscuring the previous refertilisation event.

Appendix A3

Table A3.1: Major elements content (wt%) of GP orthopyroxenes

Sample	**GP9**	**GP9**	**GP9**	**GP13**	**GP13**	**GP13**	**CD305**	**CD305**	**GP30**	**GP30**	**GP30**	**GP25**	**GP25**
phase	opx	opx	opx	opx	opx	opx	opx	opx	opx	opx	opx	opx	opx
rim/core	core	rim	core	rim	core	core	core	rim	rim	core	core	rim	core
Host rock	Lh exs	Lh	Lh	Lh	Lh	Lh	Hz	Hz	Lh	Lh	Lh	Lh	Lh
Group	Lh 1	Lh1	Lh 1	Lh 1	Lh 1	Lh 1	Lh2	Lh2	Lh2	Lh2	Lh2	Lh2	Lh2
SiO_2	55.54	56.28	55.89	55.09	54.85	55.10	55.41	55.22	55.82	55.32	55.18	55.57	55.09
TiO_2	0.04	0.09	0.14	0.09	0.09	0.09	0.13	0.11	0.13	0.11	0.13	0.09	0.12
Al_2O_3	3.22	2.60	3.01	4.23	4.28	4.12	4.70	4.46	4.18	4.34	4.49	4.75	4.92
FeOtot	5.62	5.57	5.70	5.63	5.59	5.77	5.14	5.08	4.99	5.10	4.98	5.62	5.69
MnO	0.13	0.14	0.15	0.13	0.13	0.16	0.11	0.12	0.12	0.10	0.12	0.11	0.12
MgO	33.80	34.12	33.61	32.74	32.57	32.53	34.02	34.11	34.55	34.23	34.22	34.01	33.78
CaO	0.57	0.55	0.70	0.94	0.94	0.94	1.05	0.98	0.92	0.99	0.92	0.96	1.01
Na_2O	0.03	0.08	0.09	0.15	0.14	0.14	0.13	0.11	0.11	0.12	0.16	0.12	0.09
K_2O	0.01	0.00	0.00	0.00	0.00	0.00	0.01	0.01	0.00	0.01	0.02	0.01	0.01
Cr_2O_3	0.72	0.46	0.55	0.666	0.643	0.603	0.68	0.79	0.76	0.80	0.97	0.70	0.73
Tot	99.69	99.91	99.84	99.11	98.68	98.94	101.38	100.99	101.58	101.12	101.19	101.94	101.56
Fe_2O_3	0.120	0.060	0.030	0.010	0.000	0.000	0.41	0.46	0.42	0.50	0.55	0.45	0.49
FeO	5.510	5.520	5.670	5.620	5.610	5.880	4.77	4.67	4.61	4.65	4.49	5.21	5.25
Si	1.919	1.938	1.929	1.914	1.914	1.920	1.877	1.878	1.886	1.878	1.872	1.875	1.867
Ti	0.001	0.002	0.004	0.002	0.002	0.002	0.003	0.003	0.003	0.003	0.003	0.002	0.003
Al	0.131	0.106	0.122	0.173	0.176	0.169	0.188	0.179	0.166	0.174	0.180	0.189	0.197
Fe III	0.003	0.002	0.001	0.000	0.000	0.000	0.010	0.012	0.011	0.013	0.014	0.011	0.013
Fe II	0.159	0.159	0.164	0.163	0.164	0.172	0.135	0.133	0.130	0.132	0.127	0.147	0.149
Mn	0.004	0.004	0.004	0.004	0.004	0.005	0.003	0.003	0.003	0.003	0.003	0.003	0.003
Mg	1.740	1.751	1.729	1.695	1.694	1.689	1.718	1.728	1.739	1.732	1.730	1.710	1.706
Ca	0.021	0.020	0.026	0.035	0.035	0.035	0.038	0.036	0.033	0.036	0.033	0.035	0.037
Na	0.002	0.005	0.006	0.010	0.009	0.009	0.009	0.007	0.007	0.008	0.011	0.008	0.006
K	0.000	0.000	0.000	0.000	0.000	0.000	0.000	0.000	0.000	0.000	0.001	0.000	0.000
Cr	0.020	0.013	0.015	0.003	0.002	0.003	0.018	0.021	0.020	0.021	0.026	0.019	0.020
SumCat	4.000	4.000	4.000	4.000	4.000	4.000	3.999	4.000	3.998	4.000	4.000	3.999	4.001
XFeII	0.09	0.09	0.09	0.10	0.10	0.10	0.08	0.08	0.07	0.08	0.07	0.09	0.09
mg#	91.47	91.60	91.31	91.20	91.21	90.95	92.19	92.29	92.51	92.29	92.45	91.51	91.36

Lh Lherzolites, Hz Harzburgites, n number of average analyse. Lh 1: *Lh Group 1*, Lh 2: *Lh Group 3*, Hz 3: *Hz Group 3. Exs:exsolution lamellae*

Table A3.1: Continued

Sample	**GP25**	**GP84**	**GP84**	**GP84**	**GP28**	**GP28**	**GP28**	**GP81**	**GP81**	**GP81**	**GP78**	**GP78**
phase	opx	opx	opx	opx	opx	opx	opx	opx	opx	opx	opx	opx
rim/core	rim	rim	core	core	core	core	rim	rim	rim	core	core	core
Host rock	Lh	Lh	Lh	Lh	Lh	Lh	Lh	HZ	Hz	Hz	Hz	Hz
Group	Lh2	Lh2	Lh2	Lh2	Lh2	Lh2	Lh2	Hz3	Hz3	Hz3	Hz3	Hz3
SiO_2	55.04	55.68	55.70	55.76	56.35	56.40	56.29	56.35	55.76	55.94	56.27	56.60
TiO_2	0.10	0.05	0.01	0.04	0.14	0.08	0.04	0.11	0.07	0.11	0.04	0.01
Al_2O_3	4.67	4.50	4.59	4.65	4.02	4.14	3.98	3.33	3.21	3.44	2.67	2.45
FeOtot	5.58	5.54	5.63	5.59	4.98	5.05	4.89	5.32	5.06	5.31	5.33	5.32
MnO	0.11	0.15	0.14	0.12	0.11	0.13	0.11	0.11	0.07	0.14	0.11	0.12
MgO	33.45	33.93	33.87	33.67	34.42	34.60	34.49	34.47	34.56	34.66	34.75	35.09
CaO	0.95	1.02	1.01	1.09	0.90	0.90	0.94	0.95	1.01	0.97	1.05	0.94
Na_2O	0.10	0.07	0.07	0.06	0.09	0.09	0.10	0.09	0.07	0.06	0.03	0.01
K_2O	0.01	0.01	0.01	0.00	0.00	0.01	0.01	0.03	0.00	0.00	0.02	0.00
Cr_2O_3	0.41	0.46	0.71	0.85	0.82	0.81	0.70	0.70	0.52	0.91	0.82	0.74
Tot	100.42	101.41	101.74	101.83	101.83	102.21	45.22	101.46	100.33	101.54	101.09	101.28
Fe_2O_3	0.31	0.33	0.32	0.19	0.14	0.26	0.23	0.31	0.44	0.49	0.44	0.43
FeO	5.30	5.24	5.34	5.42	4.86	4.82	4.69	5.04	4.66	4.87	4.93	4.94
Si	1.885	1.888	1.885	1.887	1.902	1.895	1.902	1.909	1.906	1.894	1.913	1.919
Ti	0.003	0.001	0.000	0.001	0.004	0.002	0.001	0.003	0.002	0.003	0.001	0.000
Al	0.189	0.180	0.183	0.186	0.160	0.164	0.159	0.133	0.129	0.137	0.107	0.098
Fe III	0.008	0.008	0.008	0.005	0.003	0.007	0.006	0.008	0.011	0.012	0.011	0.011
Fe II	0.152	0.149	0.151	0.153	0.137	0.135	0.132	0.143	0.133	0.138	0.140	0.140
Mn	0.003	0.004	0.004	0.003	0.003	0.004	0.003	0.003	0.002	0.004	0.003	0.003
Mg	1.708	1.715	1.708	1.698	1.731	1.733	1.737	1.741	1.761	1.748	1.761	1.773
Ca	0.035	0.037	0.037	0.040	0.033	0.032	0.034	0.034	0.037	0.035	0.038	0.034
Na	0.007	0.005	0.005	0.004	0.006	0.006	0.007	0.006	0.005	0.004	0.002	0.001
K	0.000	0.000	0.000	0.000	0.000	0.000	0.000	0.001	0.000	0.000	0.001	0.000
Cr	0.011	0.012	0.019	0.023	0.022	0.022	0.019	0.019	0.014	0.024	0.022	0.020
SumCat	4.001	3.999	4.000	4.000	4.001	4.000	4.000	4.000	4.000	3.999	3.999	3.999
XFeII	0.09	0.09	0.09	0.09	0.08	0.08	0.08	0.08	0.08	0.08	0.08	0.08
mg#	91.44	91.61	91.47	91.48	92.50	92.43	92.62	92.02	92.40	92.09	92.07	92.16

Table A3.1: Continued

Sample	**GP78**	**GP23**	**GP23**	**GP23**
phase	opx	opx	opx	opx
rim/core	rim	core	core	rim
Host rock	Hz	Hz	Hz	Hz
Group	Hz3	Hz3	Hz3	Hz3
SiO_2	56.58	55.78	55.72	56.28
TiO_2	0.00	0.04	0.05	0.04
Al_2O_3	2.33	2.80	2.91	2.71
FeOtot	5.21	5.15	5.12	5.02
MnO	0.14	0.14	0.09	0.11
MgO	35.15	35.20	34.85	35.13
CaO	1.01	0.97	1.03	0.95
Na_2O	0.02	0.04	0.03	0.05
K_2O	0.01	0.00	0.02	0.00
Cr_2O_3	0.71	0.66	0.71	0.72
Tot	101.16	100.78	100.53	101.01
Fe_2O_3	0.49	0.75	0.60	0.51
FeO	4.77	4.47	4.58	4.56
Si	1.920	1.897	1.901	1.910
Ti	0.000	0.001	0.001	0.001
Al	0.093	0.112	0.117	0.108
Fe III	0.012	0.019	0.015	0.013
Fe II	0.135	0.127	0.131	0.129
Mn	0.004	0.004	0.003	0.003
Mg	1.778	1.784	1.772	1.777
Ca	0.037	0.035	0.038	0.035
Na	0.001	0.003	0.002	0.003
K	0.000	0.000	0.001	0.000
Cr	0.019	0.018	0.019	0.019
SumCat	3.999	4.000	4.000	3.998
XFeII	0.08	0.07	0.07	0.07
mg#	92.32	92.41	92.39	92.58

Table A3.2: Trace elements (ppm) of GP orthopyroxenes

Sample	**GP9**	**GP9**	**GP13**	**CD305**	**GP30**	**GP25**	**GP 84**	**GP28**	**GP81**
phase	opx	opx	opx	opx	opx	opx	opx	opx	opx
Host rock	Lh	Lh	Lh	Lh	Lh	Lh	Lh	Lh	Hz
n	3	1(exs)	3	3	2	5	3	4	8
Group	Lh1	Lh1	Lh1	Lh2	Lh2	Lh2	Lh2	Lh2	Hz3
Li7					1.940	1.934			8.325
Cs	0.002	<0.032	0.003		0.008		0.002		0.026
Rb	0.004	<0.064	0.004	0.021	0.035	0.043	0.046	0.035	0.034
Ba	0.003	<0.0251	0.006	0.047		0.043	0.080	0.080	0.561
Th	0.000	<0.00	0.000		0.008	0.009	0.015	0.039	0.017
U	0.000	0.000	0.000	0.008	0.003	0.026	0.003	0.005	0.009
Nb	0.020	0.035	0.021	0.109	0.036	0.073	0.091	0.078	0.089
Ta	0.000	<0.0029	0.000						0.009
La	0.005	0.004	0.004		0.008	0.011	0.010	0.012	0.045
Ce	0.019	0.015	0.019	0.037	0.016	0.025	0.033	0.042	0.073
Pr	0.005	0.003	0.005	0.007	0.005	0.004	0.008	0.006	0.019
Sr	0.246	0.148	0.256	0.220	0.276	0.088	0.113	0.126	0.374
Nd	0.036	0.025	0.035	0.049	0.084	0.014	0.059	0.055	0.069
Zr	2.290	0.819	2.400		1.249	0.440	0.451		0.955
Hf	0.054	0.017	0.057		0.039	0.026	0.010		0.045
Sm	0.024	0.013	0.022	0.019	0.028	0.017	0.042	0.022	0.025
Eu	0.010	0.010	0.011	0.006	0.011	0.010	0.004	0.011	0.010
Ti	603.50	1023.89	624.35	462.51	517.97	355.62	174.86	437.88	285.74
Gd	0.048	0.029	0.050	0.059	0.056	0.048	0.019	0.058	0.029
Tb	0.012	0.011	0.012		0.020		0.012		0.008
Dy	0.124	0.086	0.120	0.127	0.098	0.111	0.053	0.096	0.066
Y	0.956	0.573	1.004	0.933	0.894	0.877	0.401	0.775	0.409
Ho	0.033	0.018	0.035	0.041	0.026	0.040	0.015	0.030	0.018
Er	0.133	0.076	0.137	0.155	0.116	0.133	0.066	0.116	0.060
Tm	0.028	0.017	0.029		0.011	0.025	0.009		0.008
Yb	0.202	0.141	0.214	0.189	0.208	0.163	0.159	0.158	0.088
Lu	0.040	0.025	0.040	0.030	0.038	0.041	0.027	0.029	0.015

Table A3.3: Major elements content (wt%) of GP clinopyroxenes

Sample	**GP9**	**GP9**	**GP9**	**GP13**	**GP13**	**GP13**	**CD305**	**CD305**	**CD305**	**GP30**	**GP30**	**GP30**
phase rim/core	cpx1 exs	cpx1 core	cpx1 rim	cpx1 core	cpx1 core	cpx1 core	cpx1 core	cpx1 rim	cpx1 core	cpx1 core	cpx1 core	cpx1 core
Host rock	Lh	Lh	Lh	Lh	Lh	Lh	Lh	Lh	Lh	Lh	Lh	Lh
Group	Lh 1	Lh 1	Lh1	Lh 1	Lh 1	Lh 1	Lh 2	Lh2	Lh2	Lh2	Lh2	Lh2
SiO_2	52.72	52.41	52.71	52.33	52.21	52.05	52.09	51.78	52.47	51.93	52.20	52.22
TiO_2	0.50	0.21	0.41	0.33	0.29	0.33	0.40	0.56	0.32	0.26	0.32	0.33
Al_2O_3	3.74	4.19	3.55	5.93	5.91	6.02	4.19	4.44	5.99	5.70	5.86	5.74
FeOtot	2.10	2.25	2.15	2.59	2.51	2.55	2.11	2.45	2.37	2.10	2.25	2.22
MnO	0.08	0.08	0.08	0.08	0.09	0.10	0.06	0.06	0.09	0.09	0.05	0.07
MgO	16.25	16.09	16.39	15.75	15.82	15.66	17.02	16.72	16.59	16.45	16.62	16.54
CaO	22.23	21.45	22.30	19.48	19.58	19.49	22.70	22.07	20.26	20.33	20.12	20.27
Na_2O	0.99	0.99	0.90	1.68	1.57	1.65	0.74	0.92	1.47	1.42	1.39	1.47
K_2O	0.01	0.00	0.00				0.00	0.04	0.01	0.00	0.01	0.00
Cr_2O_3	1.11	1.58	1.27	1.42	1.29	1.41	1.51	1.87	1.40	1.55	1.48	1.53
Tot	99.75	99.26	99.77	98.29	98.04	97.95	100.82	100.91	100.97	99.83	100.30	100.39
Fe_2O_3	0.21	0.06	0.22	0.19	0.15	0.18	0.66	0.71	0.50	0.50	0.41	0.50
FeO	1.91	2.20	1.95	2.42	2.38	2.39	1.52	1.81	1.92	1.65	1.88	1.77
Si	1.914	1.913	1.914	1.912	1.912	1.908	1.869	1.859	1.870	1.872	1.873	1.872
Ti	0.011	0.006	0.011	0.009	0.008	0.009	0.011	0.015	0.009	0.007	0.009	0.009
Al	0.152	0.18	0.152	0.255	0.255	0.26	0.177	0.188	0.252	0.242	0.248	0.243
Fe III	0.006	0.002	0.006	0.005	0.004	0.005	0.018	0.019	0.013	0.014	0.011	0.014
Fe II	0.059	0.067	0.059	0.074	0.073	0.073	0.046	0.054	0.057	0.050	0.057	0.053
Mn	0.002	0.002	0.002	0.002	0.003	0.003	0.002	0.002	0.003	0.003	0.002	0.002
Mg	0.887	0.875	0.887	0.857	0.863	0.856	0.910	0.895	0.881	0.884	0.889	0.884
Ca	0.868	0.839	0.868	0.762	0.768	0.766	0.873	0.849	0.774	0.785	0.774	0.779
Na	0.063	0.07	0.063	0.119	0.111	0.117	0.051	0.064	0.102	0.099	0.097	0.102
K	0	0	0	0.001	0.001	0	0.000	0.002	0.000	0.000	0.000	0.000
Cr	0.036	0.046	0.036	0.002	0.001	0.002	0.043	0.053	0.039	0.044	0.042	0.043
SumCat	4	4	4	4	4	4	4.000	4.000	4.000	4.000	4.002	4.001
FeII/Mg	0.066	0.077	0.067	0.086	0.085	0.085	0.051	0.060	0.065	0.057	0.064	0.060
mg#	93.24	92.71	93.15	91.55	91.81	91.62	93.51	92.40	92.57	93.31	92.95	93.00

Table A3.3: Continued

Sample	GP25	GP25	GP25	GP84	GP84	GP84	GP28	GP28	G28	GP81	GP81
phase rim/core	cpx1 core	cpx1 core	cpx1 core	cpx1 rim	cpx1 core	cpx1 rim	cpx1 core	cpx1 rim	cpx1 core	cpx1 rim	cpx1 core
Host rock	Lh	Lh	Lh	Lh	Lh	Lh	Lh	Lh	Lh	Hz	Hz
Group	Lh2	Lh2	Lh2	Lh2	Lh2	Lh2	Lh2	Lh2	Lh2	Hz3	Hz3
SiO_2	52.54	52.51	52.09	52.88	52.50	52.95	52.92	53.35	52.76	53.17	53.04
TiO_2	0.20	0.19	0.21	0.09	0.11	0.08	0.28	0.28	0.28	0.22	0.15
Al_2O_3	6.42	6.40	6.42	5.31	5.80	5.33	5.27	4.87	5.59	4.06	4.18
FeOtot	2.50	2.57	2.61	2.51	2.60	2.57	2.09	2.16	2.26	2.49	2.51
MnO	0.09	0.07	0.09	0.09	0.11	0.10	0.06	0.08	0.09	0.08	0.07
MgO	16.54	16.39	16.45	17.04	16.96	17.13	16.97	17.11	17.07	17.49	17.15
CaO	20.00	20.37	20.18	21.03	20.45	20.84	21.10	20.83	20.15	21.27	21.12
Na_2O	1.42	1.40	1.44	1.10	1.13	0.99	1.17	1.14	1.23	1.00	0.99
K_2O	0.00	0.00	0.01	0.02	0.01	0.01	0.02	0.03	0.01	0.01	0.00
Cr_2O_3	1.35	1.24	1.20	1.17	1.38	1.18	1.68	1.42	1.68	1.32	1.44
Tot	101.06	101.14	100.70	101.24	101.05	101.18	101.56	101.27	101.12	101.11	100.65
Fe_2O_3	0.35	0.41	0.58	0.49	0.42	0.31	0.38	0.21	0.27	0.52	0.34
FeO	2.18	2.20	2.08	2.07	2.22	2.29	1.75	1.97	2.02	2.02	2.20
Si	1.871	1.869	1.861	1.882	1.872	1.887	1.88	1.90	1.88	1.897	1.903
Ti	0.005	0.005	0.006	0.002	0.003	0.002	0.01	0.01	0.01	0.006	0.004
Al	0.269	0.269	0.270	0.223	0.244	0.224	0.22	0.20	0.24	0.171	0.177
Fe III	0.009	0.011	0.016	0.013	0.011	0.008	0.01	0.01	0.01	0.014	0.009
Fe II	0.065	0.066	0.062	0.062	0.066	0.068	0.05	0.06	0.06	0.060	0.066
Mn	0.003	0.002	0.003	0.003	0.003	0.003	0.00	0.00	0.00	0.002	0.002
Mg	0.878	0.870	0.876	0.904	0.901	0.910	0.90	0.91	0.91	0.930	0.917
Ca	0.763	0.777	0.772	0.802	0.781	0.796	0.80	0.79	0.77	0.813	0.812
Na	0.098	0.097	0.100	0.076	0.078	0.068	0.08	0.08	0.09	0.069	0.069
K	0.000	0.000	0.000	0.001	0.000	0.000	0.00	0.00	0.00	0.000	0.000
Cr	0.038	0.035	0.034	0.033	0.039	0.033	0.05	0.04	0.05	0.037	0.041
SumCat	3.999	4.001	4.000	4.001	3.998	3.999	4.00	4.00	4.00	3.999	4.000
FeII/Mg	0.074	0.076	0.071	0.069	0.073	0.075	0.058	0.065	0.066	0.065	0.072
mg#	92.19	91.92	91.83	92.36	92.09	92.22	93.54	93.39	93.09	92.61	92.41

Table A3.3: Continued

Sample	**GP81**	**GP78**	**GP78**	**GP78**	**GP23**	**GP23**	**GP23**
phase rim/core	cpx1 core	cpx1 rim	cpx1 core	cpx1 core	cpx1 rim	cpx1 rim	cpx1 core
Host rock	Hz	Hz	Hz	Hz	Lh	Lh	Lh
Group	Hz3	Hz3	Hz3	Hz3	Hz3	Hz3	Hz3
SiO_2	53.08	53.74	53.65	53.08	52.91	52.71	52.81
TiO_2	0.17	0.01	0.03	0.04	0.04	0.03	0.11
Al_2O_3	4.37	2.32	2.33	2.46	3.13	3.01	3.39
FeOtot	2.51	2.22	2.37	2.20	2.08	2.17	2.11
MnO	0.08	0.08	0.07	0.08	0.10	0.06	0.08
MgO	17.41	18.72	18.71	18.52	18.01	18.11	17.96
CaO	20.92	22.90	22.75	22.69	22.04	22.12	22.02
Na_2O	1.03	0.20	0.20	0.21	0.61	0.61	0.61
K_2O	0.01	0.01	0.01	0.00	0.01	0.01	0.01
Cr_2O_3	1.66	0.95	0.92	1.10	1.32	1.48	1.45
Tot	101.24	101.15	101.04	100.38	100.25	100.31	100.55
Fe_2O_3	0.44	0.47	0.47	0.51	0.57	0.74	0.56
FeO	2.11	1.80	1.94	1.74	1.56	1.51	1.60
Si	1.892	1.92	1.919	1.911	1.904	1.896	1.896
Ti	0.005	0.00	0.001	0.001	0.001	0.001	0.003
Al	0.184	0.10	0.098	0.104	0.133	0.128	0.143
Fe III	0.012	0.01	0.013	0.014	0.016	0.020	0.015
Fe II	0.063	0.05	0.058	0.053	0.047	0.045	0.048
Mn	0.002	0.00	0.002	0.002	0.003	0.002	0.002
Mg	0.925	1.00	0.997	0.994	0.966	0.971	0.961
Ca	0.799	0.88	0.872	0.875	0.850	0.853	0.847
Na	0.071	0.01	0.014	0.015	0.043	0.043	0.042
K	0.000	0.00	0.000	0.000	0.000	0.000	0.000
Cr	0.047	0.03	0.026	0.031	0.038	0.042	0.041
SumCat	4.000	4.00	4.000	4.000	4.001	4.001	3.998
FeII/Mg	0.068	0.05	0.058	0.053	0.049	0.046	0.050
mg#	92.52	93.76	93.36	93.75	93.92	93.70	93.82

Table A3.3: Trace elements (ppm) of GP clinopyroxenes

Sample	**GP9**	**GP9**	**GP13**	**GP30**	**GP25**	**GP84**	**GP28**	**GP81**	**GP78**	**GP23**
phase	cpx/exs	cpx	cpx	cpx	cpx	cpx	cpx	cpx	cpx	cpx
Host rock	Lh	Lh	Lh	Lh	Lh	Lh	Lh	Hz	Hz	Hz
n	1	4	3	3	6	2	1	8	1	2
Group	Lh1	Lh1	Lh1	Lh2	Lh2	Lh2	Lh2	Hz3	Hz3	Hz3
Cs	0.061	0.074	0.007	0.072	0.007	0.012	0.025	0.016		<0.014
Rb	0.121	0.147	0.013	0.041	0.192	0.034	0.159	0.061	0.110	<0.047
Ba	0.050	0.063	0.127	0.428	0.427	0.225	0.024	6.874	1.020	<0.17
Th	0.104	0.089	0.005	0.018	0.010	0.028		0.025	0.023	0.061
U	0.036	0.018	0.001	0.006	0.006	0.013		0.008		0.052
K				60.881	71.397	74.718	0.169	49.812		41.510
Nb	1.224	1.323	0.093	0.144	0.101	0.328		0.328	0.345	0.193
Ta	0.024	0.104	0.015	0.013	0.005	0.040	0.538	0.011		0.017
La	1.246	2.097	0.984	1.139	0.325	0.974	2.543	1.652	1.155	0.837
Ce	4.070	7.028	4.380	4.453	1.333	2.357	0.537	5.938	2.200	2.780
Pr	0.624	1.136	0.823	0.834	0.254	0.280	42.223	0.984	0.246	0.363
Sr	91.95	135.97	74.98	82.80	24.64	21.41	3.43	71.13	15.13	29.43
Nd	3.140	5.780	4.733	5.040	1.547	1.070		4.050	1.000	2.260
Zr	9.570	16.998	35.633	19.397	6.610	2.800		12.455		4.520
Hf	0.276	0.387	0.858	0.650	0.235	0.087	1.233	0.376		0.127
Sm	0.956	1.689	1.501	1.797	0.706	0.223	0.496	1.240	0.250	0.570
Eu	0.335	0.619	0.575	0.800	0.400	0.062	1247.047	0.506	0.080	0.144
Ti	1334.87	2615.09	2184.41	1684.26	1264.86	509.60	1.68	1144.55	96.535	301.985
Gd	1.175	1.857	1.831	2.100	1.202	0.227		1.304		0.420
Tb	0.180	0.300	0.328	0.398	0.282	0.093	2.035	0.208		0.065
Dy	1.25	1.87	2.32	2.41	1.90	0.708	9.80	1.07	0.250	0.58
Y	5.920	9.373	12.673	13.027	10.763	4.570	0.386	5.052	0.935	3.150
Ho	0.228	0.366	0.473	0.518	0.446	0.200	1.000	0.207	0.056	0.151
Er	0.743	0.964	1.379	1.365	1.325	0.586		0.400	0.166	0.490
Tm	0.080	0.130	0.204	0.197	0.150	0.096	0.840	0.075		0.032
Yb	0.642	0.865	1.279	1.105	1.010	0.668	0.114	0.417	0.170	0.470
Lu	0.085	0.126	0.184	0.131	0.142	0.098		0.086	0.025	0.068

Table A3.5: Major elements content (wt%) of GP olivines

Sample	GP9	GP9	GP9	GP13	GP13	GP13	CD305	CD305	CD305	GP30	GP30	GP30
phase	ol1	ol1	ol1	ol1	ol1	ol1	ol1	ol1	ol1	ol1	ol1	ol1
rim/core	core	rim	core	core	rim	core	core	rim	core	rim	core	core
Host rock	Lh	Lh	Lh	Lh	Lh	Lh	Lh	Lh	Lh	Lh	Lh	Lh
Group	Lh 1	Lh 1	Lh 1	Lh 1	Lh 1	Lh 1	Lh2	Lh2	Lh2	Lh2	Lh2	Lh2
SiO_2	40.99	41.29	41.18	40.69	41.02	40.94	41.56	41.36	41.17	41.43	41.03	41.40
TiO_2	0.00	0.01	0.00	0.00	0.01	0.01	0.05	0.00	0.02	0.00	0.02	0.01
Al_2O_3	0.02	0.01	0.01	0.02	0.02	0.03	0.03	0.02	0.03	0.02	0.02	0.03
FeO	8.86	8.39	8.73	9.07	9.16	9.12	7.69	8.18	7.51	7.52	7.24	7.41
MnO	0.12	0.10	0.12	0.15	0.14	0.13	0.15	0.12	0.11	0.10	0.11	0.12
MgO	49.29	49.44	49.44	49.07	48.80	48.86	51.57	50.82	51.30	51.60	51.31	51.28
CaO	0.05	0.04	0.04	0.09	0.07	0.08	0.10	0.10	0.08	0.06	0.06	0.06
Na_2O	0.00	0.00	0.00	0.00	0.00	0.00	0.02	0.02	0.03	0.00	0.01	0.00
K_2O	0.00	0.00	0.00	0.00	0.00	0.00	0.00	0.00	0.01	0.01	0.02	0.00
Cr_2O_3	0.01	0.00	0.01	0.02	0.03	0.05	0.07	0.09	0.06	0.11	0.08	0.05
NiO	0.40	0.39	0.41	0.40	0.38	0.39	0.37	0.33	0.41	0.35	0.40	0.41
Tot	99.74	99.67	99.94	99.51	99.63	99.61	101.17	100.62	100.26	100.74	99.82	100.31
Si	1.004	1.009	1.005	1.001	1.007	1.005	0.995	0.997	0.994	0.995	0.993	0.997
Ti	0.000	0.000	0.000	0.000	0.000	0.000	0.001	0.000	0.000	0.000	0.000	0.000
Al	0.001	0.000	0.000	0.001	0.001	0.001	0.001	0.001	0.001	0.001	0.001	0.001
Fe	0.181	0.171	0.178	0.186	0.188	0.187	0.154	0.165	0.152	0.151	0.147	0.149
Mn	0.002	0.002	0.002	0.003	0.003	0.003	0.003	0.002	0.002	0.002	0.002	0.002
Mg	1.799	1.800	1.799	1.798	1.785	1.788	1.839	1.826	1.845	1.846	1.851	1.841
Ca	0.001	0.001	0.001	0.002	0.002	0.002	0.003	0.003	0.002	0.002	0.002	0.002
Na	0.000	0.000	0.000	0.000	0.000	0.000	0.001	0.001	0.001	0.000	0.000	0.000
K	0.000	0.000	0.000	0.000	0.000	0.000	0.000	0.000	0.000	0.000	0.001	0.000
Cr	0.000	0.000	0.000	0.000	0.001	0.001	0.001	0.002	0.001	0.002	0.002	0.001
Ni	0.008	0.008	0.008	0.008	0.008	0.008	0.007	0.006	0.008	0.007	0.008	0.008
Sum Ca	2.996	2.991	2.995	2.999	2.993	2.994	3.004	3.003	3.006	3.005	3.006	3.002
mg#	90.84	91.31	90.98	90.60	90.47	90.52	92.28	91.72	92.41	92.44	92.66	92.50

Table A3.5: Continued

Sample	GP25	GP25	GP25	GP84	GP84	GP84	GP28	GP28	GP28	GP81	GP81	GP81
phase	ol1	ol1	ol1	ol1	ol1	ol1	ol1	ol1	ol1	ol1	ol1	ol1
rim/core	rim	rim	rim	core	rim	core	rim	core	core	rim	rim	core
Host rock	Lh	Lh	Lh	Lh	Lh	Lh	Lh	Lh	Lh	Hz	Hz	Hz
Group	Lh2	Lh2	Lh2	Lh2	Lh2	Lh2	Lh2	Lh2	Hz3	Hz3	Hz3	Hz3
SiO_2	41.46	40.89	41.50	41.63	41.52	41.81	41.73	41.74	41.82	41.26	41.27	41.49
TiO_2	0.00	0.02	0.01	0.07	0.00	0.02	0.02	0.00	0.03	0.01	0.00	0.03
Al_2O_3	0.01	0.01	0.02	0.03	0.03	0.02	0.01	0.02	0.02	0.02	0.01	0.01
FeO	8.26	8.62	8.48	7.66	8.88	8.34	7.61	7.49	7.37	8.28	7.76	7.77
MnO	0.15	0.14	0.11	0.13	0.20	0.10	0.14	0.09	0.12	0.13	0.14	0.17
MgO	50.95	50.38	50.55	51.32	50.04	50.76	51.79	51.19	51.66	50.66	51.39	51.25
CaO	0.10	0.15	0.17	0.14	0.27	0.08	0.07	0.08	0.08	0.14	0.10	0.09
Na_2O	0.00	0.01	0.01	0.01	0.01	0.00	0.01	0.06	0.00	0.03	0.00	0.01
K_2O	0.01	0.02	0.01	0.01	0.00	0.01	0.00	0.00	0.01	0.00	0.01	0.00
Cr_2O_3	0.16	0.05	0.00	0.19	0.05	0.10	0.27	0.01	0.15	0.01	0.05	0.00
NiO	0.37	0.35	0.37	0.24	0.34	0.40	0.39	0.40	0.40	0.35	0.40	0.38
Tot	100.94	100.24	100.86	101	100.95	101.14	101.38	100.67	101.11	100.53	100.68	100.82
Si	0.996	0.993	1.000	0.997	1.001	1.002	0.994	1.002	0.998	0.997	0.993	0.997
Ti	0.000	0.000	0.000	0.001	0.000	0.000	0.000	0.000	0.001	0.000	0.000	0.001
Al	0.000	0.000	0.001	0.001	0.001	0.001	0.000	0.001	0.001	0.001	0.000	0.000
Fe	0.166	0.175	0.171	0.153	0.179	0.167	0.152	0.150	0.147	0.167	0.156	0.156
Mn	0.003	0.003	0.002	0.003	0.004	0.002	0.003	0.002	0.002	0.003	0.003	0.003
Mg	1.824	1.823	1.815	1.832	1.798	1.813	1.839	1.832	1.838	1.824	1.843	1.835
Ca	0.003	0.004	0.004	0.004	0.007	0.002	0.002	0.002	0.002	0.004	0.003	0.002
Na	0.000	0.000	0.000	0.000	0.000	0.000	0.000	0.003	0.000	0.001	0.000	0.000
K	0.000	0.001	0.000	0.000	0.000	0.000	0.000	0.000	0.000	0.000	0.000	0.000
Cr	0.003	0.001	0.000	0.004	0.001	0.002	0.005	0.000	0.003	0.000	0.001	0.000
Ni	0.007	0.007	0.007	0.005	0.007	0.008	0.007	0.008	0.008	0.007	0.008	0.007
Sum Ca	3.003	3.007	3.001	3.000	2.999	2.997	3.003	2.999	3.000	3.004	3.007	3.003
mg#	91.66	91.24	91.40	92.27	90.94	91.56	92.38	92.41	92.59	91.60	92.19	92.16

Table A3.5: Continued

Sample	GP78	GP78	GP78	GP23	GP23	GP23
phase	ol1	ol1	ol1	ol1	ol1	ol1
rim/core	rim	core	core	rim	core	core
Host rock	Hz	Hz	Hz	Hz	Hz	Hz
Group	Hz3	Hz3	Hz3	Hz3	Hz3	Hz3
SiO_2	41.09	41.26	41.79	41.14	41.19	40.95
TiO_2	0.01	0.00	0.00	0.00	0.00	0.00
Al_2O_3	0.01	0.01	0.02	0.01	0.01	0.02
FeO	7.70	8.02	7.85	7.71	7.71	7.65
MnO	0.11	0.09	0.14	0.12	0.12	0.14
MgO	51.12	51.41	52.28	51.33	51.55	51.39
CaO	0.14	0.07	0.07	0.07	0.06	0.08
Na_2O	0.00	0.02	0.01	0.00	0.01	0.02
K_2O	0.00	0.01	0.01	0.00	0.01	0.00
Cr_2O_3	0.11	0.01	0.08	0.02	0.02	0.00
NiO	0.41	0.40	0.40	0.40	0.38	0.40
Tot	100.18	100.89	102.17	100.38	100.66	100.25
Si	0.993	0.992	0.991	0.993	0.992	0.990
Ti	0.000	0.000	0.000	0.000	0.000	0.000
Al	0.000	0.000	0.001	0.000	0.000	0.001
Fe	0.156	0.161	0.156	0.156	0.155	0.155
Mn	0.002	0.002	0.003	0.002	0.002	0.003
Mg	1.841	1.842	1.847	1.846	1.849	1.852
Ca	0.004	0.002	0.002	0.002	0.002	0.002
Na	0.000	0.001	0.000	0.000	0.000	0.001
K	0.000	0.000	0.000	0.000	0.000	0.000
Cr	0.002	0.000	0.002	0.000	0.000	0.000
Ni	0.008	0.008	0.008	0.008	0.007	0.008
Sum Ca	3.006	3.009	3.009	3.007	3.009	3.011
mg#	92.21	91.95	92.23	92.23	92.26	92.29

Table A3.6: Major element content in GP spinels

Sample	GP9	GP9	GP9	GP13	GP13	GP13	CD305	CD305	CD305	GP30	GP30	GP30
phase	sp 1	sp 1	sp 1	sp 1	sp 1	sp 1	sp 1	sp 1	sp 1	sp 1	sp 1	sp 1
rim/core	core	rim	rim	core	core	core	core	rim	core	core	rim	core
Host rock	Lh	Lh	Lh	Lh	Lh	Lh	Hz	Hz	Hz	Lh	Lh	Lh
Group	Lh1	Lh1	Lh1	Lh1	Lh1	Lh1	Lh2	Lh2	Lh2	Lh2	Lh2	Lh2
SiO_2	0.02	0.01	0.01	0.06	0.09	0.05	0.06	0.08	0.05	0.06	0.04	0.05
TiO_2	0.26	0.28	0.34	0.17	0.15	0.17	0.16	0.17	0.19	0.17	0.15	0.17
Al_2O_3	38.94	38.5	38.11	45.9	47.36	47.7	48.41	48.43	48.43	46.05	46.51	46.33
FeOtot	12.86	13.01	13.07	10.48	10.34	10.12	9.73	9.60	9.80	9.80	7.92	9.71
MnO	0.1	0.09	0.13	0.09	0.09	0.11	0.08	0.07	0.09	0.09	0.10	0.11
MgO	17.72	17.82	17.79	19.91	19.91	19.88	20.50	20.58	20.63	20.06	21.21	20.15
CaO	0.00	0.00	0.00	0.01	0.01	0.02	0.01	0.02	0.02	0.00	0.04	0.01
Na_2O	0.00	0.00	0.00	0.00	0.00	0.00	0.00	0.00	0.00	0.00	0.00	0.00
K_2O	0.00	0.00	0.00	0.00	0.00	0.00	0.00	0.01	0.00	0.01	0.00	0.00
NiO	0.23	0.25	0.22	0.26	0.29	0.30	0.32	0.31	0.26	0.30	0.25	0.27
Cr_2O_3	29.22	29.63	30.15	20.6	21.13	20.83	21.58	21.45	21.90	24.20	24.20	24.34
Total	99.57	99.84	100.07	97.76	99.53	99.32	100.85	100.72	101.37	100.74	100.42	101.14
Fe_2O_3	2.21	2.54	2.5	2.8	1.74	1.54	1.42	1.44	1.47	1.20	1.13	1.05
FeO	10.87	10.72	10.82	7.96	8.77	8.73	8.45	8.31	8.48	8.72	6.90	8.76
Si	0.001	0	0	0.002	0.002	0.001	0.002	0.002	0.001	0.002	0.001	0.001
Ti	0.006	0.006	0.007	0.004	0.003	0.003	0.003	0.003	0.004	0.003	0.003	0.003
Al	1.291	1.276	1.262	1.485	1.504	1.515	1.511	1.512	1.504	1.454	1.460	1.456
FeIII	0.05	0.05	0.05	0.06	0.04	0.03	0.030	0.030	0.030	0.020	0.020	0.020
Fe II	0.26	0.25	0.25	0.18	0.2	0.2	0.190	0.180	0.190	0.200	0.150	0.200
Mn	0.002	0.002	0.003	0.002	0.002	0.003	0.002	0.002	0.002	0.002	0.002	0.002
Mg	0.743	0.746	0.745	0.814	0.799	0.798	0.809	0.812	0.810	0.801	0.842	0.801
Ca	0.00	0.00	0.00	0.00	0.00	0.00	0.000	0.001	0.001	0.000	0.001	0.000
Na	0.00	0.00	0.00	0.00	0.00	0.00	0.000	0.000	0.000	0.000	0.000	0.000
K	0.00	0.00	0.00	0.00	0.00	0.00	0.000	0.000	0.000	0.000	0.000	0.000
Ni	0.01	0.01	0.01	0.01	0.01	0.01	0.007	0.007	0.006	0.006	0.005	0.006
Cr	0.65	0.658	0.67	0.447	0.45	0.444	0.452	0.449	0.456	0.512	0.509	0.513
SumCat	3.008	2.994	2.992	3.000	3.006	3.001	3.006	2.998	3.004	3.000	2.993	3.002
mg#	71.06	70.94	70.81	77.20	77.44	77.79	78.97	79.25	78.96	78.49	82.67	78.72
cr#	33.48	34.04	34.67	23.14	23.03	22.65	23.03	22.90	23.27	26.04	25.85	26.05
XFeII	0.26	0.25	0.25	0.18	0.20	0.20	0.19	0.18	0.19	0.20	0.15	0.20
FeII/Mg	0.350	0.335	0.336	0.221	0.250	0.251	0.235	0.222	0.235	0.250	0.178	0.250

Table A3.6: Continued

Sample	**GP25**	**GP25**	**GP25**	**GP84**	**GP84**	**GP28**	**GP28**	**GP28**	**GP81**	**GP81**	**GP23**	**GP23**
phase	sp 1	sp 1	sp 1	sp 1	sp 1	sp 1	sp 1	sp 1	sp 1	sp 1	sp 1	sp 1
rim/core	core	core	rim	core	rim	core	rim	core	core	rim	core	rim
Host rock	Lh	Lh	Lh	Lh	Lh	Lh	Lh	Lh	Hz	Hz	Hz	Hz
Group	Lh2	Lh2	Lh2	Lh2	Lh2	Lh2	Lh2	Lh2	Hz3	Hz3	Hz3	Hz3
SiO_2	0.06	0.06	0.07	0.05	0.07	0.05	0.06	0.05	0.04	0.12	0.06	0.03
TiO_2	0.09	0.12	0.08	0.06	0.14	0.18	0.20	0.13	0.22	1.26	0.06	0.08
Al_2O_3	52.91	52.96	53.53	49.57	38.55	44.60	44.27	45.29	35.65	27.00	32.46	32.21
FeOtot	9.93	10.00	8.69	10.18	10.85	9.85	10.09	9.70	12.74	14.52	11.55	11.20
MnO	0.11	0.10	0.11	0.11	0.20	0.09	0.08	0.07	0.12	0.14	0.11	0.11
MgO	20.87	20.77	21.57	20.15	19.04	19.97	19.91	19.98	17.99	16.77	17.29	17.96
CaO	0.00	0.00	0.03	0.00	0.01	0.01	0.01	0.01	0.00	0.01	0.00	0.00
Na_2O	0.00	0.00	0.01	0.00	0.00	0.05	0.02	0.00	0.00	0.00	0.03	0.02
K_2O	0.00	0.01	0.02	0.01	0.04	0.01	0.02	0.00	0.00	0.02	0.01	0.02
NiO	0.37	0.32	0.30	0.32	0.12	0.26	0.25	0.25	0.24	0.19	0.16	0.16
Cr_2O_3	16.91	16.97	16.92	20.88	31.83	26.25	26.38	26.14	34.20	41.02	38.84	38.77
Total	101.25	101.31	101.33	101.33	100.85	101.32	101.29	101.62	101.20	101.05	100.57	100.56
Fe_2O_3	1.48	1.30	1.23	1.12	1.95	1.36	1.43	0.74	2.50	2.85	1.00	1.79
FeO	8.60	8.83	7.58	9.17	9.10	8.63	8.81	9.03	10.49	11.95	10.65	9.59
Si	0.002	0.002	0.002	0.001	0.002	0.001	0.002	0.001	0.001	0.004	0.002	0.001
Ti	0.002	0.002	0.002	0.001	0.003	0.004	0.004	0.003	0.005	0.028	0.001	0.002
Al	1.618	1.619	1.626	1.538	1.256	1.409	1.402	1.425	1.178	0.929	1.095	1.084
FeIII	0.030	0.030	0.020	0.020	0.040	0.030	0.030	0.010	0.050	0.060	0.020	0.040
Fe II	0.190	0.190	0.160	0.200	0.210	0.190	0.200	0.200	0.250	0.290	0.250	0.230
Mn	0.002	0.002	0.002	0.002	0.005	0.002	0.002	0.002	0.003	0.003	0.003	0.003
Mg	0.807	0.803	0.828	0.791	0.784	0.798	0.797	0.795	0.752	0.730	0.738	0.764
Ca	0.000	0.000	0.001	0.000	0.000	0.000	0.000	0.000	0.000	0.000	0.000	0.000
Na	0.000	0.000	0.000	0.000	0.000	0.003	0.001	0.000	0.000	0.000	0.002	0.001
K	0.000	0.000	0.001	0.000	0.001	0.000	0.001	0.000	0.000	0.001	0.000	0.001
Ni	0.008	0.007	0.006	0.007	0.003	0.006	0.005	0.005	0.005	0.004	0.004	0.004
Cr	0.347	0.348	0.345	0.435	0.695	0.556	0.560	0.552	0.758	0.947	0.879	0.875
SumCat	3.006	3.003	2.993	2.995	2.999	2.999	3.004	2.993	3.002	2.996	2.994	3.005
mg#	78.93	78.73	81.56	77.90	75.77	78.33	77.86	78.59	71.56	67.30	72.74	74.08
cr#	17.66	17.69	17.50	22.05	35.62	28.30	28.54	27.92	39.15	50.48	44.53	44.67
XFeII	0.19	0.19	0.16	0.20	0.21	0.19	0.20	0.20	0.25	0.28	0.25	0.23
FeII/Mg	0.235	0.237	0.193	0.253	0.268	0.238	0.251	0.252	0.332	0.397	0.339	0.301

Table A3.7: Major element content in GP glasses

Sample	**CD305**	**CD305**	**CD305**	**GP30**	**GP25**	**GP25**	**GP25**	**GP84**	**GP84**	**GP84**
phase	glass	glass	glass	glass	glass	glass	glass	glass	glass	glass
Host rock	Lh	Lh	Lh	Lh	Lh	Lh	Lh	Lh	Lh	Lh
Group	Lh 2	Lh 2	Lh 2	Lh 2	Lh 2	Lh 2	Lh 2	Lh 2	Lh 2	Lh 2
SiO_2	63.50	64.60	63.00	65.30	61.70	62.28	64.00	65.60	64.00	64.3
TiO_2	1.50	1.80	1.50	0.70	0.50	1.10	1.02	0.84	0.82	1.2
Al_2O_3	18.20	18.20	19.30	17.00	22.08	20.70	20.12	17.20	18.50	18
FeOtot	2.10	1.20	2.10	2.30	0.70	1.10	1.17	1.70	1.60	1.8
MnO	0.02	0.01	0.01	0.03	0.00	0.00	0.00	0.02	0.01	0.04
MgO	1.01	0.69	0.96	0.70	0.20	0.40	0.55	1.20	1.10	1.10
CaO	0.10	0.53	0.16	0.08	0.25	0.09	0.15	0.11	0.11	0.19
Na_2O	7.80	6.75	7.60	6.80	7.17	7.15	6.83	6.80	7.29	6.76
K_2O	6.10	6.30	5.40	7.05	7.50	7.20	7.15	6.55	6.56	6.48
Tot	100.33	100.08	100.03	99.96	100.10	100.02	100.99	100.02	99.99	99.87
TiO2 + K2O	7.60	8.10	6.90	7.75	8.00	8.30	8.17	7.39	7.38	7.68
CaO+Na2O	7.90	7.28	7.76	6.88	7.42	7.24	6.98	6.91	7.40	6.95
Na2O/K2O	0.78	0.93	0.71	1.04	1.05	1.01	1.05	0.96	0.90	0.96
Na2O+K2O	13.90	13.05	13.00	13.85	14.67	14.35	13.98	13.35	13.85	13.24
SiO_2/Al_2O_3	3.49	3.55	3.26	3.84	2.79	3.01	3.18	3.81	3.46	3.57
mg#	46.15	50.58	44.89	35.16	33.74	39.32	45.58	55.71	55.06	52.13

Table A3.7: Continued

GP28 glass Lh Lh 2	**GP28** glass Lh Lh 2	**GP28** glass Lh Lh 2	**GP81** glass Hz Hz 3	**GP81** glass Hz Hz 3	**GP81** glass Hz Hz 3	**GP78** glass Hz Hz 3	**GP78** glass Hz Hz 3	**GP23** glass Hz Hz 3	**GP23** glass Hz Hz 3	**GP23** glass Hz Hz 3
64.93	63.48	65.84	61.52	60.45	66.32	67.56	67.38	65.75	66.00	63.70
0.33	0.38	1.60	2.10	2.90	0.85	0.97	0.87	1.33	1.68	2.52
20.10	19.35	18.18	19.30	18.60	16.13	14.12	14.50	15.30	15.68	18.15
0.48	0.80	0.82	2.59	2.80	2.24	2.42	2.59	2.21	2.11	1.76
0.01	0.02	0.00	0.03	0.00	0.00	0.03	0.01	0.02	0.02	0.00
0.18	3.10	0.40	0.78	1.00	1.15	1.75	1.56	1.89	1.43	0.72
0.15	0.14	0.07	0.27	0.12	0.12	0.06	0.05	0.07	0.10	0.14
6.30	5.99	5.77	7.59	8.10	6.60	6.60	6.37	6.61	5.81	5.75
7.50	7.20	7.30	5.80	6.00	6.56	6.47	6.69	6.80	7.20	7.28
99.98	100.46	99.98	99.98	99.97	99.97	99.98	100.02	99.98	100.03	100.02
7.83	7.58	8.90	7.90	8.90	7.41	7.44	7.56	8.13	8.88	9.80
6.45	6.13	5.84	7.86	8.22	6.72	6.66	6.42	6.68	5.91	5.89
1.19	1.20	1.27	0.76	0.74	0.99	0.98	1.05	1.03	1.24	1.27
13.80	13.19	13.07	13.39	14.10	13.16	13.07	13.06	13.41	13.01	13.03
3.23	3.28	3.62	3.19	3.25	4.11	4.78	4.65	4.30	4.21	3.51
40.06	87.35	46.50	34.92	38.89	47.78	56.31	51.77	60.38	54.70	42.16

Table A3.8: Trace elements (ppm) of GP glasses

Sample	**GP25**	**GP25**	**GP25**	**GP25**	**GP25**	**GP84**	**GP84**	**GP84**	**GP84**
phase	cpx	cpx	cpx	cpx	cpx	cpx	cpx	cpx	cpx
Host rock	Lh	Lh	Lh	Lh	Lh	Lh	Lh	Lh	Lh
Group	Lh2	Lh2	Lh2	Lh2	Lh2	Lh2	Lh2	Lh2	Lh2
Cs	0.81	0.86	1.59	2.03	1.32	0.23	0.18	0.46	0.29
Rb	123.91	169.54	274.20	253.60	205.31	17.86	11.41	31.92	20.40
Ba	156.67	163.30	111.00	288.17	179.79	78.75	62.71	91.75	77.74
Th	6.42	3.05	3.85	4.61	4.48	1.28	0.97	1.55	1.27
U	0.84	0.88	1.51	1.03	1.07	0.44	0.34	0.43	0.40
K	60687.62	0.00	59359.30	0.00	30011.73	0.00	0.00	55374.34	18458.11
Nb	35.97	42.97	56.88	63.05	49.72	4.15	2.90	9.10	5.38
Ta	1.95	2.14	2.16	2.66	2.23	0.24	0.15	0.50	0.30
La	30.45	22.40	25.00	33.96	27.95	5.06	5.19	7.50	5.92
Ce	47.77	39.08	45.39	68.44	50.17	8.52	10.24	12.23	10.33
Pr	4.97	3.43	4.18	6.13	4.68	0.99	1.27	1.31	1.19
Sr	77.12	93.53	76.23	164.69	102.89	33.59	49.92	67.29	50.27
Nd	14.84	12.27	10.44	18.25	13.95	3.25	5.52	4.76	4.51
Zr	92.87	105.27	112.77	139.80	112.68	91.79	76.95	80.55	83.10
Hf	4.80	1.77	1.75	2.67	2.75	2.02	2.07	1.96	2.02
Sm	1.45	1.60	1.84	3.12	2.00	0.38	1.27	0.98	0.87
Eu	<0.080	<0.150	0.72	0.67	0.70	0.17	0.29	0.15	0.20
Ti	3238.23	5026.04	3777.22	9655.79	5424.32	656.50	1078.72	1238.36	991.19
Gd	1.48	1.00	1.70	2.52	1.68	0.50	0.66	0.75	0.64
Tb	0.49	0.33	0.17	0.39	0.34	0.07	0.16	0.12	0.12
Dy	0.89	0.93	0.32	1.09	0.81	0.38	1.08	0.78	0.75
Y	6.80	6.42	6.52	8.96	7.18	3.21	5.48	4.48	4.39
Ho	0.25	0.27	<0.00	0.28	0.27	0.11	0.25	0.15	0.17
Er	1.03	<0.44	0.34	1.38	0.92	0.24	0.44	0.50	0.39
Tm	0.19	0.07	0.17	<0.163	0.14	0.03	0.07	0.07	0.06
Yb	2.96	0.91	1.12	<0.62	1.66	0.17	0.53	0.36	0.35
Lu	0.23	0.11	0.08	<0.100	0.14	0.07	0.10	0.05	0.07

Table A3.9: Degree of melt(F) on the basis of major and trace elements

Method			F OPX	F OPX-SP	F CPX	F CPX HREE	F reliable value	mg#	cr#
GP13	Lh	protogranular	12	11	12	8	11	90.57	23.87
GP9	Lh	protogranular		15		10	13	91.00	34.11
CD305	Lh	protogranular		12	18		15	92.00	25.76
GP25	Lh	protogranular		12		10	11	91.42	18.59
GP30	Lh	protogranular		13	15	9	12	92.52	32.62
GP84	Lh	protogranular		12		15	14	91.57	28.84
GP28	Lh	protogranular		14	16	10	13	92.23	30.00
GP81	Hz	protogranular		17	19	17	18	92.04	44.82
GP23	Hz	protogranular		19		19	19	92.26	44.60
GP78	Hz	protogranular				23	23	92.13	83.33

mg# = [100 * Mg/(Mg+ FeTot)]; cr# =[100*Cr/Cr+Al)]

Chapter 4. Handler Ridge Mantle xenoliths

4.1 Introduction

Mantle xenoliths from Handler Ridge (HR, Fig. 4.1), locality of the Northern Victoria Land, occur in scoria cones aligned along Cenozoic dikes. The study of the new occurrence of HR (Fig. 4.1) xenolith population provide an opportunity to extend the petrological characterization over a large portion of the West Antarctic Rift System (WARS) from Mt. Melbourne (74_21'S 164_42'E) to Handler Ridge (72_31'S 167_18'E), about 400 km from each other. Moreover, the characterization of this area provides interesting analogies and differences with the Mt. Melbourne district, in term of melt extraction, enrichment processes and thermo-barometric constrains, in term of space and time.

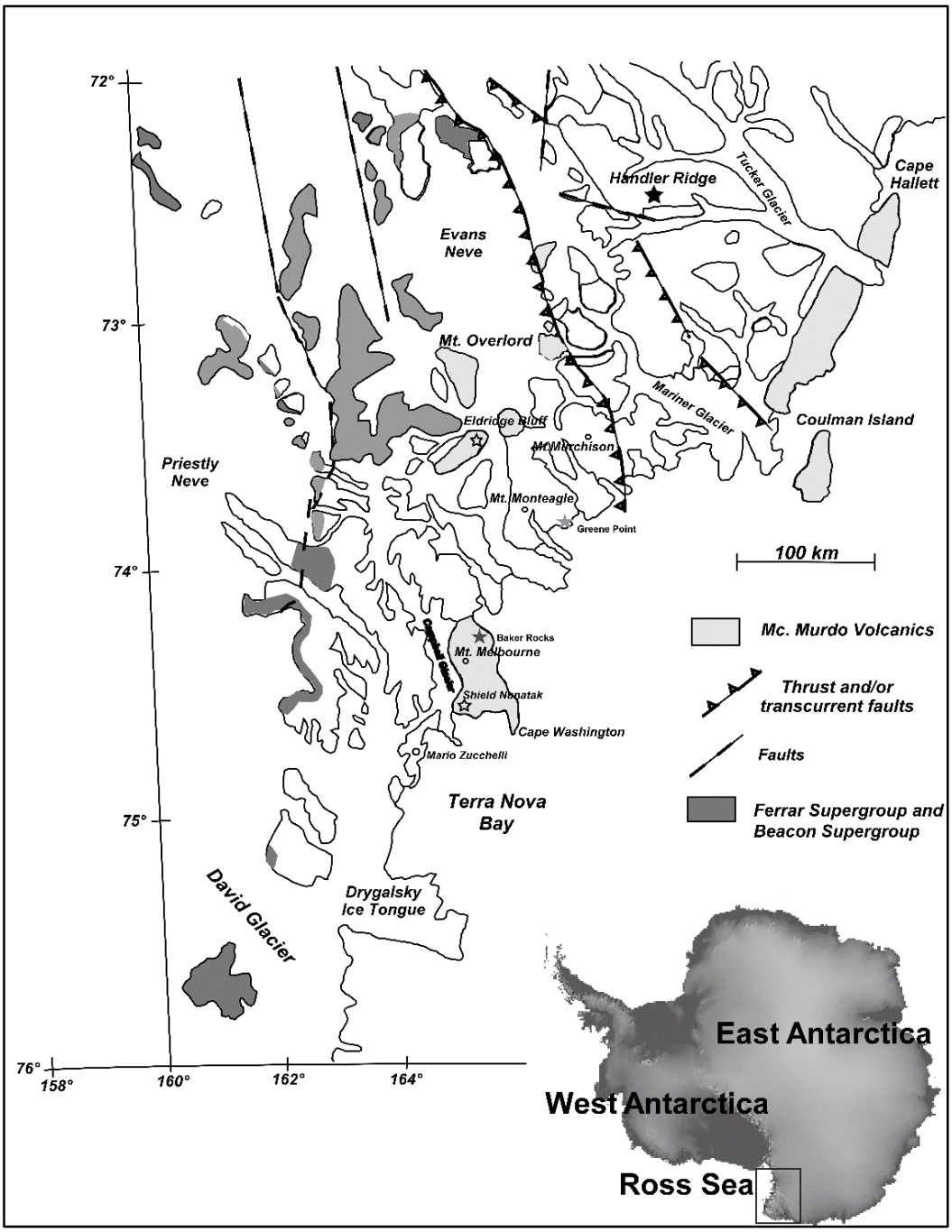

Fig. 4.1 Map of the Northern Victoria Land with the localization of Handler Ridge outcrop.

4.2 Petrography

Most of HR xenoliths were classified as anhydrous spinel-Lherzolite (Lh), although few wehrlites (Wh) and one harzburgite (Hz) also occur (Fig. 4.2). Modal composition was estimated by point counting and averaging two runs with more than 2,000 points for each thin section (Table 4.1). Lh contain olivine (ol, 47-72 vol.%), orthopyroxene (opx, 8-32 vol.%), clinopyroxene (cpx, 8-20 vol.%) and spinel (sp, 2-5 vol.%); Wh contain ol (68-80 vol%), cpx

(15-30 vol.%), and sp (2 % vol.%), while Hz contains ol (66 vol.%), opx (25 vol.%), cpx (5 vol.%) and sp (2 % vol.%).

Modal percentage was also confirmed by those derivate from a new methodological approach based on X ray diffraction analysis (Gentili et al., 2015).

Following Mercier and Nicolas (1975), textures vary from protogranular to coarse and fine equigranular types. The first is observed only in Lh samples; it is characterized by large grain of ol and opx, while cpx is always smaller and often associated to sp, the latter occurring as both large lobated (Fig. 4.2f) and small elongated grains (Fig. 4.2a). Opx can be present as exolution lamellae in cpx (i.e. HR9), or as large grain and can reach dimension up to 5 mm (i.e. in HR5, Fig. 4.2c).

In HR6 harzburgite is evident a crystal orientation mainly due to opx and sp grains. Equigranular texture, is observed in both Lh and Wh, becoming clearly mosaic type in Wh.

A few lherzolites (i.e HR4, HR2, HR10 Figs. 2b, e, f) and all wehrlites (Figs. 2g and h) show textural evidences of periodotite-melt interaction such as spongy rim of primary cpx core, newly formed small secondary cpx (cpx2) and glass; the latter present both as veinlets and patches, sometimes contain microcrystalline of K-Feldpsar and Plagioclase.

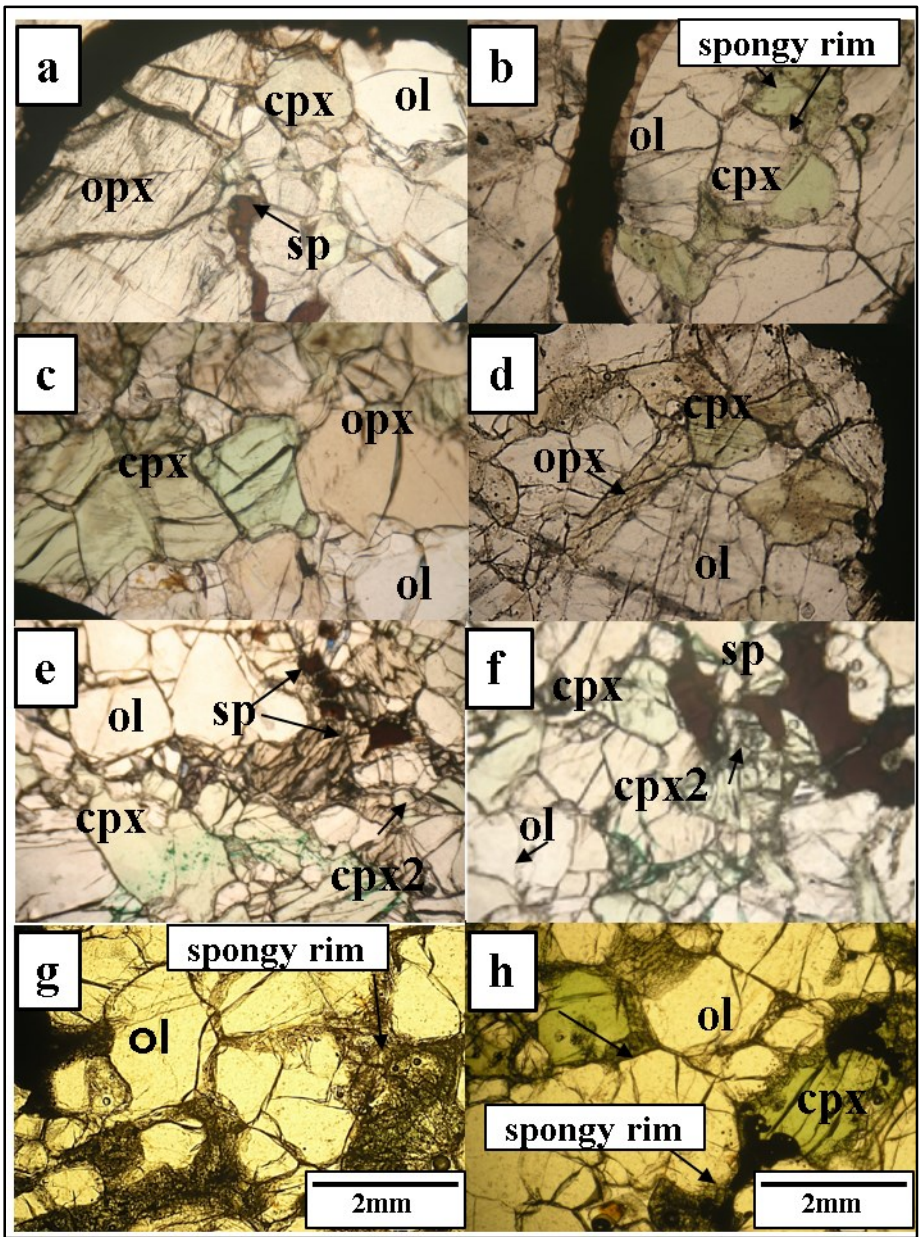

Fig. 4.2 Photomicrographs of representative microstructures in HR xenoliths. Protogranular lherzolites including large olivine and smaller clinopyroxene (a and b); harzburgites with large grains of orthopyroxene, olivine and small grains of clinopyroxene (c and d); lherzolite characterised by a equigranular texture with olivine and clinopyroxene similar in size and elongated spinel; lobated sp surrounding cpx and secondary cpx (cpx2) (e, f); g) and h) wehrlites with mosaic equigranular texture, characterized by the presence of spongy rim in clinopyroxene and triple junction in olivine.

Table 1. Textural features, Modes, T, fO2 estimates of HR mantle xenoliths

Sample	lithology	group	ol	opx	cpx	sp	glass	ol/opx	opx/ol	opx/cpx	T (°C)*	1σ	T (°C) ~	1σ	T (°C) ¨	1σ	Δ log fO_2
HR1	Lh	A	67	21	10	2		3.19	0.31	2.6	1037	40	1011	45	1057	44	0.08
HR2	Lh	B	72	17	8	3	trace	4.24	0.24	1.1	1016	21	1056	42	1136	82	0.17
HR3	Lh	A	55	24	16	4		2.29	0.44	3.0	1027	10	867	34			-0.05
HR4	Lh	A	60	20	8	5	trace	3.00	0.33	1.1	1029	18	977	57	1154-1188	100	-0.07
HR5	Lh	A	47	32	18	2		1.47	0.68	5.3	979	37	792	16			-0.26
HR6	Hz	A	66	25	6	2	trace	2.64	0.38	2.1	1026	22	1091	17			0.39
HR9	Lh	A	64	18	12	3		3.56	0.28	1.2	1028	3	857	40			-0.08
HR10A	Lh	B	70	10	15	2	trace	7.00	0.14	0.5	962	29	984	10			0.31
HR10	Lh	B	70	8	20	2		8.75	0.11	0.5	1012	18	971	35			0.33
HR7	Wh	C	68	0	30	2	trace	-	0.00	-	857	32					-0.22
HR11	Wh	C	80	0	15	2	trace	-	0.00	-	875	33					-0.18

ol is for olivine, opx for orthopyroxene, cpx for orthopyroxene and sp spinel. Lh for Lherzolite, Hz for Harzburgite, Wh for Wehrlite

T (°C)*: T from O'Neil and Wall (1987), modified by Ballhaus et al., 1991

T (°C)~: T from Brey and Kôhler

T (°C) ¨: T from Liang et al., 2013

Δ log fO_2 is calculated using T from O'Neil and Wall (1987), modified by Ballhaus et al., 1991

4.3 Mineral Chemistry

4.3.1 Major Elements

On the basis of phase major element contents, three different groups were identified: Group A (Lh HR 3, HR1, HR4, HR5, HR9 and Hz HR6), Group B (Lh HR2, HR10A and HR10B), Group C (Wh HR7 and HR11).

Olivine

On the whole, ol in Lh and Hz present mg# values varying between 87.54 and 90.98 (Fig. 4.3a, Table A4.1), with group B showing the most fertile character (mg# ranging from 87.54 to 88.63). As expected, ol of Group C (Wehrlites) present the lowest mg# values (84.60-86.12, Fig. 4.3a). In the entire suite NiO content is 0.38 wt.% on average (Fig. 4.3a), matching the typical mantle value, but Wh are characterized by a quite large variation (0.20-0.40 wt.%). CaO is below 0.13 wt.% for both Group A and B, while in Group C is slightly higher (~0.15 wt.%). Secondary ol (ol2) are rare and often associated to spongy rim; they do not show relevant differences in mg# if compared with primary ol, but even though they tend to have slightly lower Ni and higher CaO.

Orthopyroxene

Opx seems to be texturally well equilibrated, although geochemically it shows large compositional variation. As no opx has been found in the wherlitic samples HR7 and HR11, it is not possible to identify the three different groups in term of mg# vs. Al_2O_3 for the opx (Fig. 4.3b). Lh groups (A and B) are clearly distinct, reflecting equilibrium condition between ol and opx phases, which show an overall mg# and Al_2O_3 ranging from 88.14 to 90.94 and 2.89 to 4.98wt.% respectively (Table A4.2), with the more fertile group (Group B) characterized by low mg# values (Fig. 4.3b).

CaO (0.3 -1.23 wt.%) and Na_2O (0.01- 0.16 wt.%) content show a slightly negative correlation with mg# values for the more fertile group (Group B), but no correlation is evident for the other samples (not showed in figures).

Clinopyroxene

Cpx is Cr-rich augites (Morimoto, 1989) in composition (Table A4.3).

Primary cpx from Lh (Group A and B) show an almost constant values of Al_2O_3 (~5.62-6.52 wt.%, Table A4.3), while Hz HR6 (Group A) presents lower Al_2O_3 contents (up to 4.33 wt.%, Table A4.3). In sample HR2 some cpx have mg# values (~87.20) coherent with group B, but other (~ 90.50) match the group A (Fig. 4.3c). The large intramineral variation in Al_2O_3 contents observed in cpx from wehrlites and from Group B (Fig. 4.3c) is mainly due to the presence of spongy rim.

In the entire suite, secondary cpx (cpx2) and spongy rims of cpx1 are characterized by TiO_2 contents always $\geq$ 0.65 wt.% (Fig. 4.4a)

Overall Na_2O contents vary between 0.36 and 1.40 wt.%, with the tendency of spongy rim and cpx2 to have constant values (~0.5 wt.%): it is worth noting that, three texturally equilibrated samples show an anomalous enrichment (up to 1.60 wt.%) at high mg# (90.81-92.15), (Fig. 4.4b).

Spinel

Sp is Mg-Al rich in composition. Overall mg# values range between 53.88 and 77.33, and cr# [=Cr/(Cr+Al) *100 mol] from 9.65 to 33.58 (Table A4.4), with the usual negative correlation between the two parameters (Fig. 4.3d), suggesting partial melting as the main evolution process.

Glass

Glass, found in four samples (HR2, HR4, HR10A), is present as veinlets and patches with different size.

HR glasses are SiO_2 (55.50-62.80 wt.%) oversaturated, with TiO_2 contents between 0.33 and 1.90 wt% and Na_2O/K_2O comprised between 0.80 and 15 (Table A4.5).

4.3.2 Trace Elements

Orthopyroxene

Chondrite-normalized opx trace element patterns are characterized by strong positive Ti and negative Sr anomalies and depleted LREE pattern (La_N: 0.0069-1) with respect to HREE (Lu_N: 1.23-4). In HR2 an anomalous enrichment in HREE (Lu_N ~ 4) is observed, while HR4 shows LREE systematic enrichment in (La_N ~1 and Ce_N ~0.63) with respect to the other samples (Fig. 4.5).

Clinopyroxene

Cpx show variable enrichment in incompatible elements, they are depleted in LILE with respect to LREE. Irrespective to lithology they show slight to marked Zr, Sr and Ti negative (Fig. 4.6a and 7a) and positive Nd and Sm anomalies.

Considering the REE profiles, it is possible to highlight some differences between the studied samples (Fig.6b and 7b):

HR1 is characterized by an enrichment of LREE with respect to MREE (that are slightly fractionated) and HREE, in particular from Tb to Lu the pattern is almost flat (Tb/Lu ~1).

In HR2 most of the cpx present a convex upward pattern enriched in Ce, Pr and Nd and values of HREE close to10 times chondrite (Lu_N˜10.23).

HR4 cpx tend to be LREE depleted (La_N = 1.16) with respect to HREE (Lu_N = 11.18); LREE-enriched (La_N: 4.14) cpx is probably attributable to secondary cpx (cpx2).

The two wehrlites (Fig. 4.6b) have a cpx displaying a convex-upward chondrite-normalized REE pattern, with HR11 showing patent profiles; these patterns recall those of cpx crystallised from alkali basalt.

Glass

Trace element in glasses were performed for few samples only (Lh HR2, HR4 and Wh HR11), due to the critically small size. On the whole, they present patterns variably enriched in LILE with respect to LREE, with Rb and Ba positive anomalies (not showed in figures).

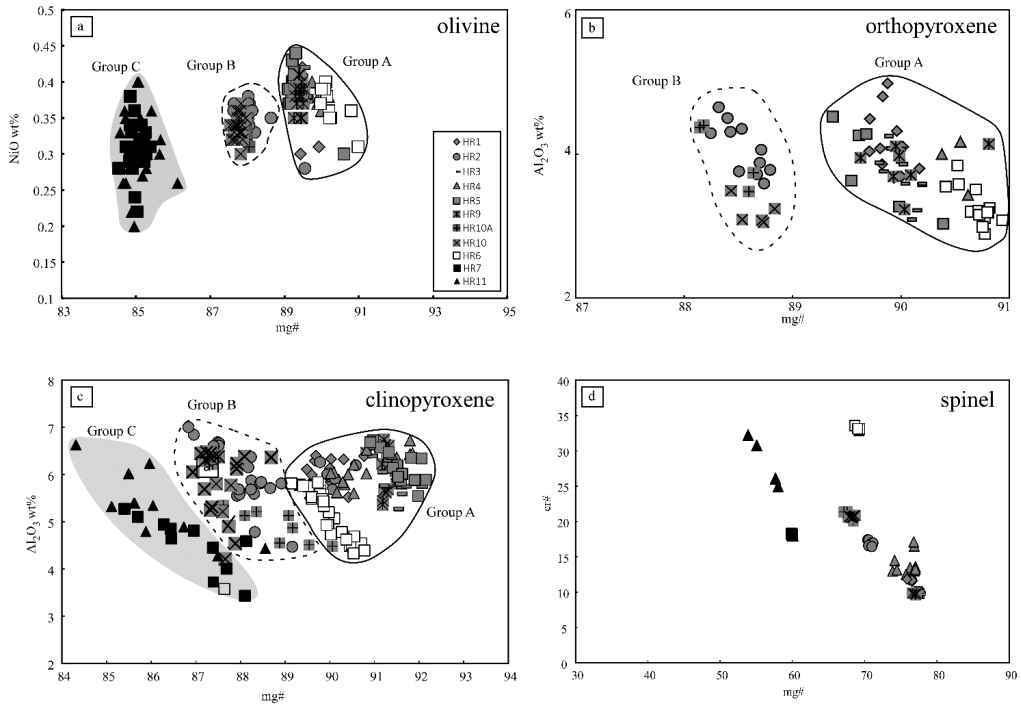

Fig. 4.3 (a) Mineral chemistry composition of olivines (NiO vs. mg#, a), orthopyroxenes (Al_2O_3 vs. mg# b) clinopyroxene (Al_2O_3 vs. mg#, c) and spinel (cr# vs. mg#, d) of HR Group A, b, and c mantle xenoliths. mg# and cr# are calculated as [(Mg/Mg+Fe_{tot}) at. %] and [Cr//(Cr+Al) at. %] Grey symbols are for lherzolites, white for harzburgites and black for wehrlites respectively.

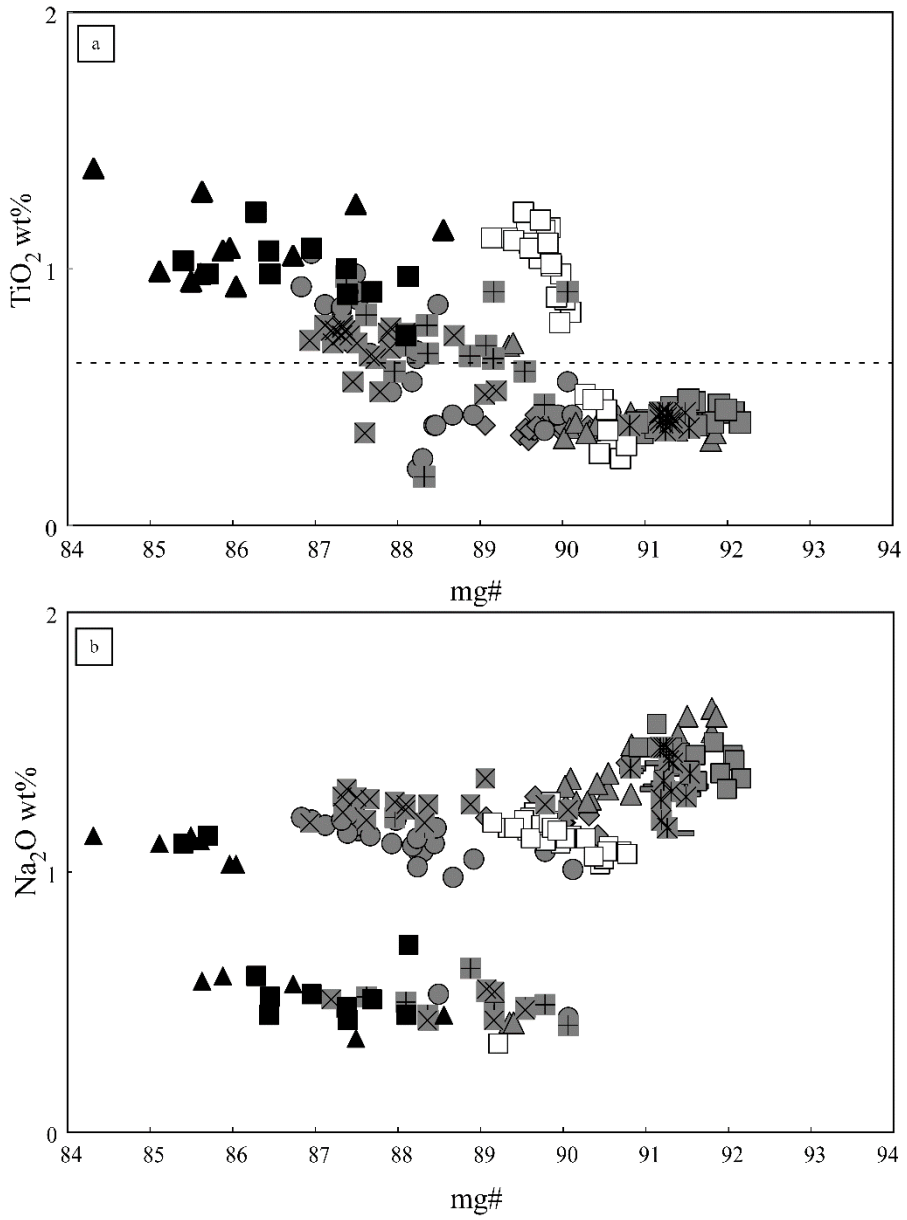

Fig. 4.4 TiO_2 (a) and Na_2O (b) vs. mg# of clinopyroxene of HR mantle xenoliths. The dotted line in (a) outlines primary/secondary HR clinopyroxenes. Symbols as in Fig. 4.3,

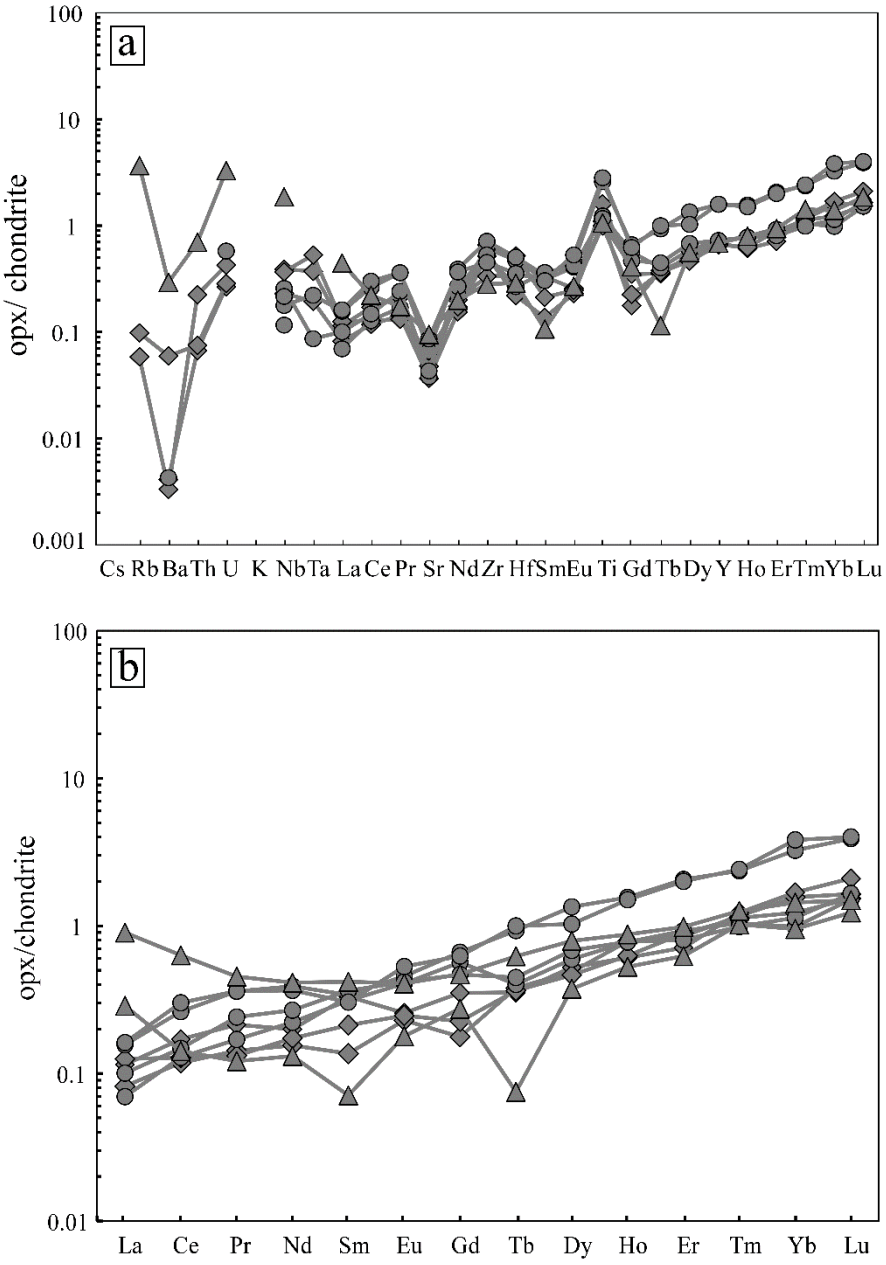

Fig. 4.5 Chondrite-normalised trace element a) and rare earth element (REE), b) patterns of HR orthopyroxenes. Symbols as in Fig. 4.3 (referring only to samples Lh HR1, HR2, HR4).

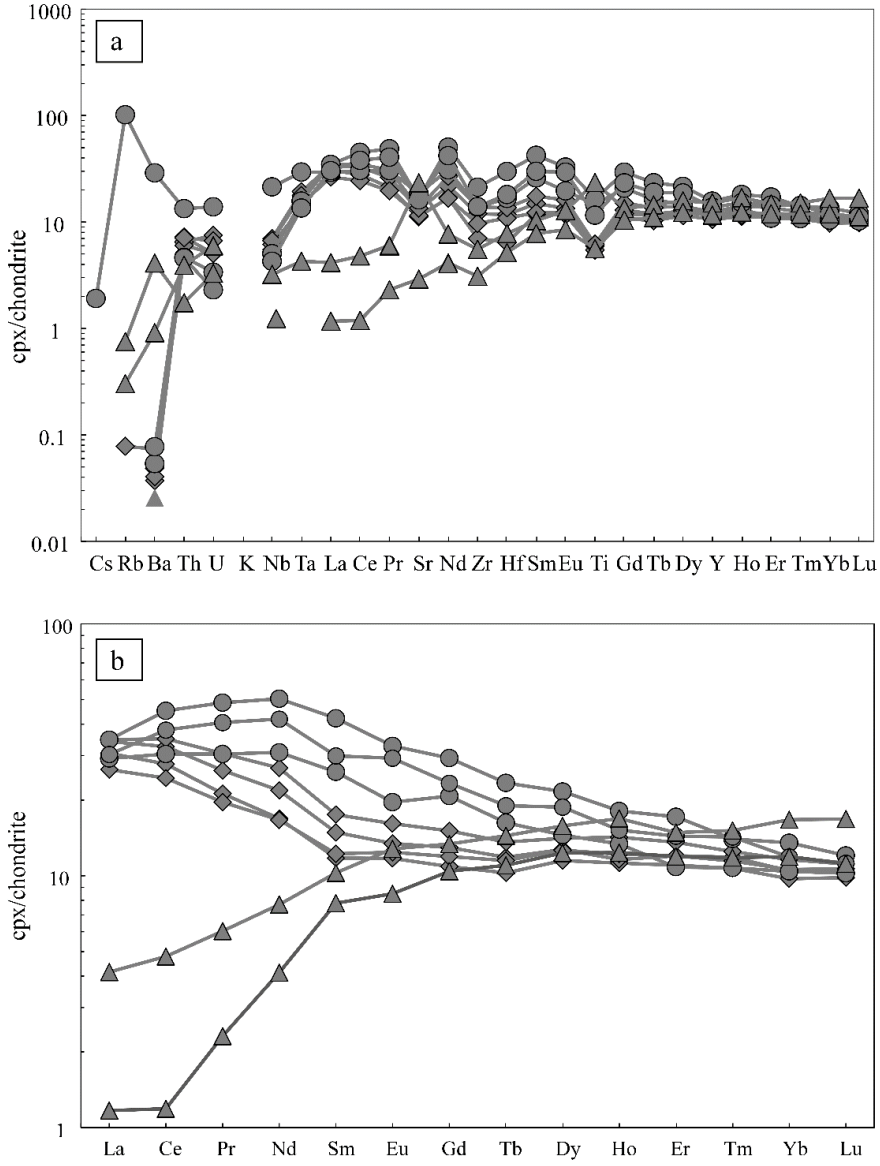

Fig. 4.6 Chondrite-normalised trace element a) and rare earth element (REE), b) patterns of HR clinopyroxene in lherzolites. Symbols as in Fig. 4.3, (referring only to samples Lh HR1, HR2, HR4).

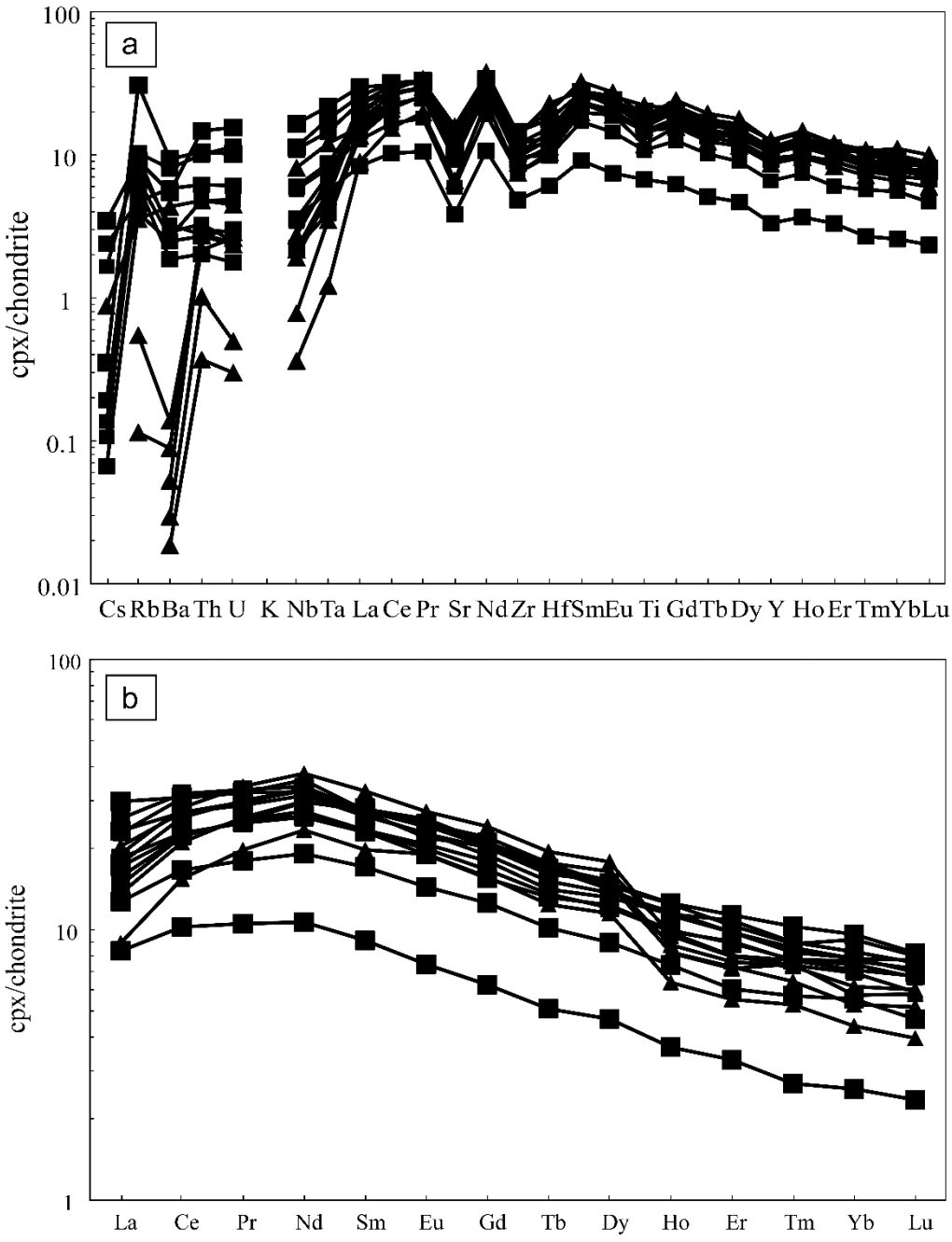

Fig. 4.7 Chondrite-normalised trace element a) and rare earth element (REE), b) patterns of HR clinopyroxene in wehrlites. Symbols as in Fig. 4.3, (referring only to samples Wh HR7, HR11).

4.4 Isotopic Data

Sr and Nd isotopic ratio were determined for clinopyroxene separates for four samples (Wh HR7 and HR11 and Lh HR1 and HR12) and data are reported in Table A4.9. The measurements isotopic data ratios fall within the following ranges 0.702895-0.703027 for $^{87}Sr/^{86}Sr$ ratios and 0.512927- 0.513159 for $^{143}Nd/^{144}Nd$. No remarkable differences are detected among the different lithology. In the Sr-Nd space, HR1, HR7 and HR12 clinopyroxenes plot between the depleted mantle (DMM, Workman and Hart, 2004) and the high-μ (HIMU) reservoirs, while HR11 ($^{143}Nd/^{144}Nd$: 0.512927, and $^{87}Sr/^{86}Sr$: 0.703027) falls in the HIMU field, presenting a clearly less Nd radiogenic character with respect to the other (Fig. 4.8).

Isotopic results were compared with data from hydrous and anhydrous xenoliths from Northern Victoria Land (Perinelli et al., 2011, Melchiorre et al., 2011; Pelorosso et al., 2016) and with those from alkaline lavas in which samples are hosted (Nardini et al., 2009) (Fig. 4.8).

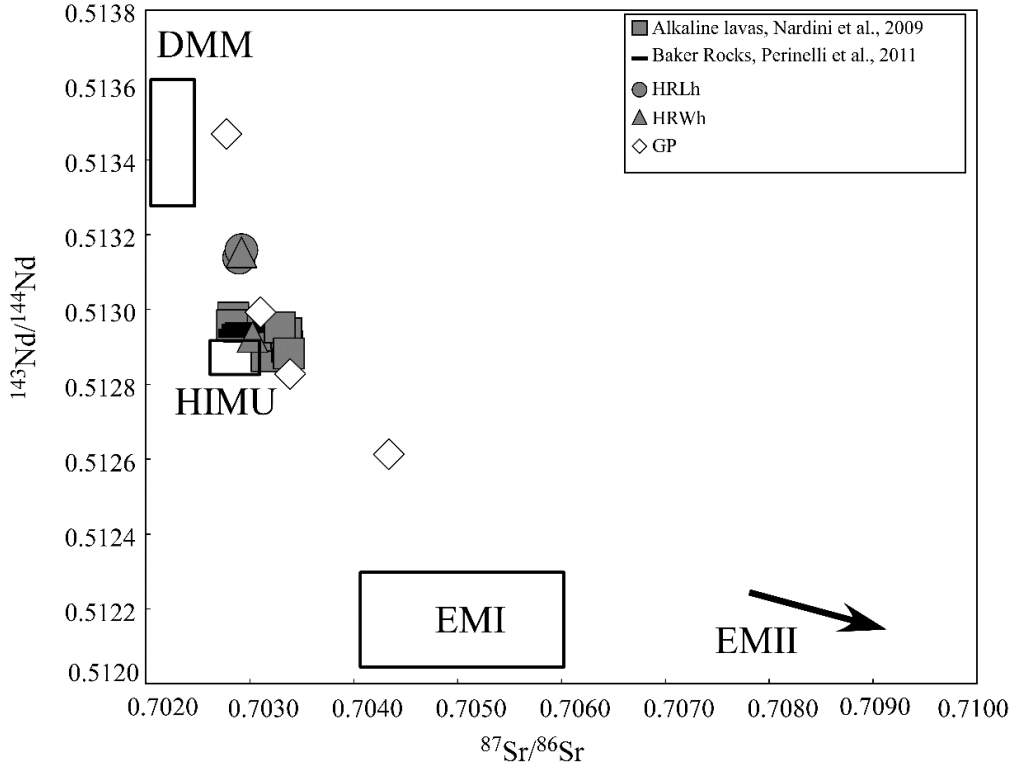

Fig. 4.8 $^{143}Nd/^{144}Nd$ vs $^{87}Sr/^{86}Sr$ plot for HR Ridge clinopyroxenes, DMM is from Workman and Hart (2004); EMI, EMII and HIMU are from Zindler and Hart (1986). Samples from other NVL xenolith bearing localities (Greene Point, Pelorosso et al., 2016; Baker Rocks, Perinelli et al, 2011) and from NVL lavas (Nardini et al, 2009) are reported.

4.5 Mineral Equilibrium Condition, Temperature and Oxygen Fugacity Estimates

In order to evaluate the chemical equilibrium among the various phases, Fe/Mg molar ratios of ol, opx and cpx from peridotites are calculated and plotted in Fig. 4.9 a, b, and c.

In all samples ol and opx reveal a general equilibrium lying close to the theoretical curves (calculated between 900 and 1100 °C) (Fig. 4.9a). With respect to $Fe/Mg^{sp/ol}$, sp appears also in equilibrium with ol with the majority of samples clustering to the 1100 °C curve (Fig. 4.9b). On the other hand, cpx-opx Fe/Mg distribution points out a low (~800-900°C) mantle temperature for some Lh (HR3, HR5, HR9).

As stated above, temperatures were calculated at a pressure arbitrarily assumed as 15 Kbar, using the Fe/Mg distribution in ol-sp (O'Neill and Wall, 1987, as modified by Ballhaus et al., 1991) and opx-cpx (Brey and Kohler, 1990). Moreover, the REE equilibria (Liang et al., 2013) was also applied for three lherzolites (Table 4.1).

Temperatures obtained with both ol-sp and opx-cpx equilibria vary between ~ 960 and 1090 °C in Lh and Hz, while they are close to 850 °C in Wh (Table 4.1) with the expected exception of three Lh samples evidencing opx/cpx disequilibrium (Fig 9c, Table 4.1).

Temperatures calculated on the basis of Kd opx/cpx REE thermometer (Liang et al., 2013) are in the range of 1050 and 1200 °C. Only Lh HR1 records T values in agreement with the other methods (Table 4.1); Lh HR2 and Lh HR4 present systematically higher REE temperatures.

Temperatures values (obtained by Ballhaus et al., 1991) were used for oxygen fugacity calculations according to Ballhaus et al. (1991) equation, based on the ol-opx-sp assemblage, HR samples yield $\Delta \log fO_2$ (QFM) ranging from -0.26 to +0.4 (Fig. 4.10).

Comparing these results with the average values from Northern (Perinelli et al., 2012; Bonadiman et al., 2014; Pelorosso et al., 2016) and Southern (Martin et al., 2015) Victoria Land, HR peridotites show the highest temperatures and oxidizing conditions (Fig.10)

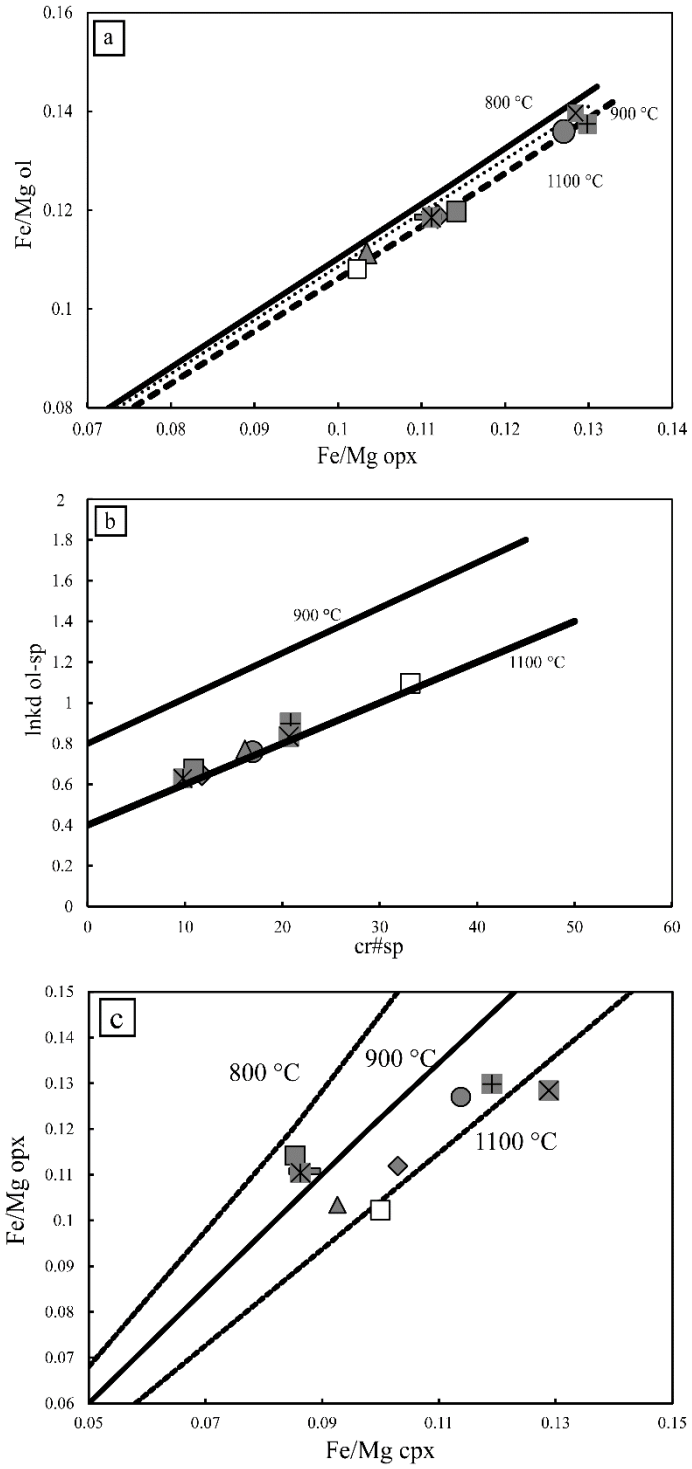

Fig. 4.9 Fe/Mg equilibrium diagrams for olivine *vs.* orthopyroxene (a), olivine *vs.* spinel (b) and orthopyroxene vs clinopyroxene (c). In (a) the equilibrium lines are from Brey and Köhler (1990) at 800, 900 and 1100 °C. In (b) Kd Spinel-Olivine is Fe-Mg partitioning between olivine and spinel determined on the basis of the Liermann and Ganguly (2003) model.

(Fe/Mg) indicates Fe^{2+}/Mg, as calculated by stoichiometry for each mineral. Symbols as in Fig. 4.3

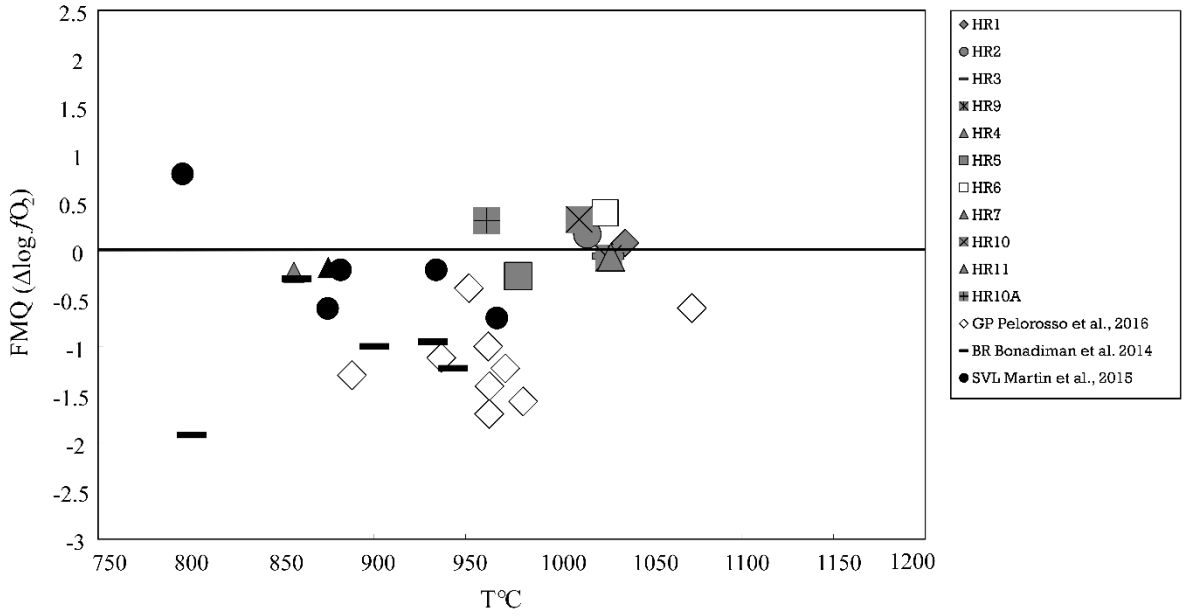

Fig. 4.10 Temperature and ($\Delta\log fO_2$) QFM = fO_2 relative to the buffer reaction QFM calculated with the formula of Ballhaus et al. (1991). P is fixed at 15 Kbar. Data from Greene Point (NVL, Pelorosso et al., 2016); Baker Rock (NVL, Bonadiman et al., 2014) and from Southern Victoria Land (Martin et al., 2015) are also reported.

4.6 Melting Models

As it is known, during partial melting processes the most fusible elements (i.e. Al, Ti) and Ca progressively decrease in minerals while mg# increases. Melting models, based on major elements mineral chemistry, have been applied in order to estimate the role of partial melting process.

The melting degrees (F) in spinel stability field, were determined from the Primitive Mantle (PM) modal and geochemical composition (McDonough and Sun 1995), using a mass-balance calculation between the four peridotite phases (ol, cpx, opx and sp) and the progressive melting residua derived from the experimental results of Herzberg (2004) (see also Bonadiman and Coltorti 2011; Upton et al. 2011; Faccini et al., 2013).

Considering in opx Al_2O_3 vs. MgO plot (Fig. 4.11a), HR samples are roughly distributed along the theoretical melting curve, indicating a degree of partial melting between 7 and 18%; this result is also replicated in the cpx Al_2O_3 vs MgO theoretical curve (Fig 11b), except for

some samples evidencing opx/cpx disequilibrium (HR3, 5, 9, Fig. 4.9c); these latter record anomalously low F values (≤5%) with respect to the opx melt curve (F ≥ 7 %).

This latter result is in discordance with the first model suggesting that melting process is not the solely process that influence the Al- Mg distribution between opx and cpx (Pelorosso et al., 2016; Matusiak-Malek et al, 2014).

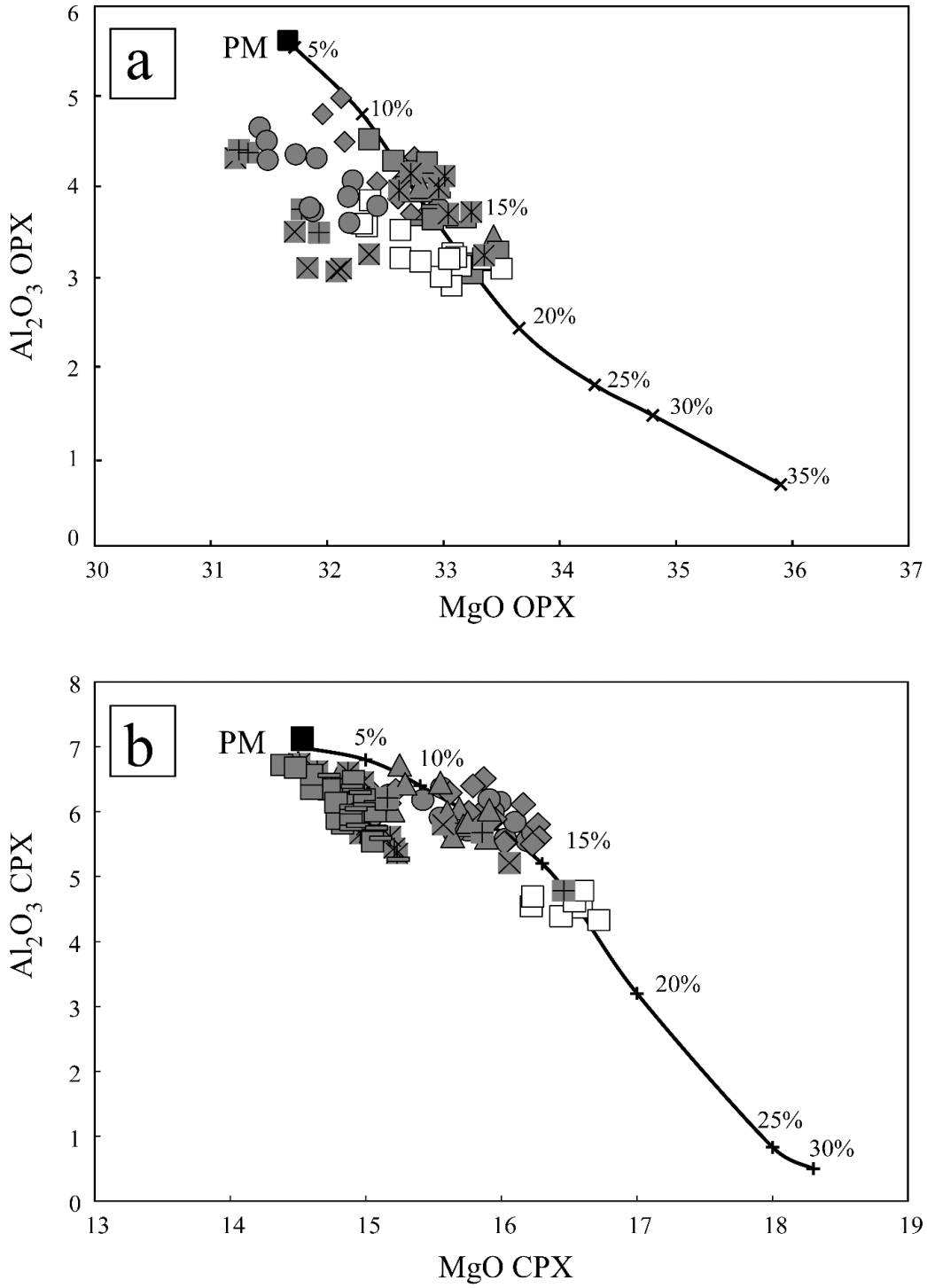

Fig. 4.11 Plot of Al_2O_3 *vs.* MgO melting trends (Upton et. Al, 2011) for orthopyroxene (a), and clinopyroxene (b) of HR xenoliths. The Al_2O_3 and MgO contents of PM were calculated on the basis of the primitive mantle composition of McDonough and Sun (1995). Model parameters as in Bonadiman *et al*. (2005) and Faccini *et al*. (2013). Thick marks on curves

indicate partial melting percentages (F), numbers in brackets are ideal clinopyroxene modal contents at F. Symbols as in Fig. 4.3

4.7 Nature of Metasomatism agent

The most efficient metasomatizing agents able to modify mantle portions are represented by silicate and carbonatite melts, containing variable amount of volatiles (i.e. Schneider and Eggler, 1986; O'Reilly and Griffin, 1988; Ionov, 1998; Coltorti et al. 1999; Grégoire et al. 2000; Beccaluva et al. 2001; Pfänder et al., 2012; Ackerman et al., 2013). To understand the nature and the extent as well the efficiency of the percolating melts through HR peridotitic matrix, we applied a least squares mass balance (MB) method (Wright and Doherty, 1970). MB calculation is widely used in petrology to obtain modal proportions in igneous and metamorphic rocks, using chemical composition of whole rock and mineral major element compositions (Laube et al., 1996; Marthy, 1973; Paktunc, 1998; Gentili et al., 2015). The results are originated by trial and error procedures that, with repeated attempts minimizes the differences between the measured and calculated whole rock.

The textural characteristics of HR samples (Fig. 4.2) reveal the coexistence of primary and secondary phases including glass; this allows to evaluate the chemical exchange between primary and metasomatized phases due to the interaction with percolating melt/s.

The major elements composition of the melt was obtained resolving the following equation:

$$x1ol1 + x2opx1 + x3cpx1 + x4sp + x5melt = x6ol2 + x7cpx2 + x8sp2 + x9glass$$

Where x_i is the molar fraction; *ol1*, *opx1*, *cpx1*, *sp1* and *melt* (unknown) are considered as reactants and *ol2*, cpx2, sp2 and *glass* are the products (see also Coltorti et al., 1999).

The most suitable sample to test this model is Lh HR 4, where primary and secondary phases plus glass evidence that metasomatic process is ongoing. The equation coefficients, the primary and secondary phases used in the model are summarised in Table 4.2. The difference between primary and secondary xi reflects the effective modal content of the secondary assemblage.

The petrological interpretation of these results lies in the fact that, as expected, ol almost does not take part to the process whereas the most participative phases are cpx and, to a lesser extent, sp.

This means that the metasomatic reaction enriched the system in newly formed cpx (cpx2) together with small amount of sp and glass, as observed in thin sections (Fig. 4.2).

Subsequently, these results were independently verified considering the trace element distribution among opx, cpx and glass (Table 4.3 and Fig. 4.12).

The resulting metasomatic melt is Na_2O-rich (3-4 wt.%), SiO_2 undersaturated (Table 4.2) close in composition to primary lavas from HR district (McMurdo Volcanic Group, Kyle 1986). In term of trace element contents, as expected, that melt is enriched with respect to glass and lavas (Fig. 4.12), with HREE content close to 100 times chondrites (i.e. $Lu_N = 107$) and remarkable positive Nb, Ta and Ti anomalies, reflecting a pure intraplate geochemical features.

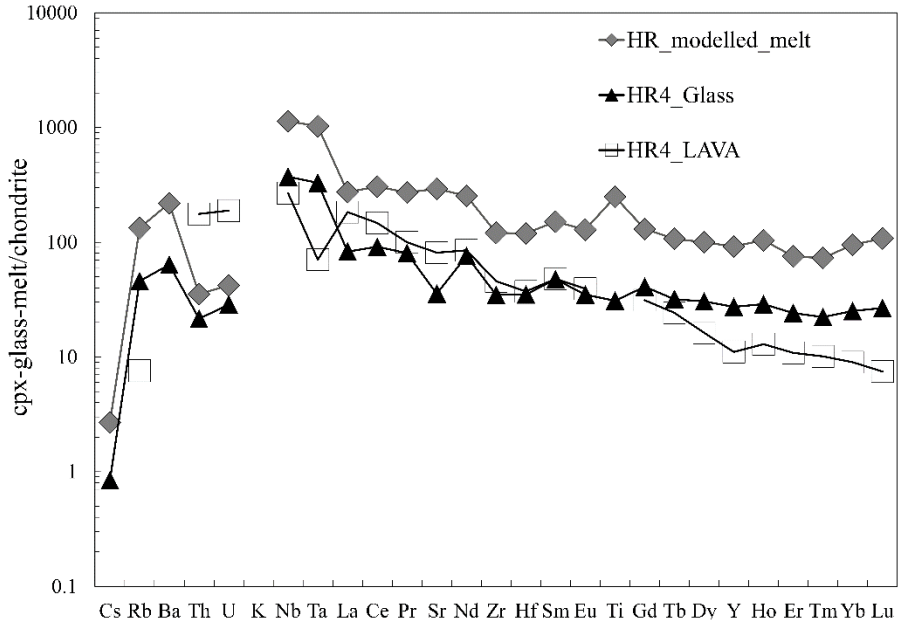

Fig. 4.12 Chondrite-normalized trace element pattern for calculated melt, obtained using bilmass coefficients, for comparison also HR lava and glass were reported.

Table 2. Major element of primary and secondary paragenesis used for bilmass calculation

Phases	*ol1*	*opx1*	*cpx1*	*sp1*	*melt*	*glass*	*cpx2*	*ol2*	*sp2*
SiO_2	41.01	55.37	52.04	0.07	44.15	55.00	52.01	41.30	0.12
TiO_2	0.00	0.09	0.38	0.25	3.65	0.32	0.71	0.01	0.69
Al_2O_3	0.03	4.19	6.12	53.68	12.67	24.74	3.74	0.04	49.23
FeO	9.83	6.06	2.71	8.38	12.73	1.26	3.36	9.51	9.98
MgO	49.03	33.04	15.87	21.75	11.14	2.55	16.87	49.01	20.31
CaO	0.08	0.69	20.54	0.04	11.19	11.20	21.88	0.12	0.11
Na_2O	0.00	0.11	1.38	0.00	2.85	4.58	0.42	0.00	0.00
K_2O	0.00	0.02	0.00	0.00	1.18	0.20	0.00	0.00	0.00
Cr_2O_3	0.02	0.42	0.96	15.83	0.45	0.14	1.01	0.01	19.57
xi	0.21	0.19	0.94	0.17	0.09	0.23	0.67	0.02	0.12

ol is for olivine, opx for orthopyroxene, cpx for orthopyroxene
and sp spinel. ol1, opx1, cpx1, sp1 and melt are reacts, glass, cpx, ol2 and sp are products
xi is bilmass coefficents

Table 3. Trace element composition (ppm) used for BM calculation

	opx1	opx1*xi	cpx	cpx1*xi	glass	glass*xi	cpx2	cpx2*xi	calculated melt
Cs	0.02	0.00	0.00	0.00	0.16	0.04	0.01	0.01	0.50
Rb	1.28	0.23	0.11	0.10	16.01	3.84	0.26	0.20	46.42
Ba	0.71	0.13	2.20	1.98	153.59	36.86	9.93	7.45	527.54
Th	0.02	0.00	0.11	0.10	0.62	0.15	0.05	0.04	1.02
U	0.03	0.00	0.05	0.04	0.23	0.05	0.03	0.02	0.34
K		0.00		0.00		0.00		0.00	0.00
Nb	0.46	0.08	0.22	0.20	91.44	21.95	0.79	0.59	278.25
Ta	0.00	0.00	0.00	0.00	4.60	1.10	0.06	0.05	14.35
La	0.11	0.02	0.28	0.25	19.61	4.71	0.98	0.74	64.69
Ce	0.14	0.02	0.73	0.65	55.88	13.41	2.93	2.20	186.62
Pr	0.02	0.00	0.22	0.20	7.63	1.83	0.57	0.43	25.76
Sr	0.69	0.12	21.10	18.99	258.02	61.92	169.26	126.95	2121.95
Nd	0.09	0.02	1.93	1.73	35.49	8.52	3.59	2.69	118.25
Zr	1.09	0.20	11.98	10.78	134.28	32.23	21.40	16.05	466.23
Hf	0.03	0.01	0.55	0.50	3.73	0.90	0.83	0.62	12.70
Sm	0.02	0.00	1.19	1.07	7.27	1.74	1.57	1.18	23.10
Eu	0.02	0.00	0.49	0.44	2.02	0.49	0.74	0.56	7.46
Ti	471.01	84.78	2503.17	2252.85	13734.83	3296.36	10481.43	7861.07	110247.47
Gd	0.08	0.02	2.14	1.93	8.42	2.02	2.75	2.06	26.75
Tb	0.00	0.00	0.41	0.37	1.19	0.29	0.54	0.41	4.00
Dy	0.14	0.03	3.13	2.82	7.76	1.86	4.01	3.01	25.34
Y	1.07	0.19	18.21	16.39	43.00	10.32	23.71	17.78	144.01
Ho	0.04	0.01	0.70	0.63	1.63	0.39	0.96	0.72	5.88
Er	0.16	0.03	1.98	1.78	3.99	0.96	2.46	1.85	12.45
Tm	0.04	0.01	0.30	0.27	0.57	0.14	0.39	0.29	1.85
Yb	0.24	0.04	2.03	1.82	4.28	1.03	2.84	2.13	16.13
Lu	0.05	0.01	0.28	0.26	0.68	0.16	0.43	0.32	2.73

ol is for olivine, opx for orthopyroxene, cpx for orthopyroxene and sp spinel.
ol1, opx1, cpx1, sp1 and melt are reacts, glass, cpx, ol2 and sp are products
xi is bilmass coefficents

4.7.1 Metasomatic Melt in Time and Space

The incompatible element zoning in mineral mantles makes possible to evaluate the efficiency of the mantle metasomatic processes in timing the elemental mobility (Sneeringer et al., 1984; Van Orman et al., 2001; Cherniak, 2003; Tirone et al., 2005).

The "inward diffusion" model of Griffin et al. (1996, derived by the application of the Crank's equation (1975), was here applied

$(C\text{-}C1)/(C0\text{-}C1) = erf\ [X/2(tD)^{1/2})]$

The most depleted cpx is assumed as "unmetasomatized" cpx (C_0), while using the enriched cpx coefficient of REE (Van Orman, 2001) we calculated the hypothetical time occurred to reach the C composition (Fig. 4.13). The model has been applied for Yb, considering that, among the REE, it has the lowest diffusion coefficient (cpx: $D_{Yb} \sim 7x10^{-20}$; Van Orman, 2001).

Lh HR4 shows textural and chemical disequilibrium among the phases, preserving both melting and enrichment features. In this regard the HR4 cpx core is assumed as C_0 at t = 0 (Fig.13). Its enriched rim (C) is acquired at 1mm from the core. The C composition (Yb) is reached in a time span of ~50 years.

In turn, HR1 has geochemical evidences of enrichment event only, that even if does not increase the modal cpx, it completely obscures the residual character of the phases. Lh HR1 minerals result well equilibrated for both major and trace elements at T~ 1040 ° C (Table 4.1). Therefore, this sample may be considered as the final result of the continuous interaction between the metasomatic melt and the HR peridotite. Considering an average grain size of 1.5 mm (Figs. 2 and 13), ~ 200 years are required to completely modify the geochemical characteristics of the original mantle parageneses (Fig. 4.13)

This becomes evident in the "inversion diagram" of Liang e al. (2013), where REE cation ratio is plotted as function of the opx/cpx partition coefficient (Fig. 4.14). Notwithstanding the enriched cpx the HR1 opx/cpx pairs perfectly match the predicted REE equilibrium. On the other hand, both HR4 residual and enriched cpx show strong discrepancy between measured and theoretical REE partition coefficients (Fig. 4.14).

4.7.2 Isotopic Evidences of Percolation of Melts

Evidences for metasomatic melts circulating within the Victoria Land SCLM have been widely documented, also using isotopic modelling (Melchiorre et al. 2011; Pelorosso et al.,

2016). A linear mixing model between DMM end member and an asthenospheric component (Ferrar CFB ~ 5 %) accounts for the isotopic features of some portion of the Northern Victoria Land (Pelorosso et al., 2016). HR isotopic data are in agreement with the average values from the HIMU-like signature of hydrous and anhydrous NVL mantle xenoliths and alkaline lavas from McMurdo Volcanic Group (Nardini et al., 2009; Perinelli et al., 2006; 2008; 2011; Fig. 4.8), testifying for the solely imprinting of the alkaline metasomatic melt.

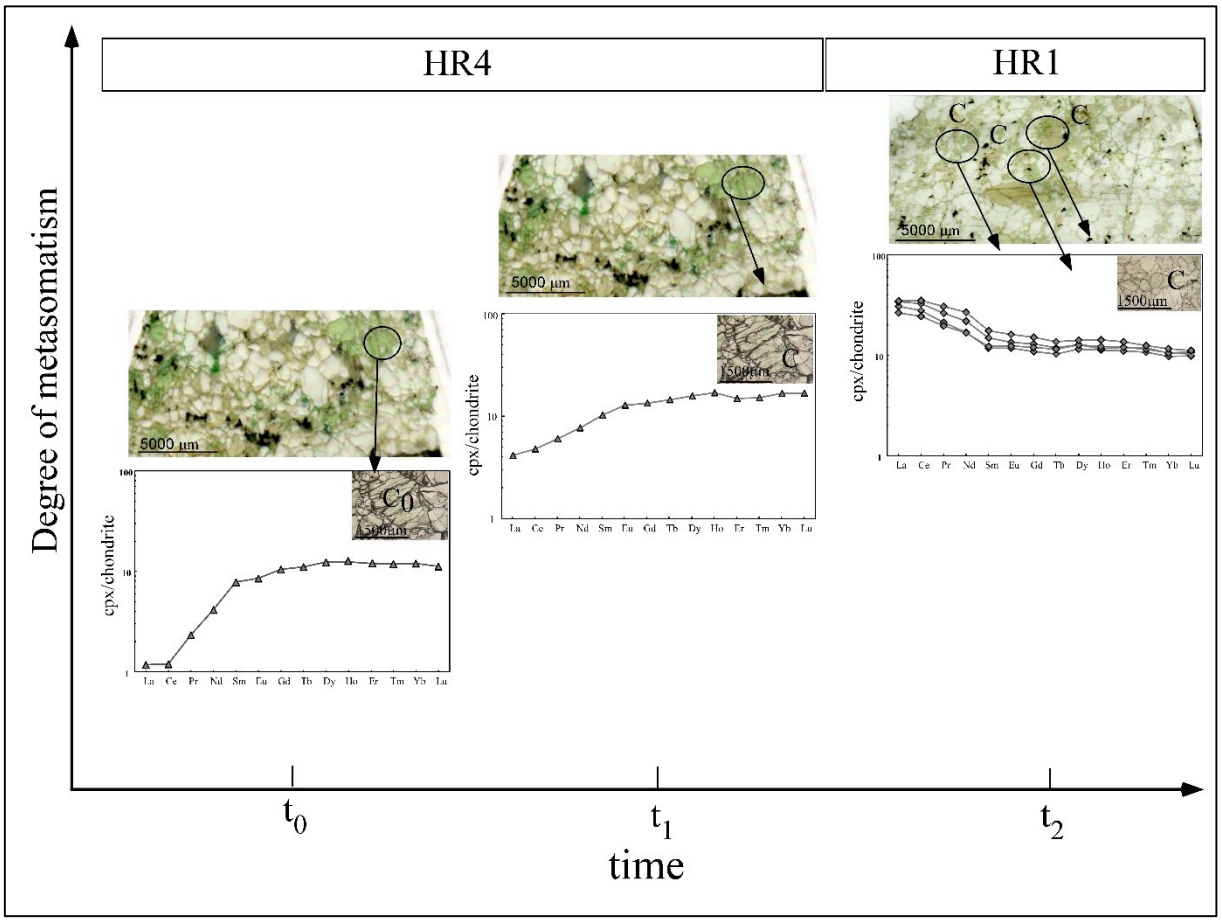

Fig. 4.13 Sketch of the possible temporal evolution of the chemical composition induced by metasomatism at Handler Ridge.

Chondrite-normalized REE composition of HR4 and HR1 are taken as reference, the time is calculated using the semi-infinite media plane equation of Crank (1975) : $(C\text{-}C1)/(C0\text{-}C1) = erf\ [X/2(tD)^{1/2})]$, where C1 is the concentration of the diffusive material, C0 is the concentration of the initially depleted composition (recorded only in HR4), x is the linear

distance of the diffusion front from the crystal border, D is the diffusion coefficient (Van Orman, et al., 2001), C is the most enriched cpx composition recorded in HR4 and HR1.
The calculated time (t1) necessary to achieve the HR4 enriched composition is evaluated to be in the order of years (~50 years); the t_2, time calculated to get the HR1 enriched composition is in the range of 200 years.

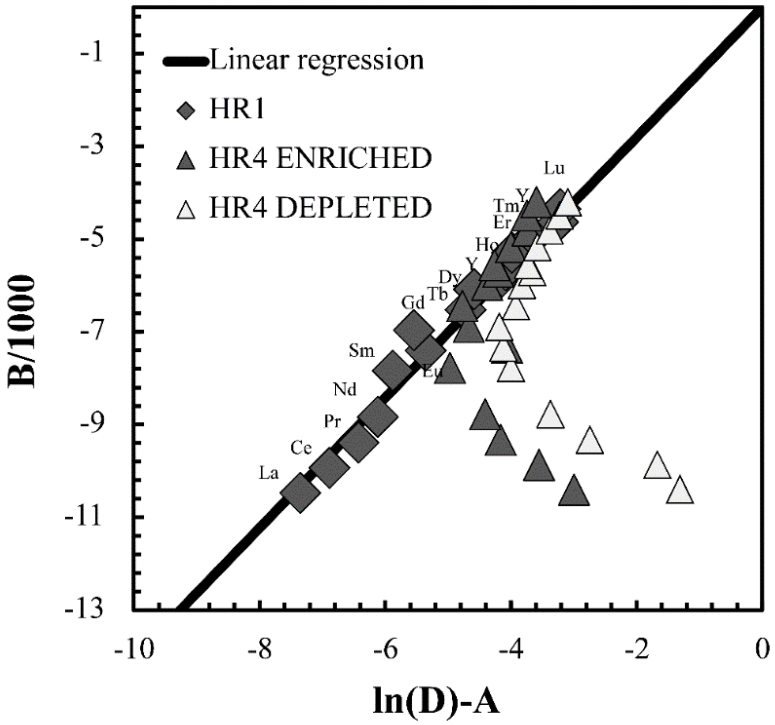

Fig. 4.14 Application of REE-in-two-pyroxene thermometer (Liang et al., 2014) to samples HR1, HR4 and comparison between measured and predicted REE partition coefficients between opx and cpx in the same sample. Symbols as in Fig. 4.3

4.8 Conclusion

Mantle xenoliths from the newly found area of Handle Ridge, allowed to identify and characterize another portion of the Antarctic sub continental lithosphere mantle that presents interesting affinities and some differences with other well-known areas in Northern Victoria Land:

1. The HR portion sub continental lithosphere mantle records the highest temperatures (>1000 °C) and fugacity conditions (Δlog close to QFM or higher) of the entire region.

2. HR peridotite represent a residuum after ~7 to 18% of partial melting in the spinel stability field, which was variably modified by interaction with lithospheric alkaline melt that was able to strongly change the chemical composition of the mantle, but not the modal proportion of the mineral phases.
3. The complete hiding of the primary (residual) peridotite by metasomatic feeding is extremely fast; it occurs in a time-span of 200 years only, taking into account a size of the crystal of 1500 μm, confirming that this process is strictly related to the magma rising event.
4. Handler Ridge alkaline metasomatism can be related to the Cenozoic magmatism as indicated by the similarity between the inferred metasomatizing melt and the lavas that brought up the xenoliths during the WARS opening.

Appendix A4

Table A4.1 Major element content of HR olivines

Sample	HR1	HR1	HR1	HR2	HR2	HR2	HR3	HR3	HR3	HR4	HR4	HR4	HR5	HR5	HR5
phase	ol	ol	ol	ol	ol	ol	ol	ol	ol	ol	ol	ol	ol	ol	ol
rim/core	rim	rim	core	core	rim	core	rim	core	core	rim	core	core	core	core	rim
Host rock	Lh	Lh	Lh	Lh	Lh	Lh	Lh	Lh	Lh	Lh	Lh	Lh	Lh	Lh	Lh
Group	A	A	A	B	B	B	A	A	A	A	A	A	A	A	A
SiO_2	40.60	40.65	40.77	40.52	40.39	40.64	40.52	40.74	40.42	40.75	40.98	41.15	40.55	40.96	40.80
TiO_2	0.03	0.00	0.00	0.00	0.02	0.03	0.00	0.01	0.01	0.01	0.00	0.01	0.00	0.02	0.01
Al_2O_3	0.03	0.03	0.04	0.03	0.03	0.03	0.02	0.02	0.02	0.03	0.03	0.04	0.00	0.05	0.01
FeO	10.27	10.17	10.08	11.45	11.80	10.05	10.33	10.06	10.13	9.64	9.88	9.47	10.24	8.99	10.41
MnO	0.14	0.16	0.14	0.20	0.21	0.19	0.17	0.13	0.14	0.16	0.15	0.15	0.16	0.16	0.15
MgO	48.08	48.04	48.26	47.32	46.92	48.33	48.10	48.17	47.92	48.58	48.48	48.83	47.97	48.63	47.86
CaO	0.11	0.09	0.10	0.11	0.10	0.23	0.07	0.07	0.07	0.08	0.09	0.12	0.04	0.24	0.04
Na_2O	0.00	0.00	0.00	0.00	0.00	0.00	0.00	0.00	0.00	0.00	0.00	0.00	0.00	0.00	0.00
K_2O	0.00	0.00	0.00	0.00	0.00	0.00	0.00	0.00	0.00	0.00	0.00	0.00	0.00	0.00	0.00
Cr_2O_3	0.02	0.03	0.04	0.01	0.02	0.10	0.01	0.00	0.00	0.03	0.00	0.01	0.00	0.05	0.00
NiO	0.40	0.37	0.39	0.34	0.36	0.28	0.38	0.38	0.39	0.38	0.40	0.38	0.44	0.30	0.37
P_2O_5	0.01	0.01	0.00	0.02	0.00	0.00	0.02	0.02	0.00	0.01	0.00	0.00	0.00	0.00	0.00
Tot	99.69	99.55	99.82	100.00	99.85	99.88	99.62	99.60	99.10	99.67	100.01	100.16	99.40	99.40	99.65
Si	1.002	1.004	1.003	1.002	1.002	1.000	1.001	1.005	1.003	1.003	1.005	1.006	1.003	1.007	1.007
Ti	0.001	0.000	0.000	0.000	0.000	0.001	0.000	0.000	0.000	0.000	0.000	0.000	0.000	0.000	0.000
Al	0.001	0.001	0.001	0.001	0.001	0.001	0.001	0.001	0.001	0.001	0.001	0.001	0.000	0.001	0.000
Fe	0.212	0.210	0.207	0.237	0.245	0.207	0.213	0.207	0.210	0.198	0.203	0.194	0.212	0.185	0.215
Mn	0.003	0.003	0.003	0.004	0.004	0.004	0.004	0.003	0.003	0.003	0.003	0.003	0.003	0.003	0.003
Mg	1.768	1.768	1.770	1.744	1.735	1.772	1.771	1.770	1.771	1.781	1.772	1.779	1.769	1.782	1.760
Ca	0.003	0.002	0.003	0.003	0.003	0.006	0.002	0.002	0.002	0.002	0.002	0.003	0.001	0.006	0.001
Na	0.000	0.000	0.000	0.000	0.000	0.000	0.000	0.000	0.000	0.000	0.000	0.000	0.000	0.000	0.000
K	0.000	0.000	0.000	0.000	0.000	0.000	0.000	0.000	0.000	0.000	0.000	0.000	0.000	0.000	0.000
Cr	0.000	0.001	0.001	0.000	0.000	0.002	0.000	0.000	0.000	0.001	0.000	0.000	0.000	0.001	0.000
Ni	0.008	0.007	0.008	0.007	0.007	0.006	0.008	0.008	0.008	0.008	0.008	0.007	0.009	0.006	0.007
summ cat	2.997	2.996	2.996	2.998	2.997	2.998	2.999	2.995	2.997	2.997	2.995	2.994	2.997	2.992	2.993
mg#	89.30	89.38	89.51	88.05	87.63	89.55	89.25	89.51	89.40	89.98	89.74	90.19	89.30	90.60	89.12

Lh for Lherzolite, Hz for Harzburgite, Wh for Wehrlite

mg# = [(Mg/Mg+Fetot at. %]

Table A4.1 Continued

Sample	HR6	HR6	HR6	HR9	HR9	HR9	HR10A	HR10A	HR10A	HR10
phase	ol	ol	ol	ol	ol	ol	ol	ol	ol	ol
rim/core	core	core	core	core	rim	core	core	core	core	core
Host rock	Hz	Hz	Hz	Lh	Lh	Lh	Lh	Lh	Lh	Lh
Group	A	A	A	A	A	A	B	B	B	B
SiO_2	41.37	40.93	40.74	40.69	40.57	40.59	40.51	40.37	40.20	40.75
TiO_2	0.02	0.03	0.01	0.00	0.01	0.00	0.03	0.00	0.02	0.01
Al_2O_3	0.02	0.01	0.04	0.02	0.02	0.01	0.05	0.02	0.03	0.03
FeO	8.75	9.33	9.59	10.34	10.20	10.07	11.45	11.47	11.44	11.53
MnO	0.14	0.14	0.15	0.15	0.14	0.15	0.20	0.17	0.19	0.19
MgO	49.55	48.39	48.26	48.20	48.26	48.32	46.80	46.85	47.28	47.22
CaO	0.22	0.11	0.12	0.07	0.05	0.05	0.17	0.10	0.10	0.14
Na_2O	0.00	0.00	0.00	0.00	0.00	0.00	0.00	0.00	0.00	0.00
K_2O	0.00	0.00	0.00	0.00	0.00	0.00	0.00	0.00	0.00	0.00
Cr_2O_3	0.18	0.03	0.03	0.00	0.01	0.03	0.05	0.01	0.05	0.08
NiO	0.31	0.35	0.37	0.35	0.38	0.39	0.34	0.35	0.31	0.35
P_2O_5	0.00	0.00	0.02	0.00	0.00	0.00	0.00	0.00	0.00	0.09
Tot	100.56	99.32	99.33	99.82	99.64	99.61	99.60	99.34	99.62	100.39
Si	1.004	1.008	1.005	1.002	1.001	1.001	1.006	1.005	0.998	1.005
Ti	0.000	0.001	0.000	0.000	0.000	0.000	0.001	0.000	0.000	0.000
Al	0.001	0.000	0.001	0.001	0.001	0.000	0.001	0.001	0.001	0.001
Fe	0.178	0.192	0.198	0.213	0.210	0.208	0.238	0.239	0.238	0.238
Mn	0.003	0.003	0.003	0.003	0.003	0.003	0.004	0.004	0.004	0.004
Mg	1.793	1.776	1.775	1.770	1.775	1.776	1.731	1.738	1.750	1.735
Ca	0.006	0.003	0.003	0.002	0.001	0.001	0.005	0.003	0.003	0.004
Na	0.000	0.000	0.000	0.000	0.000	0.000	0.000	0.000	0.000	0.000
K	0.000	0.000	0.000	0.000	0.000	0.000	0.000	0.000	0.000	0.000
Cr	0.003	0.001	0.001	0.000	0.000	0.001	0.001	0.000	0.001	0.002
Ni	0.006	0.007	0.007	0.007	0.008	0.008	0.007	0.007	0.006	0.007
summ cat	2.994	2.991	2.994	2.998	2.999	2.999	2.993	2.995	3.001	2.994
mg#	90.98	90.24	89.97	89.26	89.40	89.53	87.93	87.92	88.05	87.95

Table A4.1 Continued

Sample	HR10	HR10	HR7	HR7	HR7	HR11	HR11	HR11
phase	ol	ol	ol	ol	ol	ol	ol	ol
rim/core	core	core	core	rim	rim	core	rim	rim
Host rock	Lh	Lh	We	We	We	We	We	We
Group	B	B	C	C	C	C	C	C
SiO_2	40.24	40.39	40.94	40.72	40.23	39.69	40.25	40.61
TiO_2	0.00	0.02	0.04	0.01	0.04	0.05	0.03	0.04
Al_2O_3	0.04	0.05	0.06	0.03	0.07	0.03	0.06	0.02
FeO	11.83	11.59	14.11	13.69	13.94	13.58	14.16	14.07
MnO	0.19	0.20	0.21	0.21	0.30	0.17	0.19	0.27
MgO	46.64	46.64	44.34	44.89	44.40	44.63	43.64	43.79
CaO	0.12	0.10	0.12	0.16	0.15	0.18	0.13	0.14
Na_2O	0.00	0.00	0.00	0.00	0.06	0.07	0.00	0.00
K_2O	0.00	0.00	0.01	0.00	0.05	0.02	0.01	0.03
Cr_2O_3	0.04	0.01	0.06	0.05	0.01	0.05	0.00	0.05
NiO	0.34	0.34	0.34	0.31	0.29	0.36	0.28	0.26
P_2O_5	0.07	0.00	0.00	0.00	0.00	0.00	0.00	0.00
Tot	99.51	99.34	100.23	100.07	99.54	98.83	98.75	99.28
Si	1.003	1.006	1.020	1.015	1.011	1.004	1.019	1.022
Ti	0.000	0.000	0.001	0.000	0.001	0.001	0.001	0.001
Al	0.001	0.001	0.002	0.001	0.002	0.001	0.002	0.001
Fe	0.246	0.241	0.294	0.285	0.293	0.287	0.300	0.296
Mn	0.004	0.004	0.004	0.004	0.006	0.004	0.004	0.006
Mg	1.732	1.731	1.646	1.667	1.663	1.683	1.646	1.642
Ca	0.003	0.003	0.003	0.004	0.004	0.005	0.004	0.004
Na	0.000	0.000	0.000	0.000	0.003	0.003	0.000	0.000
K	0.000	0.000	0.000	0.000	0.002	0.001	0.000	0.001
Cr	0.001	0.000	0.001	0.001	0.000	0.001	0.000	0.001
Ni	0.007	0.007	0.007	0.006	0.006	0.007	0.006	0.005
summ cat	2.997	2.994	2.978	2.984	2.990	2.997	2.980	2.978
mg#	87.54	87.76	84.85	85.39	85.02	85.42	84.60	84.72

T*able A4.2 Major element content (wt%) of HR orthopyroxenes*

Sample	HR1	HR1	HR1	HR2	HR2	HR2	HR3	HR3	HR3	HR4	HR4	HR4	HR5
phase	1	1	1	1	1	1	1	1	2	1	inter	1	1
rim/core	rim	core	core	core	rim	rim	rim	core	core	rim	rim	core	rim
Host rock	Lh	Lh	Lh	Lh	Lh	Lh	Lh	Lh	Lh	Lh	Lh	Lh	Lh
Group	A	A	A	B	B	B	A	A	A	A	A	A	A
SiO_2	55.38	55.18	54.52	54.79	54.59	54.34	55.37	55.26	55.44	55.05	56.02	55.32	54.79
TiO_2	0.06	0.08	0.12	0.10	0.21	0.27	0.09	0.12	0.07	0.09	0.09	0.08	0.12
Al_2O_3	4.04	3.80	4.98	3.78	4.35	4.29	3.88	3.90	3.59	4.17	3.43	4.00	4.52
Fe_2O_3	0.00	0.06	0.12	0.16	0.15	0.15	0.00	0.00	0.00	0.09	0.02	0.16	0.00
FeO	6.63	6.35	6.34	7.15	7.19	7.34	6.68	6.55	6.38	6.03	6.15	6.08	6.86
MnO	0.14	0.15	0.15	0.17	0.19	0.17	0.16	0.14	0.15	0.14	0.15	0.15	0.15
MgO	32.43	32.96	32.12	32.43	31.73	31.49	32.87	32.93	32.79	32.85	33.43	32.80	32.36
CaO	1.02	0.49	1.01	0.50	0.96	1.12	0.34	0.41	0.86	0.69	0.58	0.91	0.52
Na_2O	0.08	0.07	0.13	0.06	0.14	0.11	0.08	0.04	0.04	0.11	0.11	0.16	0.05
K_2O	0.01	0.01	0.00	0.00	0.02	0.02	0.01	0.00	0.00	0.02	0.00	0.02	0.02
Cr_2O_3	0.32	0.29	0.40	0.29	0.43	0.43	0.32	0.29	0.21	0.42	0.24	0.35	0.32
Tot	100.11	99.45	99.89	99.43	99.96	99.74	99.80	99.64	99.53	99.66	100.22	100.04	99.71
Fetot	6.63	6.40	6.45	7.29	7.32	7.47	6.68	6.55	6.38	6.11	6.17	6.22	6.86
Si	1.915	1.915	1.888	1.910	1.897	1.895	1.918	1.916	1.925	1.908	1.928	1.909	1.902
Ti	0.002	0.002	0.003	0.003	0.005	0.007	0.002	0.003	0.002	0.002	0.002	0.002	0.003
Al	0.165	0.155	0.203	0.155	0.178	0.176	0.158	0.159	0.147	0.170	0.139	0.163	0.185
Fe III	0.000	0.002	0.003	0.004	0.004	0.004	0.000	0.000	0.000	0.002	0.001	0.004	0.000
Fe II	0.192	0.184	0.184	0.208	0.209	0.214	0.194	0.190	0.185	0.174	0.177	0.176	0.199
Mn	0.004	0.004	0.004	0.005	0.006	0.005	0.005	0.004	0.004	0.004	0.004	0.004	0.004
Mg	1.671	1.705	1.657	1.684	1.643	1.636	1.696	1.702	1.696	1.695	1.714	1.687	1.674
Ca	0.038	0.018	0.037	0.019	0.036	0.042	0.013	0.015	0.032	0.026	0.021	0.034	0.019
Na	0.005	0.005	0.009	0.004	0.009	0.007	0.005	0.003	0.003	0.007	0.007	0.011	0.003
K	0.000	0.000	0.000	0.000	0.001	0.001	0.000	0.000	0.000	0.001	0.000	0.001	0.001
Cr	0.009	0.008	0.011	0.008	0.012	0.012	0.009	0.008	0.006	0.011	0.007	0.010	0.009
Al iv	0.085	0.085	0.112	0.090	0.103	0.105	0.082	0.084	0.075	0.094	0.073	0.091	0.098
Al vi	0.079	0.074	0.097	0.073	0.082	0.079	0.075	0.074	0.070	0.081	0.068	0.080	0.087
Alvi r	0.079	0.071	0.091	0.065	0.075	0.071	0.076	0.075	0.071	0.076	0.066	0.072	0.087
Mg M1	0.817	0.828	0.803	0.819	0.802	0.801	0.820	0.822	0.830	0.823	0.838	0.826	0.805
Mg M2	0.855	0.878	0.855	0.865	0.842	0.836	0.877	0.879	0.866	0.873	0.876	0.862	0.870
Fe2+ M1	0.094	0.090	0.089	0.101	0.102	0.105	0.094	0.092	0.091	0.085	0.086	0.086	0.096
Fe2+ M2	0.098	0.095	0.095	0.107	0.107	0.109	0.100	0.099	0.095	0.090	0.090	0.090	0.103
SumCa	4	4	4	4	4	4	4	4	4	4	4	4	4
mg#	89.71	90.17	89.88	88.79	88.53	88.25	89.76	89.96	90.16	90.55	90.62	90.38	89.37

Lh for Lherzolite, Hz for Harzburgite, Wh for Wehrlite

mg# =[(Mg/Mg+Fetot) at. %]

Table A4.2 Continued

Sample	HR5	HR5	HR6	HR6	HR6	HR9	HR9	HR10A	HR10A	GR10A	HR10	HR10	HR107
phase	1	1	2	1	1	1	1	2	1	2	1	1	1
rim/core	rim	core	core	core	core	core	rim	core	core	rim	core	core	rim
Host rock	Lh	Lh	Hz	Hz	Hz	Lh	Lh	Lh	Lh	Lh	Lh	Lh	Lh
Group	A	A	A	A	A								
SiO_2	54.95	55.85	55.09	55.71	55.71	54.96	55.31	54.21	54.82	54.33	55.18	55.43	54.38
TiO_2	0.08	0.08	0.35	0.11	0.09	0.10	0.07	0.19	0.12	0.20	0.11	0.01	0.18
Al_2O_3	4.28	3.03	3.84	3.21	3.08	3.95	3.69	4.37	3.74	4.40	3.09	3.08	4.31
Fe_2O_3	0.00	0.00	0.00	0.00	0.10	0.12	0.07	0.13	0.13	0.06	0.05	0.00	0.00
FeO	6.68	6.30	6.04	6.04	5.86	6.62	6.53	7.39	7.14	7.41	7.30	7.28	7.41
MnO	0.16	0.14	0.14	0.14	0.15	0.17	0.15	0.16	0.20	0.20	0.18	0.18	0.21
MgO	32.57	33.25	32.37	33.11	33.50	32.62	33.04	31.32	31.78	31.24	31.83	32.12	31.21
CaO	0.48	0.30	1.19	0.87	0.56	0.66	0.44	1.09	1.02	1.05	1.06	0.83	1.08
Na_2O	0.03	0.08	0.12	0.07	0.12	0.08	0.05	0.12	0.15	0.14	0.14	0.11	0.09
K_2O	0.00	0.01	0.02	0.02	0.00	0.00	0.01	0.01	0.01	0.01	0.00	0.00	0.00
Cr_2O_3	0.31	0.18	0.70	0.54	0.50	0.35	0.29	0.47	0.41	0.57	0.35	0.28	0.51
Tot	99.54	99.50	99.87	99.82	99.67	99.63	99.65	99.46	99.51	99.62	99.28	99.32	99.38
Fetot	6.68	6.30	6.04	6.04	5.95	6.73	6.59	7.51	7.26	7.46	7.34	7.28	7.41
Si	1.909	1.938	1.910	1.928	1.927	1.908	1.917	1.896	1.913	1.898	1.931	1.936	1.904
Ti	0.002	0.002	0.009	0.003	0.002	0.003	0.002	0.005	0.003	0.005	0.003	0.000	0.005
Al	0.175	0.124	0.157	0.131	0.126	0.162	0.151	0.180	0.154	0.181	0.127	0.127	0.178
Fe III	0.000	0.000	0.000	0.000	0.003	0.003	0.002	0.003	0.003	0.002	0.001	0.000	-0.001
Fe II	0.194	0.191	0.176	0.175	0.169	0.192	0.189	0.216	0.208	0.217	0.214	0.213	0.218
Mn	0.005	0.004	0.004	0.004	0.004	0.005	0.004	0.005	0.006	0.006	0.005	0.005	0.006
Mg	1.686	1.719	1.672	1.707	1.727	1.688	1.707	1.632	1.653	1.626	1.660	1.672	1.629
Ca	0.018	0.011	0.044	0.032	0.021	0.025	0.016	0.041	0.038	0.039	0.040	0.031	0.041
Na	0.002	0.005	0.008	0.005	0.008	0.005	0.003	0.008	0.010	0.009	0.009	0.007	0.006
K	0.000	0.000	0.001	0.001	0.000	0.000	0.000	0.000	0.000	0.000	0.000	0.000	0.000
Cr	0.009	0.005	0.019	0.015	0.014	0.010	0.008	0.013	0.011	0.016	0.010	0.008	0.014
Al iv	0.091	0.062	0.090	0.072	0.073	0.092	0.083	0.104	0.087	0.102	0.069	0.064	0.096
Al vi	0.082	0.060	0.064	0.058	0.058	0.076	0.071	0.083	0.073	0.082	0.061	0.063	0.080
Alvi r	0.084	0.062	0.067	0.058	0.052	0.070	0.068	0.076	0.067	0.079	0.058	0.063	0.082
Mg M1	0.812	0.839	0.820	0.838	0.846	0.821	0.829	0.797	0.813	0.793	0.822	0.824	0.794
Mg M2	0.874	0.881	0.853	0.870	0.880	0.866	0.878	0.836	0.840	0.834	0.838	0.848	0.835
Fe2+ M1	0.094	0.093	0.087	0.086	0.083	0.094	0.092	0.106	0.102	0.106	0.106	0.105	0.106
Fe2+ M2	0.101	0.098	0.090	0.089	0.086	0.099	0.097	0.111	0.106	0.111	0.108	0.108	0.112
SumCa	4	4	4	4	4	4	4	4	4	4	4	4	4
mg#	89.68	90.39	90.52	90.71	90.94	89.63	89.93	88.14	88.64	88.18	88.54	88.72	88.24

Table A4.3 Major Element content (wt.%) in HR clinopyroxenes

Sample	HR1	HR1	HR1	HR2	HR2	HR2	HR3	HR3	HR3	HR4	HR4	HR4	HR5	HR5	HR5
phase	1	1	1	1	1	1	1	1	1	1	1	1		1	1
rim/core	rim	rim	core	core	rim	core	rim	core	rim	rim	core	core	rim	core	core
Host rock	Lh	Lh	Lh	Lh	Lh	Lh	Lh	Lh	Lh	Lh	Lh	Lh	Lh	Lh	Lh
Group	A	A	A	A	B	B	A	A	A	A	A	A	A	A	A
SiO_2	51.97	52.04	51.72	51.52	51.40	51.23	51.97	51.79	51.66	51.75	51.75	52.18	52.36	51.64	52.36
TiO_2	0.35	0.42	0.36	0.44	0.52	0.68	0.45	0.45	0.44	0.34	0.37	0.36	0.44	0.40	0.48
Al_2O_3	6.11	5.53	6.39	5.91	5.55	5.84	5.27	6.11	6.05	6.03	6.02	6.45	5.82	6.68	5.87
Fe_2O_3	0.27	0.40	0.31	0.30	0.38	0.43	0.27	0.28	0.23	0.37	0.12	0.22	0.15	0.10	0.17
FeO	3.14	2.86	2.44	2.61	3.62	3.44	2.30	2.31	2.40	2.81	2.63	2.26	2.14	2.49	2.28
MnO	0.08	0.10	0.09	0.09	0.13	0.13	0.07	0.09	0.10	0.10	0.05	0.10	0.09	0.09	0.07
MgO	16.16	16.03	15.00	15.55	16.19	16.10	15.24	14.99	14.93	15.91	15.20	15.55	14.83	14.48	14.89
CaO	20.01	20.71	21.15	21.37	19.67	19.90	22.15	21.46	21.49	20.11	20.88	20.07	21.92	21.16	21.74
Na_2O	1.19	1.19	1.42	1.08	1.11	1.13	1.15	1.40	1.32	1.33	1.30	1.60	1.43	1.48	1.45
K_2O	0.00	0.03	0.02	0.01	0.00	0.01	0.01	0.00	0.01	0.00	0.00	0.04	0.01	0.01	0.01
Cr_2O_3	0.65	0.72	0.84	0.81	0.75	0.70	0.62	0.74	0.72	0.90	0.97	1.02	0.78	0.82	0.68
Tot	99.93	100.03	99.74	99.69	99.32	99.58	99.50	99.62	99.35	99.66	99.29	99.85	99.96	99.35	100.00
Fetot	3.38	3.22	2.72	2.88	3.96	3.83	2.54	2.56	2.61	3.14	2.74	2.46	2.27	2.58	2.43
Si	1.878	1.881	1.875	1.871	1.874	1.863	1.892	1.880	1.882	1.875	1.886	1.883	1.895	1.881	1.894
Ti	0.010	0.011	0.010	0.012	0.014	0.019	0.012	0.012	0.012	0.009	0.010	0.010	0.012	0.011	0.013
Al	0.260	0.236	0.273	0.253	0.239	0.250	0.226	0.261	0.260	0.258	0.259	0.274	0.248	0.287	0.250
Fe III	0.007	0.011	0.008	0.008	0.010	0.012	0.007	0.008	0.006	0.010	0.003	0.006	0.004	0.003	0.005
Fe II	0.095	0.087	0.074	0.079	0.110	0.104	0.070	0.070	0.073	0.085	0.080	0.068	0.065	0.076	0.069
Mn	0.002	0.003	0.003	0.003	0.004	0.004	0.002	0.003	0.003	0.003	0.002	0.003	0.003	0.003	0.002
Mg	0.870	0.864	0.810	0.842	0.880	0.872	0.827	0.811	0.811	0.859	0.825	0.836	0.800	0.786	0.803
Ca	0.775	0.802	0.822	0.832	0.768	0.775	0.864	0.835	0.839	0.781	0.815	0.776	0.850	0.826	0.843
Na	0.083	0.083	0.100	0.076	0.078	0.080	0.081	0.099	0.093	0.093	0.092	0.112	0.100	0.104	0.102
K	0.000	0.001	0.001	0.000	0.000	0.000	0.000	0.000	0.000	0.000	0.000	0.002	0.000	0.000	0.000
Cr	0.019	0.021	0.024	0.023	0.022	0.020	0.018	0.021	0.021	0.026	0.028	0.029	0.022	0.024	0.019
Al iv	0.122	0.119	0.125	0.129	0.126	0.137	0.108	0.120	0.118	0.125	0.114	0.117	0.105	0.119	0.106
Al vi	0.153	0.138	0.165	0.141	0.133	0.136	0.132	0.157	0.154	0.153	0.151	0.169	0.151	0.173	0.153
Alvi r	0.139	0.117	0.148	0.124	0.113	0.113	0.118	0.142	0.142	0.133	0.144	0.158	0.143	0.167	0.144
Mg M1	0.745	0.764	0.742	0.760	0.747	0.747	0.779	0.752	0.751	0.748	0.742	0.737	0.757	0.725	0.754
Mg M2	0.126	0.101	0.070	0.082	0.132	0.126	0.049	0.059	0.060	0.112	0.083	0.101	0.043	0.061	0.049
Fe2+ M1	0.081	0.077	0.068	0.071	0.094	0.089	0.066	0.065	0.068	0.074	0.072	0.060	0.061	0.070	0.065
Fe2+ M2	0.014	0.010	0.006	0.008	0.017	0.015	0.004	0.005	0.005	0.011	0.008	0.008	0.003	0.006	0.004
SumCa	4	4	4	4	4	4	4	4	4	4	4	4	4	4	4
mg#	89.49	89.87	90.77	90.59	87.93	88.23	91.44	91.25	91.08	90.02	90.82	91.85	92.07	90.91	91.60

Table A4.3 Continued

Sample	HR6	HR6	HR6	HR9	HR9	HR9	HR10A	HR10A	HR10A	HR10
phase	1	1	1	1	1	1	core	core	core	rim
rim/core	core	core	core	core	rim	core	1	1	2	1
Host rock	Hz	Hz	Hz	Lh	Lh	Lh	Lh	Lh	Lh	Lh
Group	A	A	A	A	A	A	A	A	A	A
SiO_2	52.23	52.31	52.06	52.20	51.63	51.75	51.49	52.36	51.47	51.19
TiO_2	0.31	0.45	0.49	0.44	0.38	0.42	0.60	0.19	0.60	0.56
Al_2O_3	4.39	4.33	4.62	5.36	5.90	5.62	5.68	4.78	3.85	5.80
Fe_2O_3	0.13	0.25	0.18	0.25	0.41	0.29	0.32	0.22	0.18	0.21
FeO	2.86	2.89	2.99	2.40	2.10	2.33	3.58	3.68	3.20	3.79
MnO	0.08	0.08	0.09	0.08	0.07	0.08	0.11	0.12	0.10	0.13
MgO	16.44	16.72	16.60	15.23	14.98	15.18	15.86	16.46	16.15	15.57
CaO	20.16	20.18	19.93	21.77	21.79	21.91	19.81	19.36	22.05	19.43
Na_2O	1.07	1.08	1.06	1.28	1.38	1.17	1.21	1.17	0.48	1.23
K_2O	0.02	0.00	0.02	0.01	0.00	0.03	0.01	0.00	0.00	0.01
Cr_2O_3	1.31	1.35	1.33	0.59	0.73	0.70	0.90	1.01	1.07	1.17
Tot	99.00	99.63	99.37	99.60	99.37	99.48	99.57	99.35	99.15	99.09
Fetot	2.98	3.11	3.15	2.62	2.47	2.59	3.87	3.88	3.36	3.98
Si	1.909	1.900	1.896	1.897	1.879	1.884	1.874	1.907	1.892	1.875
Ti	0.009	0.012	0.013	0.012	0.010	0.011	0.016	0.005	0.017	0.015
Al	0.189	0.185	0.198	0.230	0.253	0.241	0.244	0.205	0.167	0.250
Fe III	0.004	0.007	0.005	0.007	0.011	0.008	0.009	0.006	0.005	0.006
Fe II	0.087	0.088	0.091	0.073	0.064	0.071	0.109	0.112	0.098	0.116
Mn	0.002	0.002	0.003	0.002	0.002	0.002	0.003	0.004	0.003	0.004
Mg	0.896	0.905	0.901	0.825	0.812	0.824	0.860	0.893	0.885	0.850
Ca	0.790	0.785	0.778	0.847	0.850	0.855	0.773	0.756	0.868	0.762
Na	0.076	0.076	0.075	0.090	0.097	0.083	0.085	0.083	0.034	0.087
K	0.001	0.000	0.001	0.000	0.000	0.001	0.000	0.000	0.000	0.000
Cr	0.038	0.039	0.038	0.017	0.021	0.020	0.026	0.029	0.031	0.034
Al iv	0.091	0.100	0.104	0.103	0.121	0.116	0.126	0.093	0.108	0.125
Al vi	0.105	0.099	0.104	0.139	0.154	0.140	0.135	0.124	0.068	0.136
Alvi r	0.098	0.085	0.095	0.126	0.132	0.125	0.118	0.112	0.059	0.125
Mg M1	0.776	0.781	0.771	0.770	0.765	0.769	0.738	0.753	0.800	0.721
Mg M2	0.120	0.124	0.131	0.055	0.047	0.056	0.123	0.141	0.085	0.129
Fe2+ M1	0.076	0.076	0.078	0.068	0.060	0.066	0.093	0.095	0.089	0.098
Fe2+ M2	0.012	0.012	0.013	0.005	0.004	0.005	0.016	0.018	0.009	0.018
SumCa	4	4	4	4	4	4	4	4	4	4
mg#	90.78	90.53	90.37	91.18	91.53	91.26	87.96	88.32	89.54	87.46

Table A4.3 Continued

Sample	HR10	HR10	HR7	HR7	HR7	HR11	HR11	HR11
phase	rim	core	rim	core	rim	rim	rim	core
rim/core	1	1	2	2	2	2	2	2
Host rock	Lh	Lh	We	We	We	We	We	We
Group	A	A	C	C	C	C	C	C
SiO_2	51.33	51.81	50.74	50.97	51.36	50.52	50.23	50.76
TiO_2	0.52	0.36	1.07	0.97	0.91	1.15	1.25	1.07
Al_2O_3	5.77	5.21	4.85	4.59	4.00	4.43	4.27	4.79
Fe_2O_3	0.20	0.39	0.04	-0.14	-0.06	0.08	0.19	0.04
FeO	3.70	3.70	4.23	3.83	3.93	3.47	3.77	4.30
MnO	0.12	0.12	0.07	0.12	0.13	0.11	0.12	0.06
MgO	15.65	16.06	15.26	15.43	15.49	15.38	15.47	14.80
CaO	19.29	19.43	21.96	20.81	21.84	22.32	22.25	22.05
Na_2O	1.28	1.29	0.45	0.72	0.51	0.45	0.36	0.60
K_2O	0.01	0.00	0.01	0.00	0.02	0.00	0.02	0.00
Cr_2O_3	1.17	1.11	1.22	1.54	1.31	1.32	1.08	1.08
Tot	99.04	99.48	99.90	98.84	99.44	99.23	99.01	99.54
Fetot	3.88	4.05	4.27	3.70	3.88	3.54	3.94	4.34
Si	1.879	1.887	1.862	1.884	1.891	1.864	1.859	1.870
Ti	0.014	0.010	0.030	0.027	0.025	0.032	0.035	0.030
Al	0.249	0.224	0.210	0.200	0.174	0.193	0.186	0.208
Fe III	0.006	0.011	0.001	-0.004	-0.002	0.002	0.005	0.001
Fe II	0.113	0.113	0.130	0.118	0.121	0.107	0.117	0.132
Mn	0.004	0.004	0.002	0.004	0.004	0.003	0.004	0.002
Mg	0.854	0.872	0.834	0.850	0.850	0.846	0.853	0.813
Ca	0.757	0.758	0.863	0.824	0.861	0.882	0.882	0.870
Na	0.091	0.091	0.032	0.052	0.036	0.032	0.026	0.043
K	0.000	0.000	0.000	0.000	0.001	0.000	0.001	0.000
Cr	0.034	0.032	0.035	0.045	0.038	0.038	0.032	0.031
Al iv	0.121	0.113	0.138	0.116	0.109	0.136	0.141	0.130
Al vi	0.139	0.132	0.074	0.076	0.061	0.061	0.055	0.080
Alvi r	0.128	0.110	0.072	0.084	0.064	0.057	0.045	0.078
Mg M1	0.723	0.741	0.746	0.744	0.765	0.773	0.777	0.739
Mg M2	0.131	0.130	0.089	0.106	0.086	0.073	0.077	0.073
Fe2+ M1	0.096	0.096	0.116	0.104	0.109	0.098	0.106	0.120
Fe2+ M2	0.017	0.017	0.014	0.015	0.012	0.009	0.010	0.012
SumCa	4	4	4	4	4	4	4	4
mg#	87.79	87.60	86.44	88.13	87.69	88.56	87.49	85.88

Table A4.4 Major Element content (wt.%) of HR spinels

Sample	HR1	HR1	HR1	HR2	HR2	HR2	HR3	HR3	HR3	HR4	HR4	HR4	HR5	HR5	HR5
phase	1	1	1	1	1	1	1	1	1	1	1	1	1	1	1
Host rock	Lh	Lh	Lh	Lh	Lh	Lh	Lh	Lh	Lh	Lh	Lh	Lh	Lh	Lh	Lh
Group	A	A	A	B	B	B	A	A	A	A	A	A	A	A	A
SiO_2	0.06	0.07	0.11	0.08	0.09	0.10	0.07	0.06	0.07	0.09	1.86	0.05	0.05	0.23	0.05
TiO_2	0.12	0.11	0.10	0.54	0.43	0.45	0.07	0.07	0.11	0.11	0.38	0.10	0.08	0.08	0.08
Al_2O_3	56.00	54.77	54.91	49.61	49.56	49.99	57.36	56.44	57.15	53.79	48.31	53.25	57.99	49.37	57.60
$Fe2O_3$	2.87	3.92	3.73	4.72	4.71	4.37	3.04	3.09	3.01	3.84	1.67	3.81	2.42	1.69	2.19
FeO	8.94	7.88	8.10	10.04	9.85	10.41	8.48	8.43	8.36	7.64	10.87	8.42	8.52	9.42	8.89
MnO	0.10	0.10	0.06	0.15	0.15	0.11	0.09	0.10	0.09	0.08	0.13	0.10	0.09	0.10	0.07
MgO	20.72	21.01	21.00	19.56	19.53	19.30	21.09	20.86	21.07	21.25	19.93	20.76	21.06	19.56	20.82
CaO	0.01	0.01	0.00	0.00	0.00	0.01	0.00	0.00	0.00	0.01	0.07	0.00	0.01	0.09	0.00
Na_2O	0.00	0.00	0.00	0.00	0.00	0.00	0.00	0.00	0.00	0.00	0.00	0.00	0.00	0.00	0.00
K_2O	0.00	0.00	0.00	0.00	0.00	0.00	0.00	0.00	0.00	0.00	0.00	0.00	0.00	0.00	0.00
Cr_2O_3	11.08	10.78	10.83	15.07	15.07	14.83	9.36	9.85	9.27	12.50	14.89	13.43	9.21	17.96	9.67
NiO	0.39	0.40	0.37	0.34	0.37	0.34	0.37	0.41	0.39	0.37	0.38	0.39	0.44	0.25	0.37
Total	100.30	99.05	99.20	100.11	99.75	99.91	99.92	99.31	99.52	99.68	98.49	100.31	99.86	98.75	99.74
Fetot	11.52	11.41	11.46	14.29	14.09	14.34	11.22	11.21	11.07	11.10	12.37	11.85	10.70	10.94	10.86
Si	0.002	0.002	0.003	0.002	0.002	0.003	0.002	0.002	0.002	0.010	0.001	0.001	0.001	0.006	0.001
Ti	0.002	0.002	0.002	0.011	0.009	0.009	0.001	0.001	0.002	0.010	0.002	0.002	0.002	0.002	0.002
Al	1.709	1.691	1.693	1.561	1.564	1.575	1.744	1.731	1.744	1.426	1.641	1.730	1.760	1.568	1.754
Fe	0.060	0.080	0.070	0.090	0.090	0.090	0.060	0.060	0.060	0.100	0.070	0.020	0.050	0.030	0.040
Fe II	0.190	0.170	0.180	0.220	0.220	0.230	0.180	0.180	0.180	0.200	0.180	0.220	0.180	0.210	0.190
Mn	0.002	0.002	0.001	0.003	0.003	0.002	0.002	0.002	0.002	0.003	0.002	0.002	0.002	0.002	0.002
Mg	0.800	0.820	0.819	0.778	0.779	0.769	0.811	0.809	0.813	0.807	0.809	0.770	0.808	0.785	0.802
Ca	0.000	0.000	0.000	0.000	0.000	0.000	0.000	0.000	0.000	0.004	0.000	0.000	0.000	0.003	0.000
Na	0.000	0.000	0.000	0.000	0.000	0.000	0.000	0.000	0.000	0.000	0.000	0.000	0.000	0.000	0.000
K	0.000	0.000	0.000	0.000	0.000	0.000	0.000	0.000	0.000	0.000	0.000	0.000	0.000	0.000	0.000
Cr	0.227	0.223	0.224	0.318	0.319	0.313	0.191	0.203	0.190	0.439	0.278	0.247	0.187	0.382	0.198
Ni	0.008	0.008	0.008	0.007	0.008	0.007	0.008	0.009	0.008	0.006	0.008	0.008	0.009	0.005	0.008
Cr/Cr+Al	0.117	0.117	0.117	0.169	0.169	0.166	0.099	0.105	0.098	0.236	0.145	0.125	0.096	0.196	0.101
Mg/BIV	0.803	0.824	0.821	0.774	0.777	0.766	0.814	0.813	0.816	0.799	0.813	0.774	0.813	0.785	0.806
Fe II/BIV	0.195	0.174	0.178	0.223	0.220	0.232	0.184	0.184	0.182	0.198	0.185	0.224	0.185	0.212	0.193
Fe III/TRIV	0.028	0.039	0.037	0.048	0.048	0.044	0.030	0.030	0.029	0.049	0.038	0.008	0.024	0.017	0.021
Cr/TRIV	0.114	0.112	0.113	0.161	0.161	0.159	0.096	0.102	0.095	0.224	0.139	0.124	0.094	0.193	0.099
Al/TRIV	0.858	0.849	0.851	0.791	0.791	0.797	0.875	0.868	0.875	0.727	0.823	0.868	0.883	0.790	0.880
mg#	76.20	76.63	76.55	70.92	71.17	70.56	77.00	76.82	77.22	77.33	74.15	75.73	77.80	76.10	77.34
cr#	11.73	11.65	11.68	16.92	16.94	16.58	9.87	10.50	9.82	23.54	14.49	12.49	9.60	19.59	10.14

Lh for Lherzolite, Hz for Harzburgite, Wh for Wehrlite

mg# =[(Mg/Mg+Fetot) at. %]; cr# [cr/(cr+Al) at. %]

Table A4.4 Continued

Sample	HR6	HR6	HR6	HR9	HR9	HR9	HR10A	HR10A
phase	1	1	1	1	1	1	1	1
Host rock	Hz	Hz	Hz	Lh	Lh	Lh	Lh	Lh
Group	A	A	A	A	A	A	B	B
SiO_2	0.09	0.06	0.05	0.05	0.07	0.03	0.13	0.07
TiO_2	1.01	1.04	1.04	0.10	0.09	0.11	0.37	0.38
Al_2O_3	37.64	37.54	37.31	57.93	57.15	57.09	45.97	46.33
$Fe2O_3$	4.64	4.36	4.35	2.90	3.18	3.02	5.43	5.05
FeO	10.40	10.64	10.85	8.60	8.40	8.34	10.29	11.03
MnO	0.12	0.13	0.12	0.10	0.10	0.10	0.14	0.12
MgO	18.50	18.22	18.15	21.16	21.06	20.99	18.46	18.44
CaO	0.00	0.01	0.00	0.01	0.00	0.01	0.27	0.02
Na_2O	0.00	0.00	0.00	0.00	0.00	0.00	0.00	0.00
K_2O	0.00	0.00	0.00	0.00	0.00	0.00	0.00	0.00
Cr_2O_3	27.75	27.73	28.13	9.25	9.27	9.30	17.19	18.10
NiO	0.29	0.30	0.23	0.40	0.40	0.42	0.28	0.30
Total	100.43	100.03	100.23	100.49	99.72	99.41	98.53	99.85
Fetot	14.58	14.56	14.76	11.21	11.26	11.06	15.18	15.57
Si	0.003	0.002	0.001	0.001	0.002	0.001	0.004	0.002
Ti	0.021	0.022	0.022	0.002	0.002	0.002	0.008	0.008
Al	1.241	1.244	1.236	1.750	1.742	1.745	1.491	1.487
Fe	0.100	0.090	0.090	0.060	0.060	0.060	0.110	0.100
Fe II	0.240	0.250	0.260	0.180	0.180	0.180	0.240	0.250
Mn	0.003	0.003	0.003	0.002	0.002	0.002	0.003	0.003
Mg	0.771	0.763	0.760	0.808	0.811	0.811	0.757	0.748
Ca	0.000	0.000	0.000	0.000	0.000	0.000	0.008	0.001
Na	0.000	0.000	0.000	0.000	0.000	0.000	0.000	0.000
K	0.000	0.000	0.000	0.000	0.000	0.000	0.000	0.000
Cr	0.614	0.616	0.625	0.187	0.189	0.191	0.374	0.390
Ni	0.007	0.007	0.005	0.008	0.008	0.009	0.006	0.007
Cr/Cr+Al	0.331	0.331	0.336	0.097	0.098	0.099	0.201	0.208
Mg/BIV	0.758	0.751	0.747	0.813	0.815	0.816	0.759	0.747
Fe II/BIV	0.239	0.246	0.251	0.185	0.183	0.182	0.238	0.251
Fe III/TRIV	0.050	0.047	0.047	0.028	0.031	0.030	0.057	0.052
Cr/TRIV	0.314	0.316	0.320	0.094	0.095	0.096	0.189	0.197
Al/TRIV	0.636	0.637	0.633	0.878	0.874	0.875	0.754	0.751
mg#	69.33	69.02	68.65	77.07	76.91	77.17	68.42	67.83
cr#	33.10	33.12	33.58	9.65	9.79	9.87	20.05	20.78

Table A4.4 Continued

Sample	HR10A	HR10	HR10	HR10	HR7	HR7	HR11	HR11	HR11
phase	1	1	1	1	1	1	1	1	1
Host rock	Lh	Lh	Lh	Lh	We	We	We	We	We
Group	B	B	B	B	C	C	C	C	C
SiO_2	0.07	0.05	0.08	0.08	0.06	0.08	0.09	0.04	0.12
TiO_2	0.37	0.35	0.36	0.37	0.98	1.02	1.44	1.57	1.31
Al_2O_3	46.12	46.70	46.17	46.25	45.24	44.81	35.72	34.81	39.77
$Fe2O_3$	4.79	5.09	5.55	5.19	6.50	5.95	6.83	6.93	7.10
FeO	11.53	10.87	10.30	10.84	13.91	13.92	15.31	15.86	14.18
MnO	0.13	0.15	0.17	0.14	0.17	0.14	0.26	0.23	0.20
MgO	18.17	18.60	18.87	18.51	16.56	16.20	14.77	14.49	15.97
CaO	0.00	0.00	0.02	0.02	0.00	0.00	0.06	0.05	0.04
Na_2O	0.00	0.00	0.00	0.00	0.00	0.00	0.00	0.00	0.00
K_2O	0.00	0.00	0.00	0.00	0.00	0.01	0.00	0.00	0.00
Cr_2O_3	18.69	18.00	18.13	18.00	15.09	14.79	23.65	24.69	19.71
NiO	0.30	0.30	0.33	0.31	0.27	0.32	0.27	0.27	0.30
Total	100.17	100.11	99.98	99.71	98.78	97.24	98.39	98.94	98.70
Fetot	15.84	15.45	15.29	15.51	19.76	19.27	21.46	22.10	20.57
Si	0.002	0.001	0.002	0.002	0.002	0.002	0.003	0.001	0.003
Ti	0.008	0.007	0.007	0.008	0.021	0.022	0.032	0.035	0.028
Al	1.480	1.493	1.478	1.486	1.487	1.495	1.233	1.203	1.339
Fe	0.100	0.100	0.110	0.110	0.140	0.130	0.150	0.150	0.150
Fe II	0.260	0.250	0.230	0.250	0.320	0.330	0.370	0.390	0.340
Mn	0.003	0.003	0.004	0.003	0.004	0.003	0.006	0.006	0.005
Mg	0.737	0.752	0.764	0.752	0.688	0.683	0.645	0.633	0.680
Ca	0.000	0.000	0.001	0.001	0.000	0.000	0.002	0.002	0.001
Na	0.000	0.000	0.000	0.000	0.000	0.000	0.000	0.000	0.000
K	0.000	0.000	0.000	0.000	0.000	0.000	0.000	0.000	0.000
Cr	0.402	0.386	0.389	0.388	0.333	0.331	0.548	0.572	0.445
Ni	0.007	0.007	0.007	0.007	0.006	0.007	0.006	0.006	0.007
Cr/Cr+Al	0.214	0.205	0.209	0.207	0.183	0.181	0.308	0.322	0.250
Mg/BIV	0.735	0.750	0.763	0.750	0.677	0.673	0.628	0.616	0.664
Fe II/BIV	0.262	0.246	0.234	0.247	0.319	0.324	0.365	0.378	0.331
Fe III/TRIV	0.050	0.052	0.057	0.054	0.070	0.065	0.078	0.079	0.079
Cr/TRIV	0.203	0.195	0.197	0.196	0.170	0.170	0.284	0.297	0.230
Al/TRIV	0.747	0.753	0.746	0.750	0.760	0.766	0.639	0.624	0.691
mg#	67.14	68.19	68.73	68.01	59.89	59.95	55.08	53.88	58.04
cr#	21.36	20.54	20.84	20.70	18.30	18.13	30.77	32.23	24.94

Table A4.5 Major elements (wt.%) of HR glass

Sample			HR2		
Host rock			Lh		
Group			B		
SiO_2	59.18	54.48	60.40	62.13	58.01
TiO_2	1.44	0.91	1.57	0.90	0.69
Al_2O_3	21.71	20.85	19.20	17.68	24.95
FeO	1.12	2.89	1.41	1.20	1.76
MnO					0.03
MgO	1.05	3.80	0.90	1.42	0.82
CaO	5.37	4.95	1.13	1.48	0.95
Na_2O	6.79	6.37	6.44	5.76	5.05
K_2O	3.06	5.38	7.52	6.84	4.90
Cr_2O_3					0.03
NiO					
Cl	0.00	0.07	0.04	0.02	
BaO	0.00	0.14	0.10	0.02	
SO_2	0.00	0.00	0.00	0.04	
P_2O_5	0.19	0.35	0.21	0.22	
Total	99.91	100.18	98.92	97.70	97.19
mg#	62.71	70.06	53.25	67.92	45.45
Na_2O/K_2O	2.22	1.18	0.86	0.84	1.03
TiO_2+K_2O	4.50	6.29	9.10	7.74	5.59
$CaO+Na_2O$	12.16	11.32	7.57	7.23	6.00
Na_2O+K_20	9.85	11.75	13.97	12.60	9.95

Table A4.5 Continued

Sample	HR10A					
Host rock	Lh					
Group	B					
SiO_2	62.10	62.78	54.59	55.08	53.53	62.42
TiO_2	0.76	0.94	0.60	0.51	0.20	1.88
Al_2O_3	20.21	20.23	22.37	23.99	22.34	20.31
FeO	1.05	0.95	1.50	1.46	2.74	1.63
MnO						
MgO	0.38	0.41	1.86	0.77	6.11	0.21
CaO	0.47	0.48	3.17	1.75	7.20	2.29
Na_2O	6.13	6.44	8.44	7.86	5.45	8.90
K_2O	6.19	6.24	6.36	6.80	0.36	1.45
Cr_2O_3						
NiO						
Cl	0.05	0.08	0.09	0.06	0.03	0.01
BaO	0.02	0.05	0.05	0.05	0.02	0.08
SO_2	0.03	0.00	0.01	0.03	0.01	0.00
P_2O_5	0.38	0.43	0.79	0.50	0.14	0.28
Total	97.77	99.03	99.82	98.84	98.14	99.45
mg#	39.46	43.59	68.93	48.45	79.89	18.39
Na_2O/K_2O	0.99	1.03	1.33	1.16	14.98	6.14
TiO_2+K_2O	6.95	7.18	6.97	7.30	0.57	3.33
$CaO+Na_2O$	6.60	6.92	11.61	9.61	12.65	11.19
Na_2O+K_20	12.32	12.68	14.80	14.66	5.82	10.35

Table A4.5 Continued

Sample	HR7			HR11	
Host rock	We			We	
Group	C			C	
SiO_2	55.16	54.49	54.53	56.66	55.84
TiO_2	1.20	0.55	0.58	0.91	0.66
Al_2O_3	21.86	25.82	23.39	22.84	20.00
FeO	1.89	0.64	1.20	1.13	2.02
MnO	0.04	0.00	0.01	0.02	0.07
MgO	0.25	0.20	0.19	0.13	2.86
CaO	3.29	6.76	0.48	0.19	4.16
Na_2O	9.57	7.45	7.97	7.49	7.10
K_2O	5.18	2.01	10.12	9.42	6.30
Cr_2O_3	0.05	0.02	0.02	0.05	0.17
NiO	0.00	0.01	0.02	0.01	0.03
Cl					
BaO					
SO_2					
P_2O_5					
Total	97.95	98.50	100.08	98.84	99.21
mg#	19.17	35.57	22.05	16.48	71.61
Na_2O/K_2O	1.85	3.70	0.79	0.79	1.13
TiO_2+K_2O	6.38	2.56	10.70	10.33	6.97
$CaO+Na_2O$	12.85	14.21	8.45	7.68	11.26
Na_2O+K_20	14.75	9.46	18.08	16.91	13.40

Table A4.6 Trace element content (ppm) of HR orthopyroxenes

Sample		HR1			HR2		HR4	
Host rock		Lh			Lh		Lh	
Group		A			B		A	
Cs	0.003	0.004	0.004	0.004	0.006	0.003	0.017	0.007
Rb	0.005	0.021	0.034	0.008	0.012	0.005	1.281	2.071
Ba	0.010	0.008	0.144	0.006	0.009	0.010	0.705	9.790
Th	0.002	0.006	0.002	0.000	0.000	0.000	0.020	0.066
U	0.002	0.003	0.002	0.000	0.000	0.005	0.026	0.024
K								
Nb	0.057	0.096	0.091	0.029	0.044	0.063	0.458	2.877
Ta	0.003	0.005	0.007	0.002	0.003	0.001	0.004	0.119
La	0.019	0.027	0.030	0.017	0.037	0.024	0.105	0.330
Ce	0.072	0.104	0.078	0.079	0.161	0.090	0.136	0.605
Pr	0.014	0.020	0.013	0.016	0.034	0.023	0.017	0.062
Sr	0.265	0.346	0.482	0.276	0.482	0.313	0.687	3.650
Nd	0.072	0.093	0.081	0.104	0.182	0.125	0.093	0.293
Zr	2.004	1.294	2.544	2.360	2.760	2.050	1.093	2.457
Hf	0.023	0.036	0.056	0.050	0.054	0.029	0.031	0.066
Sm	0.021	0.051	0.033	0.048	0.052	0.056	0.016	0.097
Eu	0.013	0.015	0.014	0.024	0.026	0.024	0.016	0.035
Ti	491.2	713.5	442.0	549.3	1150.0	519.6	471.0	773.6
Gd	0.036	0.072	0.046	0.116	0.136	0.096	0.084	0.144
Tb	0.014	0.013	0.014	0.015	0.035	0.017	0.004	0.036
Dy	0.124	0.133	0.118	0.151	0.342	0.173	0.142	0.302
Y	1.098	1.072	1.031	1.125	2.480	1.140	1.072	2.069
Ho	0.044	0.034	0.036	0.044	0.088	0.044	0.045	0.074
Er	0.141	0.118	0.147	0.153	0.341	0.133	0.155	0.244
Tm	0.030	0.031	0.029	0.027	0.060	0.025	0.036	0.045
Yb	0.266	0.286	0.209	0.167	0.552	0.193	0.236	0.356
Lu	0.042	0.053	0.039	0.039	0.099	0.042	0.047	0.057

Table A4.7 Trace element content (ppm) of HR clinopyroxenes

Host rock	HR1				HR2			HR4	
Group	Lh				Lh			Lh	
	A				B			A	
Cs	0.0057	0.0059	0.0061	0.0061	0.359	0.0071	0.0077	0.0117	0.0037
Rb	0.0113	0.0274	0.0112	0.0115	35.58	0.0132	0.015	0.263	0.1059
Ba	0.117	0.177	0.0898	0.0979	69.57	0.1296	0.186	9.93	2.199
Th	0.2087	0.1882	0.1751	0.2058	0.386	0.135	0.1334	0.0506	0.1138
U	0.0404	0.06	0.0405	0.0533	0.1112	0.027	0.0184	0.0264	0.0479
K									
Nb	1.512	1.717	1.355	1.639	5.25	1.24	1.051	0.79	0.2176
Ta	0.1906	0.27	0.2062	0.248	0.413	0.22	0.189	0.0601	0.0007
La	7.27	8.09	6.26	8.23	6.93	8.23	7.19	0.983	0.277
Ce	17.01	19.94	14.96	21.43	18.63	27.66	23.2	2.929	0.727
Pr	2.013	2.493	1.864	2.906	2.892	4.63	3.86	0.573	0.2195
Sr	81.28	93.68	83.4	97.96	134.23	119.44	116.92	169.26	21.1
Nd	7.88	10.2	7.78	12.52	14.44	23.56	19.58	3.59	1.926
Zr	27.14	46.12	37.44	53.64	53.43	82.09	53.91	21.4	11.98
Hf	0.685	1.254	1.161	1.452	1.77	3.18	1.93	0.83	0.551
Sm	1.798	2.276	1.872	2.679	3.96	6.46	4.58	1.572	1.192
Eu	0.68	0.78	0.719	0.935	1.137	1.903	1.701	0.742	0.492
Ti	2425.2	2754.1	2657.4	2742.9	6500.5	7315.1	5147.6	10481.4	2503.2
Gd	2.238	2.66	2.45	3.1	4.26	6.03	4.79	2.75	2.142
Tb	0.384	0.443	0.43	0.509	0.608	0.874	0.711	0.54	0.412
Dy	2.92	3.23	3.21	3.58	3.69	5.49	4.76	4.01	3.13
Y	16.61	17.99	17.78	19.49	17.77	24.63	21.57	23.71	18.21
Ho	0.636	0.657	0.69	0.805	0.757	1.024	0.86	0.956	0.7
Er	1.824	1.987	1.988	2.25	1.793	2.84	2.38	2.46	1.976
Tm	0.273	0.292	0.302	0.318	0.274	0.357	0.364	0.386	0.301
Yb	1.655	1.801	1.78	1.971	1.77	2.3	2.02	2.84	2.027
Lu	0.25	0.271	0.262	0.283	0.26	0.306	0.285	0.427	0.284

Table A4.7 Continued

Host rock Group					HR7 Wh C				
Cs	0.0361	0.653	0.448	0.311	0.02	0.0054	0.0662	0.0125	0.0256
Rb	3.61	3.19	1.642	3.4	2.814	2.138	10.77	1.366	2.335
Ba	19.32	13.17	14.02	6.96	7.82	4.48	22.59	6	6.4
Th	0.291	0.427	0.1793	0.0951	0.0803	0.0587	0.303	0.0783	0.1389
U	0.091	0.1243	0.0488	0.0198	0.0195	0.0141	0.0811	0.0241	0.0387
K									
Nb	2.685	4.06	1.479	0.88	0.837	0.55	2.788	0.879	1.408
Ta	0.2027	0.305	0.1219	0.1005	0.0797	0.0548	0.249	0.078	0.1128
La	5.49	7.06	4.36	4.06	4.16	3.47	6.1	1.976	3.01
Ce	16.61	18.87	13.93	13.73	15.92	13.56	19.48	6.27	10.16
Pr	2.739	3.06	2.356	2.382	2.85	2.419	3.13	1	1.709
Sr	94.75	90.51	80	69.67	79.92	67.01	83.47	27.83	43.17
Nd	14.65	15.06	12.18	12.32	15.48	12.8	15.8	4.98	8.92
Zr	46.18	56.28	37.44	36.78	39.85	35.24	46.71	18.69	29.01
Hf	1.633	1.887	1.061	1.11	1.344	1.185	1.401	0.648	1.05
Sm	4.02	4.17	3.51	3.52	4.31	3.57	4.2	1.396	2.61
Eu	1.32	1.269	1.155	1.099	1.429	1.198	1.407	0.432	0.835
Ti	8841.7	8961.5	6447.0	6555.6	8098.8	6526.8	7266.1	2991.1	4790.5
Gd	3.88	4.17	3.42	3.18	4.33	3.69	4.18	1.285	2.58
Tb	0.566	0.629	0.507	0.494	0.616	0.527	0.616	0.1906	0.38
Dy	3.48	3.59	3.06	3.13	3.77	3.34	3.69	1.188	2.28
Y	15.95	16.94	14.46	14.86	17.6	16.25	17.62	5.24	10.33
Ho	0.659	0.639	0.557	0.564	0.71	0.646	0.704	0.208	0.419
Er	1.619	1.617	1.498	1.476	1.877	1.791	1.715	0.547	0.999
Tm	0.21	0.2187	0.1963	0.1976	0.262	0.229	0.226	0.0687	0.1452
Yb	1.337	1.328	1.205	1.304	1.635	1.409	1.562	0.438	0.942
Lu	0.1771	0.1964	0.1712	0.1822	0.2084	0.1917	0.203	0.0596	0.1186

Table A4.7 Continued

			HR11			
Host rock			Wh			
Group			C			
Cs	0.008	0.165	0.006	0.007	0.009	0.008
Rb	0.016	1.248	0.012	0.015	0.040	0.191
Ba	0.071	10.430	0.045	0.126	0.213	0.332
Th	0.030	0.139	0.011	0.079	0.086	0.063
U	0.004	0.036	0.002	0.019	0.023	0.021
K						
Nb	0.192	1.998	0.089	0.533	0.675	0.470
Ta	0.049	0.168	0.017	0.079	0.094	0.072
La	3.220	3.720	2.114	4.820	5.380	4.510
Ce	12.870	13.600	9.430	16.590	18.740	17.300
Pr	2.471	2.407	1.875	2.815	3.052	3.220
Sr	68.210	81.560	48.030	107.340	114.750	79.170
Nd	13.940	13.810	10.900	15.300	16.720	17.680
Zr	39.730	52.870	28.860	34.030	37.400	54.010
Hf	1.529	2.450	1.112	1.219	1.368	2.144
Sm	4.200	4.270	3.020	4.070	4.210	4.980
Eu	1.395	1.489	1.105	1.312	1.433	1.587
Ti	8065.9	9857.7	5253.2	6957.2	7679.3	8345.3
Gd	4.300	4.310	3.220	4.130	4.510	4.950
Tb	0.658	0.637	0.464	0.600	0.660	0.727
Dy	3.740	3.860	2.920	3.840	4.170	4.530
Y	16.740	16.520	13.600	17.660	19.900	19.540
Ho	0.703	0.698	0.543	0.748	0.830	0.806
Er	1.812	1.788	1.374	1.894	1.993	1.982
Tm	0.230	0.265	0.183	0.264	0.271	0.277
Yb	1.367	1.415	1.113	1.545	1.880	1.698
Lu	0.197	0.220	0.151	0.229	0.254	0.224

Table A4.8 Trace element (ppm) of HR glass

	HR2		HR4	HR11
Host rock	Lh		Lh	We
Group	B		A	C
Cs	0.353	0.753	0.158	193.43
Rb	50.88	63.05	16.01	79.84
Ba	642.93	754.36	153.59	5452.38
Th	6.46	6.62	0.624	21.1
U	2.07	2.06	0.229	6.09
K				
Nb	93.66	99.54	91.44	263.28
Ta	5.36	6.88	4.6	15.09
La	47.37	47.46	19.61	177.56
Ce	97.56	98.52	55.88	360.57
Pr	11.49	11.7	7.63	40.97
Sr	889.54	1068.63	258.02	3999.63
Nd	46.91	48.15	35.49	142.3
Zr	253.79	263.97	134.28	682.41
Hf	6	5.58	3.73	13.79
Sm	9.92	9.85	7.27	23.81
Eu	3.09	3.16	2.023	7.99
Ti	27271.1	29094.8	13734.8	31608.1
Gd	8.18	8.93	8.42	21.94
Tb	1.08	1.295	1.193	3.34
Dy	6.41	7.1	7.76	19.14
Y	35.92	36.63	43	98.24
Ho	1.299	1.45	1.632	3.69
Er	3.81	4.54	3.99	9.46
Tm	0.519	0.54	0.568	1.5
Yb	3.49	3.43	4.28	11.73
Lu	0.603	0.456	0.677	1.62

Table A4.9 Isotopic composition of HR clinopyroxene

	143Nd/144Nd	error	87Sr/86Sr	error
HR1	0.513139	+/- 15	0.702895	+/-9
HR7	0.513153	+/-26	0.702920	+/-18
HR11	0.512927	+/- 15	0.703027	+/- 12
HR12	0.513159	+/- 8	0.702918	+/- 28
La Jolla	0.512855	+/- 18		
NBS 987			0.71025	+/-35

La Jolla and NBS 987 standards were regularly run during mesasurements

Table A4.10 Major elements (wt.%) composition of HR lavas

	HR2	HR4	HR5b	HR6b	HR7
SiO_2	42.41	43.09	42.20	41.66	41.50
TiO_2	3.59	3.44	3.56	3.55	3.65
Al_2O3	12.46	12.24	12.15	14.44	14.44
Fe_2O_3	1.83	1.69	1.84	1.80	1.84
FeO	13.58	12.52	13.65	13.36	13.66
MnO	0.20	0.18	0.20	0.22	0.24
MgO	9.90	10.95	10.61	6.76	6.26
CaO	11.42	10.92	11.29	10.98	11.11
Na2O	2.80	2.88	2.76	3.70	4.64
K2O	1.41	1.16	1.35	1.48	1.53
$P2O_5$	0.41	0.44	0.40	1.10	1.14
Totale	100	100	100	100	100
mg#	56.42	60.83	57.99	47.33	44.87
Na_2O+K_2O	4.21	4.04	4.11	5.18	6.17

Table A4.11 Trace element (ppm) composition of HR lavas

	HR2	HR5b	HR4r	HR6b	HR7	HR4
Rb	29.36	14.37	15.37	28.77	37.49	17.43
Sr	823.19	557.07	483.72	1053.43	1201.24	588.14
Y	23.82	16.35	14.08	33.42	34.04	17.35
Zr	212.96	212.51	172.18	335.77	361.00	174.18
Nb	76.21	79.64	63.48	109.41	119.92	64.17
La	51.48	44.82	39.27	75.28	77.15	43.40
Ce	102.56	93.92	84.65	151.90	149.17	90.15
Pr	10.85	9.78	8.65	16.45	16.25	9.26
Nd	45.20	40.21	35.99	67.36	67.88	38.80
Sm	8.33	7.31	6.62	11.88	11.82	7.11
Eu	2.60	2.28	2.05	3.49	3.44	2.22
Gd	7.42	6.43	5.69	10.48	10.26	6.20
Tb	1.06	0.90	0.79	1.46	1.43	0.87
Dy	4.91	4.08	3.60	6.63	6.54	4.00
Ho	0.87	0.72	0.63	1.18	1.16	0.71
Er	2.17	1.75	1.53	2.89	2.85	1.74
Tm	0.32	0.26	0.22	0.42	0.42	0.25
Yb	1.89	1.46	1.27	2.42	2.44	1.45
Lu	0.24	0.18	0.16	0.31	0.32	0.18
Hf	4.59	4.61	3.86	6.56	7.00	3.84
Ta	1.12	1.17	0.92	1.44	1.60	0.96
Th	6.44	4.28	4.25	8.32	8.02	5.12
U	1.60	1.40	1.34	2.22	2.51	1.40

Chapter 5. Harrow Peaks Mantle xenoliths

5.1 Introduction

As it is widely known the amphibole represents a key mineral in mantle parageneses (Coltorti et al., 2004), as it is one of the main acceptor of alkalies and incompatible elements. Its role is crucial in basalt petrogenesis even at high degrees of partial melting (Beccaluva et al., 1998), as well as in mantle glass genesis via decompression or in situ melting processes (Chazot et al., 1996; Yaxley and Kamenetsky, 1999; Yaxley et al., 1997).

As suggested by Coltorti et al. (2004) the amphibole in mantle xenoliths from Baker Rocks (BR), Northern Victoria Land is the product of reaction between under-saturated alkaline-silicate metasomatic fluids and pre-existing clinopyroxene and spinel.

The new occurrence of Harrow Peaks (HP, Fig 5.1) mantle xenoliths offers the opportunity to explore the Antarctica SCLM extending petrological characterisation in its amphibole - bearing portion.

In this chapter it is presented a geochemical comparison between BR locality and HP in order to identify differences within hydrous suites and shed a light on the different stages of matrix metasomatizing melts interactions.

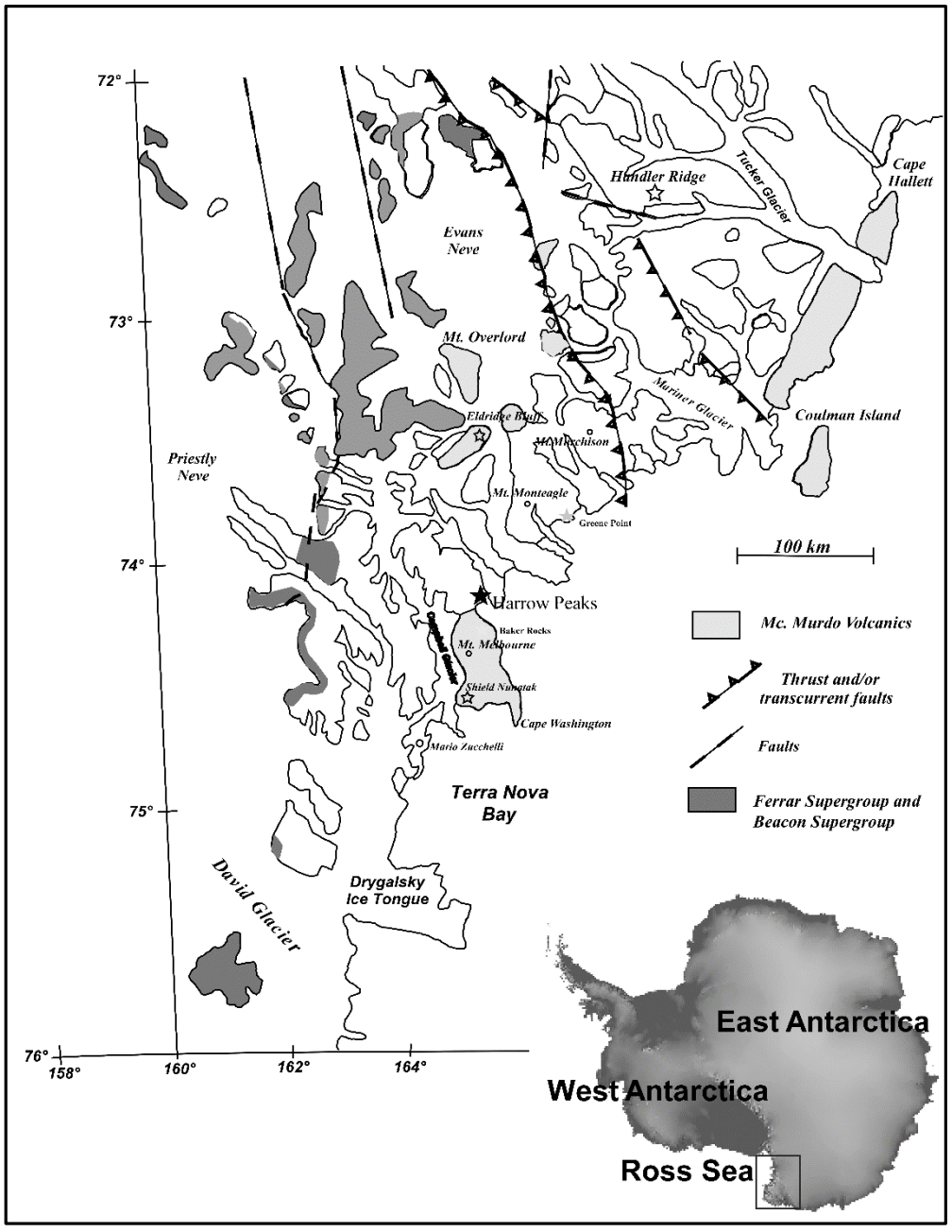

Fig. 5.1 Map of Northern Victoria Land and localization of Harrow Peaks.

5.2 Petrography

Anhydrous and hydrous peridotites from HP, vary in composition from lherzolite to harzburgite, despite a wehrlite and an orthopyroxenite also occur. This latter, clearly cumulitic in origin was discharged from this study.

The modal proportion was estimated by point counting and averaging two runs with more than 2,000 points for each thin section (Table 5.1). The lherzolites (Lh) contain olivine (ol, 62-76 vol%), orthopyroxene (opx, 17-28 vol%), clinopyroxene (cpx, 6-10 vol%) and spinel (sp, 0-1 vol%); the harzburgites (Hz) contain ol (75-84 vol%), opx (10-21 vol%), cpx (3-4

vol%), and sp (~1 vol%), the only wehrlite present (HP124) contains ol (90 vol%) and cpx (10 vol%).

They have protogranular to phorphyroclastic textures with from medium to coarse grain size. Some samples show a slight orientation due to elongated sp (i.e. HP 143) and rarely aligned opx (HP 151).

Primary olivine (ol) appears always as large grain (Fig. 5.2 b), opx occurs as large crystals (opx1) or as elongated grain. Primary unmetasomatized clinopyroxenes (cpx1) is always smaller with respect to the other phases: they often exhibit spongy rim, or consists of resorbed grains and/or newly formed small crystals (cpx2, Fig. 5.2 b, f). Spinel (sp) occurs as small anhedral crystals, or larger, often dendritic primary grains (Fig. 5.2 b). Amphiboles (amph) are present both as disseminated and in veins (Fig. 5.2 a), the latter often associated to cpx2 (Fig.5.2b). Rare glassy patches are associated to spongy/resorbed cpx and sp.

Table 5.1: Textural features, modes, T, fO_2 estimates of HP mantle xenoliths

Sampe	OL	OPX	CPX	SP	AMPH	glass	ol/opx	opx/ol	opx/cpx	T (°C)*	1σ	Δ log $f O_2$	1σ
HP121	75	21	4	1		-	3.66	0.27	4.8	795.12	18	-2.07	0.620
HP124	90	0	10	-	3	trace	-	0.00	0.0	857	67.04	-0.69	0.135
HP143	64	28	7	-	1.5	-	2.29	0.44	4.0	890.98	11	-1.04	0.137
HP144	84	10	4	1		trace	8.40	0.12	2.5	1059.17	73	-0.38	0.118
HP151	76	17	6	-		trace	4.47	0.22	2.8	1066.31		-1.03	
HP164	62	24	10	1	2.3	trace	2.58	0.39	2.4	800.62	31	-1.70	0.293
HP166	70	20	7	-		-	3.50	0.29	2.9	891.09	55	-0.73	0.335

Ol is for *olivine, opx* for *orthopyroxene, cpx* for *clinopyroxene, sp* for *spinel, amph* for *amphibole*
T(°C) *: T from O'Neil and Wall (1987), modified by Ballhaus et al., 1991
Δ log fO_2 is calculated using T from O'Neil and Wall (1987), modified by Ballhaus et al., 1991

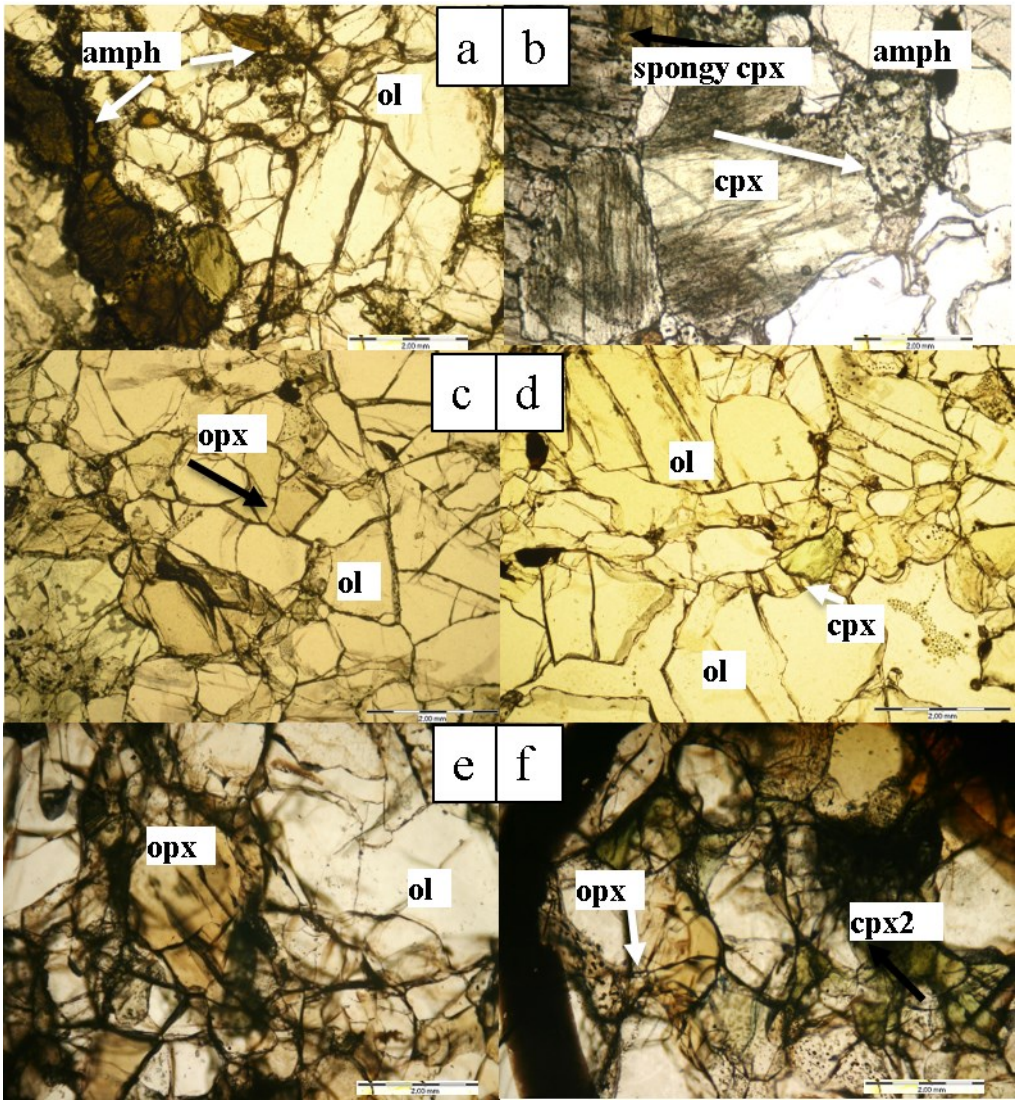

Fig. 5.2: Photomicrograph of HP xenoliths that shows the most common petrographic features amph presence (in vein: a) and disseminated: b), primary ol, opx (a, d), primary cpx (d), spongy rim of cpx (b) and secondary cpx (cpx2: f).

5.3 Geochemistry

5.3.1 Major elements

Ol in unmetasomatized xenoliths presents mg# ranging between 85.6 and 90.6, on the whole NiO (0.28 to 0.41 wt.%) contents are in the range of residual mantle values (Fig. 5.3 a, Table A5.1).

In term of mg#, opx is coherent with primary ol, it presents values between 87.47 and 90.7 and Al_2O_3 varying from 1.24 to 3.32 wt.% (Fig 5.3 b Table A5.2)

In cpx, mg# (87.94 and 94.06) is slightly negatively correlate with Al_2O_3 (0.49-7.57 wt.%, Fig. 5.3c, Table A5.3). Cpx1 contain TiO_2 from 0.17 to 0.50 wt%, while cpx2 presents TiO_2 content up to 1.43 wt.%.

Sp follows the expected negative correlation between Cr# [=Cr_2O_3/(Cr_2O_3+Al_2O_3) *100 mol] and mg#, with mg# varying between 56.17 and 71.17 and cr# from 22.70 to 74.25 (Fig. 5.3 d, Table A5.4). Amph are pargasites (mg# 82.86 to 92.02) with TiO_2 content ranging from 1.65 to 3.80 wt.% (Table A5.5). In Fig. 5.4a) Al_2O_3 and b) TiO_2 contents in amph and cpx2 are positively correlated, reflecting a common formation process. Small glassy patches are present, they are SiO_2-rich with TiO_2 content ranging between 0.11 and 1.43 wt.%. Fig. 5.5 shows HP glasses plotted on major element discrimination diagrams in order to identify the nature of the metasomatic agents (Coltorti et al., 2000). From this diagram it is evident that glasses are mainly related to Na-alkali silicate metasomatism, although some samples plot in the carbonatite affinity-field.

Considering ol-opx major elements, Lh and Hz from HP show a more residual character respect to the amph-bearing peridotites of BR. In the frame of cpx-amp evolution trend, BR shows the tendency to a larger enrichment of Al_2O_3 and TiO_2 with respect to HP.

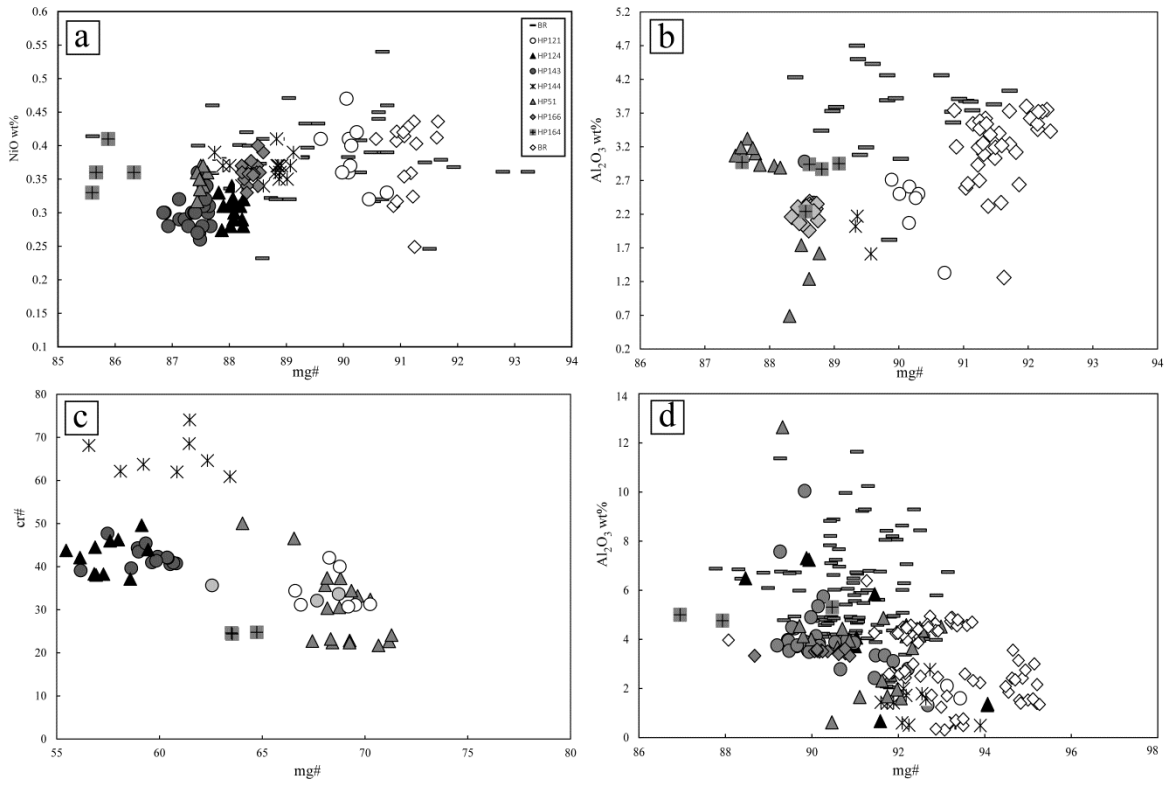

Fig. 5.3: (a) olivine compositional variation in terms of NiO *vs* mg# [(Mg/Mg+FeOtot at. %]; b) orthopyroxene compositional variation in terms of Al_2O_3 vs. mg#; d) spinel compositional

variation in terms of cr# [Cr/(Cr+Al) at. %] vs. mg#; c) clinopyroxene compositional variation in terms of Al_2O_3. Grey symbols are for lherzolites, white for harzburgites and black for wehrlites. In a), b), and d) BR composition is also reported for comparison (grey tick market and white diamonds).

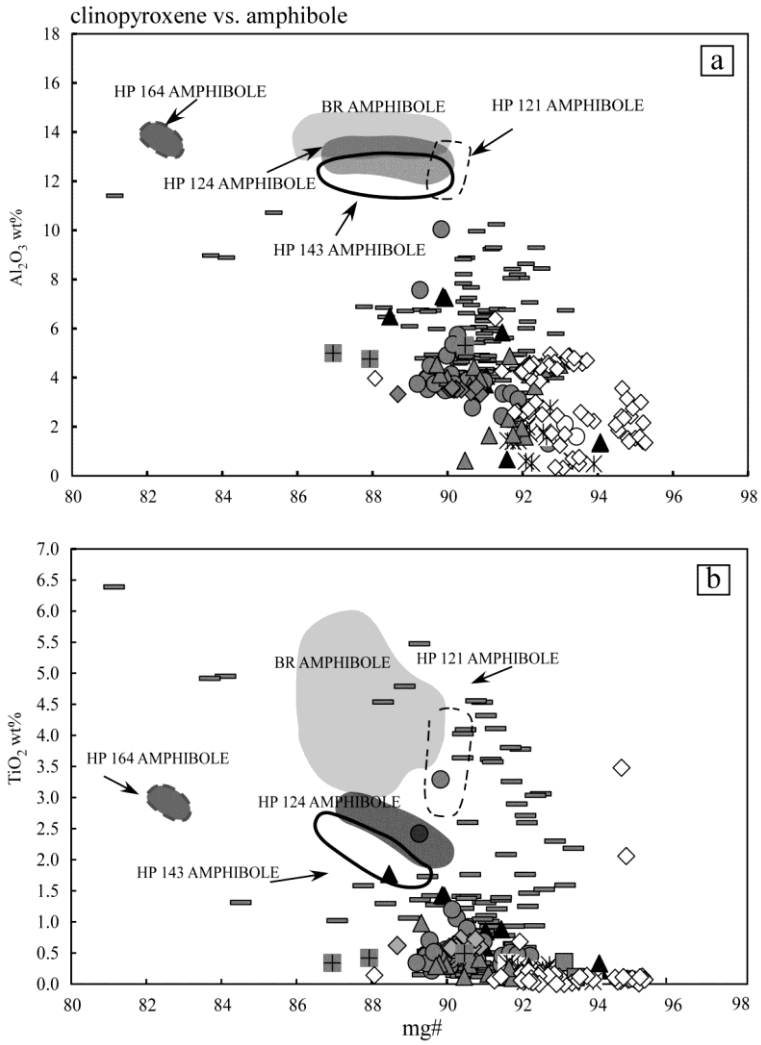

Fig. 5.4: a) clinopyroxene compositional variation in terms of Al_2O_3, and in term of TiO_2, amph are also reported (different areas). Symbols as in Fig. 5.3. For comparison also cpx (grey tick marks and white diamonds) and amph (grey area) from BR are included.

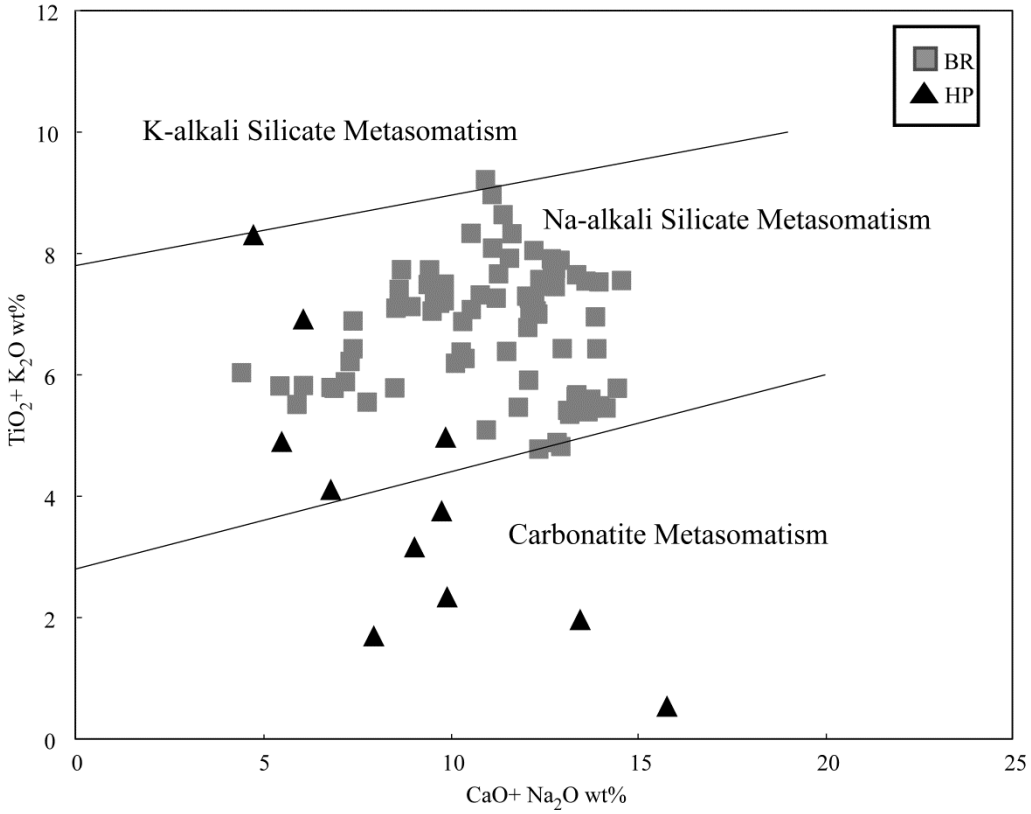

Fig. 5.5: HP and BR glasses on major element discrimination diagrams (after Coltorti et al., 2000).

5.3.2 Trace elements

Opx present the characteristic chondrite-normalised LREE depleted pattern with spotty LREE enriched shown by HP144 (Fig. 5.6, Table A5.7).

Cpx chondrite-normalized trace elements pattern show slight to marked Zr, Sr and Ti negative anomalies (Fig.5.7a, Table A5.8). HP 121 shows a typical "spoon shape" REE pattern, enriched in LREE (La_N 27.97); HP144 is characterised by a relatively enrichment in LREE, a slight to marked Eu negative anomaly and an almost flat M- to HREE pattern (Fig.5.7b), HP151 shows a slight enrichment in LREE with Eu negative anomaly. It also presents the highest values on HREE Lu_N=20.78. HP164 is characterised by a slightly upward convex (La_N= 8.98; Nd_N= 10.51) pattern and an almost flat HREE pattern (Fig. 5.7b).

Amph presents variable contents of LILE, with systematic enrichment in LREE, M and HREE fractionated pattern (Fig 5.8, Table A5.9).

Trace elements in glasses, were performed for one samples (HP144) because of their small size. This sample presents pattern variably enriched in LILE with respect to LREE, and flat

for HREE (~10X), it also presents systematic positive Ti, Ta and negative Pr, Hf, La, Eu anomalies (Fig. 5.9).

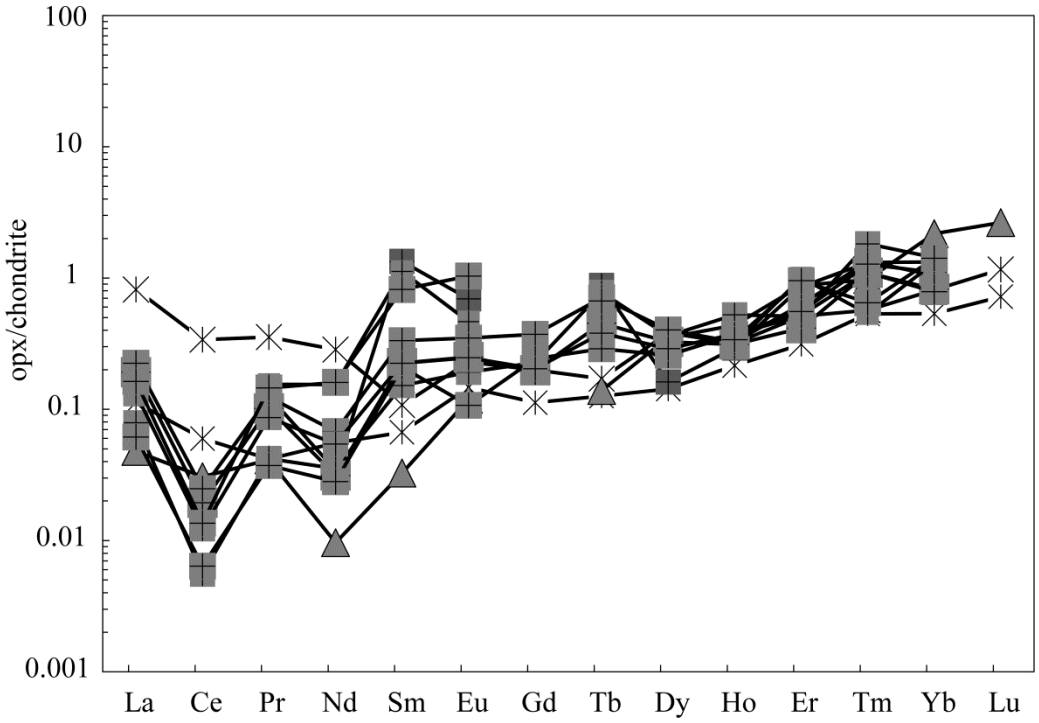

Fig 5.6 (REE) patterns of orthopyroxenes in HP xenoliths. Symbols as in Fig. 5.3 only referring to samples: HP 144, 151 and 164.

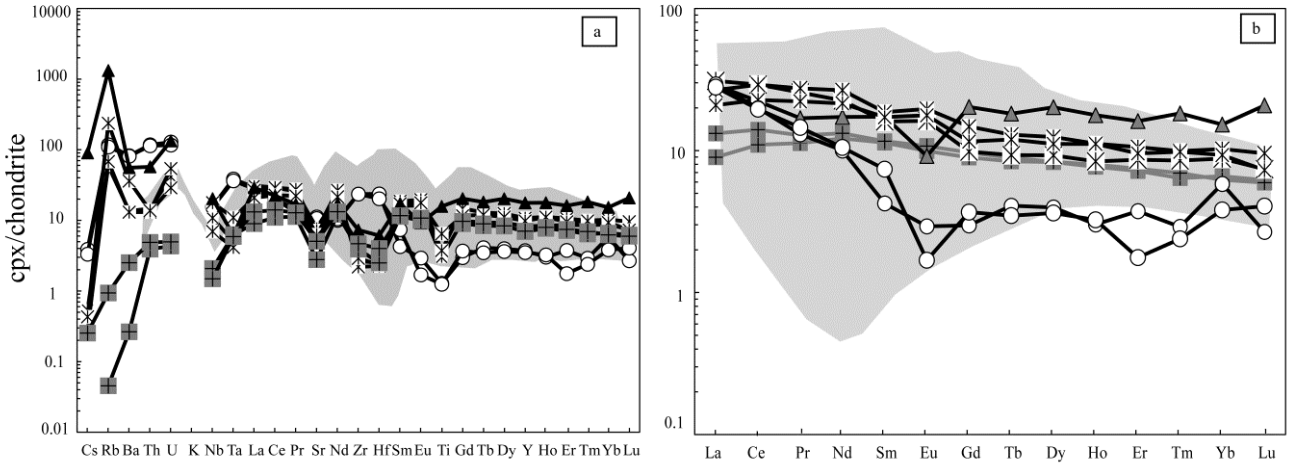

Fig. 5.7 Chondrite normalised trace element a), and (REE) b) patterns of clinopyroxene in HP xenoliths. Symbols as in Fig. 5.3 only referring to samples: HP121, 144, 151, 164. Shaded areas are referred to BR composition

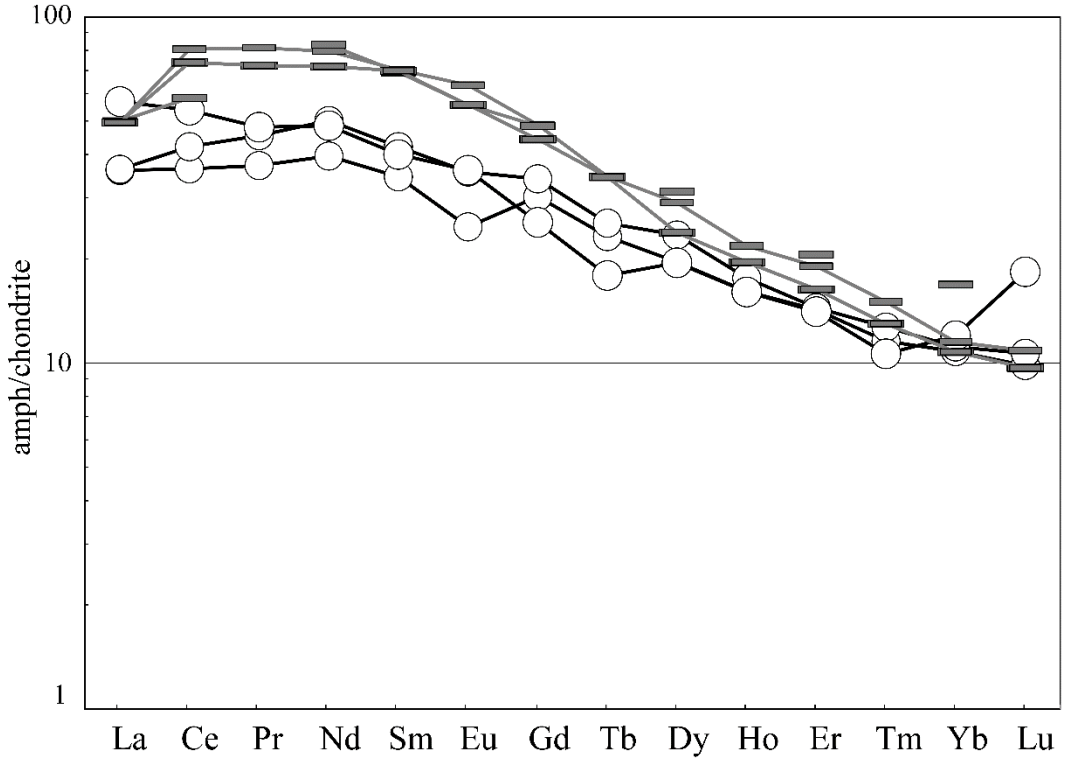

Fig. 5.8: REE Chondrite-normalised pattern for HP amphibole, symbols are in Fig. 5.3 only referring to samples HP121. For comparison samples from BR are also reported gray tick marks

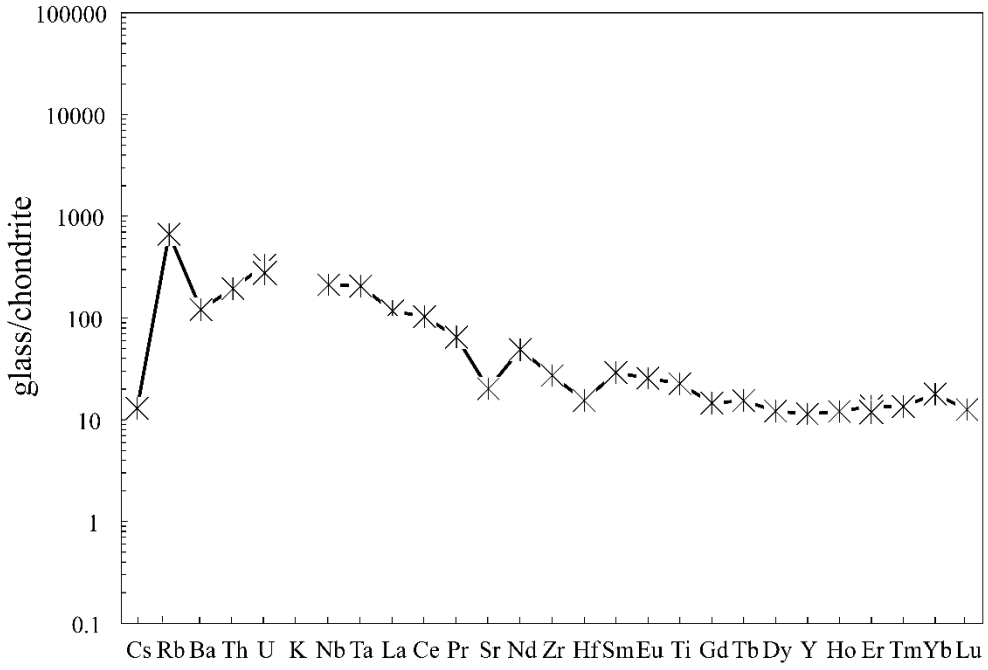

Fig. 5.9 Chondrite-normalised incompatible element diagrams of glasses in HP xenoliths. Symbols are in Fig. 5.3 only referring to sample HP144

5.4 Equilibrium conditions and Geothermobarometric constrains

In order to test the chemical equilibrium between the HP silicate phases, the Kd $Fe/Mg^{sp/ol}$ *vs* cr# in sp (Liermann and Ganguly, 2003) are plotted in Fig 5.10; this reveals that sp and ol are in equilibrium, as well as ol and opx which are basically equilibrated, as already argued from geochemical data.

Considering the general equilibrium between ol, opx and sp, and in order to provide a comparison between HP and the other Antarctic localities, the ol-sp thermometer of O'Neill & Wall (1987), as modified by Ballhaus et al. (1991), was applied.

In Fig. 5.11 are reported T vs fO_2 conditions. HP amphibole consists of a new mineralogical type (Gentili et al. 2014; 2015) and the fugacity conditions are strongly affected by its presence. In some samples (HP124 and HP164), in fact, the fugacity conditions, calculated on the basis of anhydrous parageneses largely deviate from those calculated on the basis of amphibole dehydration equilibrium and the application of the dissociation reaction (ΔQFM = +5; + 6.8, Gentili et al., 2015) (Fig. 5.11). On the whole considering anhydrous parageneses, the fugacity conditions vary from $\Delta\log fO_2$ (QFM) -2.78 to -0.24. The temperatures range from 800 °C to 1100 °C, with the highest temperatures registered for anhydrous samples HP144 and HP151.

These thermo-barometric data highlighted a different history for HP than those observed in BR (T~ 900 °C; fO_2 ~QFM-1; Bonadiman et al., 2014).

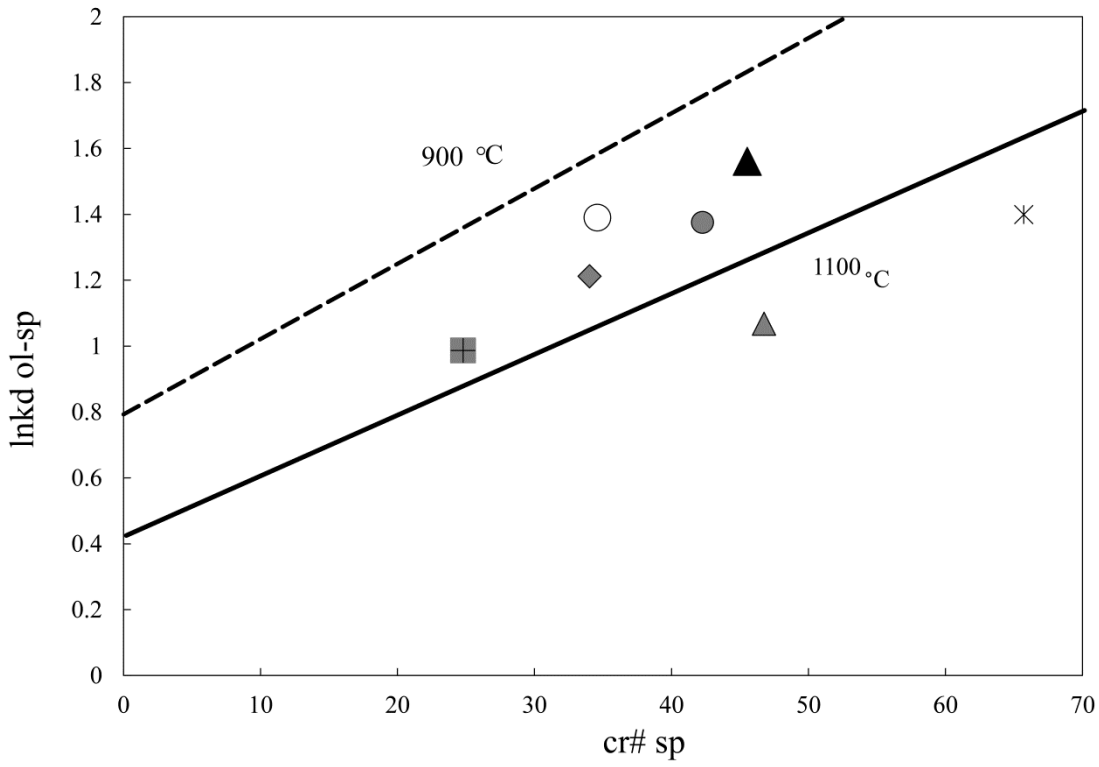

Fig 5.10: Kd Spinel-Olivine is Fe-Mg partitioning between olivine and spinel determined on the basis of the Liermann & Ganguly (2003) model. (Fe/Mg) indicates Fe^{2+}/Mg, as calculated by stoichiometry for each mineral. Symbols as in Fig. 5.3.

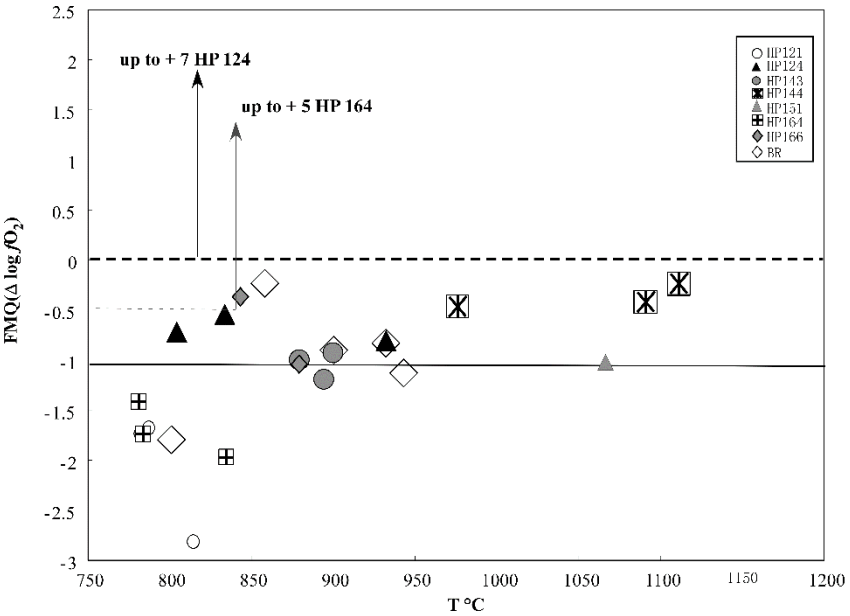

Fig 5.11 HP, Temperature and ($\Delta \log fO_2$) FQM = fO_2 relative to the buffer reaction FMQ calculated with the formula of Ballhaus et al. (1991). P is fixed at 15 Kbar. T-fO_2 conditions from BR are also reported, for comparison. fO_2 for HP164 and HP124 calculated with Popp et al. (2006) oxy-amphibole equilibrium are also reported (Gentili et al., 2015).

5.5 Amphibole genesis and conclusions

As concluded by Coltorti et al. (2004), amphibole from BR is formed by reaction between the metasomatic melt and the primary anhydrous parageneses, mainly at the expense of clinopyroxene and spinel. HP xenoliths probably record a different step of the melt-peridotite interaction processes, from that observed in BR.

Looking at Fig.5.4 a) and, b) it is possible to recognise two similar evolution trends, that at HP is characterised by lower enrichment in TiO_2 and Al_2O_3 contents both in cpx and amph, taking into account that HP peridotite matrix presents a more residual character with respect to BR, the HP newly formed assemblage show different level of elementary enrichment; however, HP 121 it is not included in this frame.

Overall geochemical data reveal a relative disequilibrium condition between amph and the other peridotite phases, this can be also deduced by fO_2 estimates. While in BR the fugacity conditions obtained from sp and amp (Bonadiman et al., 2014) are coherent each other, in HP a strong discrepancy between the fO_2 values obtained by amphibole (Gentili et al., 2015) and those obtain considering only anhydrous parageneses (this study) is observed. This supports the hypothesis that the amph at HP is at the initial stage of its genesis.

Appendix A5

Table A5.1: Major elements content (wt%) of HP olivines

Sample	HP121	HP121	HP121	HP124	HP124	HP124	HP143	HP143	HP1434	HP144
Host rock	Lh	Lh	Lh	Wh	Wh	Wh	Lh	Lh	Lh	Hz
phase	ol	ol	ol	ol	ol	ol	ol	ol	ol	ol
rim/core	rim	core	rim	core	core	rim	core	rim	core	core
SiO2	41.5	41.21	41.54	40.57	40.34	40.23	40.44	40.18	40.54	40.51
TiO2	0.02	0.02	0	0	0	0.01	0	0	0	0
Al2O3	0	0	0.01	0	0	0	0.01	0.05	0.01	0.01
FeO	9.4	9.6	9.55	11.34	11.54	11.35	11.81	12.3	12.1	10.65
MnO	0.09	0.1	0.08	0.18	0.18	0.17	0.17	0.16	0.17	0.11
MgO	47.99	48.37	48.52	47.07	46.67	47.03	46.82	46.7	46.6	47.69
CaO	0.02	0.05	0.03	0.02	0.03	0.05	0.04	0.07	0.04	0.02
Na2O	0.03	0.04	0.03	0	0	0	0	0	0	0
K2O	0	0	0.04	0	0	0	0	0	0	0
Cr2O3	0	0.01	0.05	0.03	0	0.01	0.01	0.01	0.02	0
NiO	0.41	0.36	0.47	0.31	0.33	0.29	0.34	0.32	0.28	0.37
Tot	99.46	99.76	100.32	99.52	99.09	99.14	99.64	99.79	99.76	99.36
mg#	90.10	89.98	90.05	88.09	87.82	88.07	87.60	87.12	87.28	88.86
Si	1.019	1.011	1.013	1.007	1.007	1.004	1.005	1.000	1.007	1.004
Ti	0.000	0.000	0.000	0.000	0.000	0.000	0.000	0.000	0.000	0.000
Al	0.000	0.000	0.000	0.000	0.000	0.000	0.000	0.000	0.000	0.000
Fe	0.193	0.197	0.195	0.235	0.241	0.237	0.245	0.249	0.251	0.221
Mn	0.002	0.002	0.002	0.004	0.004	0.004	0.004	0.004	0.004	0.002
Mg	1.757	1.769	1.764	1.741	1.735	1.745	1.734	1.739	1.725	1.761
Ca	0.001	0.001	0.001	0.001	0.001	0.001	0.001	0.002	0.001	0.001
Na	0.001	0.002	0.001	0.000	0.000	0.000	0.000	0.000	0.000	0.000
K	0.000	0.000	0.001	0.000	0.000	0.000	0.000	0.000	0.000	0.000
Cr	0.000	0.000	0.001	0.001	0.000	0.000	0.000	0.000	0.000	0.000
Ni	0.008	0.007	0.009	0.006	0.007	0.006	0.007	0.005	0.006	0.007
Summcat	3	3	3	3	3	3	3	3	3	3

Table A5.1: Continued

Sample	HP144	HP144	HP151	HP151	HP151	HP164	HP164	HP164	HP166	HP166	HP166
Host rock	Hz	Hz	Lh	Lh	Lh	Lh	Lh	Lh	Lh	Lh	Lh
phase	ol	ol	ol	ol	ol	ol	ol	ol	ol	ol	ol
rim/core	rim	rim	rim	rim	core	core	rim	core	rim	core	rim
SiO2	40.47	40.41	40.43	40.32	40.51	39.55	40.1	40.26	40.66	40.533	40.42
TiO2	0.01	0.01	0	0	0.01	0	0.02	0.01	0.03	0	0
Al2O3	0	0.01	0.02	0.01	0.01	0.05	0.01	0	0.01	0	0.01
FeO	10.67	10.88	11.96	11.88	11.96	13.51	13.31	13.27	10.99	11.092	10.98
MnO	0.16	0.17	0.14	0.18	0.15	0.19	0.21	0.22	0.14	0.145	0.16
MgO	47.61	47.43	46.97	46.88	46.89	45.06	44.64	45.28	47.4	47.333	47.43
CaO	0.03	0.03	0.02	0.03	0.04	0.09	0.07	0.07	0.01	0.007	0.01
Na2O	0	0	0	0	0	0.02	0.03	0.01	0	0	0
K2O	0	0	0	0	0	0	0.01	0	0	0	0
Cr2O3	0.01	0	0.02	0	0	0	0	0.05	0	0.016	0.01
NiO	0.41	0.34	0.37	0.34	0.35	0.33	0.36	0.41	0.37	0.377	0.4
Tot	99.37	99.28	99.93	99.64	99.92	98.8	98.76	99.58	99.61	99.504	99.42
mg#	88.83	88.60	87.50	87.55	87.48	85.60	85.67	85.88	88.49	88.38	88.50
Si	1.002	1.004	1.002	1.002	1.004	1.000	1.012	1.008	1.006	1.007	1.003
Ti	0.000	0.000	0.000	0.000	0.000	0.000	0.000	0.000	0.001	0.000	0.000
Al	0.000	0.000	0.001	0.000	0.000	0.001	0.000	0.000	0.000	0.000	0.000
Fe	0.222	0.226	0.248	0.247	0.248	0.286	0.281	0.278	0.227	0.232	0.228
Mn	0.003	0.004	0.003	0.004	0.003	0.004	0.004	0.005	0.003	0.003	0.003
Mg	1.762	1.755	1.735	1.737	1.732	1.698	1.679	1.690	1.748	1.744	1.754
Ca	0.001	0.001	0.001	0.001	0.001	0.002	0.002	0.002	0.000	0.001	0.000
Na	0.000	0.000	0.000	0.000	0.000	0.001	0.001	0.000	0.000	0.000	0.000
K	0.000	0.000	0.000	0.000	0.000	0.000	0.000	0.000	0.000	0.000	0.000
Cr	0.000	0.000	0.000	0.000	0.000	0.000	0.000	0.001	0.000	0.000	0.000
Ni	0.007	0.007	0.007	0.007	0.007	0.007	0.007	0.008	0.007	0.007	0.008
summ cat	3	3	3	3	3	3	3	3	3	3	3

Lh is for Lherzolite, Hz for Harzburgite, Wh for Wehrlite

mg# = [100 * Mg/(Mg+ FeTot)]

Table A5.2: Major elements content (wt%) of HP orthopyroxenes

Sample	HP121	HP121	HP121	HP143	HP143	HP144	HP144	HP144	HP151	HP151
Host rock	Lh	Lh	Lh	Lh	Lh	Hz	Hz	Hz	Lh	Lh
phase	opx	opx	opx	opx	opx	opx	opx	opx	opx	opx
rim/core	core	core	rim	core	rim	core	rim	rim	rim	rim
SiO_2	57.14	55.94	56.79	55.49	55.82	56.26	56.34	57.16	55.10	57.22
TiO_2	0.08	0.2	0.19	0.07	0.06	0.09	0.10	0.03	0.13	0.03
Al_2O_3	1.33	2.61	2.5	2.98	2.37	2.02	2.17	0.46	3.32	0.69
Fe_2O_3	0	0	0	0.15	0.19	0.00	0.00	0.00	0.00	0.00
FeO	7	8.4	7.5	7.33	7.26	7.07	7.01	7.82	8.02	7.94
MnO	0.24	0.15	0.1	0.20	0.20	0.20	0.19	0.23	0.19	0.19
MgO	33.66	32.56	33.09	32.37	32.67	33.21	33.03	33.29	31.96	33.66
CaO	0.23	0.56	0.58	0.96	0.96	0.46	0.56	0.22	0.71	0.16
Na_2O	0.02	0	0	0.07	0.09	0.05	0.05	0.02	0.05	0.02
K_2O	0.01	0.02	0.02	0.02	0.00	0.00	0.01	0.00	0.00	0.00
Cr_2O_3	0.13	0.39	0.44	0.42	0.28	0.37	0.34	0.09	0.42	0.13
Tot	99.0	98.7	100.2	100.1	99.9	99.7	99.8	99.3	99.9	100.0
Fetot	7	8.4	7.5	7.46	7.43	7.07	7.01	7.82	8.02	7.94
mg#	89.55	87.35	88.72	88.5	88.7	89.3	89.4	88.4	87.7	88.3
Si	1.993	1.962	1.963	1.926	1.939	1.954	1.956	1.998	1.92	1.985
Ti	0.002	0.005	0.005	0.002	0.002	0.002	0.003	0.001	0.003	0.001
Al	0.055	0.108	0.102	0.122	0.097	0.083	0.089	0.019	0.136	0.028
Fe III	0	0	0	0.004	0.005	0	0	0	0.002	0
Fe II	0.203	0.212	0.213	0.213	0.211	0.205	0.204	0.23	0.231	0.231
Mn	0.007	0.004	0.003	0.006	0.006	0.006	0.006	0.007	0.006	0.006
Mg	1.75	1.702	1.704	1.675	1.691	1.719	1.709	1.734	1.66	1.74
Ca	0.009	0.021	0.021	0.036	0.036	0.017	0.021	0.008	0.026	0.006
Na	0.001	0	0	0.005	0.006	0.003	0.003	0.001	0.003	0.001
K	0	0.001	0.001	0.001	0	0	0	0	0	0
Cr	0.004	0.011	0.012	0.012	0.008	0.01	0.009	0.002	0.012	0.004
Al iv	0.007	0.038	0.037	0.074	0.061	0.046	0.044	0.002	0.08	0.015
Al vi	0.024	0.043	0.04	0.056	0.046	0.036	0.039	0.008	0.061	0.012
Alvi r	0.048	0.07	0.064	0.048	0.036	0.037	0.045	0.017	0.056	0.013
Mg M1	0.864	0.83	0.832	0.829	0.844	0.85	0.844	0.867	0.813	0.868
Mg M2	0.886	0.873	0.873	0.846	0.847	0.869	0.865	0.867	0.847	0.872
Fe2+ M1	0.094	0.097	0.098	0.105	0.105	0.102	0.102	0.117	0.113	0.115
Fe2+ M2	0.097	0.102	0.103	0.107	0.106	0.104	0.105	0.117	0.118	0.116
SumCa	4	4	4	4	4	4	4	4	4	4
Fe/Mg	0.12	0.12	0.13	0.13	0.12	0.12	0.12	0.13	0.14	0.13

Table A5.2: Continued

Sample	HP151	HP164	HP164	HP164	HP166	HP166	HP166
Host rock	Lh	Lh	Lh	Lh	Lh	Lh	Lh
phase	opx	opx	opx	opx	opx	opx	opx
rim/core	core	core	rim	rim	rim	core	rim
SiO_2	55.40	56.60	56.26	55.94	55.30	55.66	55.83
TiO_2	0.14	0.15	0.10	0.12	0.20	0.22	0.19
Al_2O_3	3.07	2.95	2.97	2.94	2.38	2.34	2.16
Fe_2O_3	0.00	0.00	0.00	0.00	0.01	0.00	0.02
FeO	8.19	8.18	9.01	8.03	7.43	7.44	7.67
MnO	0.18	0.14	0.12	0.12	0.19	0.20	0.19
MgO	32.09	32.38	31.65	32.17	32.50	32.51	32.70
CaO	0.58	0.62	0.52	0.50	0.63	0.63	0.52
Na_2O	0.03	0.00	0.05	0.05	0.00	0.00	0.03
K_2O	0.00	0.00	0.01	0.02	0.00	0.00	0.02
Cr_2O_3	0.34	0.38	0.43	0.43	0.38	0.37	0.35
Tot	100.0	100.2	100.1	99.6	99.0	99.4	99.7
Fetot	8.19	8.18	9.01	8.03	7.44	7.44	7.69
mg#	87.5	87.6	86.2	87.7	88.6	88.6	88.3
Si	1.929	1.961	1.96	1.951	1.94	1.946	1.946
Ti	0.004	0.004	0.003	0.003	0.005	0.006	0.005
Al	0.126	0.12	0.122	0.121	0.098	0.096	0.089
Fe III	0	0	0	0	0	0	0.001
Fe II	0.238	0.235	0.261	0.233	0.218	0.218	0.223
Mn	0.005	0.004	0.004	0.004	0.006	0.006	0.006
Mg	1.665	1.672	1.643	1.672	1.699	1.694	1.699
Ca	0.022	0.023	0.019	0.019	0.024	0.024	0.019
Na	0.002	0	0.003	0.003	0	0	0.002
K	0	0	0	0.001	0	0	0.001
Cr	0.009	0.01	0.012	0.012	0.011	0.01	0.01
Al iv	0.071	0.039	0.04	0.049	0.06	0.054	0.054
Al vi	0.056	0.051	0.054	0.053	0.039	0.037	0.036
Alvi r	0.055	0.082	0.082	0.072	0.038	0.042	0.035
Mg M1	0.815	0.812	0.797	0.813	0.838	0.835	0.84
Mg M2	0.85	0.86	0.846	0.859	0.86	0.859	0.86
Fe2+ M1	0.116	0.107	0.12	0.109	0.108	0.109	0.11
Fe2+ M2	0.121	0.113	0.127	0.115	0.11	0.112	0.113
SumCa	4	4	4	4	4	4	4
Fe/Mg	0.14	0.14	0.16	0.14	0.13	0.13	0.13

Table A5.3: Major elements content (wt%) of HP clinopyroxenes

Sample	HP121	HP121	HP124	HP124	HP124	HP143	HP143	HP143	HP144
Host rock	Lh	Lh	Wh	Wh	Wh	Lh	Lh	Lh	Hz
phase	cpx	cpx	cpx	cpx	cpx	cpx	cpx	cpx	cpx
rim/core	rim	core	rim	core	core	rim	rim	rim	core
SiO_2	54.58	54.47	54.49	49.87	47.73	52.81	52.19	50.53	54.22
TiO_2	0.35	0.11	0.11	0.88	1.42	0.35	0.45	1.06	0.28
Al_2O_3	2.1	1.6	0.67	5.84	7.24	3.57	3.35	5.74	1.42
Fe_2O_3	0	0	0.19	0.43	0.5	0.29	0.25	0.38	0.09
FeO	3.04	2.23	2.63	2.11	2.39	3.02	2.45	2.62	2.98
MnO	0.05	0.08	0.09	0.05	0.06	0.1	0.11	0.1	0.11
MgO	18.36	17.8	17.1	14.99	14.24	16.57	16.11	15.41	19.46
CaO	21.29	22.8	23.14	23.72	23.42	21.72	23.45	21.62	19.38
Na_2O	0.4	0.4	0.63	0.49	0.39	0.8	0.47	0.96	0.59
K_2O	0	0.04	0	0.02	0.02	0.02	0	0.02	0
Cr_2O_3	0.55	0.38	0.74	1.89	1.78	0.55	0.93	1.07	1.21
Tot	100.06	99.91	99.79	100.29	99.19	99.8	99.77	99.51	99.74
Fetot	2.42	2.23	2.80	2.50	2.84	3.28	2.67	2.96	3.06
mg#	93.13	93.43	91.58	91.45	89.93	90.00	91.48	90.26	91.89
Si	1.971	1.973	1.984	1.817	1.764	1.919	1.905	1.846	1.961
Ti	0.01	0.003	0.003	0.024	0.039	0.01	0.012	0.029	0.008
Al	0.089	0.068	0.029	0.251	0.315	0.153	0.144	0.247	0.061
Fe III	0	0	0.005	0.012	0.014	0.008	0.007	0.01	0.002
Fe II	0.084	0.068	0.08	0.064	0.074	0.092	0.075	0.08	0.09
Mn	0.002	0.002	0.003	0.002	0.002	0.003	0.003	0.003	0.003
Mg	0.988	0.961	0.928	0.814	0.784	0.897	0.876	0.839	1.049
Ca	0.824	0.885	0.903	0.926	0.927	0.846	0.917	0.846	0.751
Na	0.028	0.028	0.044	0.035	0.028	0.056	0.033	0.068	0.041
K	0	0.002	0	0.001	0.001	0.001	0	0.001	0
Cr	0.016	0.011	0.021	0.054	0.052	0.016	0.027	0.031	0.035
Al iv	0.029	0.027	0.016	0.183	0.236	0.081	0.095	0.154	0.039
Al vi	0.041	0.04	0.023	0.091	0.106	0.087	0.063	0.113	0.026
Alvi r	0.06	0.041	0.013	0.068	0.079	0.072	0.049	0.093	0.021
Mg M1	0.853	0.883	0.882	0.78	0.746	0.812	0.834	0.764	0.86
Mg M2	0.135	0.079	0.046	0.035	0.039	0.086	0.043	0.076	0.188
Fe2+ M1	0.071	0.062	0.076	0.062	0.07	0.083	0.071	0.073	0.074
Fe2+ M2	0.011	0.005	0.004	0.003	0.004	0.009	0.004	0.007	0.016
SumCa	4	4	4	4	4	4	4	4	4
Fe/Mg	0.08	0.07	0.09	0.08	0.09	0.10	0.09	0.10	0.09

Table A5.3: Continued

Sample	HP144	HP144	HP151	HP151	HP151	HP164	HP164	HP164	HP166	HP166	HP166
Host rock	Hz	Hz	Lh	Lh	Lh	Lh	Lh	Lh	Lh	Lh	Lh
phase	cpx	cpx	cpx	cpx	cpx	cpx	cpx	cpx	cpx	cpx	cpx
rim/core	core	core	core	core	core	rim	rim	rim	core	core	core
SiO_2	53.98	54.55	51.67	53.54	52.38	52.53	51.97	52.02	52.2	52.4	51.85
TiO_2	0.34	0.04	0.14	0.16	0.31	0.49	0.42	0.34	0.58	0.6	0.63
Al_2O_3	1.44	0.6	4.16	1.6	3.67	5.31	4.76	5	3.43	3.33	3.55
Fe_2O_3	0.16	0.27	0.25	0.14	0.24	-0.43	-0.01	-0.02	0.33	0.23	0.41
FeO	2.91	2.44	2.12	2.48	2.75	3.34	3.81	4.11	2.63	2.69	2.72
MnO	0.11	0.12	0.06	0.1	0.09	0.08	0.11	0.14	0.08	0.11	0.08
MgO	18.68	17.52	16.21	16.96	16.03	15.73	15.54	15.3	16.16	16.19	16
CaO	20.47	22.52	23.48	23.12	23.33	20.83	21.18	20.85	22.86	23.01	22.78
Na_2O	0.59	0.72	0.31	0.45	0.49	0.85	0.81	0.9	0.65	0.58	0.68
K_2O	0	0.01	0	0.01	0	0	0	0.02	0.01	0	0.01
Cr_2O_3	1.16	0.96	1.69	0.84	0.69	0.65	0.79	0.79	0.94	0.78	0.93
Tot	99.84	99.75	100.1	99.4	99.98	99.38	99.38	99.46	99.87	99.92	99.64
Fetot	3.05	2.68	2.34	2.61	2.97	2.95	3.80	4.09	2.93	2.90	3.09
mg#	91.60	92.09	92.49	92.06	90.59	90.47	87.93	86.95	90.77	90.87	90.23
Si	1.956	1.983	1.88	1.957	1.907	1.917	1.903	1.905	1.902	1.909	1.894
Ti	0.009	0.001	0.004	0.004	0.008	0.013	0.012	0.009	0.016	0.016	0.017
Al	0.061	0.026	0.178	0.069	0.157	0.228	0.206	0.216	0.147	0.143	0.153
Fe III	0.004	0.007	0.007	0.004	0.007	-0.012	0	0	0.009	0.006	0.011
Fe II	0.088	0.074	0.065	0.076	0.084	0.102	0.117	0.126	0.08	0.082	0.083
Mn	0.003	0.004	0.002	0.003	0.003	0.002	0.003	0.004	0.002	0.003	0.002
Mg	1.009	0.949	0.879	0.924	0.87	0.855	0.848	0.835	0.877	0.879	0.871
Ca	0.795	0.877	0.915	0.906	0.91	0.814	0.831	0.818	0.892	0.898	0.892
Na	0.041	0.051	0.022	0.032	0.035	0.06	0.058	0.064	0.046	0.041	0.048
K	0	0	0	0	0	0	0	0.001	0	0	0
Cr	0.033	0.028	0.049	0.024	0.02	0.019	0.023	0.023	0.027	0.022	0.027
Al iv	0.044	0.017	0.12	0.043	0.093	0.083	0.097	0.095	0.098	0.091	0.106
Al vi	0.026	0.023	0.072	0.034	0.078	0.121	0.108	0.119	0.067	0.064	0.07
Alvi r	0.017	0.009	0.058	0.026	0.064	0.145	0.109	0.12	0.049	0.052	0.047
Mg M1	0.861	0.886	0.822	0.87	0.822	0.746	0.753	0.737	0.824	0.826	0.819
Mg M2	0.148	0.063	0.057	0.055	0.048	0.11	0.095	0.099	0.054	0.053	0.053
Fe2+ M1	0.075	0.069	0.06	0.071	0.079	0.089	0.104	0.111	0.075	0.077	0.078
Fe2+ M2	0.013	0.005	0.004	0.004	0.005	0.013	0.013	0.015	0.005	0.005	0.005
SumCa	4	4	4	4	4	4	4	4	4	4	4
Fe/Mg	0.09	0.08	0.07	0.08	0.10	0.12	0.14	0.15	0.09	0.09	0.10

Table A5.4: Major elements content (wt%) of HP spinels

Sample	HP121	HP121	HP121	HP124	HP124	HP124	HP143	HP143	HP143	HP144
Host rock	Lh	Lh	Lh	Wh	Wh	Wh	Lh	Lh	Lh	Hz
phase	sp	sp	sp	sp	sp	sp	sp	sp	sp	sp
SiO_2	0.03	0.02	0.02	0	0	0	0	0	0.01	0.03
TiO_2	0.36	0.28	0.26	1.04	0.6	0.64	0.5	0.39	0.44	0.21
Al_2O_3	40.07	37.54	40.48	33.68	29.5	31.85	32.74	28.14	32.73	20.26
Fe_2O_3	1.16	0.69	0.3	4.26	3.18	6.32	3.22	2.98	2.95	3.71
FeO	13.2	13.22	12.25	15.75	15.65	16.31	14.43	15.37	14.42	11.97
MnO	0.2	0.22	0.14	0.19	0.24	0.24	0.15	0.18	0.19	0.16
MgO	16.14	15.49	16.59	14.73	14.11	13.79	14.91	13.69	14.87	14.9
CaO	0	0	0	0	0	0	0	0.01	0	0.03
Na_2O	0	0	0.02	0	0	0	0	0	0	0
K_2O	0	0.01	0.01	0	0	0	0	0	0	0
Cr_2O_3	27.28	29.62	27.7	31.35	37.75	31.36	33.58	38.59	33.86	47.43
NiO	0.22	0.24	0.17	0.16	0.12	0.15	0.15	0.16	0.11	0.1
Total	98.67	97.33	97.94	101.18	101.14	100.67	99.68	99.51	99.58	98.80
Fetot	14.24	13.84	12.52	19.58	18.51	22.00	17.33	18.05	17.07	15.31
Si	0.001	0.001	0.001	0	0	0	0	0	0	0.001
Ti	0.008	0.006	0.006	0.023	0.013	0.014	0.011	0.009	0.01	0.005
Al	1.344	1.29	1.359	1.146	1.024	1.103	1.13	0.998	1.131	0.74
Fe	0.02	0.02	0.01	0.09	0.07	0.14	0.07	0.07	0.06	0.09
Fe II	0.31	0.32	0.29	0.38	0.39	0.4	0.35	0.39	0.35	0.31
Mn	0.005	0.005	0.003	0.005	0.006	0.006	0.004	0.005	0.005	0.004
Mg	0.685	0.673	0.704	0.634	0.619	0.604	0.65	0.614	0.649	0.688
Ca	0	0	0	0	0	0	0	0	0	0.001
Na	0	0	0.001	0	0	0	0	0	0	0
K	0	0	0	0	0	0	0	0	0	0
Cr	0.614	0.682	0.624	0.716	0.879	0.728	0.777	0.917	0.784	1.162
Ni	0.005	0.006	0.004	0.004	0.003	0.004	0.004	0.004	0.003	0.002
Cr/Cr+Al	0.3135	0.346	0.3146	2.998	3.004	2.999	0.4075	0.4791	0.4096	0.6109
Mg/BIV	0.6821	0.6725	0.7047	0.3843	0.4618	0.3977	0.6457	0.6107	0.6446	0.6864
Fe II/BIV	0.3131	0.3221	0.292	0.6221	0.6128	0.5975	0.3506	0.3847	0.3507	0.3094
Fe III/TRIV	0.0126	0.0076	0.0032	0.3733	0.3813	0.3966	0.0359	0.034	0.0328	0.0435
Cr/TRIV	0.3095	0.3434	0.3135	0.0474	0.0357	0.0709	0.3929	0.4628	0.3962	0.5843
Al/TRIV	0.6779	0.649	0.6832	0.3661	0.4453	0.3695	0.5712	0.5032	0.571	0.3722
Cr#	31.36	34.58	31.47	38.45	46.19	39.76	40.74	47.89	40.94	61.09
mg#	66.88	66.60	70.25	57.27	57.60	52.77	60.53	57.47	60.81	63.43
Fe/Mg	0.45	0.48	0.41	0.60	0.63	0.66	0.54	0.64	0.54	0.45

cr# =[100*Cr/Cr+Al)]

Table A5.4: Continued

Sample	HP144	HP144	HP151	HP151	HP151	HP164	HP164	HP164	HP166	HP166	HP166
Host rock	Hz	Hz	Lh	Lh	Lh	Lh	Lh	Lh	Lh	Lh	Lh
phase	sp	sp	sp	sp	sp	sp	sp	sp	sp	sp	sp
SiO_2	0.04	0.03	0	0.04	0.03	0.08	0.04	0.09	0.03	0.04	0.03
TiO_2	0.22	0.09	0.08	0.07	0.05	0.25	0.2	0.2	0.34	0.36	0.56
Al_2O_3	18.26	18.85	37.01	28.12	29.88	43.85	43.58	43.9	39.61	38.2	35.92
Fe_2O_3	3.23	2.64	2.65	2.98	2.54	1.88	1.87	1.92	1.91	2.26	2.79
FeO	12.62	14.08	11.69	13.1	12.02	14.25	14.15	13.69	12.57	11.78	13.97
MnO	0.14	0.19	0.1	0.12	0.17	0.18	0.16	0.16	0.15	0.13	0.14
MgO	14.42	13.41	17.42	15.77	15.97	15.59	15.46	15.88	16.78	17.03	15.45
CaO	0.02	0.02	0.04	0.02	0.04	0	0.03	0.02	0	0.01	0
Na_2O	0	0	0	0	0	0	0	0.03	0	0	0
K_2O	0	0	0	0	0	0	0	0	0	0	0
Cr_2O_3	50.23	49.83	33.09	42.36	39.08	21.28	21.47	21.76	28.23	29.18	29.92
NiO	0.07	0.07	0.18	0.06	0.14	0.24	0.27	0.33	0.19	0.21	0.16
Total	99.25	99.20	102.26	102.65	99.91	97.60	97.23	97.98	99.81	99.21	98.94
Fetot	15.53	16.46	14.07	15.78	14.31	15.94	15.83	15.42	14.29	13.81	16.48
Si	0.001	0.001	0	0.001	0.001	0.002	0.001	0.003	0.001	0.001	0.001
Ti	0.005	0.002	0.002	0.002	0.001	0.005	0.004	0.004	0.007	0.008	0.012
Al	0.672	0.697	1.214	0.96	1.033	1.467	1.465	1.461	1.315	1.279	1.227
Fe	0.08	0.06	0.06	0.06	0.06	0.04	0.04	0.04	0.04	0.05	0.06
Fe II	0.33	0.37	0.27	0.32	0.29	0.34	0.34	0.32	0.3	0.28	0.34
Mn	0.004	0.005	0.002	0.003	0.004	0.004	0.004	0.004	0.004	0.003	0.003
Mg	0.671	0.627	0.722	0.681	0.698	0.659	0.657	0.668	0.704	0.721	0.667
Ca	0.001	0.001	0.001	0	0.001	0	0.001	0.001	0	0	0
Na	0	0	0	0	0	0	0	0.002	0	0	0
K	0	0	0	0	0	0	0	0	0	0	0
Cr	1.239	1.235	0.728	0.97	0.907	0.478	0.484	0.486	0.628	0.655	0.686
Ni	0.002	0.002	0.004	0.001	0.003	0.005	0.006	0.007	0.004	0.005	0.004
Cr/Cr+Al	0.6485	0.6394	0.3749	0.5026	0.4673	0.2455	0.2483	0.2495	0.3234	0.3388	0.3584
Mg/BIV	0.6681	0.6261	0.7247	0.68	0.7001	0.6581	0.6582	0.6714	0.7016	0.7181	0.6612
Fe II/BIV	0.3282	0.3688	0.2729	0.3169	0.2956	0.3376	0.338	0.3247	0.2948	0.2788	0.3354
Fe III/TRIV	0.0382	0.0312	0.0277	0.0326	0.0281	0.0202	0.0202	0.0206	0.0205	0.0244	0.0309
Cr/TRIV	0.6237	0.6194	0.3645	0.4862	0.4542	0.2406	0.2433	0.2444	0.3168	0.3305	0.3473
Al/TRIV	0.3381	0.3494	0.6078	0.4812	0.5178	0.7392	0.7365	0.7351	0.6628	0.6451	0.6218
Cr#	64.84	63.92	37.49	50.26	46.75	24.58	24.83	24.96	32.32	33.87	35.86
mg#	62.34	59.22	68.80	64.04	66.55	63.54	63.50	64.73	67.67	68.72	62.55
Fe/Mg	0.49	0.59	0.37	0.47	0.42	0.52	0.52	0.48	0.43	0.39	0.51

Table A5.5: Major elements content (wt%) of HP amphiboles

Sample	HP121	HP121	HP121	HP124	HP124	HP124	HP143	HP143	HP143	HP164
Host rock	Lh	Lh	Lh	Wh	Wh	Wh	Lh	Lh	Lh	Lh
phase	amph	amph	amph	amph	amph	amph	amph	amph	amph	amph
SiO_2	43.33	43.33	42.95	42.88	43.26	43.77	44.18	44.23	46.83	42.33
TiO_2	3.27	3.77	3.39	2.53	2.36	1.86	1.85	2.09	2.68	3.06
Al_2O_3	13.03	12.73	12.66	12.58	12.39	13.56	12.2	12.68	8.81	14.86
Fe_2O_3	0	0	0	0	0	0	1.07	0.7	0	0.91
FeO	3.25	3.31	3.49	3.79	3.86	3.66	3.08	3.75	3.74	5.1
MnO	0.08	0.08	0.03	0.05	0.03	0.04	0.05	0.04	0.07	0.1
MgO	17.15	17.04	16.96	17.48	17.78	13.93	17.86	17.66	13.93	16.06
CaO	12.08	11.94	12.04	12.55	12.66	19.98	11.65	11.88	22.59	11.56
Na_2O	2.99	2.61	2.57	3.37	3.3	1.25	3.22	3.43	0.683	3.08
K_2O	0.5	0.76	0.65	0.21	0.18	0.2	0.1	0.166	0	0.977
Cr_2O_3	1.48	1.61	1.5	1.51	1.33	1.42	1.71	1.61	1.48	1.256
NiO	0.05	0.1	0.13	0.05	0.08	0.05	0.08	0.109	0.079	0.091
Tot	97.19	97.3	96.37	97.02	97.27	99.74	96.99	98.28	100.89	99.29
Fetot	3.25	3.31	3.49	3.79	3.86	3.66	4.04	4.38	3.74	5.92
mg#	90.39	90.17	89.65	89.15	89.14	87.15	88.73	87.78	86.91	82.86
Si	6.197	6.193	6.202	6.172	6.204	6.188	6.283	6.241	6.573	5.97
Ti	0.352	0.405	0.368	0.274	0.255	0.198	0.198	0.222	0.283	0.325
Al	2.197	2.145	2.155	2.134	2.095	2.26	2.045	2.109	1.458	2.47
Ni	0	0	0	0	0	0	0.115	0.075	0	0.097
Fe II	0.389	0.396	0.421	0.456	0.463	0.433	0.367	0.442	0.439	0.602
Mn	0.01	0.01	0.004	0.006	0.004	0.005	0.006	0.005	0.008	0.012
Mg	3.655	3.63	3.65	3.749	3.8	2.935	3.785	3.714	2.914	3.375
Ca	1.851	1.828	1.863	1.935	1.945	3.026	1.775	1.796	3.397	1.747
Na	0.829	0.723	0.72	0.94	0.918	0.343	0.888	0.938	0.186	0.842
K	0.091	0.139	0.12	0.039	0.033	0.036	0.018	0.03	0	0.176
Cr	0.167	0.182	0.171	0.172	0.151	0.159	0.192	0.18	0.164	0.14
Ni	0.006	0.011	0.015	0.006	0.009	0.006	0.009	0.012	0.009	0.01

Table A5.6: Major elements content (wt%) of HP glasses

Sample	HP143 Lh	HP144 Hz	HP144 Hz	HP144 Hz	HP151 Lh	HP151 Lh	HP151 Lh
Na_2O	3.00	5.99	3.81	6.90	5.58	5.25	5.84
SiO_2	62.00	68.35	61.23	63.10	61.40	56.20	62.61
MgO	0.35	0.06	0.05	0.20	0.05	0.39	0.22
Al_2O_3	22.00	17.89	20.95	21.93	22.34	24.76	17.94
K2O	6.00	3.60	7.72	2.88	4.71	1.34	6.29
CaO	3.51	0.83	0.93	2.87	4.29	8.22	0.24
FeO	0.30	0.74	0.34	1.10	0.34	0.97	0.80
TiO_2	0.19	0.52	0.59	0.88	0.27	0.63	0.64
Cl	0.02	0.08	0.00	0.12	0.00	0.00	0.43
BaO	0.00	0.00	0.08	0.03	0.08	0.00	0.00
SO_2	0.00	0.01	0.00	0.02	0.01	0.00	0.00
P_2O_5	0.00	0.02	0.00	0.01	0.00	0.05	0.00
Total	97.37	98.06	95.72	100.03	99.05	97.81	95.01
TIO_2+K_2O	6.19	4.11	8.31	3.76	4.97	1.97	6.92
Na_2O+CaO	6.51	6.81	4.75	9.77	9.87	13.47	6.08

Table 5.7: Trace elements (ppm) of HP orthopyroxenes

Sample	HP144	HP144	HP151	HP151	HP164	HP164
Host Rock	Hz	Hz	Lh	Lh	Lh	Lh
Cs	0.024	0.017	0.024	0.017	0.007	0.004
Rb	0.354	14.300	0.354	14.300	0.014	0.008
Ba	6.130	17.580	6.130	17.580	0.008	0.005
Th	0.050	0.079	0.050	0.079	0.002	0.001
U	0.027	0.089	0.027	0.089	0.000	0.000
K						
Nb	0.187	1.190	0.187	1.190	0.154	0.084
Ta	0.010	0.028	0.010	0.028	0.027	0.010
La	0.027	0.194	0.027	0.194	0.019	0.045
Ce	0.037	0.207	0.037	0.207	0.003	0.012
Pr	0.004	0.034	0.004	0.034	0.004	0.010
Sr	1.234	2.853	1.234	2.853	0.022	0.142
Nd	0.026	0.133	0.026	0.133	0.017	0.015
Zr	0.180	1.590	0.180	1.590	0.015	0.008
Hf	0.006	0.003	0.006	0.003	0.029	0.014
Sm	0.010	0.017	0.010	0.017	0.023	0.034
Eu	0.009	0.013	0.009	0.013	0.011	0.015
Ti	246.735	374.945	246.735	374.945	192.780	134.125
Gd	0.023	0.041	0.023	0.041	0.047	0.041
Tb	0.005	0.006	0.005	0.006	0.029	0.017
Dy	0.036	0.097	0.036	0.097	0.092	0.083
Y	0.349	0.610	0.349	0.610	0.497	0.375
Ho	0.012	0.018	0.012	0.018	0.030	0.018
Er	0.052	0.085	0.052	0.085	0.084	0.069
Tm	0.014	0.015	0.014	0.015	0.047	0.028
Yb	0.091	0.138	0.091	0.138	0.244	0.140
Lu	0.018	0.030	0.018	0.030	0.004	0.004

Table 5.8: Trace elements (ppm) of HP clinopyroxenes

Sample	HP121	HP121	HP144	HP144	HP144	HP151	HP164	HP164
Host Rock	Lh	Lh	Hz	Hz	Hz	Lh	Lh	Lh
Cs	0.729	0.625	0.101	0.050	0.081	16.940	0.007	0.048
Rb	41.010	38.340	20.560	23.810	82.870	461.340	0.016	0.328
Ba	198.280	195.650	32.790	31.470	86.810	133.880	0.636	6.050
Th	3.400	3.300	0.424	0.381	0.397	1.664	0.114	0.141
U	1.027	0.932	0.330	0.231	0.433	1.064	0.035	0.040
K								
Nb	3.870	3.780	2.650	1.712	4.370	4.970	0.512	0.366
Ta	0.539	0.508	0.071	0.058	0.153	0.086	0.088	0.082
La	6.940	6.620	7.340	6.320	4.950	6.850	2.130	3.130
Ce	12.190	11.970	17.840	17.810	13.900	13.620	6.720	8.580
Pr	1.236	1.383	2.436	2.605	2.109	1.606	1.072	1.217
Sr	81.380	77.110	56.790	52.020	45.440	37.710	20.140	36.700
Nd	4.680	4.910	10.520	12.420	10.030	8.050	5.680	6.180
Zr	91.130	91.220	10.280	8.490	11.200	28.300	15.130	18.050
Hf	2.520	2.160	0.268	0.241	0.249	0.650	0.266	0.425
Sm	0.650	1.130	2.450	2.850	2.630	2.650	1.741	1.781
Eu	0.170	0.098	0.939	1.139	1.028	0.530	0.576	0.624
Ti	571.65	555.30	1332.71	1663.91	2863.24	7001.36	2706.84	3285.85
Gd	0.610	0.757	2.020	3.030	2.380	4.170	1.837	1.990
Tb	0.153	0.130	0.348	0.484	0.448	0.680	0.314	0.333
Dy	1.010	0.922	2.350	3.170	2.830	5.130	2.105	2.120
Y	5.840	5.500	12.920	16.860	15.380	27.730	10.890	11.060
Ho	0.171	0.184	0.475	0.633	0.630	1.005	0.435	0.450
Er	0.620	0.292	1.425	1.753	1.580	2.670	1.189	1.234
Tm	0.074	0.061	0.217	0.253	0.250	0.466	0.163	0.177
Yb	0.990	0.649	1.494	1.743	1.580	2.590	1.121	1.058
Lu	0.068	0.103	0.188	0.243	0.185	0.528	0.157	0.151

Table A5.9: Trace elements (ppm) of HP amphiboles

Sample	HP121	HP121	HP121
Host Rock	Lh	Lh	Lh
Cs	0.0382	0.0229	0.223
Rb	5.85	4.9	52.38
Ba	107.56	192.88	184.29
Th	0.613	0.368	0.802
U	0.2203	0.0622	0.272
K			
Nb	20.58	24.3	20.82
Ta	1.192	1.505	0.946
La	8.53	8.6	13.5
Ce	22.29	25.81	32.88
Pr	3.53	4.31	4.56
Sr	215.04	389.43	153.71
Nd	18.51	23.42	22.63
Zr	60.37	61.77	63.17
Hf	1.997	2.143	1.06
Sm	5.28	6.45	6.12
Eu	1.435	2.067	2.09
Ti	20365.4	26601.3	22592.4
Gd	6.21	6.99	5.24
Tb	0.867	0.949	0.669
Dy	4.97	5.95	4.95
Y	22.78	25.98	23.39
Ho	0.911	0.995	0.908
Er	2.36	2.39	2.33
Tm	0.295	0.324	0.271
Yb	1.836	1.893	2.04
Lu	0.25	0.271	0.466

Table A5.10: Trace elements (ppm) of HP glasses

Sample	HP144	HP144
Host Rock	Hz	Hz
Cs	2.44	526.31
Rb	232.86	31144.86
Ba	292.65	46009.5
Th	5.64	73.99
U	2.66	2.22
K		
Nb	52.3	2865.44
Ta	2.89	194.12
La	27.79	18.82
Ce	63.28	11.82
Pr	6.17	2.8
Sr	146.77	622.34
Nd	22.92	3.36
Zr	105.51	363.99
Hf	1.65	10.85
Sm	4.46	1.83
Eu	1.486	0.51
Ti	10097.585	351154.45
Gd	3	5.88
Tb	0.577	0.52
Dy	3.09	2.22
Y	17.87	10.65
Ho	0.684	0.37
Er	2.25	1.97
Tm	0.344	0.50
Yb	3.05	1.56
Lu	0.32	0.14

Chapter 6. Comparison and conclusions

6.1 Geochemical composition of Antarctica SCLM

The parallel study of the three mantle xenolith suites highlighted strong geochemical heterogeneity in the SCLM beneath Northern Victoria Land.

The examined mantle domain suffered a major melt extraction event, that was followed by, at least two enrichment processes, probably acting in different periods, Jurassic and Cenozoic.

In the volcanic district of Mt. Melbourne, Greene Point and Harrow Peaks mantle xenolith suites show relevant geochemical differences, highlighting the above mentioned secondary events:

HP-amphibole bearing peridotites record evidence of an alkaline metasomatic process, widely observed in the previously studied amphibole bearing Baker Rocks mantle, as also evidenced by the features of the different glasses occurred in the various localities (Fig. 6.4, 6.5). Comparing the clinopyroxene (Fig. 6.3) and amphibole composition, it is evident lower geochemical supply for HP, due to the most residual character of HP (Fig, 6.2), and/or to a more limited time span of melt/rock interaction.

In turn, lherzolites from Greene Point show a pervasive refertilisation process, so far never observed in Antarctica SCLM, that have permeated the peridotite matrix involving large volumes of magmas, causing a complete geochemical rearrangement of the peridotite phases (enrichment on Al_2O_3 in pyroxenes and cpx garnet signature) (Fig. 6.2, 6.3). This event has been temporally placed as Jurassic tholeiitic magmatism, followed by a limited effect of alkaline metasomatism.

Handler Ridge, 400 km far from Mt. Melbourne district, was, on the other hand, interested by extensive alkaline metasomatism, but surely under different physic-chemical conditions (i.e. higher Temperatures) and volatile contents, since with respect to BR and HP amphibole is inhibited.

The textural and chemical features of this latter population allowed to identify the different stages of metasomatism process, and to estimate the possible temporal evolution, confirming that metasomatism in the NVL lithospheric mantle, is an extremely fast process (~200 years).

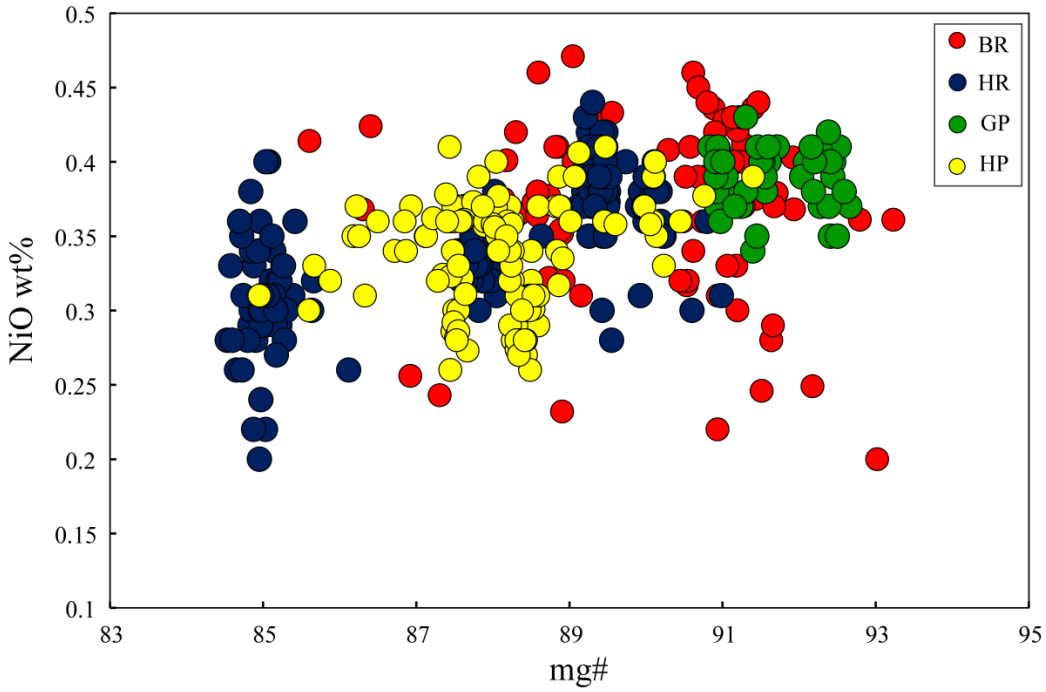

Fig. 6.1 Comparison of olivine compositions of the three mantle xenolith suites. Data from Baker Rocks are also reported (red circles)

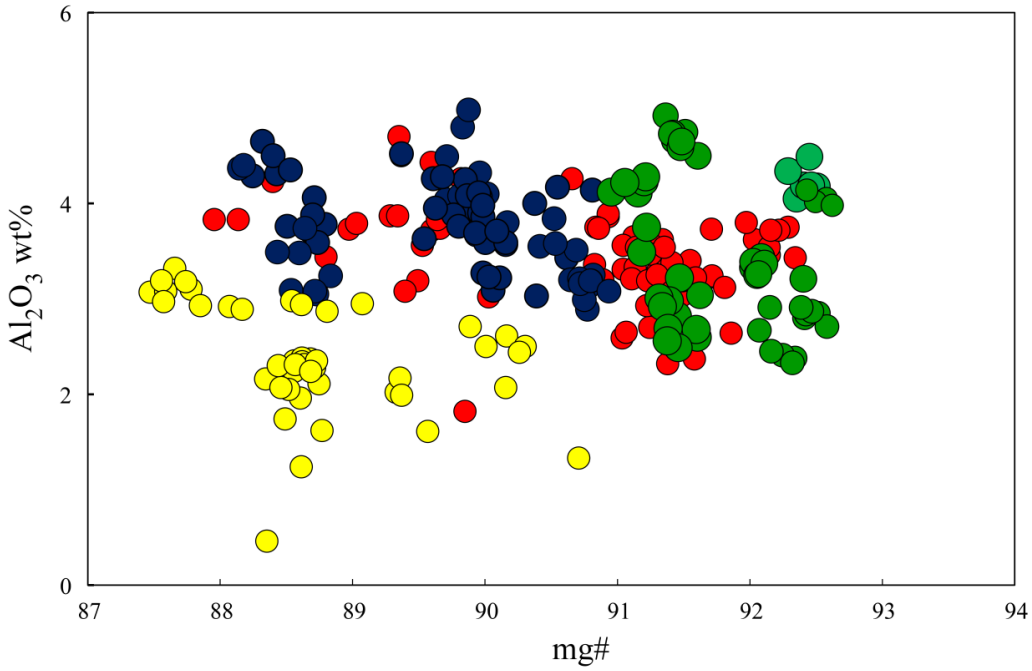

Fig. 6.2 Comparison of orthopyroxene compositions of the three mantle xenolith suites. Data from Baker Rocks are also reported (red circles).

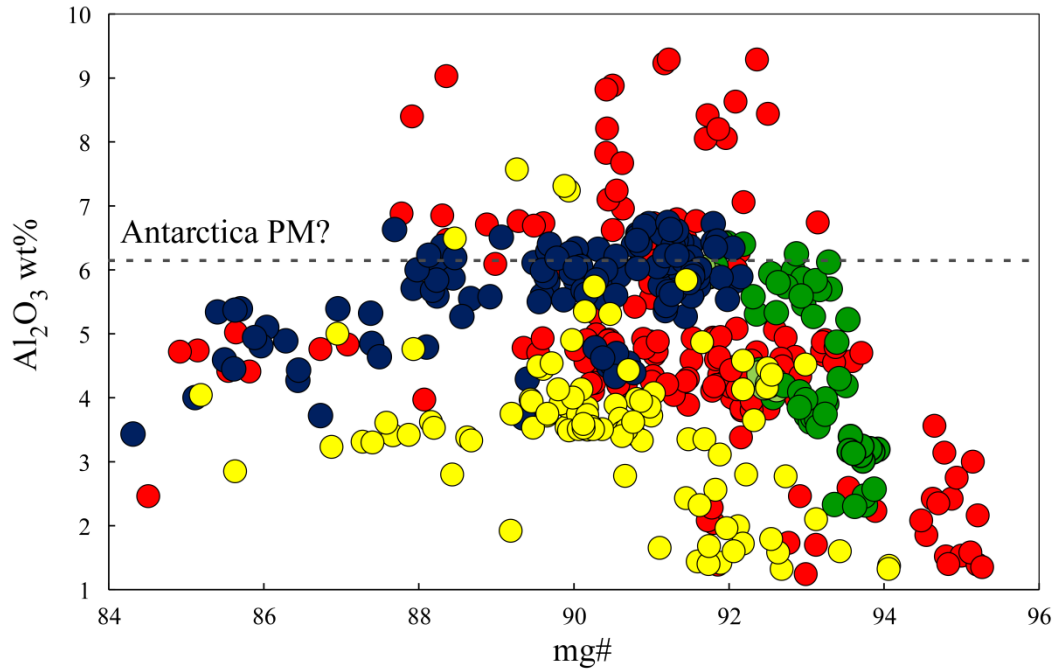

Fig 6.3 Comparison of clinopyroxene compositions of the three mantle xenoliths suites. Data from Baker Rocks are also reported (red circles). Dotted line represents the possible more primitive cpx composition in Antarctica SCLM.

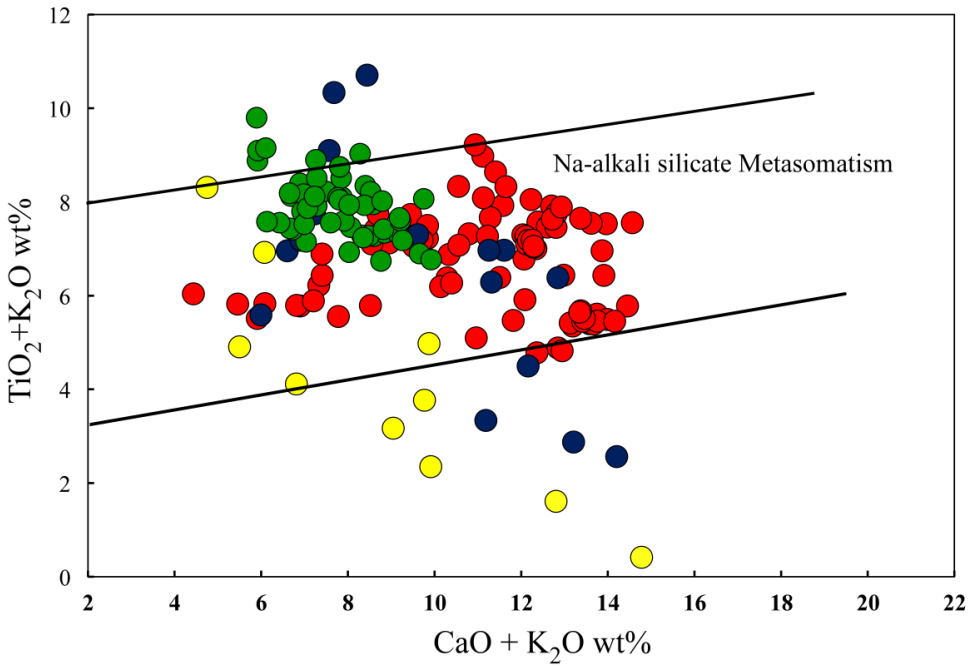

Fig. 6.4 Antarctic glasses plotted in the discrimination diagram after Coltorti et al. (2000).

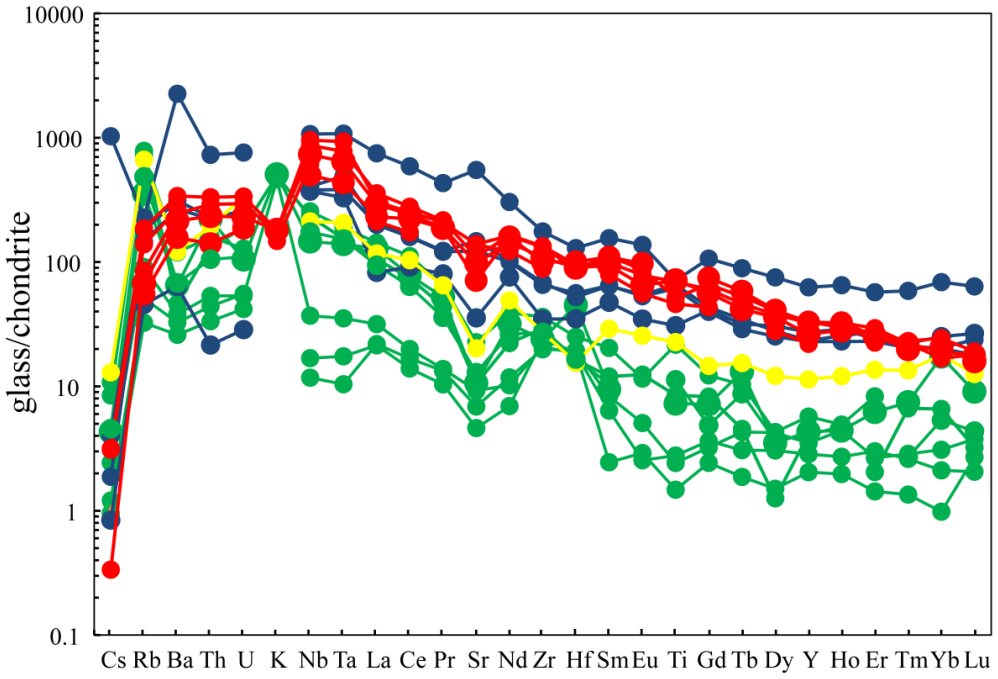

Fig. 6.5 Chondrite normalised trace element pattern of Antarctic glasses

6.2 Geothermobarometric constrains

One of the most important outputs of this study consists in the thermo-barometric constrains of this large portion of the Antarctica SCLM (Fig. 6.6).

On the whole, applying the popular method based on the mantle Fe/Mg mineral exchange, data reveal that amphibole-bearing xenolith population (HP, BR) show the lowest temperatures (~850 °C) of the region.

The highest temperatures (up to ~1050 °C) are recorded in HR mantle domain, and by the anhydrous group of HP. The presence of equilibrated hydrous phase seems do not influence the redox conditions that are comparable in GP, HP and BR (see also, Bonadiman et al., 2014).

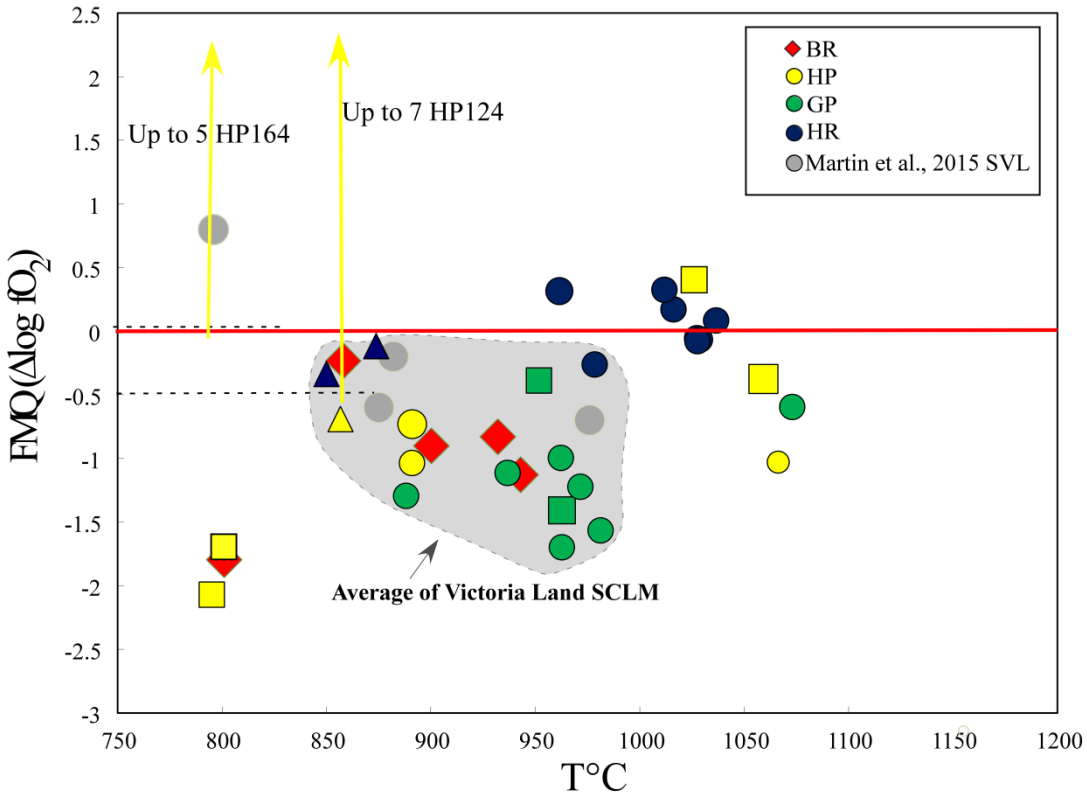

Fig. 6.6 Temperature and ($\Delta \log fO_2$) FQM = fO_2 relative to the buffer reaction FMQ calculated with the formula of Ballhaus et al. (1991) for NVL. P is fixed at 15 Kbar. Data from South Victoria Land (Martin et al., 2014) and data of fO_2 for HP164 and HP124 calculated by oxygeothermobarometer with oxy-amphibole equilibrium Popp et al. (2006) are also reported Gentili et al. (2015).

6.3 Melting Modelling

Melt models were applied only to anhydrous suites (Fig. 6.7), as they are calibrated only for unmetasomatized equilibrated lherzolites (Upton et al., 2011; Faccini et al., 2013).

However, these models allowed also to evaluate the nature enrichment processes that have variably affected the mantle portion considered. Basically samples affected by metasomatism tend to be shifted toward lower MgO values in the cpx model (Fig. 6.7 b, this work, Faccini et al., 2013), indicating disequilibrium between primary opx and secondary cpx, while a shift toward higher MgO (or higher Al_2O_3) in both the curves (Fig. 6.7 a and 6.7 b), suggest a most pervasive processes able to increase Al_2O_3 content from that expected by the theoretical residual trend.

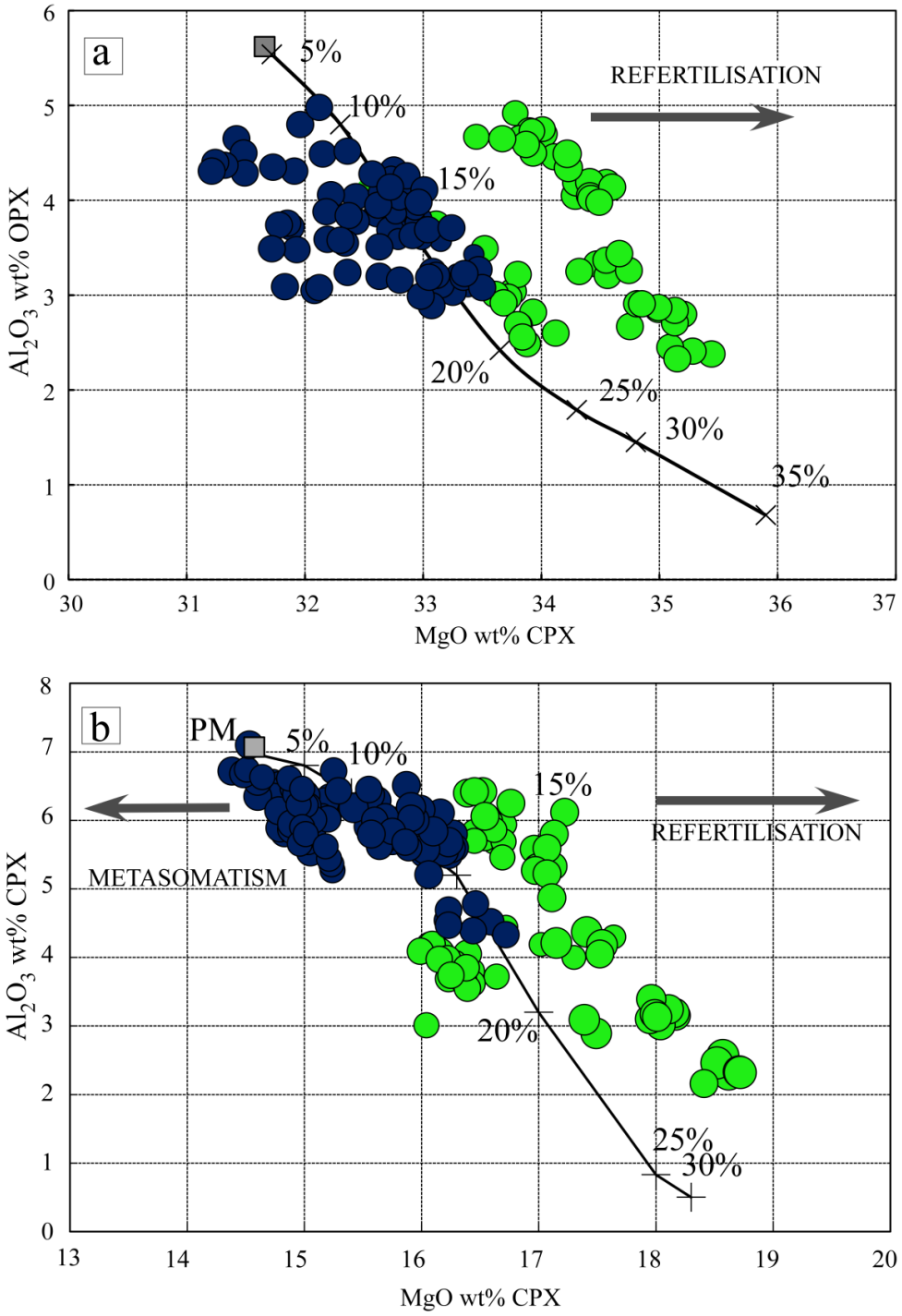

Fig. 6.7 Al_2O_3 vs. MgO melting trends (Upton, 2011) for opx (a) and cpx (b) in GP and HR peridotitic samples. The Al_2O_3 and MgO contents of primitive mantle (PM) opx and cpx (PMopx, PMcpx) were calculated on the basis of the primitive mantle composition of McDonough & Sun (1995). Tick marks on curves indicate partial melting percentages (F%).

6.4 Conclusions

To summarise this study, the sub continental lithospheric mantle of NVL suffered at least two enrichment processes related to two important geological events, firstly the tholeiitic magmatism that preceded the Gondwana break up in Jurassic and the locality that shows more the imprinting of this event is Greene Point, where the event is well testified by the Ferrar dolerites (Fig. 6.8). During Cenozoic, the alkaline metasomatism widely observed in NVL (Fig. 6.9), related to the WARS opening, locally interacted with the previously re-fertilised peridotitic system, and in some case (Baker Rocks and Harrow Peaks mantle segments) almost completely obscuring the previous refertilisation event. This last event is well identifiable where the interaction with the melt produced amphibole, even if it is possible to observe the different stage of these processes that are geochemically distinct.

Finally, HR, 400 km far from Mt. Melbourne district, reflects the presence of an alkaline metasomatism, strictly related to the Cenozoic magmatism, that in a time span of 200 years was able to completely blur the cpx primary features, but not the modal proportion among the peridotite minerals.

Notwithstanding, refertilisation vs. metasomatism processes are still matter of debate, the present study allowed to shed a light on the nature of these different enrichment styles, constraining their characteristics in term of geochemistry, melts involved and time space/ framework.

Fig. 6.8 Ferrar dolerites outcrops

Fig. 6.9 Cenozoic outcrops

References

Ackerman, L., ŠpaČek, P., Magna, T., Ulrych, J., Svojtka, M., Hegner, E. and Balogh, K., 2013. Alkaline and carbonate-rich melt metasomatism and melting of subcontinental lithospheric mantle: evidence from mantle xenoliths, NE Bavaria, Bohemian Massif. Journal of Petrology, v. 54, p. 2597–2633.

Antonini, P., Piccirillo, E.M., Petrini, R., Civetta, L., D'Antonio, M. and Orsi, G., 1999. Enriched mantle–Dupal signature in the genesis of the Jurassic Ferrar tholeiites from Prince Albert Mountains (Victoria Land, Antarctica). Contribution to Mineralogy and Petrology 136, 1–19.

Balestrieri, M.L., Bigazzi, G., Ghezzo, C., Lombardo, B., 1994. Fission track dating of apatites from the Granite Harbour Intrusive suite and uplift/denudation history of the Transantarctic Mountains in the area between David and Mariner Glaciers (Northern Victoria Land, Antarctica). Terra Antarctica 1 (1), 82–87.

Ballhaus, C., Berry, R. F., and Green, D., H., 1991. High pressure experiment calibration of the olivine–orthopyroxene–spinel oxygen barometer: implication for the oxidation state of the mantle. Contribution to Mineralogy and Petrology 107, 27–40.

Beccaluva, L., Coltorti, M., Orsi, G., Saccani, E., Siena, F., 1991. Nature and evolution of subcontinental lithospheric mantle of Antarctica: evidence from ultramafic xenoliths of the Melbourne volcanic province (northern Victoria Land, Antarctica). Memorie della Società Geologica Italiana 46, 353–370.

Beccaluva, L., Bonadiman, C., Coltorti, M., Salvini, L., Siena, F., 2001. Depletion events, nature of metasomatizing agent and timing of enrichment processes in lithospheric mantle xenoliths from the Veneto Volcanic Province. Journal of Petrology 42, 173–187.

Behrendt, J. C., LeMasurier, W. E., Cooper, A. K., Tessensohn, F., Tréhu, A., Damaske, D., 1991. Geophysical studies of the West Antarctic Rift System. Tectonics, 10(6), 1257–1273.

Behrendt, J. C., LeMasurier, W. E., Cooper, A. K., 1992. The West Antarctic Rift System-A propagating rift captured by a mantle plume? in Recent Progress in Antarctic Earth Science, edited by Y. Yoshida, K. Kaminuma, and K. Shiraishi, pp. 315–322, Terra Sci., Tokyo.

Berg, J.H., Moscasti, R.J., Herz, D.L., 1989. A petrologic geotherm from a continental rift in Antarctica. Earth and Planetary Science Letters 93, 98–108.

Bleeker, W. 2003. The late Archean record: a puzzle in ca. 35 pieces. Lithos, 71, 99–134.

Boger, S. D. 2011. Antarctica-before and after Gondwana. Gondwana Research, 19, 335–371.

Bonadiman, C., Beccaluva, L., Coltorti, M. and Siena, F., 2005. Kimberlite–like metasomatism and 'garnet signature' in spinel–peridotite xenoliths from Sal, Cape verde archipelago: relics of a subcontinental mantle domain within the Atlantic oceanic lithosphere? Journal of Petrology 46, 2465–2493.

Bonadiman, C., Coltorti, M., 2011. Numerical modelling for peridotite phase melting trends in the SiO_2–Al_2O_3–FeO–MgO–CaO system at 2 GPa. Mineralogy Magazine 75, 548.

Bonadiman, C., Nazzareni, S., Coltorti, M., Comodi, P., Giuli, G. and Faccini, B., 2014. Crystal chemistry of amphiboles: implications for oxygen fugacity and water activity in lithospheric mantle beneath Victoria Land, Antarctica. Contribution to Mineralogy and Petrology 167, 1–17

Bialas, R.W., Buck, W.R., Studinger, M., Fitzgerald, P.G., 2007. Plateau collapse model for the Transantarctic Mountains West Antarctic Rift system: insights from numerical experiments. Geology 35, 687–690.

Bradshaw J.D., Weaver S.D. and Laird M.G., 1985. Suspect Terranes and Cambrian Tectonics in Northern Victoria Land, Antarctica. In: Howell D.G. (ed.), Tectonostratigraphic Terranes of the

Circum–Pacific Region, Circum-Pacific Conference for Energyand Mineral Resources, Earth Science Series, 1, 467–479.

Brey, G. P., Köhler, T., 1990. Geothermobarometry in four–phase lherzolites II: New thermobarometers, and practical assessment of existing thermobarometers. Journal of Petrology 31, 1353–1378.

Brewer, T.S., Hergt, J.M., Hawkesworth, C.J., Rex, D. and Storey, B.C., 1992. Coats Land dolerites and the generation of Antarctic continental flood basalts, in: Magmatism and the Causes of Continental Break–up, B. Storey, T. Alabaster and R. Pankhurst, eds., Geol. Sot. London Spec. Publ. 68, 185–208.

Borg, S.G., Stump, E., Chappell, B.W., McCulloch, M.T., Wyborn, T., Armstrong, R.L., Holloway, J.R., 1987. Granitoids of Northern Victoria Land, Antarctica: implications of chemical and isotopic variations to regional crustal structure and tectonics. American Journal of Science 287, 127–169.

Borg S.G. and Stump E., 1987. Palaeozoic magmatism and associated tectonic problems of Northern Victoria Land, Antarctica. In: McKenzie, G.D. (ed.), Gondwana Six: Structure, Tectonics and Geophysics. Geophys. Monogr American Geophys. Union, 67–75.

Carmagnani, L., Ghezzo, C., Gosso, G., Lombardo, B., Meccheri, M., Montrasio, A., Pertusati, P.C., Salvini, F., 1989. Geology of the Wilson terrane in the area between David and Mariner Glaciers, Victoria Land (Antarctica). Mem. Soc. Geol. It. 33, 77–97

Campbell, I. H. & Allen, C. M. 2008. Formation of supercontinents linked to increases in atmospheric oxygen. Nature Geoscience, 1, 554–558

Cawood, P.A., McCausland, P.J.A., Dunning, G.R., 2001. Opening Iapetus: constraints from Laurentian margin in Newfoundland. Geological Society of America Bulletin 113, 443–453.

Chazot, G., Menzies, M.A., Harte, B., 1996b. Determination of partitioning coefficients between apatite, clinopyroxene, amphibole, and melt in natural spinel lherzolites from

Yemen: implication for wet melting of the lithospheric mantle. Geochimica et Cosmochima Acta 60, 423– 437.
Cherniak, D.J., 2003. REE diffusion in feldspar. Chemical Gology, v. 193, p. 25–41.

Coltorti, M., Bonadiman, C., Hinton, R.W., Siena, F., Upton, B.G.J., 1999. Carbonatite metasomatism of the oceanic upper mantle: evidence from clinopyroxenes and glasses in ultramafic xenoliths of Grande Comore, Indian Ocean. Journal of Petrology 40, 133–165.

Coltorti, M., Beccaluva, L., Bonadiman, C., Salvini, L., Siena, F., 2000. Glasses in mantle xenoliths as geochemical indicators of metasomatic agents. Earth and Planetary Science Letters. 183, 303–320.

Coltorti, M., Beccaluva, L., Bonadiman, C., Faccini, B., Ntaflos,T. & Siena, F., 2004. Amphibole genesis via metasomatic reaction with clinopyroxene in mantle xenoliths from Victoria Land, Antarctica. Lithos 75, 115–139.

Condie, K.C., 1998. Episodic continental growth and supercontinents: a mantle avalanche connection? Earth and Planetary Science Letters 163, 97–108

Cox, K. G., Macdonald, R. and Hornung, G., 1967. Geochemical and petrologic provinces in the Karoo basalts of Southern Africa. American Mineralogist 52, 1451–1474

Cox, K.G., 1988. The Karoo province. In: MacDougall, J.D. (Ed.), Continental Flood Basalts. Kluwer, Boston, MA, 239– 271.

Dalziel, I.W. D. and Elliot, D. H. 1982. West Antarctica– problem child of Gondwanaland. Tectonics, 1, 3–19

Dalziel, I. W. D. 1992. Antarctica; a tale of two supercontinents? Annual Review of Earth and Planetary Sciences, 20, 501–526.

Demarchi, G., Antonini, P., Piccirillo, E.M., Orsi, G., Civetta, L., D'Antonio, M., 2001. Significance of orthopyroxene and major element constraints on the petrogenesis of Ferrar

tholeiites from southern Prince AlbertMountains, Victoria Land, Antarctica. Contributions to Mineralogy and Petrology 142, 127–146

Dick, H. J. B. and Bullen, T.,1984. Chromian spinel as a petrogenetic indicator in abyssal and alpine–type peridotites and spatially associated lavas. Contribution to Mineralogy and Petrology 86, 54–76.

Elliot, D. H. 1975. The tectonics of Antarctica. American Journal of Science, A275, 45–106.

Elliot, D.H., 1999. Paleovolcanological setting of the middle Jurassic Mawson Formation: evidence from the Prince Albert Mountains, Victoria Land. Paper Presented at the 8th International Symposium on Antarctic Earth Sciences. Victoria Univ., Wellington, New Zealand.

Elliot, D.H., Fleming, T.H., Kyle, P.R., Foland, K. A., 1999. Long–distance transport of magmas in the Jurassic Ferrar Large Igneous Province, Antarctica. Earth and Planetary Science Letters 167, 89–104

Elliot, D.H., Fleming, T.H., 2000. Weddell triple junction: the principal focus of Ferrar and Karoo magmatism during initial breakup of Gondwana. Geology 28, 539– 542

Faccini, B., Bonadiman, C., Coltorti, M., Gregoire, M. & Siena, F., 2013. Oceanic material recycled within the sub–Patagonian lithospheric mantle (Cerro del Fraile, Argentina). Journal of Petrology 54, 1211–1258.

Faure, G., 1998, Principles and Applications of Geochemistry. Chapter. 18 pp 328–339.

Fedorov, L. V., Grikurov, G. E., Kurinin, R. G. & Masolov, V. N. 1982. Crustal structure of the Lambert Glacier area from geophysical data. In: Craddock, C. (ed.) Antarctic Geoscience. University of Wisconsin Press, Madison, WI, 931–936

Ferraccioli, F., Finn, C. A., Jordan, T. A., Bell, R. E., Anderson, L.M.& Damaske, D. 2011. East Antarctic rifting triggers uplift of the Gamburtsev Mountains. Nature, 479, 388–392.

Finn, C., Moore, D., Damaske, D., Mackey, T., 1999. Aeromagnetic legacy of early subduction along the Pacific margin of Gondwana. Geology 27, 1087–1090.

Fitzsimons, I. C. W. 2000a. A review of tectonic events in the East Antarctic Shield and their implications for Gondwana and earlier supercontinents. Journal of African Earth Sciences, 31, 3–23

Fitzgerald, P.G., 1994. Thermochronologic constraints on post–Paleozoic tectonic evolution of the central Transantarctic Mountains, Antarctica. Tectonics 13, 818–836.

Fitzgerald, P.G., Stump, E., 1997. Cretaceous and Cenozoic episodic denudation of the Transantarctic Mountains, Antarctica: new constraints from apatite fission track thermochronology in the Scott Glacier region. Journal of Geophysical Research 102 (B4), 7747–7765.

Fleming T.H., Foland K.A., Elliot D.H., 1995. Isotopic and chemical constraints on the crustal evolution and source signature of Ferrar magmas, north Victoria Land, Antarctica. Contributions to Mineralogy and Petrology 121, 217–236

Foley, S. (2010) A Reappraisal of Redox Melting in the Earth's Mantle as a Function of Tectonic Setting and Time. Journal of Petrology 52, 1363–1391.

GANOVEX–Team, 1987. Geological map of North Victoria Land, Antarctica, 1:500000 – Explanatory Notes. In: Tessensohn F & Roland N.W. (eds.), German Antarctic North Victoria Land Expedition (GANOVEX III), Vol. 2, Geologisches Jahrbuch, B 66, 7–79

Gentili, S., Biagioni, C., Comodi, P., Pasero, M., McCammon, C., Bonadiman, C., 2014. Ferri–kaersutite, IMA 2014–051. CNMNC Newsletter No.22. Mineralogical Magazine 78: 1245.

Gentili, S., Bonadiman, C., Biagioni, C, Comodi, P., Coltorti, M, Zucchini1 A., Ottolini, L., 2015. Oxo–amphiboles in mantle xenoliths: evidence for H2O–rich melt interacting with the lithospheric mantle of Harrow Peaks (Northern Victoria Land, Antarctica). Mineralogy and Petrology, DOI 10.1007/s00710–015–0404–4.

Gibson, G.M., Wright, T.O., 1985. Importance of thrust faulting in the tectonic development of northern Victoria Land, Antarctica. Nature 315, 480–483.

Goodge, J. W. 2002. From Rodinia to Gondwana: supercontinent evolution in the Transantarctic Mountains. In: Gamble, J. A., Skinner, D. N. B. & Henrys, S. (eds) Antarctica at the Close of a Millennium. Royal Society of New Zealand, Bulletin, 35, 61–74.

Green D.H., Hibberson W.,1970. The instability of plagioclase in peridotite at high pressure. Lithos 3, 209–221.

Grégoire. M., Moine, B.N., O'Reilly, S.Y., Cottin, J.Y. and Giret., A. 2000. Trace element residence and partitioning in mantle xenoliths metasomatised by high alkaline silicate and carbonatite-rich melts (Kerguelen Islands, Indian Ocean). Journal Petrology, v. 41, p. 477-509.

Griffin W.L., Schmidt, D., and Ryan, C.G. 1996. Trace element zoning in mantle minerals: metasomatism and thermal event in the upper mantle. Canadian Mineralogist, v. 34, p. 1179-1193

Griffin, W.L., Graham, S., O'Reilly, S.Y., Pearson, N.J., 2004. Lithosphere evolution beneath Kaapvaal Craton: Re–Os systematic of sulphides in mantle derived peridotites. Chemical Geology 208, 89–118.

Gurnis, M. 1988. Large–scale mantle convection and the aggregation and dispersal of supercontinents. Nature, 332, 695–699.

Harley, S. L. 2003. Archaean–Cambrian crustal development of East Antarctica: metamorphic characteristics and tectonic implications. In: Yoshida, M., Windley, B. F. & Dasgupta, S. (eds) Proterozoic East Gondwana: Supercontinent Assembly and Breakup. Geological Society, London, Special Publications, 206, 203–230.

Harley, S.L., Fitzsimons, I.C.W., Zhao, Y., 2013. Antarctica and supercontinent evolution: historical perspectives, recent advances and unresolved issues.

In: Harley, S.L., Fitzsimons, I.C.W., Zhao, Y. (Eds.), Antarctica and Supercontinent Evolution. Geological Society, London, Special Publication, 383, pp. 1–34

Harris, C., Watters, B. R. and Groenewald, P. B., 1991. Geochemistry of the Mesozoic regional basic dykes of western Dronning Maud Land, Antarctica. Contributions to Mineralogy and Petrology 107, 100–111.

Hellebrand, E., Snow, J. E., Hoppe, P. & Hofmann, A. W., 2002. Garnet-field melting and late–stage refertilization in 'residual' abyssal peridotites from the Central Indian Ridge. Journal of Petrology 43, 2305–2338.

Hergt, J.M., Chappell, B.W, Faure G., Mensing T. M., 1989a. The geochemistry of Jurassic dolerites from Portal Peak, Antarctica. Contributions to Mineralogy and Petrology 102, 298–305.

Hergt, J.M., Chappell, B.W., McCulloch, M.T., McDougall, I., Chivas, A.R., 1989b. Geochemical and isotopic constraints on the origin of the Jurassic dolerites of Tasmania. Journal of Petrology 30, 841–883.

Hergt, J.M., Peate, D.W., Hawkesworth, C.J., 1991. The petrogenesis of Mesozoic Gondwana low–Ti flood basalts. Earth and Planetary Science Letters 105, 134–148.

Hergt, J.M., 2000. Comment on "Enriched mantle-Dupal signature in the genesis of the Jurassic Ferrar tholeiites from Prince Albert Mountains (Victoria Land, Antarctica)". Contributions to Mineralogy and Petrology 139, 240–244.

Herzberg, C., 2004. Geodynamic information in peridotite petrology. Journal of Petrology 45, 2507–2530.

Ionov D. A., Griffin W.L., O'Reilly S.Y., 1997. Volatile-bearing minerals and lithophile trace elements in the upper mantle Chemical Geology 141, 153–184.

Ionov, D., 1998. Trace element composition of mantle-derived carbonates and coexisting phases in peridotite xenoliths from alkali basalts. Journal of Petrology, v. 39, p. 1931-1941

Ionov, D. A. and Hofmann, A. W., 2007. Depth of formation of subcontinental off–craton peridotites. Earth and Planetary Science Letters 261, 620–634.

Johnson, K. T. M., Dick, H. J. B. & Shimizu, N.,1990. Melting in the oceanic upper mantle: An ion microprobe study of diopsides in abyssal peridotites. Journal of Geophysical Research 90, 2661–2678.

Kaz'min, V.G., 1988. Tectonic evolution of the mozambique belt: from accretion to collision. Geotektonika 22 (3), 26–34.

Khain, V.E., 2000. Tectonics of Continents and Oceans. NauchnyiMir, Moscow. (in Russian).

Kheraskova, T.N., Bush, V.A., Didenko, A.N., Samygin, S.G., 2009. Breakup of Rodinia and early stages of evolution of the Paleoasian ocean. Geotectonics 44, 3–24

Khudolei, A. K., 2003. Doctoral dissertation in geology and mineralogy (Moscow).

Kleinschmidt, G., Tessensohn, F., 1987. Early Paleozoic westward directed subduction at the pacific margin of Antarctica. 6th Gondwana Symposium. AGU, pp. 89–105.

Kyle, P.R., 1976. Geology, Mineralogy and Geochemistry of the Late Cenozoic McMurdo Volcanic Group, Victoria Land, Antarctica. PhD thesis Victoria University of Wellington, New Zealand 444.

Kyle, P.R., 1980. Development of Heterogeneities in the Subcontinental Mantle:
Evidence from the Ferrar Group, Antarctica. Contributions to Mineralogy and Petrology 73, 89–104.

Kyle, P.R., 1990. McMurdo Volcanic Group, Western Ross Embayment, in Volcanoes of the Antarctic Plate and Southern Oceans, Antarct. Res. Ser., vol. 48, edited by W. E. Le Masurier and J. W. Thomson, pp. 19– 25, AGU, Washington, D. C.

Laube, N., Hergarten, S., Neugebauer, H.J., 1996. MODUSCAL — a computer program to calculate a mode from a geochemical rock analysis. Comput. Geosci. U. K. 22 (6), 631–637.

Le Bas, M. J., Le Maitre, R. W. & Woolley, A. R., 1992. The construction of the total alkali-silica chemical classification of the volcanic rocks. Mineralogy and Petrology 46, 1–22

Le Masurier, W. E., Rex D. C., 1989. Evolution of linear volcanic ranges in Marie Byrd Land, Antarctica. Journal of Geophysical Research 94 (B6), 7223 –7236.

Le Masurier, W. E., Thomson J. W., (Eds.) 1990. Volcanoes of the Antarctic Plate and Southern Oceans. Antarct. Res. Ser., vol. 48, 487 pp., AGU, Washington, D. C.

Li, Z.X., Bogdanova, S.V., Collins, A.S., 2008. Assembly, configuration, and breakup history of Rodinia: a synthesis. Precambrian Research 160, 179–210.

Li, Z.–X. & Zhong, S. 2009. Supercontinent-superplume coupling, true polar wander and plume mobility: late dominance in whole-mantle tectonics. Physics of the Earth and Planetary Interiors, 176, 143–156.

Liang, Y., Sun, C., Yao L., 2013. A REE-in-two-pyroxene thermometer for mafic and ultramafic rocks. Geochimica et Cosmochimica Acta, v. 102, p. 46–260

Liermann, H. P. and Ganguly, J., 2003. Fe^{2+}-Mg fractionation between orthopyroxene and spinel: experimental calibration in the system $FeO–MgO–Al_2O_3–Cr_2O_3–SiO_2$, and applications. Contribution to Mineralogy and Petrology 145, 217–227.

Lisker, F., Brown, R. & Fabel, D. 2003. Denudational and thermal history along a transect across theLambert Graben, northern Prince Charles Mountains, Antarctica, derived from apatite fission track thermochronology. Tectonics, 22, 1055, http://dx.doi.org/10.1029/2002TC001477.

Luttinen, A. V., Rämö, O. T. And Huhma, H.,1998. Nd and Sr isotopic and trace element composition of a Mesozoic CFB suite from Dronning Maud Land, Antarctica: implications for lithosphere and asthenosphere contributions to Karoo magmatism. Geochimica et Cosmochimica Acta 62, 2701–2714.

Marthy, A.K.S., 1973. A least-squares solution to mass balance around a chemical reactor. Ind. Eng. Chem. Process. Des. Dev. 12 (3), 246–248.

Martin, A. P., Price, R.C., Cooper, A. F., McCammon, C.A. 2015. Petrogenesis of the Rifted Southern Victoria Land Lithospheric Mantle, Antarctica, Inferred from Petrography, Geochemistry, Thermobarometry and Oxybarometry of Peridotite and Pyroxenite Xenoliths from the Mount Morning Eruptive Centre. Journal of Petrology 56, 193–226

Matusiak-Małek M, Puziewicz J, Ntaflos T, Grégoire, M., Benoit, M, Klügel, A., 2014. Two contrasting lithologies in off-rift sub-continental lithospheric mantle beneath Central Europe— the Krzeniów (SW Poland) case study. Journal of Petrology, v. 55, no9, 1799 — 1828

McCammon, C. and Kopylova M. G. 2004. A redox profile of the Slave mantle and oxygen fugacity control in the cratonic mantle. Contribution to mineralogy and petrology 148, 55–68

Mc Donough, W. F., and Sun S.–s., 1995. The composition of the Earth. Chemical Geology 120, 223–253.

Melchiorre, M., Coltorti, M., Bonadiman, B., Faccini, B., O'Reilly, S. Y. and Pearson, N., 2011. The role of eclogite in the rift-related metasomatism and Cenozoic magmatism of Northern Victoria Land, Antarctica. Lithos 124, 319–330.

Melchiorre, M., Coltorti, M., Gregoire, M., Benoit, M., 2015. Refertilization process in the Patagonian subcontinental lithospheric mantle of Estancia Sol de Mayo (Argentina), Tectonophysics, doi: 10.1016/j.tecto.2015.02.015

Melluso, L., Hergt J.M., Zanetti A., 2014. The late crystallization stages of low-Ti, low-Fe tholeiitic magmas: Insights from evolved Antarctic and Tasmanian rocks. Lithos 188 ,72–83

Mercier, J.C., Nicolas, A., 1975. Textures and Fabrics of the Upper-Mantle Peridotites as illustrated by Xenoliths from Basalts. Journal of Petrology 16, 454–487

Molzahn, M., Reisberg, L., Wörner G. 1996. Os, Sr, Nd, Pb, O isotope and trace element data from the Ferrar flood basalts, Antarctica: evidence for an enriched subcontinental lithospheric source. Earth and Planetary Science Letters 144, 529–546

Mossakovsky, A.A., Pushcharovsky, Yu.M., Ruzhentsev, S.V., 1996. Spatiotemporal relationships between the Pacific and Indo–Atlantic type structures in the late Precambrian and the Vendian. Doklady Akademii Nauk 350 (6), 799–802.

Morimoto, N.,1989. Nomenclature of pyroxenes. Canadian Mineralogist 27, 143–156.

Müller, P., Schmidt–Thome´, M., Kreuzer, H., Tessensohn, F., Vetter, U., 1991. Cenozoic peralkaline magmatism at the western margin of the Ross Sea, Antarctica, Memorie della Società Geologica Italiana 46, 315–336.

Nance, R. D., Murphy, J. B. & Santosh, M. 2013. The supercontinent cycle: a retrospective essay. Gondwana Research, http://dx.doi.org/10.1016/j.gr.2012.12.026

Nardini, I., Armienti, P., Rocchi, S., Dallai, L., Harrison, D., 2009. Sr–Nd–Pb–He–O isotope and geochemical constraints on the genesis of Cenozoic magmas from the West Antarctic Rift. Journal of Petrology 50, 1359–1375.

Niu, Y., 2004. Bulk-rock Major and Trace Element Compositions of Abyssal Peridotites: Implications for Mantle Melting, Melt Extraction and Post-melting Processes Beneath Mid–Ocean Ridges. Journal of Petrology 45, 2423–2458

O'Neill, H. S. C., Wall, V. J., 1987. The olivine-orthopyroxene-spinel oxygen geobarometer, the nickel precipitation curve, and the oxygen fugacity of the Earth's upper mantle. Journal of Petrology 28, 1169–1191.

Paktunc, A.D., 1998. MODAN: an interactive computer program for estimating mineral quantities based on bulk composition. Computers and Geosciences 24, p. 425–431.

Pearce, N.J.G., Perkins, W.T., Westgate, J.A., Gorton, M.P., Jackson, S.E., Neal, C.R., Chenery, S.P., 1997. A compilation of new and published major and trace data for NIST SRM 610 and NIST SRM 612 glass reference materials. Geostandards Newsletter 21, 115–144.

Pelorosso, B., Bonadiman, C., Coltorti, M., Faccini, B., Melchiorre, M., Ntaflos, T., Gregoire, M., 2016. Pervasive, tholeiitic refertilisation and heterogeneous metasomatism in Northern Victoria Land lithospheric mantle (Antarctica). Lithos, v. 248–251, p. 493–505.

Perinelli, C., Armienti, P., Dallai, L., 2006. Geochemical and O-isotope constraints on the evolution of lithospheric mantle in the Ross Sea rift area (Antarctica). Contributions to Mineralogy and Petrology 151, 245–266.

Perinelli, C., Orlando, A., Conte, A. M., Armienti, P., Borrini, D., Faccini, B. and Misiti,V., 2008. Metasomatism induced by alkaline magma on upper mantle of the Northern Victoria Land (Antarctica): an experimental approach. In: Coltorti, M. and Grégoire, M. (eds) Mantle Metasomatism in Intra–plate and Suprasubduction Settings. Geological Society, London, Special Publications 293, 197–221,

Perinelli, C., Armienti, P., Dallai, L., 2011. Thermal evolution of the lithosphere in a rift environment as inferred from the geochemistry of mantle cumulates; Northern Victoria Land, Antarctica. Journal of Petrology 52, 665–690

Perinelli C., Andreozzi, G.B., Conte, A.M., Oberti, R., Armienti, P. 2012. Redox state of subcontinental lithospheric mantle and relationships with metasomatism: insights from spinel peridotites from northern Victoria Land (Antarctica). Contribution to Mineralogy and Petrology 164, 1053–1067.

Pfänder, J. A., Jung, S., Mu¨ nker, C., Stracke, A. and Mezger, K., 2012. A possible high Nb/Ta reservoir in the continental lithospheric mantle and consequences on the global Nb budget—Evidence from continental basalts from Central Germany. Geochimica et Cosmochimica Acta, v. 77, p. 232–251.

Popp, R.K., Hibbert, H.A., Lamb, W.M., 2006. Oxy–amphibole equilibria in Ti–bearing calcic amphiboles: experimental investigation and petrologic implications for mantle–derived amphiboles. American Mineralogist 91, 54–66

Pouchou, J.L., Pichoir, F., 1991. Quantitative analysis of homogeneous or stratified microvolumes applied the model ‘‘PAP’’. In: Heinrich, K.F.J., Newbury, D.E. (Eds.), Electron Probe Quantification. Plenum Plenum, New York, London, pp. 31–35.

Preiss, W.V., 2000. The Adelaide geosyncline of south Australia and its significance in Neoproterozoic continental reconstruction. Precambrian Research 100 (1), 21–63.

Reeves, C. V., Sahu, B. K. and de Wit, M. J. 2002. A re-examination of the paleo-position of Africa's eastern neighbours in Gondwana. Journal of African Earth Sciences, 34, 101–108.

Riley, T.R, Leat P.T., Storey B.C., Parkinson I.J, Millar I.L., 2002. Ultramafic lamprophyres of the Ferrar large igneous province: evidence for a HIMU mantle component. Lithos, 66, 63–76

Riley, T. R., Leat, P.T., Curtis, M. L., Millar, I. L., Duncan, R. A. and Fazel, A., 2005. Early–Middle Jurassic Dolerite Dykes from Western Dronning Maud Land (Antarctica): Identifying Mantle Sources in the Karoo Large Igneous Province. Journal of Petrology 46, 1489–1524.

Rocchi, S., Tonarini, S., Armienti, P., Innocenti, F., Manetti, P., 1998. Geochemical and isotopic structure of the early Palaeozoic active margin of Gondwana in northern Victoria Land, Antarctica. Tectonophysics 284, 261–281

Rocchi, S., Armienti, P., D'Orazio, M., Tonarini, S., Wijbrans, J.R., Di Vincenzo, G., 2002. Cenozoic magmatism in the western Ross Embayment: role of mantle plume versus plate dynamics in the development of the West Antarctic Rift System. Journal of Geophysical Research 107, 2195.

Schmidt, D.L., Rowley, P.D., 1986. Continental rifting and transform faulting along the Jurassic Transantarctic Rift, Antarctica. Tectonics 5, 279–291

Schneider, M.E. and Eggler, D.H., 1986. Fluids in equilibrium with peridotite minerals: implications for mantle metasomatism. Geochimica et Cosmochimica Acta, v. 50, p. 711-724

Storey, B.C., Alabaster, T., 1991. Tectonomagmatic controls on Gondwana break–up models: evidence from the proto–Pacific margin of Antarctica. Tectonics 10 (6), 1274–1288.

Stump, E., 1995. The Ross Orogen of the Transantarctic Mountains, 284 pp., Cambridge Univ. Press, New York

Stump, E., Fitzgerald, P.G., 1992. Episodic uplift of the Transantarctic Mountains. Geology 20, 161–164.

Stump, E. 1995. The Ross Orogen of the Transantarctic Mountains. Cambridge University Press, Cambridge

Taylor, W.R., Green, D.H., 1988. Measurement of reduced peridotite–C–O–H solidus and implications for redox melting of the mantle. Nature 332, 349–352.

Taylor, W.R., 1998. An experimental test of some geothermometer and geoba– rometer formulations for upper mantle peridotites with application to the thermobarometry of fertile Iherzolite and garnet websterite. Neues Jahrb. Mineral. Abh. 172 (2–3), 381–408.

Tiepolo, M., Bottazzi, P., Palenzona, M., Vannucci, R., 2003. A Laser probe coupled with ICP–double–focusin sector–field mass spectrometer for in situ analysis of geological samples and U–Pb dating of zircon. The Canadian Mineralogy 41, 259– 272.

Tingey, R. J. 1991. The regional geology of Archaean and Proterozoic rocks in Antarctica. In: Tingey, R. J. (ed.) The Geology of Antarctica. Oxford University Press, Oxford, 1–73.

Tirone, M., Ganguly, J., Dohmen, R., Langenhorst, F., Hervig, R., Becker, H.W., 2005. Rare earth diffusion kinetics in garnet: Experimental studies and applications. Geochimica et Cosmochima Acta, v. 69, p. 2385– 2398.

Tohver, E., D'Agrella-Filho, M. S. & Trinidade, R. I. F. 2006. Paleomagnetic record of Africa and South America for the 1200–500 Ma interval, and evaluation of Rodinia and Gondwana assemblies. Precambrian Research, 147, 193–222.

Torsvik, T. H., Gaina, C., Redfield, T. F. 2008. Antarctica and global paleogeography: from Rodinia, through Gondwanaland and Pangea, to the birth of the Southern Ocean and the opening of gateways. In: Cooper, A. K., Barrett, P. J., Stagg, H., Storey, B., Stump, E.,Wise, W. & THE 10TH ISAES EDITORIAL TEAM (eds) Antarctica: A Keystone in a Changing World. National Academies Press, Washington, DC, 125–140.

Tonarini, S., Rocchi, S., Armienti, P., Innocenti, F., 1997. Constraints on timing of Ross Sea rifting inferred from Cainozoic intrusions from northern Victoria Land, Antarctica.
In: Ricci, C.A. (Ed.), The Antarctic Region: Geological Evolution and Processes.:
Proceedings of the 7th International Symposium on Antarctic Earth Sciences. Terra Antarctica, Siena, Italy, pp. 511–521.

Tucker, R. D., Roig,J.-Y., Delor, C., Amelin, Y., Goncalves, P., Rabarimanana, M. H., Ralison, A. V., W. Belcher, R., 2011. Neoproterozoic extension in the Greater Dharwar Craton: a reevaluation of the "Betsimisaraka suture" in Madagascar.
Canadian Journal of Earth Sciences, 2011, 48, no 2, 389–417

Upton, B. G. J., Downes, H., Kirstein, L. A., Bonadiman, C., Hill, P. G. and Ntaflos, T., 2011. The lithospheric mantle and lower crust– mantle relationships under Scotland: a xenolithic perspective. Journal of the Geological Society, London 168, 873–886.

Valentine, J. W. & Moores, E. M., 1970. Plate tectonic regulation of faunal diversity and sea level: a model. Nature, 228, 657–659.

Van Orman, J.A., Grove, T.L., N. Shimizu, N., 2001. Rare earth element diffusion in diopside: influence temperature, pressure and ionic radius, and an elastic model for diffusion in silicates, Contribution to Mineralogy and Petrology, v. 141, p. 687-703.

Vannucci R., Piccardo G.B., Rivalenti G., Zanetti A., Rampone E., Ottolini L., Oberti R., Mazzucchelli M. and Bottazzi P., 1995. Origin of LREE–depleted amphiboles in the subcontinental mantle. Geochimica et Cosmochimica Acta 59, 1763–1771.

Vaughan, A. P. M., Leat, P. T. & Pankhurst, R. J. 2005. Terrane processes at the margins of Gondwana: introduction. In: Vaughan, A. P. M., Leat, P. T. & Pankhurst, R. J. (eds) Terrane Processes at the Margin of Gondwana. Geological Society, London, Special Publications, 246, 1–21.

Weaver S.D., Bradshaw J.D. & Laird M.G., 1984. Geochemistry of Cambrian volcanics of the Bowers Supergroup and implications for the Early Palaeozoic tectonic evolution of northern Victoria Land, Antarctica. Earth and Planetary Science Letters, 68, 128 140

Williams, H., Hoffman, P. F., Lewry, J. F., Monger, J. W. H. & Rivers, T. 1991. Anatomy of North America: thematic portrayals of the continent. Tectonophysics, 187, 117–143

Workman, R., K., and Hart, S.R., 2004. Major and trace element composition of the depleted MORB mantle (DMM). Earth and Planetary Science Letters 231, 53– 72.

Wright, T.L., Doherty, P.C., 1970. A linear programming and least–squares computer method for solving petrologic mixing problems. Geol. Soc. Am. Bull. 81, 1995–2008

Yaxley, G.M., Kamenetsky, V., 1999. In situ origin for glass in mantle xenoliths from southeastern: insights from trace element compositions of glasses and metasomatic phases. Earth and Planetary Science Letters 172, 97– 109.

Yaxley, G.M., Kamenetsky, V., Green, D.H., Faloon, T.J., 1997. Glasses from mantle xenoliths from Western Victoria, Australia, and their relevance to mantle processes. Earth and Planetary Science Letters 148, 433– 446.

Zhao, Y., Liu, X. H., Liu, X. C. & Song, B. 2003. Pan-African events in Prydz Bay, East Antarctica and its inference on East Gondwana tectonics. In: Yoshida, M., Windley, B. F. & Dasgupta, S. (eds) Proterozoic East Gondwana: Supercontinent Assembly and Breakup. Geological Society, London, Special Publications, 206, 231–245.

Zindler, A., Hart, S.R., 1986. Chemical geodynamics. Annual Review of Earth and Planetary Sciences 14, 493–571.

Zipfel, J. & Wörner, G., 1992. Four– and five-phase peridotites from acontinental rift system: evidence for upper mantle uplift and coolin at the Ross Sea margin (Antarctica). Contributions to Mineralogy and Petrology 111, 24–36.

Zou, H. B. 1998. Trace element fractionation during modal and non–modal dynamic melting and open–system melting: A mathematical treatment. Geochimica et Cosmochimica Acta 62, 1937–1945.